FINAL REPORT ~ FHWA-OK-21-03

EVALUATION OF ULTRA-HIGH-PERFORMANCE CONCRETE FOR USE IN BRIDGE CONNECTIONS AND REPAIR

Royce W. Floyd, Ph.D., P.E.
Jeffery S. Volz, S.E., P.E., Ph.D.
Chandler K. Funderburg, M.S.
Amy S. McDaniel, M.S.
Trevor Looney, P.E. Ph.D. Candidate
Jake Choate, Ph.D. Candidate
Stephen Roswurm, Ph.D. Candidate
Connor Casey, M.S.
Raina Coleman, M.S.
Maranda Leggs, M.S.
Kim Serey Vuth Chea, M.S

School of Civil Engineering and Environmental Science
The University of Oklahoma
Norman, Oklahoma

February 2020

OKLAHOMA Transportation

The Oklahoma Department of Transportation (ODOT) ensures that no person or groups of persons shall, on the grounds of race, color, sex, religion, national origin, age, disability, retaliation or genetic information, be excluded from participation in, be denied the benefits of, or be otherwise subjected to discrimination under any and all programs, services, or activities administered by ODOT, its recipients, sub-recipients, and contractors. To request an accommodation please contact the ADA Coordinator at 405-521-4140 or the Oklahoma Relay Service at 1-800-722-0353. If you have any ADA or Title VI questions email ODOT-ada-titlevi@odot.org.

EVALUATION OF ULTRA-HIGH-PERFORMANCE CONCRETE FOR USE IN BRIDGE CONNECTIONS AND REPAIR

FINAL REPORT ~ FHWA-OK-21-03
ODOT SPR ITEM NUMBER 2276

Submitted to:
Office of Research and Implementation
Oklahoma Department of Transportation

Submitted by:
Royce W. Floyd, Ph.D., P.E.
Jeffery S. Volz, S.E., P.E., Ph.D.
Chandler K. Funderburg, M.S.
Amy S. McDaniel, M.S.
Trevor Looney, P.E. Ph.D. Candidate
Jake Choate, Ph.D. Candidate
Stephen Roswurm, Ph.D. Candidate
Connor Casey, M.S.
Raina Coleman, M.S.
Maranda Leggs, M.S.
Kim Serey Vuth Chea, M.S
School of Civil Engineering and Environmental Science (CEES)
The University of Oklahoma

OKLAHOMA
Transportation

February 2020

TECHNICAL REPORT DOCUMENTATION PAGE

1. REPORT NO.	2. GOVERNMENT ACCESSION NO.	3. RECIPIENT'S CATALOG NO.
FHWA-OK-21-03		

4. TITLE AND SUBTITLE	5. REPORT DATE
Evaluation of Ultra-High-Performance Concrete for use in Bridge Connections and Repair	Feb 2021
	6. PERFORMING ORGANIZATION CODE
7. AUTHOR(S)	8. PERFORMING ORGANIZATION REPORT
Royce W. Floyd, Jeffery S. Volz, Chandler K. Funderburg, Amy S. McDaniel, Trevor Looney, Jake Choate, Stephen Roswurm, Connor Casey, Raina Coleman, Maranda Leggs, Kim Serey Vuth Chea	Click here to enter text.
9. PERFORMING ORGANIZATION NAME AND ADDRESS Donald G. Fears Structural Engineering Laboratory School of Civil Engineering and Environmental Science The University of Oklahoma, 303 E. Chesapeake St., Norman, OK 73019	10. WORK UNIT NO.
	11. CONTRACT OR GRANT NO. ODOT SPR Item Number 2276
12. SPONSORING AGENCY NAME AND ADDRESS Oklahoma Department of Transportation Office of Research and Implementation 200 N.E. 21st Street, Room G18 Oklahoma City, OK 73105	13. TYPE OF REPORT AND PERIOD COVERED Final Report Oct 2016 - Oct 2020
	14. SPONSORING AGENCY CODE

15. SUPPLEMENTARY NOTES

Click here to enter text.

16. ABSTRACT

The project described in this report evaluated available proprietary ultra-high performance concrete (UHPC) materials and UHPC mix designs made with local materials for applicability to bridge joint installation and repair in Oklahoma and developed recommendations for continued usage of UHPC in bridge construction in Oklahoma. Phase 1 of the project developed a promising UHPC mix design, J3, using local materials. Two specific applications of UHPC were considered: deck slab joints and girder continuity connections. Initial investigation of deck slab joint details was conducted using small-scale flexural specimens to evaluate bond strength between UHPC and base concrete. Laboratory-scale full-depth joints were cast and tested using both the proprietary UHPC material and the OU developed J3 mix design. Laboratory-scale UHPC connections for live load continuity between precast girders were also designed and tested to failure. Two different connection details were used, one representing new construction and one representing retrofit of an existing structure. A field test involving retrofit of an existing expansion joint with UHPC joint headers was conducted on a bridge identified in conjunction with ODOT and was monitored for almost three years. Phase 2 involved slab testing for a partial depth slab joint detail, examination of reinforcement bond, and durability testing of both proprietary and non-proprietary UHPC. UHPC bond to concrete substrate was also examined for different surface preparations and base concrete saturation levels. The findings of the research indicate that UHPC provides improved performance relative to conventional materials for the applications tested and the J3 mix design exhibits similar performance to proprietary UHPC.

17. KEY WORDS	18. DISTRIBUTION STATEMENT		
UHPC, bond, slab joints, continuity, durability	No restrictions. This publication is available from the Office of Research and Implementation, Oklahoma DOT.		
19. SECURITY CLASSIF. (OF THIS REPORT)	20. SECURITY CLASSIF. (OF THIS PAGE)	21. NO. OF PAGES	22. PRICE
Unclassified	Unclassified	358	N/A

SI* (MODERN METRIC) CONVERSION FACTORS

APPROXIMATE CONVERSIONS TO SI UNITS

SYMBOL	WHEN YOU KNOW	MULTIPLY BY	TO FIND	SYMBO
		LENGTH		
in	inches	25.4	millimeters	mm
ft	feet	0.305	meters	m
yd	yards	0.914	meters	m
mi	miles	1.61	kilometers	km
		AREA		
in^2	square inches	645.2	square millimeters	mm^2
ft^2	square feet	0.093	square meters	m^2
yd^2	square yard	0.836	square meters	m^2
ac	acres	0.405	hectares	ha
mi^2	square miles	2.59	square kilometers	km^2
		VOLUME		
fl oz	fluid ounces	29.57	milliliters	m
gal	gallons	3.785	liters	L
ft^3	cubic feet	0.028	cubic meters	L
yd^3	cubic yards	0.765	cubic meters	m^3
	NOTE: volumes greater than 1000 L shall be		shown in m^3	m^3
		MASS		
oz	ounces	28.35	grams	g
lb	pounds	0.454	kilograms	kg
T	short tons (2000 lb)	0.907	megagrams (or "metric ton")	Mg (or "t")
		TEMPERATURE (exact degrees)		
°F	Fahrenheit	5 (F-32)/9 or (F-32)/1.8	Celsius	°C
		ILLUMINATION		
fc	foot-candles	10.76	lux	lx
fl	foot-Lamberts	3.426	$candela/m^2$	cd/m^2
		FORCE and PRESSURE or STRESS		
lbf	poundforce	4.45	newtons	N
lbf/in^2	poundforce per square inch	6.89	kilopascals	kPa

APPROXIMATE CONVERSIONS FROM SI UNITS

SYMBOL	WHEN YOU KNOW	MULTIPLY BY	TO FIND	SYMBO
		LENGTH		
mm	millimeters	0.039	inches	in
m	meters	3.28	feet	ft
m	meters	1.09	yards	yd
km	kilometers	0.621	miles	mi
		AREA		
mm^2	square millimeters	0.0016	square inches	in^2
m^2	square meters	10.764	square feet	ft^2
m^2	square meters	1.195	square yards	yd^2
ha	hectares	2.47	acres	ac
km^2	square kilometers	0.386	square miles	mi^2
		VOLUME		
mL	milliliters	0.034	fluid ounces	fl oz
L	liters	0.264	gallons	gal
m^3	cubic meters	35.314	cubic feet	ft^3
m^3	cubic meters	1.307	cubic yards	yd^3
		MASS		
g	grams	0.035	ounces	oz
kg	kilograms	2.202	pounds	lb
Mg (or "t")	megagrams (or "metric ton")	1.103	short tons (2000 lb)	T
		TEMPERATURE (exact degrees)		
°C	Celsius	1.8C+32	Fahrenheit	°F
		ILLUMINATION		
lx	lux	0.0929	foot-candles	fc
cd/m^2	$candela/m^2$	0.2919	foot-Lamberts	fl
		FORCE and PRESSURE or STRESS		
N	newtons	0.225	poundforce	lbf
kPa	kilopascals	0.145	poundforce per square inch	lbf/in^2

*SI is the symbol for the International System of Units. Appropriate rounding should be made to comply with Section 4 of ASTM E380. (Revised March 2003)

ACKNOWLEDGEMENTS

The work of Fears Lab Manager/Technician Mr. Michael Schmitz in providing support for this project is greatly appreciated. The following undergraduate students (at the time) who participated in the project and made a substantial contribution are acknowledged: Mathew Alvarado, Kaitlyn Anderson, Eric Budder, Richard Campos, Yana Dyachkova, Levi Kell, Jacob Starks, and Cole Walker.

The following companies provided materials and/or technical input at a reduced cost or at no cost for this project: LafargeHolcim Ductal®, Dolese Bros. Inc., Norchem Corporation, Bekaert, Phoscrete Corporation.

A research project supported by the Accelerated Bridge Construction University Transportation Center (ABC-UTC) titled “Development of Non-Proprietary UHPC Mix” provided funding that allowed for expanding the scope of this project.

EXECUTIVE SUMMARY

Deterioration of bridges can often be related to poor performance of longitudinal connections between precast members or transverse deck joints. Ultra-high performance concrete (UHPC) is a cementitious composite with mechanical and durability properties far exceeding those of conventional concrete, which makes it an ideal material for bridge deck joints. UHPC is a relatively expensive material and is most economical when use of a small quantity can have a large impact on overall performance of a structure. This consisted of two phases focused on evaluation of available proprietary UHPC materials and mix designs made with local materials for applicability to bridge joint installation and repair in Oklahoma.

In Phase 1, three promising mix designs using local materials were developed through a systematic investigation of mixture constituents and methods for obtaining optimal particle packing density. After conducting a materials property comparison, one of these mixes, mix J3, was considered for further structural testing. Two specific applications of UHPC were considered: deck slab joints and girder continuity connections. Initial investigation of deck slab joint details was conducted using small-scale flexural specimens to evaluate bond strength between UHPC and base concrete for different surface preparation methods. Laboratory-scale full-depth joints were cast between 4 ft x 4 ft slab specimens using both the proprietary UHPC material Ductal® and the OU developed J3 mix design, the joint surface preparation methods identified by small-scale testing, and reinforcing details taken from the literature and standard ODOT practice. The composite slabs were then tested in flexure. Two slabs from each group of three were load tested to failure and one slab from each group was tested using a cyclic load at the approximate magnitude of the cracking moment. Results of this testing indicated that the UHPC joint improved the capacity of the slabs and that the J3 material performed similarly to the proprietary UHPC.

Laboratory-scale girder continuity connections were designed based on standard practice and were tested to failure. Two different connection details were used, one representing new construction and one representing a retrofit of an existing structure. A series of three specimens was cast for each detail using two 18 ft long, approximately

half-scale AASHTO Type II prestressed concrete beams and the proprietary UHPC Ductal®. Both joint details produced an effective continuity connection between the precast girders with the retrofit connection providing slightly better performance.

Recommendations for use of UHPC drafted after the first year of the project were used to conduct a field test involving retrofit of an existing expansion joint with UHPC joint headers on a bridge identified in conjunction with ODOT. Only a portion of the joint was completed, but the interfaces between the UHPC materials and the bridge deck concrete were monitored for almost three years for any cracking or separation due to differential shrinkage or applied loading. Overall, the replaced section of joint performed very well. Since the full joint replacement could not be completed two demonstration joints were cast at Fears Lab; one of these joints was cast using Ductal® and one was cast with the OU J3 mix. These joint specimens were then placed outside for continued monitoring over time and exhibited similar performance to the joint in the field.

Phase 2 involved consideration of a partial depth slab joint detail using the same methods as for the full-depth joint detail, reinforcement bond, and durability of proprietary and non-proprietary UHPC and a magnesium-alumino-liquid-phosphate concrete material. The half-depth joint detail produced similar ultimate strengths to the full-depth joint detail, but a lower cracking load. UHPC bond to concrete substrate was examined for different surface preparations and base concrete saturation levels using direct pull-off tests. Results indicated that flowability and surface preparation were the most important considerations for UHPC to concrete bond. UHPC durability testing indicated excellent performance for both proprietary and non-proprietary UHPC relative to freeze-thaw and chloride ion penetration. Corrosion testing produced mixed results with the non-proprietary J3 UHPC mix design exhibiting the best performance relative to the Halo Effect. The results of both phases of the project were combined with information available in the literature to produce recommendations for draft standard specifications for UHPC materials, mixing methods, placing methods, and quality control for use in bridge connections in Oklahoma.

Table of Contents

List of Figures

List of Tables

1.0 Introduction

1.1 Overview

Deterioration of bridges can often be related to poor performance of longitudinal connections between precast members or transverse deck joints. Ultra-high performance concrete (UHPC) is a cementitious composite with mechanical and durability properties far exceeding those of conventional concrete, which makes it an ideal material for bridge deck joints. UHPC is a relatively expensive material and is most economical when use of a small quantity can have a large impact on overall performance of a structure. The project described in this report evaluated available proprietary UHPC materials and UHPC mix designs made with local materials for applicability to bridge joint installation and repair in Oklahoma and developed specifications for continued usage of UHPC in bridge construction in Oklahoma.

Phase 1 of the project developed three promising mix designs using local materials through a systematic investigation of mixture constituents and methods for obtaining optimal particle packing density. After conducting a materials property comparison, one of these mixes, mix J3, was considered for further structural testing. Two specific applications of UHPC were considered; deck slab joints and girder continuity connections. Initial investigation of deck slab joint details was conducted using small-scale flexural specimens to evaluate bond strength between UHPC and base concrete for different surface preparation methods. Laboratory-scale joints were cast between 4 ft x 4 ft slab specimens using both the proprietary UHPC material Ductal® and the OU developed J3 mix design, the joint surface preparation methods identified by small-scale testing, and reinforcing details taken from the literature and standard ODOT practice. The composite slabs were then tested in flexure. Two slabs from each group of three were load tested to failure and one slab from each group was tested using a cyclic load at the approximate magnitude of the cracking moment.

Additionally, laboratory-scale girder continuity connections were designed based on standard practice and were tested to failure. Two different connection details were used, one representing new construction and one representing retrofit of an existing structure. A series of three specimens was cast for each detail using two 18 ft long,

approximately half-scale AASHTO Type II prestressed concrete beams and the proprietary UHPC material Ductal®. Two specimens of each group of three were tested statically to failure with a loading configuration placing a maximum negative moment on the connection. The third specimen in each group was first loaded to create a positive moment on the connection before being loaded to failure.

Using recommendations for use of UHPC drafted after the first year of the project, a field test involving retrofit of an existing expansion joint with UHPC joint headers was conducted on a bridge identified in conjunction with ODOT. Only a portion of the joint was completed due to slow strength gain for the concrete, but the interfaces between the UHPC materials and the bridge deck concrete were monitored for the next three years for any cracking or separation due to differential shrinkage or applied loading. Overall, the replaced section of joint performed very well. Since the full joint replacement could not be completed, the research team cast two demonstration joints at Fears Lab in conjunction with a day-long training for ODOT personnel on UHPC for bridge joint applications. One of these joints was cast using Ductal® and one was cast with the OU J3 mix. These joint specimens were then placed outside at Fears Lab for continued monitoring for more than 2 years and exhibited similar performance to the joint in the field.

Phase 2 involved slab testing similar to what was conducted in Phase 1 for a partial depth slab joint detail, examination of reinforcement bond, and durability testing of both proprietary and non-proprietary UHPC. UHPC bond to concrete substrate was also examined for different surface preparations and base concrete saturation levels. Examination of the half-depth joint detail indicated similar ultimate load performance, but reduced service level performance due to the increased interface area between the UHPC and conventional concrete. Results of bond testing indicated similar performance between the non-proprietary J3 UHPC and proprietary material with both showing sufficient bonding capability for the FHWA recommendations for UHPC embedment length (Graybeal 2014) to be adequate. UHPC durability testing indicated excellent performance for both proprietary and non-proprietary UHPC relative to freeze-thaw and chloride ion penetration. Corrosion testing produced mixed results with the non-proprietary J3 UHPC mix design exhibiting the best performance relative to the Halo

Effect. Finally, the results of Phase 1 and Phase 2 have been combined with information available in the literature to produce recommendations for draft specifications for UHPC materials, mixing methods, placing methods, and quality control for use in bridge connections in Oklahoma.

1.2 Problem Statement

Deterioration of bridges is often related to poor performance of deck joints both longitudinal and transverse to the bridge span. UHPC is a relatively new class of cementitious composite that has fresh, mechanical and durability properties far exceeding those of conventional concrete (Graybeal 2014) and has great potential for use in bridge connections and rehabilitation in Oklahoma. The proposed research will examine available materials and potential applications of UHPC for connections and repairs with the goal of creating specifications for composition and use of UHPC in Oklahoma.

1.3 Project Objectives

The objectives of the research were designed to progress toward the goal of using UHPC to construct durable bridge component and deck joints and to create durable repairs for bridges in Oklahoma. These objectives were:

1) Identify appropriate UHPC materials for use in joint construction/repair including formulations using materials available throughout Oklahoma,
2) Evaluate structural performance of full-depth and partial-depth joint replacement details to identify best practices for bridges in Oklahoma,
3) Evaluate long-term performance of trial joints placed in an in-service Oklahoma bridge using proprietary and locally designed UHPC mixtures,
4) Evaluate bond performance of reinforcing steel cast in UHPC and the UHPC to substrate interface,
5) Examine corrosion performance of bridge joints incorporating UHPC repair materials,

6) Create specifications for materials, mixing, quality control, and placing of UHPC in Oklahoma.

This report is intended to provide information and guidance ODOT can use to implement UHPC bridge connections and repairs.

2.0 Literature Review

2.1 Ultra-High Performance Concrete (UHPC)

2.1.1 Overview

Ultra-High Performance Concrete (UHPC) is a cementitious composite material with increased durability and strength properties compared to NSC. UHPC was first developed in the late 20th century and is a product of advancements in superplasticizers, fiber reinforcement, supplementary cementitious materials, and optimized gradation of dry materials (Graybeal 2014). Its properties differ from those of typical portland cement concrete, so many of the methods for casting UHPC and determining its fresh and hardened material properties have been modified from the methods used for conventional concrete. UHPC has been successfully used in multiple applications related to connection of precast concrete bridge components due to its superior bond development characteristics with steel reinforcement, ease of placement, and long-term durability compared to conventional concrete. The long-term benefits of using UHPC in many applications are evident, but commercially available proprietary mixture formulations are very expensive and mix design using local materials is much more complicated than for conventional concrete.

The superior mechanical properties of UHPC allow for the optimization of structural elements, including bridge girders, where the enhanced tensile strength can lead to the elimination of mild steel shear reinforcement (Graybeal 2006a). It can also be used to construct relatively lightweight deck systems (Aaleti et al. 2014). The cost of commercially available UHPC is often approximately 10-20 times that of conventional concrete due to the high cementitious materials content and fiber reinforcement, but the superior mechanical properties and durability have led to much recent interest in applications where small amounts can be used for long-term gain (Graybeal 2011).

Such applications include connections between precast bridge components such as deck panels, deck bulb-tee girders, and adjacent box girders. Other applications of UHPC include precast piles, seismic retrofits, thin-bonded overlays for deteriorated decks, and blast mitigation (Graybeal 2011). UHPC formulations can also be made with local materials (e.g. Wille 2011) in order to reduce costs.

Connections cast using UHPC can extend the life of a structure and allow for less maintenance over time. Joints replaced or connections made using this material will have better durability, better resistance to impacts and abrasion, and will allow for a smaller quantity of material to be used while still obtaining adequate load transfer between connected components. Using UHPC allows for small, simple connections without the need for post-tensioning (when connecting precast elements) or large amounts of field-cast concrete (Graybeal 2010). Joints cast using UHPC also tend to behave more like monolithic construction than typical field-cast connections. The use of UHPC for connecting precast elements has been the focus of many cases studies and research projects. It has also been studied as an overlay material to repair and/or extend the life of existing bridges. However, the use of UHPC as a repair material for existing joints in bridges has not been extensively studied.

2.1.2 Material Properties

The Federal Highway Administration (FHWA) has performed extensive investigation of the properties of UHPC for use in bridge and other infrastructure components (Graybeal 2011, Graybeal 2014). FHWA defines UHPC as “a cementitious composite material composed of an optimized gradation of granular constituents, a water-to-cementitious materials ratio less than 0.25, and a high percentage of discontinuous internal fiber reinforcement. The mechanical properties of UHPC include compressive strength greater than 21.7 ksi (150 MPa) and sustained post-cracking tensile strength greater than 0.72 ksi (5 MPa). UHPC has a discontinuous pore structure that reduces liquid ingress, significantly enhancing durability as compared to conventional and high-performance concretes” (Graybeal 2011). The post-cracking tensile strength is such that it can be included in design of structural elements.

In order for UHPC to be a more valid material for everyday practice in the bridge community, several studies funded by FHWA have extensively examined UHPC material properties (Graybeal 2006, Graybeal and Stone 2012, Graybeal and Baby 2013, Swenty and Graybeal 2013). The authors followed the American Society for Testing and Materials (ASTM) and the American Association of State Highway and Transportation Officials (AASHTO) recommended procedures for the material characterization tests that would typically be done on conventional concrete. In some cases, the authors had to modify or develop new tests to adequately test specimens to get useful information due to the vast differences in material properties. These studies found the tested formulations to have the typical material properties shown in Table 1 if cured in field conditions and deployed with 2% steel fibers by volume.

Table 1. Typical material properties of field-cast UHPC (taken from Graybeal 2014)

Characteristic	Average Result
Density	155 lb/ft^3 (2,480 kg/m^3)
Compressive Strength (ASTM C39, 28-Days)	24 ksi (165 MPa)
Modulus of Elasticity (ASTM C469, 28-Days)	7,000 ksi (48 GPa)
Direct Tension Cracking Strength	1.2 ksi (8.5 MPa)
Split Cylinder Cracking Strength (ASTM C496)	1.3 ksi (9.0 MPa)
Prism Flexure Cracking Strength (ASTM C1018)	1.3 ksi (9.0 MPa)
Long-Term Creep Coefficient (ASTM C 512,11.2 ksi (77MPa) Stress)	0.78
Long-Term Shrinkage (ASTM C 157, initial reading after set)	555 με
Total Shrinkage (embedded vibrating wire strain gage)	790 με
Coefficient of Thermal Expansion (AASHTO TP60-00)	8.2 x 10^{-6} in./in./°F (14.7 x 10^{-6} in./in./°C)
Chloride Ion Permeability (ASTM C1202, 28-day test)	360 coulombs
Chloride Ion Permeability (AASHTO T259, 0.5 in. (12.7 mm) depth)	<0.10 lb/yd^3 (<0.06 kg/m^3)
Scaling Resistance (ASTM C672)	No scaling
Abrasion Resistance (ASTM C944 2x Weight, ground surface)	0.026 oz. (0.73 g) lost
Freeze-Thaw Resistance (ASTM C666A, 600 cycles)	RDM = 99%
Alkali-Silica Reaction (ASTM C1260, tested for 28 days)	Innocuous

Note: RDM = relative dynamic modulus

2.1.3 Mix Designs

The most commonly used UHPC material in the United States is a proprietary formulation produced by Lafarge under the trade name Ductal®, which has been subjected to significant testing (Graybeal 2011) and used in many previous research projects. FHWA has identified several other proprietary products available in the United

States including: BCV®, BSI®, CRC®, and Densit®. The U.S. army corps of engineers has developed their own product, Cor-Tuf® (Williams et al. 2009) and other products are available. Several state DOTs have investigated (or are currently investigating) the potential for developing non-proprietary mix designs with a reduced cost compared to the typically available formulations (Willie 2011, Willie 2013, Graybeal 2013, Berry et al. 2017, El-Tawil et al. 2016, El-Tawil et al. 2018, Mobasher et al. 2019) or are evaluating more cost effective UHPC materials developed by others (Phares 2014). Willie et al. (2011, 2012) and work by FHWA (Graybeal 2013) provided recommendations for the basic material constituents that should be utilized since the very high compressive strength requirements make the mixtures more sensitive to the quality of the component materials. Work by FHWA proposed mix designs for various regions of the United States, summarized in Table 2, but these did not consider the region including Oklahoma (Graybeal 2013). Each proposed mix included high-strength steel fibers at 1.5% by volume.

Table 2. Potential UHPC mix designs developed by FHWA for various regions of the U.S. (Graybeal 2013)

Material/Topic	UHPC-1 (B, NE)	UHPC-2 (L, Upper MW)	UHPC-3 (VR; NW)	UHPC-4 (Q; U.S.)
White Cement, lb/yd^3	1311	1268	1256	1248
Silica Fume, lb/yd^3	328	317	314	312
Fly Ash, lb/yd^3	318	308	305	303
HRWR, lb/yd^3	48	46	45	45
Fine Agg. (75 µm-1.2 mm), lb/yd^3	1966	1903	1884	1871
Agg.-to-cement ratio	1.5	1.5	1.5	1.5
w/c	0.23	0.24	0.23	0.23
Spread, in.	11.4	10.4	11.3	12.4
Avg. f'_c, ksi	26.9	24.1	23.5	29.0
Cost, \$/yd^3	494	472	496	652

Note: B = basalt aggregate, L = limestone aggregate, VR = volcanic rock aggregate, Q = quartz aggregate, all mixes do not include fibers

Exact compositions of UHPC may vary among products with the same performance goals in mind. Some characteristics and components are typical of all UHPC mixtures such as: dry components (cement, silica fume, and fine aggregates), chemical admixtures (accelerators and high range water reducers (HRWR)), water, and steel fibers. Dry components are graded to facilitate adequate flowability and supplementary cementitious materials or coarse aggregates are sometimes included

(Graybeal 2014, Wille 2011). Typical mix designs include a w/cm between 0.2 and 0.3, a cement to silica fume to supplemental material ratio of 1.0:0.25:0.25, a fine aggregate to cement ratio of 1.0 to 2.0, and fibers included at 1.0 to 2.0 percent by volume (Graybeal 2013). Wille (2011) recommended a fine aggregate to cement ratio of 1.4 and *w*/*c* between 0.16 and 0.27. Due to the low *w*/*cm* and high cementitious material content, a large portion of the cement does not hydrate and simply acts as filler material. Inert filler materials or fly ash have been considered as a partial replacement of cement with the intention of reducing the cement content and overall cost of the material (Wille 2012). The low water content of UHPC requires optimized gradation and large doses of HRWR to obtain proper rheology. Replacement of a portion of the cement with nanoparticles has shown to speed up hydration of the cement and improve material properties by improving the gradation and facilitating dispersion (Li 2016, Wille 2012). The fiber type, geometry, and volume fraction are very important to the performance of a UHPC mix design and should be carefully considered (Graybeal 2014).

Berry et al. (2017) developed a UHPC mix design using materials locally available in Montana including Type I/II portland cement, class F fly ash, fine masonry sand, silica fume and superplasticizer. El-Tawil et al. (2016, 2018) developed a mix design for use in bridge repair in Michigan that was used in an implementation project. The final mix design achieved 21.5 ksi at 28 days and consisted of Type I portland cement, slag cement, silica fume, two silica sands, superplasticizer and steel fibers. Mobasher et al. (2019) developed multiple mix designs using materials available in Arizona. Their study focused on particle packing, cement chemistry, and rheology to develop mix designs with compressive strength in excess of 22 ksi using 3 percent steel fibers by volume (Mobasher et al. 2019)

2.1.1 Mixing, Placement, and Curing

Typical UHPC mixing procedures involve dry mixing all constituents first followed by the water and then HRWR. Once the mix becomes fluid, or turns over, the fibers are added. The mixing energy required for UHPC is higher than for conventional concrete and the reduced coarse aggregate content and low water content may lead to

overheating of the mix. A high shear mixer is typically recommended for mixing UHPC. However, most conventional concrete mixers can be used to mix UHPC if the mixing energy requirements are taken into account through modified mixing procedures. UHPC can be mixed in mortar/grout mixers as well as in traditional concrete mixers; however, traditional concrete mixers and ready-mix trucks may be less efficient than mixers with higher shear (Graybeal 2014). Higher shear mixers can decrease the duration of the mixing process, since they impart greater energy into the mix. It should also be noted that, typically, the maximum amount of UHPC that should be mixed in any mixer is about half the volume of conventional concrete that could be mixed (Graybeal 2014). Cubed ice is often used to control temperature during mixing, which also helps provide additional mixing action. Tackett et al. (2009) found that a small high shear mixer, small rotating drum mixer, and a ready-mix truck produced UHPC with adequate performance. Curing procedures had more influence on final behavior than mixer type. Figure 1 shows UHPC being mixed in the field with typical mixers.

Figure 1. UHPC field mixing operations using high shear mixers (Graybeal 2014)

Placement and consolidation procedures must also be considered carefully to ensure proper fiber distribution and orientation (Graybeal 2011). It is typically placed and moved using wheelbarrows or buckets. Figure 2 depicts the process for transporting UHPC from the mixer to the site of the pour and the pouring procedure for a longitudinal connection of bridge elements. When there are two successive pours, the new UHPC should be poured directly over the most recently poured layer; sometimes

rodding is necessary to limit the amount of separation between layers. The flowability of UHPC places higher pressure on formwork and requires special attention be paid to joint seals. UHPC does not require the same type of finishing as traditional concrete. Because of its flowability and viscid nature, finishing with a trowel is not effective or necessary. UHPC can be poured into closed forms to provide a smooth top surface and minimize dehydration (Graybeal 2014). It is also common for UHPC to be cast higher than the required elevation and ground after curing to the desired surface texture or appearance.

Figure 2. UHPC placement into a longitudinal connection of bridge elements (Graybeal 2014)

Proper curing of UHPC is critical to ensure proper performance. UHPC must be sealed with an impermeable layer immediately after casting or else surface dehydration can lead to cracking and degradation of material properties (Graybeal 2011). It must remain sealed until it can self-support and not self-desiccate, often taken to be when the compressive strength reaches 14 ksi (97 MPa). Moist curing is also an option. Heat curing is helpful but must not contribute to dehydration and steam treatment is often used to enhance properties. A common steam treatment is 194 °F (90 °C) and 95% relative humidity for at least 48 hours (Graybeal 2011). Graybeal (2006) examined four different curing regimens on specimens for each of the material characterization tests. The first regimen was the control specimen that followed the manufacture's recommendation for steam curing the UHPC at 194 ºF (90 ºC) and 95 percent relative humidity for 48 hours. The second regimen was not steam cured but cured at the

standard laboratory environment from demolding until testing. The third regimen was tempered steam curing, which was similar to the steam curing recommended by the manufacturer, but the temperature was limited to 140 ºF (60 ºC). The fourth regimen was a delayed steam curing that did not begin until the 15th day after initial casting and used the same recommended specifications for steam curing by the manufacturer. Table 3 shows the average UHPC material properties determined from testing.

Table 3. Average UHPC material properties for different curing regimens (Graybeal 2006).

Material Characteristic	Steam	Untreated	Tempered Steam	Delayed Steam	Supplemental Description
Compressive Strength (MPA)	193	126	171	171	ASTM C39; 28-day strength
Modulus of Elasticity (GPa)	52.4	42.7	51.0	50.3	ASTM C469; 28-day modulus
Split Cylinder Cracking Strength (MPa)	11.7	9.0	11.7	11.7	ASTM C496
Prism Flexure Cracking Strength (MPa)	9.0	9.0	10.3	9.7	ASTM C1018; 305-mm span; corrected AASHTO T132
Mortar Briquette Cracking Strength (MPa)	8.3	6.2	9.7	6.9	AASHTO T132
Direct Tension Cracking Strength (MPa)	9.7-11.0	5.5-6.9	7.6-9.0	9.0-11.0	Axial tensile load
Prism Flexural Tensile Toughness (I_{30})	53.0	48.3	43.1	48.3	ASTM C1018; 305-mm span
Long-Term Creep (C_{cu})	0.29	0.78	0.66	0.31	ASTM C512; 77-MPa sustained load
Long-Term Shrinkage (microstrain)	850	790	--	--	Embedded vibrating wire gage
Coeff. Of Thermal Exp. ($x10^{-6}$ mm/mm/°C)	15.6	14.7	15.4	15.2	AASHTO TP60-00
Chloride Ion Penetrability (coulombs)	18	360	39	18.00	ASTM C1202; 28-day test
Chloride Ion Permeability (kg/m^3)	< 0.06	< 0.06	< 0.06	< 0.06	AASHTO T259; 12.7-mm depth
Scaling Resistance (grams lost)	No Scaling	No Scaling	No Scaling	No Scaling	ASTM C672
Abrasion Resistance (grams lost)	0.17	0.73	0.20	0.13	ASTM C944 2x weight; ground surface
Freeze-Thaw Resistance (RDM)	96%	112%	100%	99%	ASTM C666A; 600 cycles
Alkali-Silica Reaction	Innocuous	Innocuous	Innocuous	Innocuous	ASTM C1260; tested for 28 days

Multiple factors contribute to the extended initial set time observed for UHPC: temperature at time of placement, ambient temperature, admixtures, cement type, and constituent material properties (Graybeal 2014). Heat curing is often used to accelerate strength gain or an accelerator is added to the mix if high early strength is needed. Heat curing is usually done in the field by using external sources such as heating mats or lamps, or internal sources like resistance heating wires (Graybeal 2014).

2.2 UHPC as a Repair Material

2.2.1 Overview

The strength and durability properties of UHPC make it useful as a repair material that may provide a longer life to structures that are deteriorated or have been weakened. Several studies have been conducted on application of UHPC to specific types of bridge repair.

2.2.2 Overlays

Various studies have been conducted on the effectiveness of UHPC as an overlay material on bridge decks and pavements. The low permeability and high durability of UHPC lends itself to this use. The FHWA investigated the first bridge in the U.S. to use UHPC as an overlay, which was completed in 2016 in Brandon, IA, (the Laporte Road bridge). The overlay was intended to be 1.5 in. thick and the deck was ground down to remove unsound concrete, grooved, then pre-wetted for several hours prior to placing the UHPC deck overly. The substrate preparation prior to UHPC placement is shown in Figure 3.

Figure 3. Final bridge deck substrate preparation (Graybeal 2017)

Several months after completion of the overlay, a field inspection indicated there were several areas where delamination could have occurred. This prompted the FHWA to conduct an investigation on the UHPC overlay. The UHPC overlay was visually inspected, examined for delamination using the chain drag test, and the direct pull-off test according to ASTM C1583 was conducted at various locations. The chain drag test revealed eight potential areas of delamination, and two were chosen for the direct pull-off test. Also, three more regions where delamination was not indicated were also tested, including sections of roadway with and without the scarified substrate preparation. An example of the cores after testing and failure of the conventional concrete substrate are shown in Figure 4.

Figure 4. Direct pull-out test cores (Graybeal 2017)

In every pull-off test conducted, the failure occurred either in the conventional concrete substrate, or in the adhesive used to bond the testing cap to the concrete, showing that the bond strength between the UHPC overlay and conventional concrete was sufficient. An electron microscope was used to examine several bonded areas and it was noted the bonded surface was interrupted by debris or entrapped air, as shown in Figure 5. However, these bond interruptions did not appear to adversely affect the overall integrity of the UHPC overlay (Graybeal 2017).

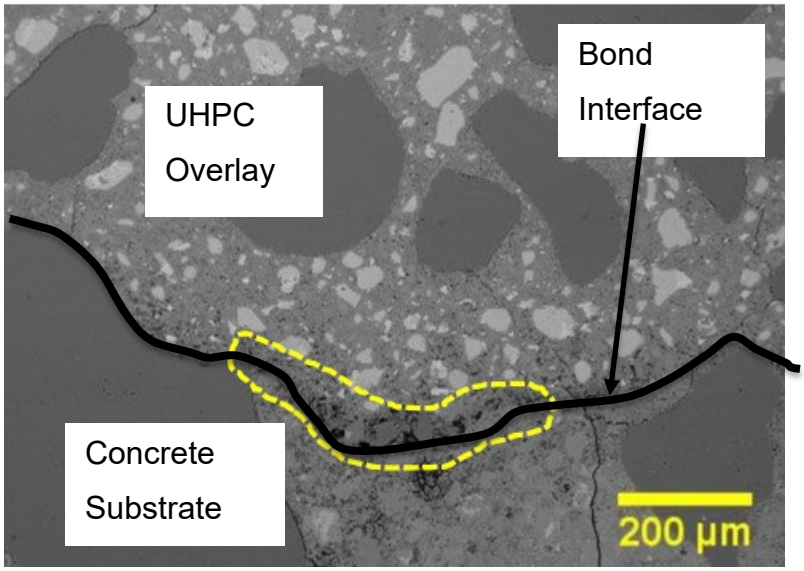

Figure 5. Area of bond interruption at UHPC-CC interface (Graybeal 2017)

Testing of a field-cast bridge overlay was also conducted by Iowa State University (Wibowo and Sritharan 2018). A 1.5 in.-thick UHPC overlay was placed on the Mud Creek bridge in Iowa as a repair for the bridge deck. A special UHPC mix (Ductal NaG3 TX) was developed by LafargeHolcim to ensure proper placement of the UHPC over the crown of the bridge. The asphalt wearing surface and damaged concrete were removed, then the deck was grooved to create an exposed aggregate surface with a 1/8 in. amplitude. Welded wire mesh was also placed at the pier locations in one lane to determine whether it can provide additional negative moment capacity. Once the UHPC overlay hardened, the surface was ground and grooved to provide adequate roughness for traffic. The final overlay is shown in Figure 6.

Figure 6. Finished overlay on the Mud Creek bridge (Wibowo and Sritharan 2018)

A chain drag test was conducted on the bridge and eight areas were noted that showed signs of delamination. Two of those areas were selected for testing with the direct pull-off test according to ASTM C1583. Three locations without suspected delamination were also tested as a control. The typical failure mode of the direct pull-off test occurred in the conventional concrete substrate and not at the bond interface, as shown in Figure 7. It was concluded that the delamination found during the chain drag test was most likely in the conventional concrete substrate prior to the application of the overlay.

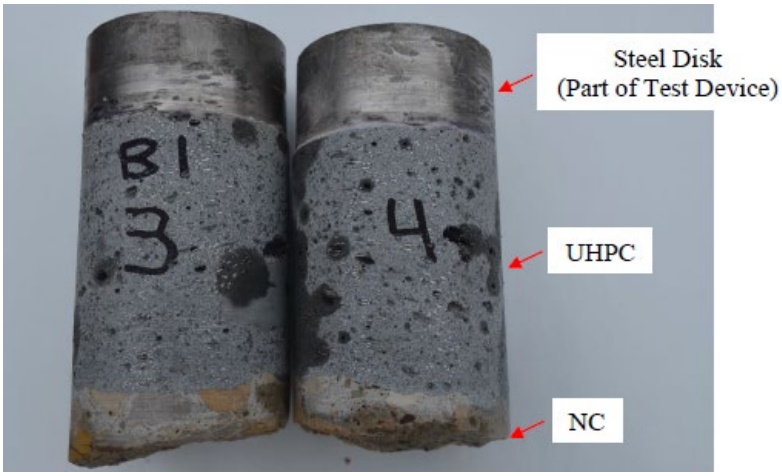

Figure 7. Typical direct pull-out test failure for the Mud Creek bridge overlay (Wibowo and Sritharan 2018)

The negative moment capacity was shown to increase in lab testing but mainly due to the additional thickness provided by the overlay. The welded wire mesh in the overlay did not appear to significantly improve the capacity due to its small area (Wibowo and Sritharan 2018).

Another study on the effectiveness of UHPC as an overlay material was conducted at Missouri University of Science and Technology (Khayat et al. 2018). The researchers first developed UHPC mix designs to be placed as overlays at thicknesses of 1 in., 1.5 in., and 2 in., using various methods to mitigate shrinkage such as lightweight sand aggregate and expansive agents. The conventional concrete substrate specimens were cured in ambient air conditions for twelve months prior to application of the overlay. A chemical retarder was applied to each surface during casting to create an exposed aggregate surface roughness. Five UHPC mix designs were used for the

overlays with varying percentages of lightweight sand and expansive agents to control shrinkage. The final slabs with overlays were stored indoors for the testing and are shown in Figure 8.

Figure 8. Final experimental panel with UHPC overlay used by Khayat et al. (2018)

The slabs were monitored for a total of 200 days. Shrinkage of the UHPC overlay was monitored over time to determine the effectiveness of the methods used to reduce shrinkage. Each slab was also examined for evidence of delamination. The surface and interfacial layer of the UHPC showed no signs of cracking throughout the testing, and there appeared to be no evidence of delamination during testing. Since all overlay thicknesses performed well, the overlay thickness of 1 in. was chosen as the most cost-effective (Khayat et al. 2018).

Both Sarkar (2010) and Denarie and Bruhwiler (2006) explored the feasibility of UHPC as an overlay repair material to be poured as a thin top layer on an existing roadway or bridge. While conducting research on the process of field implementation of a 3 cm thick UHPC overlay on a bridge in Switzerland, Denarie and Bruhwiler (2006) found that implementing UHPC in this capacity could “simplify the construction process, increase the durability of structures and their mechanical performance (stiffness and resistance), and decrease the number of interventions during their service life”. They performed analysis of the rehabilitation by noting the construction process and performing compressive and uniaxial tensile tests, ultimately determining that the benefits of implementing UHPC far outweigh the costs and surpass those of lower quality traditional solutions (Denarie and Bruhwiler 2006). Sarkar (2010) performed

extensive evaluation of UHPC and its feasibility as an overlay material by performing slant shear tests, splitting tensile tests, and third point loading flexural tests on specimens with a 1 in. thick UHPC overlay. This study found that, based on its mechanical properties and the tensile properties exhibited during testing, UHPC achieves adequate bond strength to other concrete materials and is likely feasible as a repair material.

Habel et al. (2004) also performed testing on a UHPC composite overlay configuration to determine the bending behavior of the composite element. The study used a four-point loading system, seen in Figure 9. Three different types of overlays were studied (each having different depths and rebar configurations), and the following conclusions were made: (1) the enhanced mechanical properties of UHPC contribute to improved structural response of composite elements due to its strain-hardening behavior under uniaxial tension (2) the stiffness of the composite elements was increased under service loads, and no large cracks formed until the maximum force was reached, and (3) the addition of tensile reinforcement in the UHPC layer increased resistance and stiffness of the composite elements and delayed localized macrocracks (Habel et al., 2004).

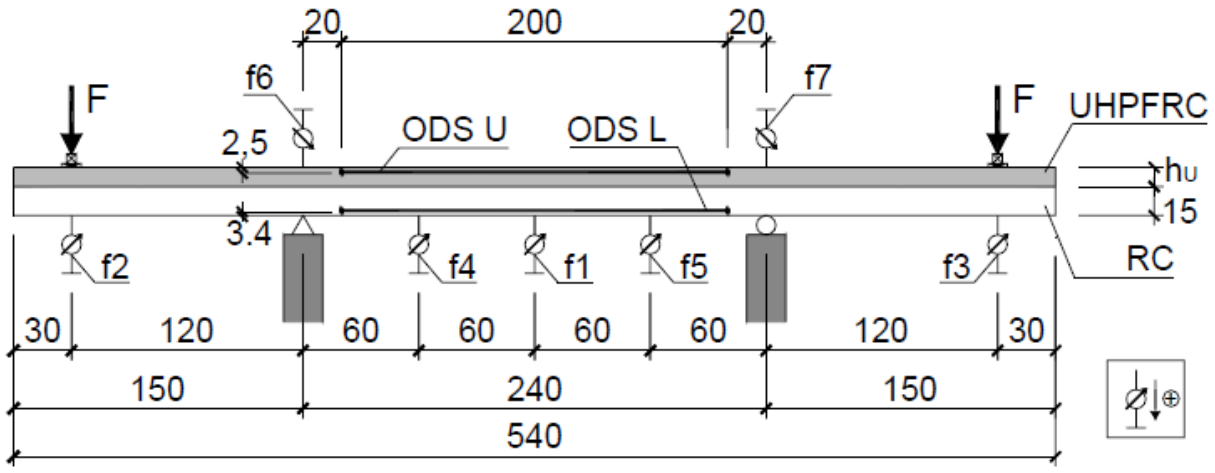

Figure 9. Four-point loading system for Habel et al. (2004) experiments. Notations f1-f7 are LVDT locations, and dimensions are given in cm.

2.2.3 Girder Repair

Some states are investigating the use of UHPC for repairs of girder end regions (Connecticut DOT 2016, Shafei et al. 2020). Researchers at the University of Connecticut conducted laboratory testing of three large-scale W21x55 girder specimens to determine the effectiveness of UHPC in restoring the bearing capacity of damaged steel girder ends. One girder was undamaged as a control test, one was artificially damaged by removing a portion of the cross section to mimic corrosion damage observed on an in-service bridge, and the last was damaged the same way and then repaired using UHPC. The damaged girder is shown in Figure 10.

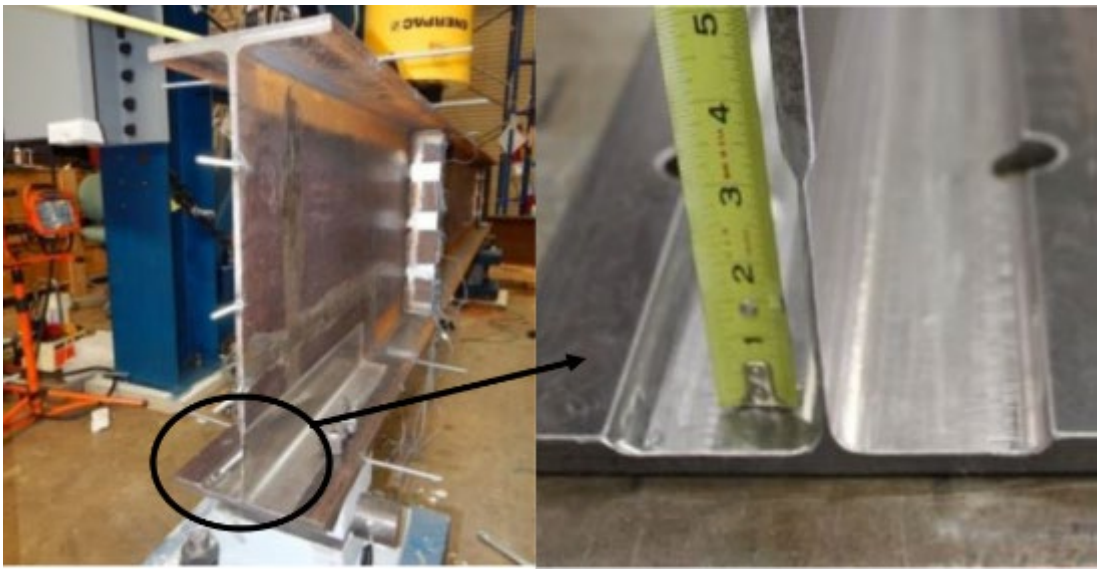

Figure 10. Damaged girder end (Zmetra 2015)

Composite action between the UHPC and the damaged girder was achieved by attaching 3/8 in. diameter, 1-1/4 in. long headed shear studs to the girder, as shown in Figure 11. The thickness of the UHPC repair was no less than 1-3/4 in. to ensure a minimum stud clear cover of ½ in. The repair was only added to the bottom two-thirds of the girder due to the strength limitations of the test setup. The final repaired girder is shown in Figure 12. Mineral oil was applied to the portion of the girder bonding to the UHPC to mimic the effect of paint on an in-service girder.

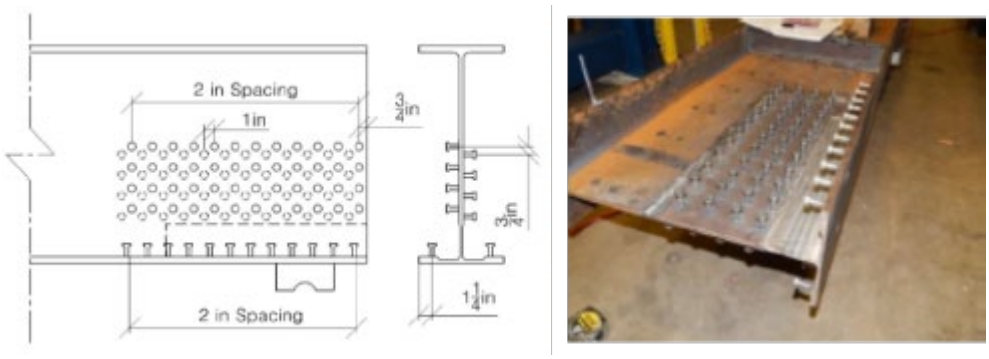

Figure 11. Shear stud layout on the repaired girder (Zmetra 2015)

Figure 12. Final repaired girder (Zmetra 2015)

A concentrated load was applied to each girder 32 in. from the rocker support and the span length of the simple supports was 12 ft. The UHPC used for the encasement achieved a flow of 11 in. and reached a compressive strength of 16,000 psi at time of testing, four days after casting. The failed girders are shown in Figures 13, 14, and 15.

The undamaged girder failed at a load of 180 kips by web buckling and the damaged girder failed at a load of 43 kips by web buckling at the location of removed material. However, the repaired girder end failed at a load of 230 kips by flexural yielding (Zmetra 2015). This change in failure mode appears to show that, at 16,000 psi, the UHPC was able to provide enough bracing to preclude a web buckling failure, thus ensuring a yield failure. Overall, the repair was able to enhance the end bearing capacity beyond that of the undamaged girder.

Figure 13. Undamaged girder failure (Zmetra 2015)

Figure 14. Damaged girder failure (Zmetra 2015)

Figure 15. Repaired girder failure (Zmetra 2015)

In another research project by Shafei (2020), an Iowa bulb-tee-C- shaped beam was used to evaluate the performance of a UHPC patch to rehabilitate induced end region damage. The web of the girder was thinned by approximately 30% to represent shear damage at the location marked in Figure 16. Forms were placed along the sides of the girder with weep holes at the top to avoid entrapped air and were wetted before casting to reduce water absorption. After the UHPC was poured and hardened, the beams were tested with the loading arrangement shown in Figure 17. It was reported that the patch demonstrated a good bond with the girder with substrate concrete failure before the UHPC patch.

Figure 16. Cut beam segment marked for controlled damage (Shafei, 2020)

Figure 17. Loading setup for beam with UHPC patch (Shafei, 2020)

2.3 UHPC to Conventional Concrete Bond Strength

2.3.1 Overview

The most important property ensuring the effectiveness of any concrete repair is the bond strength between the existing concrete substrate and the repair material.

Without adequate interfacial bond strength, the bond of the two materials could fail prematurely without any failure of the repair material itself. Several factors can affect the bond performance between conventional concrete and the repair material. Rougher surface preparations allow for better bond strength than smooth finishes. Roughening can expose more capillaries in the conventional concrete substrate, allowing the repair material an easier path to fill them. Additionally, increased surface roughness allows for a better mechanical bond between the two materials. The flowability of the repair material directly affects how well it can fill the substrate's capillaries. The more fluid the repair material, the easier capillary action is achieved. Also, exposed aggregate finishes provide improved bond strength through aggregate interlock. Another important factor affecting the bond strength is the substrate moisture content. Dryer surfaces can potentially pull water from the repair material into the substrate's capillaries, thus reducing the level of hydration of the repair material at that interface. Too much moisture can locally increase the water content of the repair material, thereby lowering its strength. Graybeal (2016) tested a relatively simple method to ensure an adequate moisture content of the conventional concrete substrate involving placing wet burlap over the bond surface for several hours prior to placing the repair material.

Various studies have been conducted to determine the bond strength of UHPC when cast against conventional concrete in both laboratory and field conditions. The tests used to evaluate the bond strength between UHPC and conventional concrete in these studies included the direct tension pull-off test, slant shear compression test, splitting cylinder test, and the flexural beam test. Momayez et al. (2005) performed a study on the bond strength between concrete substrates and various repair materials. This study included several types of tensile and shear testing, including pull-off tests, splitting prism tests, slant shear, and bi-surface shear testing. Although the study did not use UHPC as a repair material, the six repair materials used (each with a different mix design) provided useful information on the factors that affect bond strength, especially when using slant shear tests. Momayez et al. (2005) drew the following conclusions:

- The measured bond strength is highly influenced by the type of test performed. Each test that was conducted had an acceptable coefficient of variation, but it is

crucial to select tests that represent the stress state of the structure or configuration in the field.

- Slant shear testing typically yields the highest measured bond strength.
- Bond strength between the repair material and the concrete substrate increases with the amount of silica fume in the repair material.
- Preparation of the concrete substrate surface that increases the roughness leads to a higher bond strength—about 25% higher for slant shear tests.

2.3.2 Direct Tension Pull-Off Test

The direct tension pull-off test follows ASTM C1583 and consists of casting UHPC over a cured conventional concrete slab. Then, after the UHPC is cured, a core bit is used to drill though the repair material and at least 0.5 in. into the conventional concrete substrate. A steel connector is then attached to the cored concrete and a direct tension load is applied until failure of either the conventional concrete substrate, the UHPC, or the interface between the two materials. The setup for this test is shown in Figure 18.

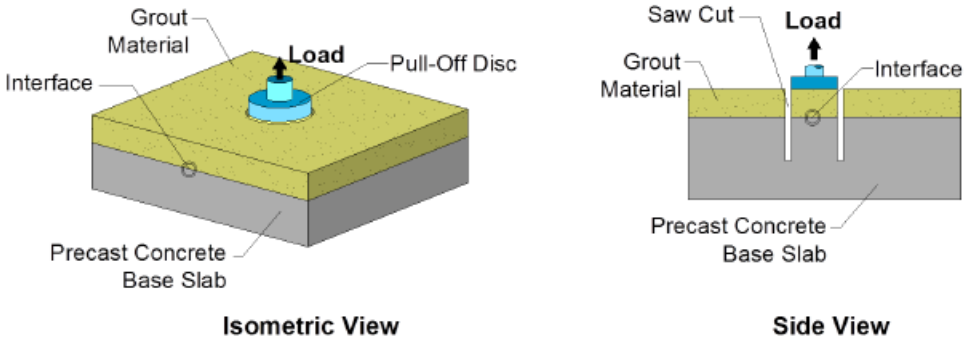

Figure 18. Direct tension pull-off test setup (Graybeal 2016)

A failure in the conventional concrete substrate indicates that the bond strength is larger than the tensile strength of the conventional concrete, thus adequate bond is provided. Failure in the UHPC is unlikely due to its relatively large strength compared to conventional concrete. The test method is an effective way to directly determine the tensile strength of the bond between the materials since the interface is only subjected to tensile stresses. Munoz et al. (2014) conducted this test for the proprietary UHPC,

Ductal®, using four different surface preparations on the conventional concrete: wire brushed, sandblasted, grooved, and exposed aggregate. All conventional concrete substrates were saturated, and their surfaces dried (SSD condition) prior to applying the UHPC. In all their pull-out tests but one, the failure occurred in the conventional concrete substrate (Munoz et al. 2014).

Graybeal (2016) conducted the direct pull-off test using different levels of aggregate exposure: high, medium, and low, as shown in Figure 19. Field-cast UHPC was used in this study. The results showed that the level of aggregate exposure did not drastically affect the bond strength between UHPC and the conventional concrete substrate, with all three levels gaining approximately 600 psi tensile strength. The effect of substrate moisture was then determined by testing the bond strength difference when the substrate was lightly sprayed, wet burlap was left on the substrate for 2-4 hours, and the SSD condition. When wet burlap and the SSD conditions were tested, the failure shifted from the bond interface to the substrate, indicating those two wetting methods improved the bond strength (Graybeal 2016).

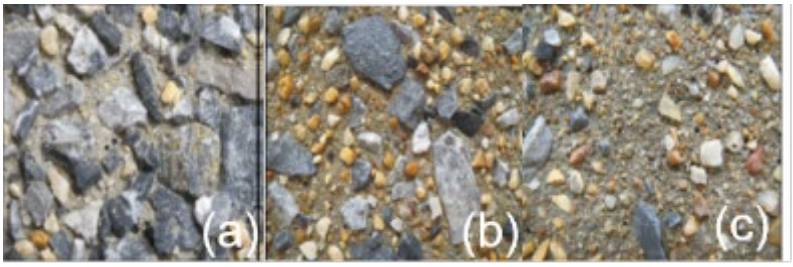

Figure 19. (a) High, (b) medium, and (c) low aggregate exposure levels (Graybeal, 2016)

2.3.3 Slant Shear Test

The slant shear compression test follows ASTM C882, utilizing UHPC in lieu of epoxy-resin. A standard compression cylinder is tilted to whichever bond angle is desired, then conventional concrete is added until the edge of the concrete reaches the opening, filling roughly half of the mold while creating a slanted bond surface. The conventional concrete is allowed to cure, and then the UHPC is placed in the remainder of the mold. When tested, a compression load is applied at the two ends of the cylinder, as shown in Figure 20.

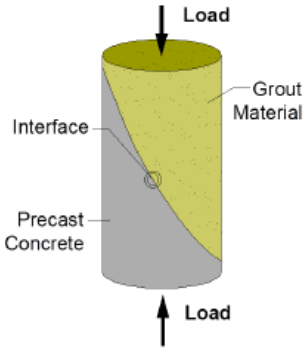

Figure 20. Slant shear compression test (Graybeal 2016)

This test creates shearing and compressive forces along the interface. The failure can either occur along the bond interface or the conventional concrete material can crush similar to a conventional compression test. Munoz et al. (2014) conducted this test with UHPC and the same surface roughness and moisture conditions used on the direct pull-out tests, at three and eight days of age. The researchers tested bond angles of 60° and 70° from the horizontal. All specimens with a wire brushed interface failed in bond, while all other tests failed in the concrete substrate. This shows that the wire brushed surface provided lower bond strength than the other surface roughness levels tested (Munoz et al. 2014). Climaco et al. (2001) performed tests on prisms of different sizes and proportions, finding that the size of the specimens had little to no effect on the results obtained from testing. Tayeh et al. (2013) performed experiments on prismatic slant shear specimens with a cross-section length and width of 100 mm, height of 300 mm, and interface angle of 60 degrees from the horizontal. Figure 21 shows an example of a prismatic specimen.

Some researchers that have adapted tests for slant shear have used a larger cylindrical version of the original ASTM C882 slant shear test. ASTM C882 specifies the cylinder size to be 3 in. by 6 in. for assessing mortar bonds, but researchers like Diab et al. (2017) used larger composite cylinders with diameters that were half of the height, finding smaller coefficients of variation and results that were more consistent. Sarkar (2010) also performed slant shear tests on cylindrical specimens, seen in Figure 22. This study utilized 3 in. by 6 in. composite cylinders composed of half normal-strength concrete and half UHPC at a 30-degree angle.

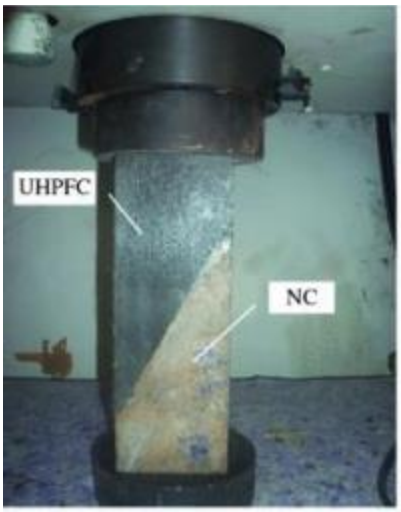

Figure 21. Prismatic specimen and testing setup for Tayeh et al. (2013) experiments

Figure 22. Cylindrical specimen and testing setup for Sarkar (2010) experiments

According to Climaco et al. (2001), the stress state in slant shear tests at failure depends on the quality of the bond. In many of the experiments in previous research, the composite specimen failure occurred within the normal concrete substrate rather than the bond, indicating that the bond could have resisted higher stresses and demonstrating the superior bond behavior of UHPC (Tayeh et al. 2013; Munoz et al. 2014). In the Munoz et al. (2014) experiments, the specimens “obtained a bond capacity, at the age of 3 days, greater than the [strength] requirements given by ACI 546-06 [Guide for Repair of Concrete Superstructures] (ACI 2006) at 7 days and also satisfies the requirements at 28 days.”

2.3.4 Splitting Tensile Strength Test

The splitting cylinder test follows ASTM C496. A standard 6 in. x 12 in. cylinder mold is typically used, but the specimen size can be modified. Typically, the cylinder is filled with a single material for testing. However, slight modification to the ASTM allows for the testing of bonded UHPC materials. During casting, the mold is placed on its side and the conventional concrete is poured into the mold until it is filled halfway. After the conventional concrete has cured, the UHPC is used to fill the remainder of the mold. Once cured, the specimens are tested on their side with the load point lining up with the bond interface, as shown in Figure 23. This load application ensures a tensile force is applied along the bonded interface.

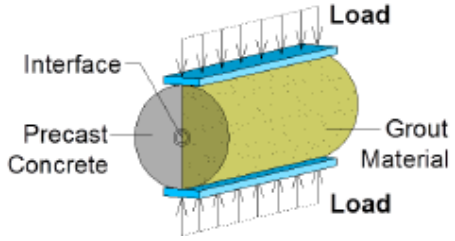

Figure 23. Splitting cylinder test (Graybeal 2016)

Munoz et al. (2014) conducted this test on rectangular specimens in lieu of circular. However, the loading was applied in the same manner to ensure tension stress at the bonded interface. For this test, the following surface preparations were tested: smooth, chipped, wire brushed, sandblasted, and grooved. All surfaces were tested in both the dry and SSD condition and testing was conducted after at least 278 days to evaluate long term bond strength. The researchers found that the specimens with a dry substrate failed during demolding except the grooved surfaces, since they provided a channel for interlocking between the UHPC and CC. The SSD condition performed excellently, with most of the specimens' splitting tensile stress at failure exceeding the expected tensile strength of the conventional concrete. Furthermore, splitting tensile specimens were tested following freeze-thaw cycles. These specimens all failed at a higher load than the original specimens, showing that freeze-thaw cycles did not adversely affect the bond strength (Munoz et al. 2014)

2.3.5 Flexural Beam Test

The flexural beam bond test follows ASTM C78. A pour stop is placed in the center of the beam mold and half of the mold is filled with the conventional concrete substrate. After curing, the other half is filled with UHPC. Bond angles typically tested are 90°, 60°, and 45° from the horizontal with various surface preparations. The beams are then subjected to third-point loading according to ASTM C78, as shown in Figure 24. The test creates flexural stresses along the surface of the bond.

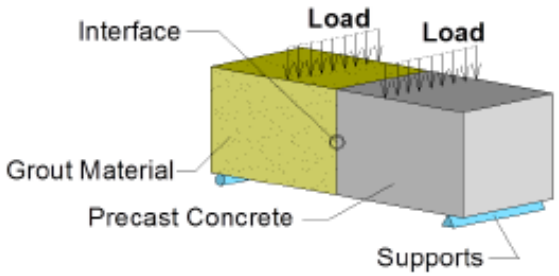

Figure 24. Flexural beam bond test (Graybeal 2016)

2.4 Reinforcement Bond Behavior in UHPC

2.4.1 Bond Behavior of Mild Steel in UHPC

A critical consideration for connections of concrete elements is bond of reinforcement with the concrete material used for the connection. The development length required for reinforcing bars embedded in UHPC is much less than for conventional concrete. Extensive research confirming the minimal development length required when using UHPC was conducted by Graybeal (2014), and is not uncharted territory due to the known effect of high compressive strength on reducing required development length. FHWA conducted pull out testing on a tension-tension lap splice configuration to characterize the bond behavior of mild steel reinforcing bars cast in UHPC (Yuan and Graybeal 2014). To recreate tension-tension lap splice configurations, the specimens consisted of a precast concrete slab with multiple rows of No. 8 reinforcing bar extending 8 inches from the face of the slab. Reinforcing bars to be tested were placed between the No. 8 reinforcing bars in each row, and rectangular strips of UHPC were cast around the reinforcing bar configurations, with the line of

reinforcing bars being on the center line of the strips, as shown in Figure 25. To recreate tension that would occur in an actual structural configuration with lap splices, a steel frame with two hydraulic rams was used to put the testing reinforcing bar into direct tension with the frame pushing against the precast concrete deck, as shown in Figure 26 (Yuan and Graybeal 2014).

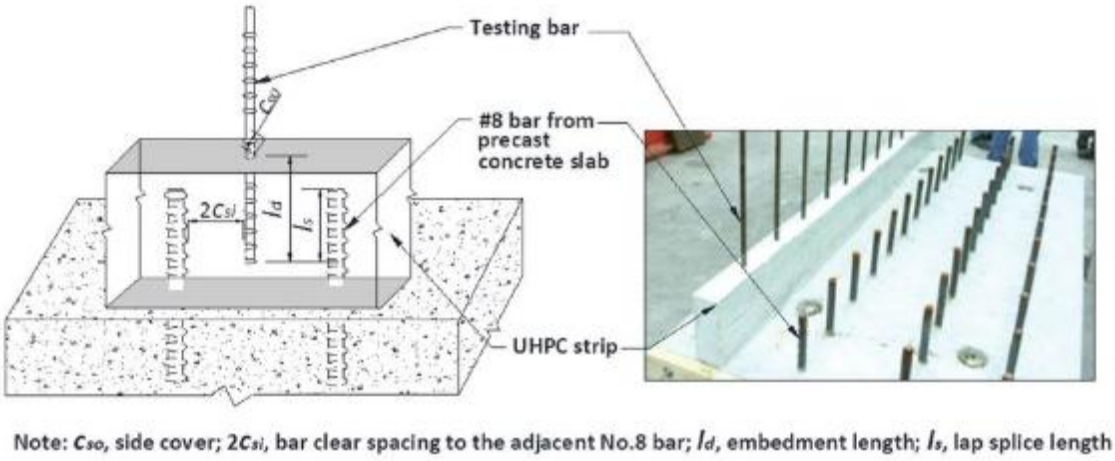

Figure 25. Overall configuration of FHWA reinforcing bar bond test specimens (Yuan and Graybeal 2014)

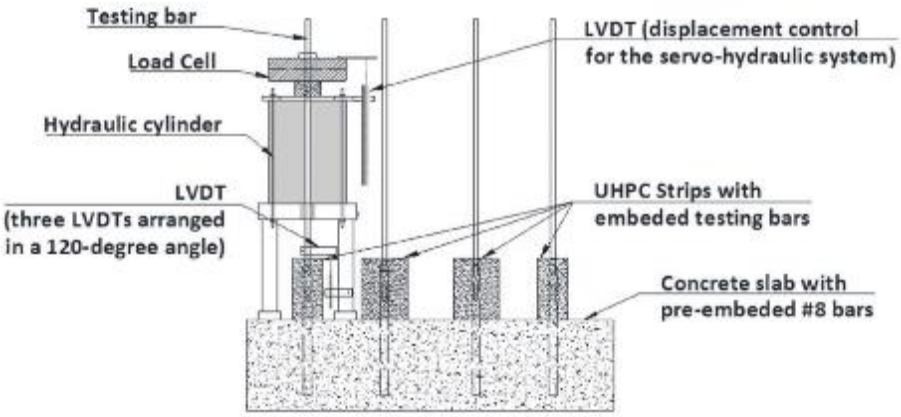

Figure 26. FHWA reinforcing bar bond test loading setup (Yuan and Graybeal 2014)

The parameters that were examined for the bond behavior of reinforcing bars in UHPC were the embedment length, concrete side cover, bar spacing, concrete compressive strength, reinforcing bar size, reinforcing bar yield strength, and casting

orientation. After conducting over 200 tests with the various parameters, the results showed a difference in bond behavior for reinforcing bars embedded in UHPC compared to normal concrete. The author concluded that increases in embedment length, side cover, and compressive strength increased the bond strength. Characteristics that decreased bond strength were epoxy-coated reinforcing bars and reinforcing bar with a larger diameter. It was also noted that a non-contact lap splice had an increased bond strength over a contact lap splice. The author stated that this was most likely due to the non-contact splice allowing fibers to fully engage around the reinforcing bar, thereby increasing bond strength, as the contact lap splice would not allow fibers to fully engage around the portion of the bars that were in contact with one another, thus decreasing the bond strength (Graybeal 2014).

Based on the results from the bond behavior tests in UHPC, the authors presented design recommendations to obtain deformed bar yield strength before bond failure. The recommendations are for bar sizes ranging from No. 4 to No. 8, either uncoated or epoxy-coated, and clear spacing of greater than $2d_b$ and lap splice length (l_s). Minimum requirements were a minimum embedment length of $8d_b$, side cover of $3d_b$, and UHPC compressive strength of 13.5 ksi (93.1 MPa). Additionally, a lap splice length of 75 percent of embedment length was recommended, as this was the percentage used for the majority of tests conducted in the FHWA study. There was also guidance for when the side cover was between $2d_b$ and $3d_b$ to use $10d_b$ for the embedment length. The possibility to reduce the minimum embedment length of $8d_b$ was noted for cases having an increase in side cover or an increase of compressive strength, and the need for increasing embedment if decreasing side cover and compressive strength was noted. These recommendations allow designers to have potential flexibility in connection design with UHPC (Yuan and Graybeal 2014).

The shorter development length required for UHPC is considered an advantage because structural elements can be connected using a smaller quantity of steel with less complicated bends and a smaller joint width and resulting amount of material can be used to make the connection. Cost and complexity of the joints both decrease with shorter development length. One example of implementation focuses on a set of bridges built in Syracuse, New York in 2013. The top and bottom mats of slab

reinforcement only required a 6 in. wide connection (Graybeal 2014). Another example of implementation was carried out for a bridge on County Road 47 in Stockholm, New York, where yet again, the specification required a minimum lap splice length of only 6 in. for two precast slabs connected by a UHPC joint (Graybeal 2014).

2.4.2 Bond Behavior of Untensioned Prestressing Strands

FHWA conducted pull out testing on a tension-tension non-contact lap splice configuration to determine the development length of untensioned prestressing strands cast in UHPC (Graybeal 2014). The test specimen was created using the standard prestressing strand grid pattern of 2 in. center to center spacing, with a splice strand added between the two main strands. This was done to recreate a splice connection that would be used for splicing prestressed members together using 0.5 and 0.6 in. prestressing strands. Figure 27 shows the geometry of the UHPC test specimen, and the strand location within the UHPC for a 0.5 in. strand (Graybeal 2014).

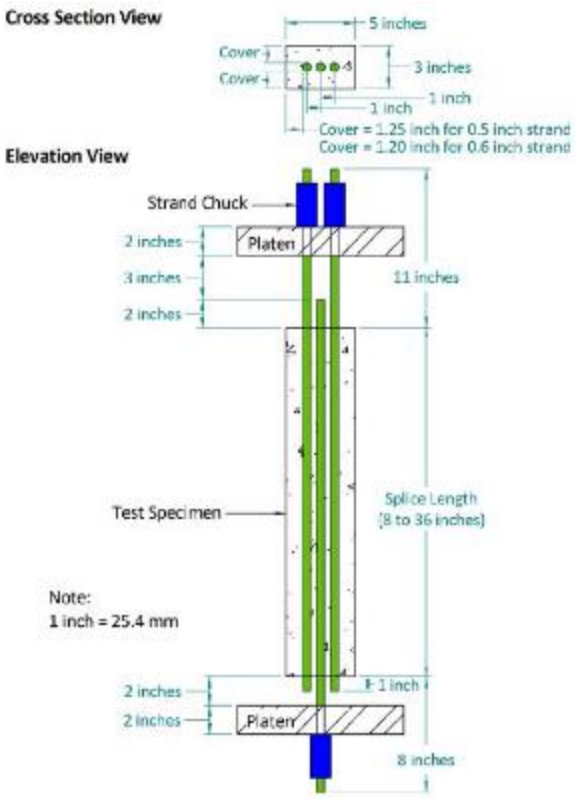

Figure 27. Geometry of FHWA prestressing strand-UHPC bond test specimen with 0.5 in. diameter strands (Graybeal 2014)

The non-contact lap splice lengths tested for the 0.5 and 0.6 in. prestressing strands ranged from 8 to 24 in. The specimens were tested using a servo-hydraulic testing machine to allow for displacement control. Tension was applied to the end with two prestressing strands (live end). Slippage and load resistance were measured at the single prestressing strand located at the dead end of the testing machine. The test was stopped for each specimen upon reaching the peak resistance, or was continued until the strand ruptured. Figure 28 shows one of the specimens in the testing frame. The authors concluded from the test results that the 0.5 in. diameter strand can be fully developed within a splice length 20 in., and the 0.6 in. diameter strands can be approximately developed within 24 in. (Graybeal 2014).

Figure 28. FHWA prestressing strand-UHPC bond test specimen in load frame (Graybeal 2014)

2.5 Previous Laboratory Testing on UHPC Slab Joints

The use of modular bridges has become more and more popular due to the advances in UHPC. In the past, modular bridge construction was much more difficult because regular concrete was not ideal for connecting modular bridges together, as the development length for reinforcing bars would require large joints and the high amount of reinforcement would lead to poor consolidation of conventional concrete in the joints. UHPC has a much higher strength which allows a reduced development length, a more feasible joint length, and has high flowability to prevent consolidation issues.

FHWA has published guidance on design and implementation of field-cast UHPC connections (Graybeal 2014). These connection types have been tested in the lab (Graybeal 2010) and in many cases also in the field (e.g. Landers 2015). Laboratory tests indicated that slab connections using UHPC performed as well or better than monolithic deck sections cast with conventional concrete (Graybeal 2010). The smaller required development and splice lengths allow for connection of adjacent elements using short, straight bars extending from each element in connections that are less complicated than those using conventional grout or concrete (Graybeal 2010). These simplified connection details can reduce reinforcement costs, reduce difficulty of fabrication, and increase the ease of field assembly while still transferring moment, shear, and tensile forces (Graybeal 2014). Precast deck panel connection designs often use only a 6 in. (150 mm) lap splice and 6 in. to 8 in. (200 mm) wide connection with female-to-female shear keys (Graybeal 2014). Precast panel to girder connections can combine the panel-to-panel connection with the panel to girder connection by relying entirely on the UHPC to carry the tensile, compressive, and shear stresses between the girder and deck through shear studs that do not extend up to the level of the slab reinforcement. The UHPC is used to fill the space between adjacent panels with edges supported on the girders and shear studs located in the gap between panels. These connections may use a female-to-female shear key or a hidden pocket configuration. An example of a female-to-female deck panel connection is shown in Figure 29. The use of UHPC can eliminate the need for overlays to reduce water ingress and congestion in the connection (Graybeal 2014). UHPC connections between adjacent box beams and deck bulb-tees are similar to those for deck panels and can eliminate the need for transverse post-tensioning and concrete overlays by creating, in essence, a continuously reinforced concrete slab at the top flange level of the boxes (Graybeal 2014).

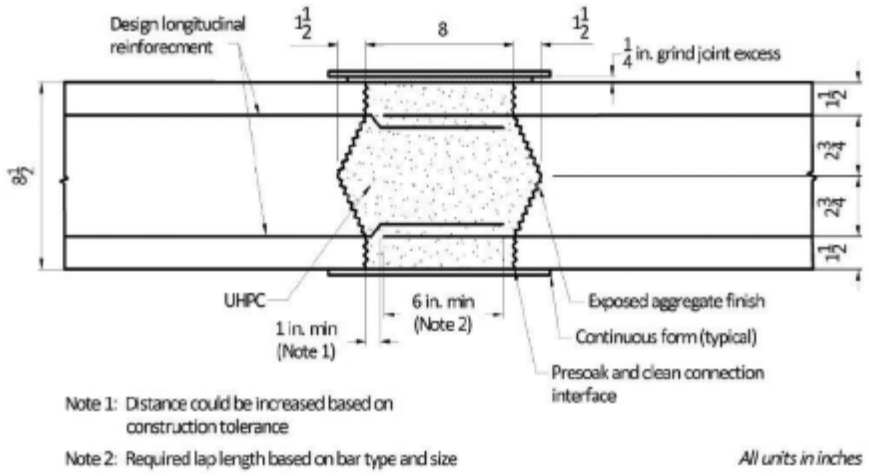

Figure 29. Deck panel connection detail (Graybeal 2014)

Apart from studying the behavior of interface bond for small-scale composite specimens, it is also beneficial to consider the bond behavior of UHPC and NSC in a slab-joint configuration. This information can be applied to similar configurations for bridges in the field and can connect small-scale testing data with field performance. Graybeal (2010) conducted research on six slab-joint configurations representing both transverse connections between precast deck panels and longitudinal connections between deck bulb-tee girders. The specimens were constructed with precast half-panels connected by a UHPC joint after about three weeks of curing. The UHPC joint was cured for two weeks before being statically and cyclically tested in flexure. Cyclic loading was performed for at least 7 million total cycles at a maximum frequency of 6 Hz. Figure 30 and Figure 31 depict the testing setup for both types of joint (transverse and longitudinal). From this testing, several promising conclusions were made (Graybeal 2010):

- Performance of the connections tested equaled or exceeded what would be anticipated from a monolithic slab with no joint at mid-span.
- The development length of the reinforcement (No. 5 mild steel reinforcing bars) proved to be less than or equal to 5.9 in. and no debonding was observed.
- The cracking behavior of the specimens was not greatly affected by cyclic loading below the cracking moment, and cyclic loading just above the cracking

moment did not greatly influence the structural behavior.

- The bond performance between the precast half-panels and the UHPC joint indicate that the precast panel bridge decking system (transverse) tested is unlikely to leak along the connection interface under cyclic service loads or static overloads.

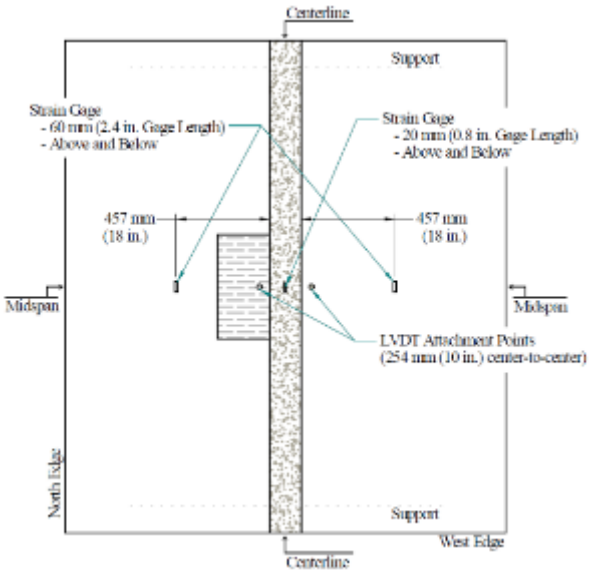

Figure 30. Layout for transverse joint specimen (Graybeal 2010)

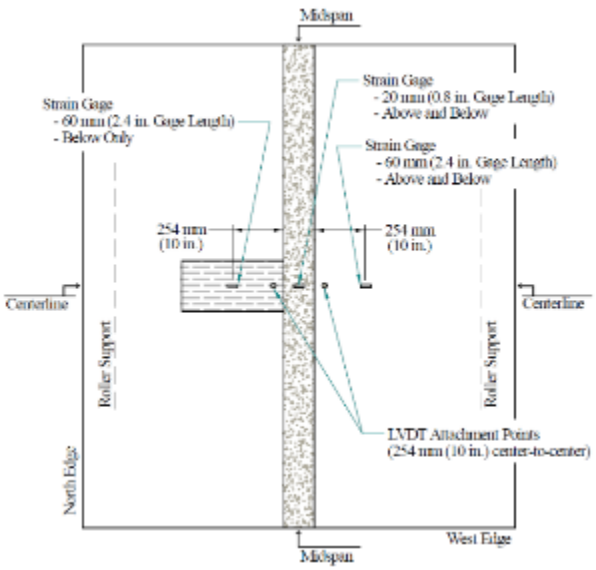

Figure 31. Layout for longitudinal joint specimen (Graybeal 2010)

2.6 UHPC Splice Connection Between two Precast Girders

Splicing precast concrete members at mid-span with post-tensioning has been a common practice but the need for post-tensioning could potentially be avoided through the use of a spliced connection between precast prestressed concrete members. To make this possible the spliced connection would use UHPC, combined with the un-tensioned prestressing strands extending from the precast members. To better understand how this type of connection would behave under loading, FHWA conducted two flexural tests with two precast, prestressed AASHTO Type BII-36 box beams in tandem connected with a splice at mid-span using UHPC (Maya and Graybeal 2017). The connection detail for the first test used a splice length of 24 in. ($40d_b$) for the un-tensioned strands. In addition, six No. 4 reinforcing bars were included in the bottom half of the connection with 6 in. extending into the joint, and 6 in. extending into the beam. Figure 32 shows the cross-sectional view of the box beams.

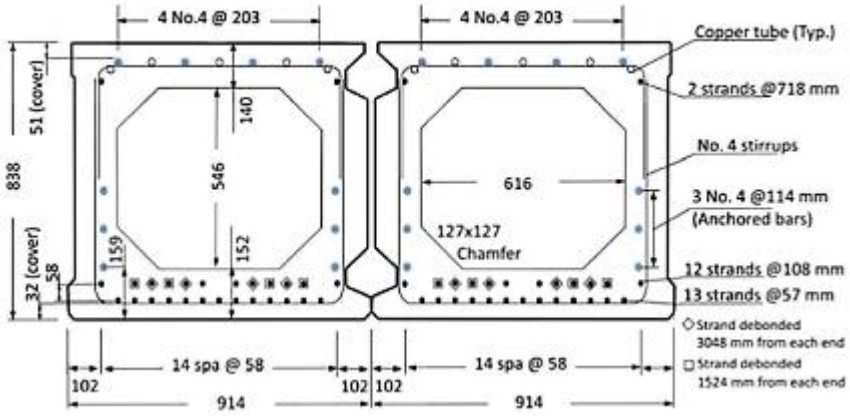

Figure 32. Cross-sectional view of box girders used for FHWA beam splice test (Maya and Graybeal 2017).

The loading configuration for the box beam test is shown in Figure 33. The first test conducted on this connection detail reached 77 percent of the anticipated ultimate flexural capacity of the tandem beams when a load drop-off occurred. A truncated pyramid failure type had occurred in the UHPC joint, indicating bond failure of the strands, but the authors stated that cracking in the joint led to no flexural capacity loss. The specimen was then reloaded up to 85 percent of the ultimate flexural capacity of

the tandem beams when failure occurred due to concrete crushing (Maya and Graybeal 2017).

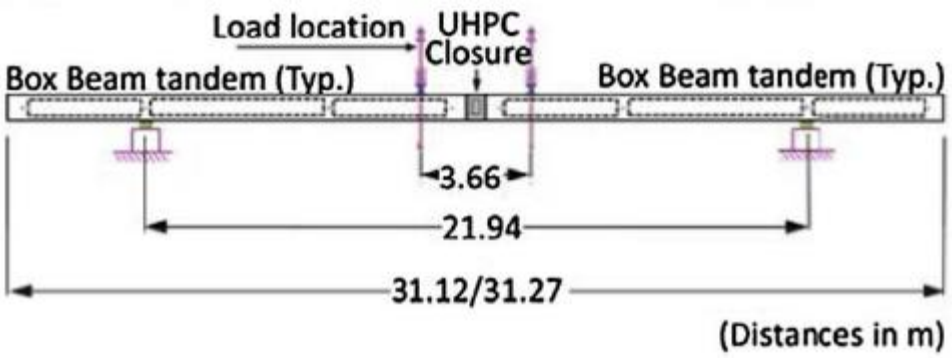

Figure 33. FHWA box beam splice test loading configuration (Maya and Graybeal 2017)

The authors conducted a second test intended to further improve the flexural capacity of the spliced connection. The second connection detail used a splice length of 30 in. ($50d_b$), and debonded alternating stands by 1 in. going into the joint. With the new detail changes from the first connection tested, the test specimen reached 90 percent of the anticipated ultimate flexural capacity of the tandem beams when failure occurred due to flexural cracking and concrete crushing. In addition, the authors noted that the second detail had no bond failures in the un-tensioned prestressing strands, which led them to suggest debonding alternating strands by 1 in. in the joint reduced the outcome of bond failure. The flexural stiffness reported was similar for both connection details, and both had an initial reduction in stiffness at the beginning of each test. The authors recommended spliced connections for mid-span to use a splice length of $50d_b$ for prestressing strands in order to achieve higher flexural capacities than that resulting from using the recommended splice length of $40d_b$. The flexural capacity could potentially be improved more with proper detailing strategies and debonding strands in the joint (Maya and Graybeal 2017).

2.7 Connection of Precast Girders Made Continuous for Live Load

A continuity joint is the connection of two simply supported beams that allows the transfer of subsequent superimposed dead loads and live loads. This type of connection has been used occasionally in pretensioned prestressed concrete girder bridges since the 1960's. Continuity joints for prestressed concrete girders are established with

composite concrete decks and the use of diaphragms or individual connection blocks at pier caps and abutments. Establishing the continuity joint allows for any future loads, beyond the self-weight of the members, to be transferred through the structure as a continuous beam, improving the strength and durability of the whole bridge. In addition, continuity between the girders helps reduce maintenance costs, improves the appearance, and improves the riding qualities of the bridge (Freyermuth 1969). Figure 34 shows a typical continuity connection between two girders.

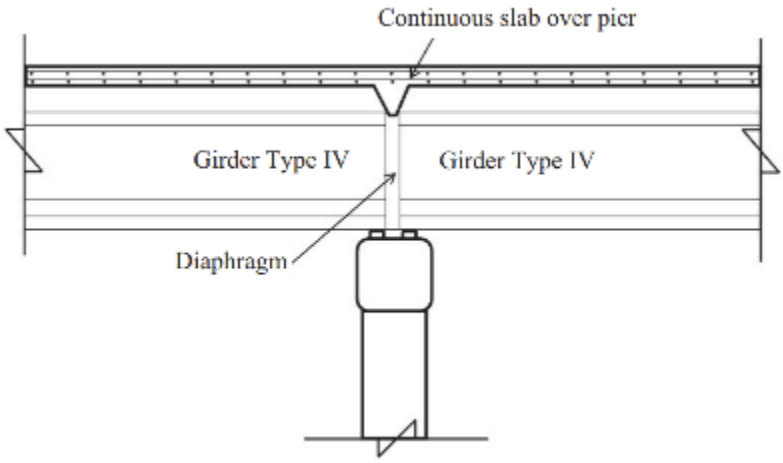

Figure 34. Typical continuity joint between girders (Eamon et al. 2016)

As a vehicle drives over a bridge, it acts as a set of point loads moving across the girders. In response the girders bend and create moments within the girders. Within the continuity joint, two types of moments occur. The first type is the negative moment that occurs in the composite deck portion over the pier and abutments when the girders are loaded. The second type is the positive moment, which occurs in the diaphragm or connection between girders in successive spans due to time dependent effects within the girders. These time dependent effects are concrete shrinkage of the girders and creep effects related to the prestress in the girders. Figure 35 shows the effects from creep and shrinkage causing upward deflection in each induvial span. Once the girders are connected with a continuity joint the ends become restrained, and additional creep effects can cause a restraint moment within the continuity joint connection preventing the girder ends from rotating.

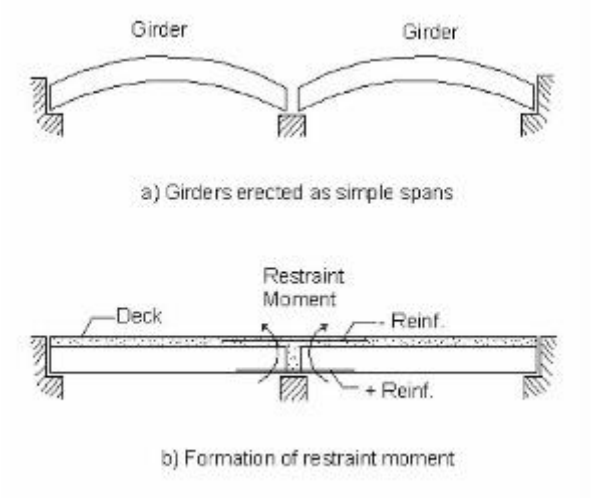

Figure 35. Formation of positive restraint moment under time dependent effects (Saadeghvaziri et al. 2004)

Early studies done by the Portland Cement Association (PCA) state that the reinforcement in the composite deck properly accounts for the negative moment, but these studies also showed that the positive moment can lead to cracking of the diaphragm if it is not properly detailed (Miller 2004). If the connection at the diaphragm cracks, the positive moment is released, the joint acts as a hinge, and continuity is lost. However, if the positive moment connection is properly detailed using reinforcement within the joint, the connection maintains continuity despite cracking and the joint still performs as designed with the reinforcement transferring the moment through the joint (Miller 2004). There are two types of reinforcement typically used for the positive moment connection. The first type of reinforcement is prestressing strands extending out of the girder for the specified length and bent upwards to form a 90-degree angle creating a hook. The second type of reinforcement is mild steel embedded into the girder and extending into the joint for a set distance and bent at a 90-degree angle to form a hook.

Miller (2004) examined six types of joint detailing for the positive moment resistance in the continuity joint. Figures 36, 37, and 38 show the joint details tested. The study was to further explore the findings in an analytical study on the positive moment connection presented in the NCHRP 322 report (Oesterle et al. 1989), since the analytical study in NCHRP 322 found that the positive moment connection for

continuity had no structural benefit in bridges. The NCHRP 322 authors' reasoning for this conclusion was if the positive moment due to time dependent effects becomes restrained at the continuity connection, the effects then also occur along the girder creating a second positive moment in the girder. As a result, the same secondary moment was observed in the typical simple span case without a continuity joint, thus no structural benefit was gained. Miller (2004) stated that any type of analytical study performed has a set of parameters, and the results observed do not necessarily reflect other types of situations. Thus, Miller (2004) concluded that continuity joints can be useful as they can still provide structural benefits by providing a connection point between girders, in case of supports being damaged, and protecting girder ends from erosion.

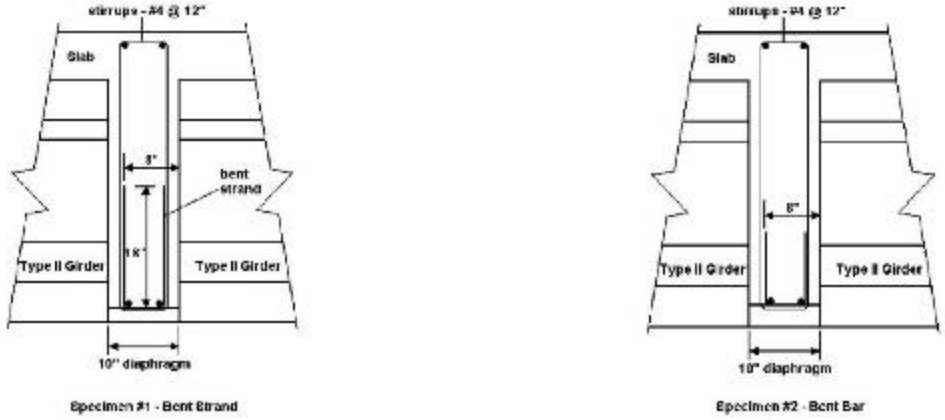

Figure 36. Details of the specimen #1 and # 2 connection (Miller 2004)

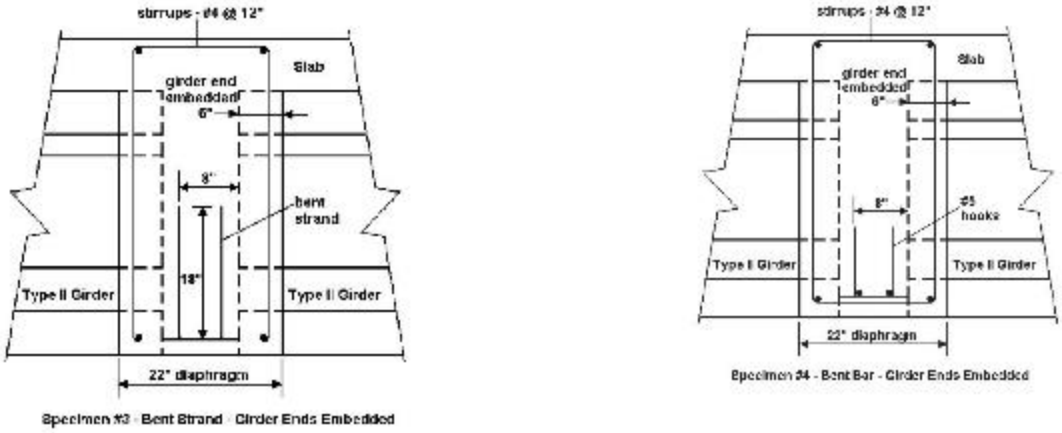

Figure 37. Details of the specimen #3 and # 4 connection (Miller 2004)

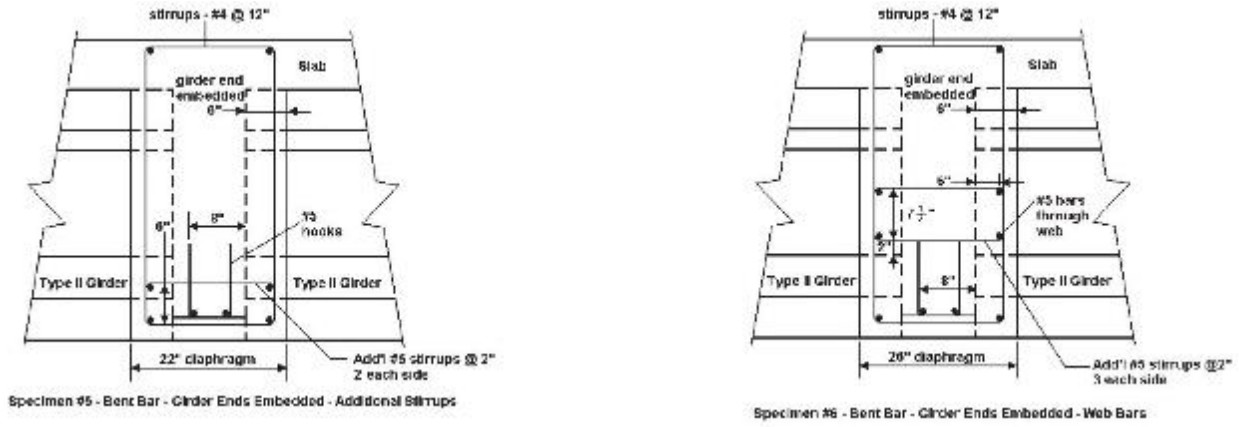

Figure 38. Details of the specimen #5 and #6 connection (Miller 2004).

The initial part of the study by Saadeghvaziri et al. (2004) was to monitor three bridges in New Jersey to determine the degree of continuity for different configurations of anchor bolts fixing the superstructure to the piers. The study found the continuity in these bridges ranged from 0 to 90 percent for service load transfer between multiple continuity connections in one span for each bridge. With only three bridges being examined for the level of continuity, and since the range of continuity for those bridges was not consistent, this study shows that the level of continuity in all continuity connections within any given bridge could be inconsistent. The researchers concluded that the difference in the level of continuity in bridges is dominated by time dependent effects. The age of the girder when continuity was established had the largest impact on continuity for the three bridges investigated. This further supported the authors theory that, if the girders were embedded into the continuity joint using elastomeric pads with little lateral deformation and have anchor bolts in each continuity joint connecting the girders to the pier, the supports act like a fixed end preventing rotation and sliding. This fixed end behavior leads to the time dependent deformation effects being completely restrained and causing cracking in the continuity joint. The authors recommended to not use anchor bolts, not embed girder ends into the diaphragm or joint, and to design only one support in the continuous span as a pin with the rest designed as “rollers” to prevent the girders acting as a fixed connection (Saadeghvaziri et al. 2004).

A finite element study was also conducted as part of the research by Saadeghvaziri et al. (2004) to determine the range of girder age when continuity should

be established between prestressed girders. The finite element model results further supported that establishing continuity between girders at an early age significantly increased the positive moment created by time dependent effects. The modeling also showed the time dependent effects of creep dominated when continuity is established at an early age with shrinkage not contributing substantially at the early age. However, when continuity is established at a later age shrinkage dominated the time dependent effects, and creep did not contribute as much at the later age. The age of the girders at the time of establishing continuity was found to have the largest impact on reducing these effects was at an age between 45 and 90 days (Saadeghvaziri et al. 2004).

2.8 UHPC Durability

While UHPC's compressive and tensile strengths are significant, its greatest strength might come from its extreme durability. With its discontinuous pore structure, low *w*/*c* ratios, and dense particle packing, liquid ingress becomes virtually impossible, greatly reducing huge factors of potential risk on exposed concrete like freeze-thaw (since UHPC has no residual water and there is no room for water to get in) and chloride ion penetration. *"Overall, the greatest impact of UHPC materials may lie in the improved durability of concrete structures, [which] leads to lower bridge repair costs and less downtime for repair. The need for a structural material to perform in harsh environments is a reality, whether the structure is a local bridge subjected to constant winter salting or a bridge pier enduring the harsh freezing and thawing of the Straits of Mackinac"* (Ahlborn 2011).

It makes sense then that intensive projects, or projects in high-risk areas, would choose to use UHPC not just for its exceptional strength, but specifically for its durability. Toutlemonde and Resplendino (2011) describe multiple projects related to durability. One exceptional case being two girders poured in 1996 made out of a Ductal® range reactive powder concrete, made to support an air-cooling tower in the Cattenom nuclear power plant in eastern France. After 10 years in service, constantly surrounded by furring water with a chloride content between 1 and 2 g/l, core sampling of the girders revealed that not only had the concrete stopped all corrosion of completely encased fibers and steel reinforcing, but ultimately had a chloride ion level of

less than 0.10 g per 100 g of cement (where 0.40 g per 100 g is typically the limit for a highly corrosive environment).

Another similar case discussed by Toutlemonde and Resplendino (2011) is a weir at Eraring power station in New South Wales, Australia, along Lake Macquarie. This weir was protected by a spray cover made of precast, pre-tensioned concrete panels, to guard against the constant ocean saltwater spray coming off nearby rocks. Using conventional concrete, these precast panels lasted a mere 14 years before they began to collapse from corrosion. UHPC replacement panels were chosen because they could then be significantly thinner, and therefore lighter, and are expected to have a lifespan of at least 100 years, if not “five times that” (Toutlemonde and Resplendino 2011).

Graybeal and Tanesi (2007) examined durability properties of a propriety UHPC material. Chloride ion penetration testing was performed using ASTM C1202 standards. For each curing regime, three specimens (51 mm thick x 102 mm in diameter) were tested for their ability to resist chloride penetration by measuring the amount of electrical current that passed through them over a 6-hour period using a 60 V direct current. During testing a 3% NaCl solution was applied to one side of each specimen while a 0.3 N NaOH solution was applied to the other side. Chloride ion penetration testing was also performed according to the AASHTO T259-80 specification, but all results were found to be below the minimum accuracy threshold for the testing method, indicating extremely low values of chlorides present in all cases (Graybeal and Tanesi 2007).

Freeze-thaw testing was performed in accordance with ASTM C666 Procedure A on three prisms for each curing regime, each 76 mm x 102 mm x 406 mm in size, by varying the freezing and thawing environment from -18°C to 4.4°C for over 690 cycles. This aggressive environment testing helps to determine the microstructure of the concrete and how well it can combat water ingress and expansion due to freezing. The resonant frequencies of each specimen were measured periodically to gauge these microstructures, as well as to calculate the relative dynamic modulus’ (RDM) of each specimen. RDM is the typical measurement in ASTM C666 to determine the deterioration of the concrete, with 100% being the starting RDM for each specimen.

RDM values between 95% and 100% were found for all of the curing regimes, except for ambient air, which got to RDM values exceeding 110%. The unusually high values for the ambient air/untreated specimens lead to further testing in which specimens of the four curing regimes were placed just in air or water for 28 days before their RDM's were measured. These tests concluded that due to greater proportions of unhydrated cementitious particles (which could be hydrated and therefore swell) untreated UHPC has an increased permeability that can allow ingress of greater amounts of water that can show up as an extremely large RDM value before it shows up as deterioration, even in harsh freeze-thaw conditions. Visible pitting on untreated/ambient air specimens during freeze-thaw testing does indicate, however, that untreated specimens could perhaps have more long-term deterioration that does not show up when only measuring RDM values (Graybeal and Tanesi 2007).

Scaling resistance, which measures concrete performance under winter conditions of high levels of freeze-thaw while also applying deicing chemicals, was measured using ASTM C672. In the Graybeal and Tanesi (2007) study, scaling resistance testing involved the testing of two slabs, each 356 mm x 356 mm x 76 mm deep, for each curing regime. Initially, the test was to be performed by ponding a solution of CaCl on the side of each slab that was cast downward, placing them in an environment that went from -18°C for 18-hours to 23°C for 6-hours, and letting them run for at least 50 cycles. Unfortunately, the lower temperature could not be reached for the first 50 cycles using a walk-in freezer, so an additional 145 cycles were performed under the prescribed values using an environmental chamber. After all of the cycles were completed, the slabs were drained and visually inspected. Less than 0.5 g of various material was collected from the surface of each slab, and there was no visual difference between any of the eight slabs, all having no surface scaling. Overall, a surface condition rating of 0 was given to all eight slabs in accordance with ASTM C672, as described in Table 4 (Graybeal and Tanesi 2007).

Table 4. Scaling surface condition rating system in accordance with ASTM C672

Rating	Condition
0	No scaling
1	Very slight scaling (3 mm [1⁄8 in.] depth, max, no coarse aggregate visible)
2	Slight to moderate scaling
3	Moderate scaling (some coarse aggregate visible)
4	Moderate to severe scaling
5	Severe scaling (coarse aggregate visible over entire surface)

Results from chloride ion penetration and freeze-thaw tests from Graybeal (2006) and Graybeal and Tanesi (2007) are given in Table 5 and Table 6.

Table 5. Graybeal (2006) chloride ion penetration results

Curing Regime	Age	Average Coulombs Passed
Steam	28	18
Ambient Air	28	360
Ambient Air	56	76
Tempered Steam	28	39
Tempered Steam	56	26
Delayed Steam	28	18

Table 6. Graybeal (2006) freeze-thaw testing results

Curing Regime	RDM after 300 cycles (%)	RDM After 690 Cycles (%)
Ambient Air	110	112
Standard Steam	97	96
Delayed Steam	99	98
Tempered Steam	100	100

All results from Graybeal and Tanesi (2007) showed what was expected: high durability properties for UHPC. Specifically, all specimens were found to have near

perfect or even exceptionally high RDM values, even after undergoing twice the necessary number of freeze-thaw cycles, as well as chloride ion levels in the negligible range (excluding ambient air specimens at 28 days, which were still in the low range). The only unexpected part of the study was the significant drop if chloride ingress between the 28 day and 56-day ambient air specimens, which is likely due to the fact that the extremely high amounts of cementitious material in UHPC (which are necessary to develop its dense particle packing) often take more than 28 days to fully cure. This is especially true of silica fume, of which there was a significant amount in the proprietary UHPC mix (Ductal®) used (Graybeal and Tanesi 2007).

Many other studies have been published since Graybeal's original UHPC studies in 2006-2007 expanding on what he found and giving comparison to his results. A study by Ahlborn (2011) examined a standard proprietary UHPC mix (Ductal®) was tested using both freeze-thaw cycling and chloride ion penetration, with a focus throughout the study also put on the different curing regimes used. These curing methods included: ambient air, 48-hour thermal steam treatment applied immediately, and 48-hour thermal steam treatment applied at a 10- and 24-day delay before curing. Care was used in this study to follow the Ductal® procedure for high shear mixing and steam curing, as well as to follow ASTM and AASHTO methods for testing as closely as possible, except where doing so might interfere with curing regimens. The only change this led to related to durability was that before freeze-thaw cycling, the specimens were not soaked in a lime bath for 48 hours like ASTM C666 outlines. However, due to the impermeability of UHPC, it is not likely that these specimens would have gotten to full saturation and it is unlikely that this change had any effect on the outcome of the freeze-thaw tests.

For this study (Ahlborn 2011), chloride ion penetration testing and preparation followed ASTM C1202 exactly for adequate comparison to other concrete types. The curing regimes tested were 28-day ambient air-cured, 7 day thermal steam treated (applied immediately), and 28 day thermal steam treated (applied immediately), with four specimens 2 in. thick x 4 in. in diameter being cast for each curing treatment. The specimens were cast 3 in. high and cut from the top one day before treatment, with the bottom surface representing the bridge or deck element surface and being exposed to the 3% NaCl during testing (with the other side being exposed to the 0.3 N NaOH). The

results of this analysis showed that no matter the curing regime, the total charge passing through the specimens was negligible (<100 coulombs), with the air cured specimens experiencing a slightly higher average total charge, 75 C, versus the thermal steam treated specimens, which experienced a 10 C average for the 7-day specimens and 15 C for the 28-day specimens. It is noted in this study that “the ionic movement was independent of whether the [thermal steam] treated specimens [were] tested at 7 or 28 days within a 95% confidence interval” (Ahlborn 2011), a statement that heavily supports the results collected by Graybeal and Tanesi (2007). Unfortunately, the large drop over time of chloride penetration of ambient air specimens could not be confirmed in this study because ambient air specimens were only tested at one age, 28 days (Ahlborn 2011). There was also a slight concern during this study of short circuiting the testing machine during chloride ion penetration testing due to the inclusion of steel fibers in the UHPC.

Freeze-thaw cycle testing was performed on four 3 in. x 4 in. x 16 in. (75 mm x 100 mm x 406 mm) beams for both ambient air and thermal steam treated (applied immediately) curing methods. All specimens were subjected to eight freezing in air and thawing in water cycles per day for at least 300 cycles in accordance with ASTM C666 Procedure B. Relative dynamic modulus (RDM), length change, and mass change were measured for these specimens approximately every 32 cycles, giving a wide range of properties for analysis of freeze-thaw resistance. Additionally, three ambient air cured and three thermal steam treated specimens were cycled in and out of a separate, ambient temperature, water bath for comparison. These wet-dry specimens were only measured for mass change and RDM values. The results for all 14 specimens are shown in Table 7 (Ahlborn 2011).

Table 7. Ahlborn (2011) freeze-thaw testing results (2011)

Curing and Testing Regime	No. of Specimens	Average RDM at End of Cycling (%)	Average Length Change (%)	Average Mass Change (%)
Air (F-T)	4	101.57	0.0004	0.54
TT (F-T)	4	100.27	0.000014	0.08
Air (W-D)	3	101.91	—	0.22
TT (W-D)	3	100.10	—	0.06

Note: F-T indicates “freeze-thaw” and W-D indicates “wet-dry”

According to ASTM C666, a specimen has considered to have failed due to freeze-thaw when its RDM reaches 60% of its initial modulus, or if the specimen has expanded 0.10% in length. As seen in Table 7, none of the specimens tested in this study reached these failure criteria, with all specimens finishing with a RDM higher than 100% (meaning that instead of deteriorating, these specimens simply continued to hydrate). It can also be seen that air cured specimens had significantly higher increases compared to the thermal steam treated specimens, primarily due to the fact that the air cured specimens have more unhydrated cement particles that become hydrated in the presence of water, even under the harsh conditions of freeze-thaw cycling, just as was experienced by Graybeal and Tanesi (2007) study, though to a significantly lesser extent. Also important to note is that the measured length and mass changes were seen to be in good correlation to the RDM values (Ahlborn 2011).

Ahlborn (2011) mentions that for materials that contain high amounts of silica fume and silica powder, like UHPC, it is very common to have a lower chloride ion movement rate than that normally found in materials without silica fume. However, no research had been done at the time to officially make this correlation for UHPC specifically.

Another similar study by Chumping et al. (2015) investigated the effects of different curing conditions on UHPC durability properties while also experiencing a flexural load. In this study, three different curing conditions were studied: standard ambient air curing, thermal steam curing, and oven curing. A special loading device was used on all loaded specimens in this study to make the specimens act as four-point bending beams under 50% ultimate flexural load. All specimens tested were 40 mm x

40 mm x 160 mm with fine steel fibers 0.2 mm in diameter x 13 mm in length. The mixing procedure for this study was not detailed, but the custom UHPC mix used is presented in Table 8. This study hoped to assess UHPC for effectiveness in areas with harsh durability conditions and high loading/intense use requirements in parallel.

Table 8. Chumping (2015) custom UHPC mix proportions (kg/m^3)

Material	Cement	Fly Ash	Silica Fume	River Sand	Superplasticizer	Water	Steel Fibers
UHPC	540	432	108	1,296	37.8	172.8	160

Chloride diffusion testing was performed by painting the specimens with epoxy on all sides except for one exposed side to be tested, which was placed in the tensile region. The specimens were then immersed in a sealed container of 10% by weight sodium chloride for 90 days, after which powder samples were collected by drilling holes at different depths in the exposed surface and free chloride contents were found using titration methods. Freeze-thaw testing was performed in accordance with Chinese standard GB/T 50082-2009, which involved alternating the specimens between -20°C and 20°C in a freeze-thaw box, with one cycle taking about 4 hours. Every 50-100 cycles, the specimens were taken out and measured for RDM and mass loss, with over 800 total cycles performed for each specimen. For both tests, loaded and non-loaded specimens were examined for comparison, with all loaded specimens simply being put into their testing conditions while also being in the loading apparatus. A summary of key test results from this study is presented in Table 9 (Chumping et al. 2015).

Table 9. Chumping (2015) chloride ion penetration and freeze-thaw test results

Curing Method	Avg. Cl Penetration at <5 mm depth-Non-Loaded (%)	Avg. Cl Penetration at <5 mm depth-Loaded (%)	Avg. Cl Penetration at 5-10 mm depth-Loaded (%)	Mass Loss After 800 Cycles-Loaded (%)	RDM After 800 Cycles-Loaded (%)
Standard	0.125	0.15	<0.05	1.10	95.30
Steam	0.13	0.15	<0.05	1.16	94.35
Oven	0.225	.275	0.125	1.35	92.62

An important testing result not reflected in Table 9 was that for all specimens, regardless of curing type or whether they were loaded or non-loaded, mass loss was similar before 300 cycles, an indication that perhaps the Ahlborn (2011) study could

have benefited from performing more cycles in their freeze-thaw testing. After 300 cycles, the loaded specimens began to exhibit more mass loss than the non-loaded ones. It should also be noted that mass loss stayed around 0.50% maximum for all curing methods without loading applied and even the worst case of oven cured specimens only got down to about 95% RDM without loading applied (Chumping et al. 2015).

These results show conclusively no failure of this UHPC mix, with all average chloride ion penetration levels well below the limit for a highly corrosive environment of 0.40% and RDM's well above the 60% ASTM C666 limit. These results also indicate that oven curing leaves the UHPC much more vulnerable to chloride ion penetration and freeze-thaw losses. This is due to the fact that oven curing causes concrete to actively lose water, leaving it with micro- cracks. Micro-cracks not only lead to paths for chloride ions to enter, but also induce spalling of the specimen surfaces in freeze-thaw testing, which is the main cause of mass loss. However, perhaps the most surprising result from this study is that while loading the specimens does of course result in a predictable decrease in durability properties, this decrease is no more dramatic than that from any other change, like curing regime. Moreover, even with loading applied and poor curing conditions (in regard to durability properties) all specimens are well within working conditions (Chumping et al. 2015).

A study by Alkaysi et al. (2016) was done using nine different UHPC mixes to try to get a better understanding of the effects that different cements and amounts of silica powder can have on UHPC. Mix proportions and designations for these nine mixes are summarized in Table 10. Three different cement types were used: a Type I white cement, a Type V portland cement, and a 50:50 blend of Type I portland cement and GGBFS (ground granulated blast-furnace slag). All mixes incorporate two types of silica sand, F100 and F12, which have a median particle size of 100 and 500 μm, respectively. All of the mix designs used steel fibers that were 19 mm long with a diameter of 0.2 mm and were mixed with a horizontal pan mixer using standard dry mixing procedures. Table 11 summarizes the results of Alkaysi et al. (2016).

Table 10. Alkaysi et al. (2016) mix designs by proportion

Name	Cement	Silica Fume	Silica Powder	Fiber (%)	F100	F12
W-25	1.0	0.25	0.25	1.50	0.26	1.06
W-15	1.0	0.25	0.15	1.50	0.29	1.14
W-00	1.0	0.25	0.00	1.50	0.31	1.26
V-25	1.0	0.25	0.25	1.50	0.26	1.05
V-15	1.0	0.25	0.15	1.50	0.28	1.14
V-00	1.0	0.25	0.00	1.50	0.31	1.26
IG-25	1.0	0.25	0.25	1.50	0.26	1.06
IG-15	1.0	0.25	0.15	1.50	0.28	1.14
IG-00	1.0	0.25	0.00	1.50	0.31	1.26

Note: W indicates white cement, V indicates Type V cement, and IG indicates Type I/GGBS cement

Table 11. Alkaysi et al. (2016) chloride ion penetration and freeze-thaw test results

UHPC Mix	Total Charge Passed- Rapid Chloride Ion Penetration (Coulombs)	Total Mass Loss after 28 Cycles (g/m^2)- Freeze-Thaw
W-25	89	98.8
W-15	295	20.7
W-00	637	17.7
V-25	939.5	18.2
V-15	488.5	18.0
V-00	57	42.2
IG-25	137.5	20.5
IG-15	229	24.2
IG-00	137.5	44.7

In this study, two cylindrical specimens, 150 mm in diameter and 300 mm in height, for each of the nine concrete mixes were cast for freeze-thaw testing. After 24 hours of curing, the cylinders were demolded and submerged in ambient temperature water for 28 days before being cut into 120 mm x 110 mm x 70 mm rectangular prisms.

From there, the lateral surfaces of the prisms were sealed with aluminum foil using butyl rubber and each prism was placed with their bottom horizontal surface in the testing liquid. Each cycle was done over a 12-hour period by varying the temperatures of the freeze-thaw system from -20°C to 20°C. This study used a modified CIF (capillary suction, internal damage, and freeze-thaw) testing procedure to properly measure the resistance of each concrete mix to combined attack from de-icing salt and frost, similar to scaling resistance testing. Moisture uptake and internal damage were measured every few cycles for at least 60 cycles (a relatively low number of cycles, though understandable for the number of mix designs tested). After 28 cycles, total mass losses (presented in Table 11) were compared to the limit for mean scaling of 1500 g/m^2 and found to be significantly lower for all nine mixes. After 60 cycles, it was also concluded that none of the nine mixes had RDM's lower than 100% (i.e., no internal damage) (Alkaysi et al. 2016).

In accordance with ASTM C1202, chloride penetration testing was done on 100 mm diameter x 500 mm width specimens, two for each of the nine mix designs, using a measurement cell with a fluid reservoir on both horizontal face of each specimen. One reservoir was filled with a 3% NaCl solution connected to a negatively charged terminal and the other with a 0.3 N NaOH solution connected to a positively charged terminal. Electrical current was then automatically measured for a standard 6-hour period with a direct current voltage of 60 V. When compared to the standards set out in Table 12 (AASHTO 1990), the results in Table 11 show that all nine test mixes resulted in a total charge passed either in the low or negligible range (with lower values/ranges being more favorable), well within acceptable standards for most projects depending on the intended use/conditions involved (Alkaysi et al. 2016).

Table 12. Chloride permeability classifications for concrete

Chloride Permeability	Charge (coulomb)	Typical Concrete
High	>4000	High w/c ratio (>0.6)
Moderate	2000-4000	Moderate w/c ratio (0.4-0.5)
Low	1000-2000	Low w/c ratio (<0.4)
Very Low	100-1000	Latex-modified concrete, internally sealed concrete
Negligible	<100	Polymer infused/polymer concrete

Due to exceedingly low numbers throughout, it is hard to compare the changes in results from mix to mix, since most differences are within the range of statistical error. The summary statement for this study can still be made, however, that overall Type V portland cement and 15% silica powder performed best for freeze-thaw resistance and the Type I portland/GGBFS blend and 0% silica powder were best for chloride ion resistance. However, it should be noted that these results are not based on any statistical trends, and simply show how unpredictable the results to changes of UHPC mixes can be. Additionally, while some differences may look exceptionally large, in relation to limits and typical values, all test results are incredibly low, and therefore all UHPC mix combinations tested would be suitable relative to durability properties for almost any project (Alkaysi et al. 2016).

2.9 Corrosion

As evident throughout Section 2.8, there is extensive research into many areas of UHPC durability. However, the reaction of bridge decks with previously corroded reinforcing steel to partial or full depth repairs using UHPC is less common. Even Graybeal (2006, 2007) only mentions corrosion of UHPC in terms of surface corrosion of steel fibers on and near the exterior of the concrete, calling it “more aptly described as surface staining”. The primary reasoning behind the concern over the likelihood of UHPC used in a bridge deck leading to further corrosion issues in the existing steel is the anodic ring phenomenon, or “Halo Effect”. The Halo Effect experienced by steel reinforcing in concrete is generally the result of the accelerated corrosion of steel in the

base material that has come into contact with fresh concrete due to the very high pH in fresh concrete as compared to concrete that has been in use for an extended period of time.

This specific kind of corrosion cell is more specifically called macrocell corrosion. Steel rebar corrosion occurs due to an oxidation process that breaks down the passive film covering steel rebar in the presence of chloride ions or carbon oxide (Jones 1996). That is to say, when an anode and a cathode are separated from each other, the concrete itself acts as an electrolyte solution and a macrocell is produced. According to Hansson (2006), a simplified definition can be used, which states that macrocell corrosion in steel rebar is when an actively corroded bar is coupled to a passive bar or one of lower corrosion rate. Coupling being either direct contact or simply being in close proximity to, since the concrete is acting as an electrolyte solution that connects the two closely located reinforcing bars. Differences in corrosion states can occur to differences in compositions (such as the use of different sizes or grades of rebar in the same section of concrete) or differences in environments (such as having rebar that goes through base concrete and the repair concrete). In these scenarios, the corroded bar becomes the anode, and the passive bar becomes the cathode.

This is all in comparison to microcell corrosion, which does not need a specific scenario to occur, only an anode and cathode present directly adjacent to one another, which is simply caused by having surface irregularities and is true of all steel reinforcing. This means that microcell corrosion occurs across every steel reinforcing bar on its own to varying degrees. Because of this, only macrocell corrosion indicates negative interaction between base concrete and repair material through the Halo Effect.

It should be noted that typically, fresh concrete has a pH of around 13, with concrete that has been allowed to age and experience carbonation from contact with the air having a pH of about 8. The high starting pH of typical concrete is mostly due to calcium hydroxide, which is a byproduct of cement hydration. However, no research has been done to find the exact pH of UHPC, in the fresh state or long-term state. It can be assumed that the low w/c ratio of UHPC that leads to often having large amounts of unhydrated cement within its densely packed matrix would lower the pH of fresh UHPC.

On the other hand, the fact that UHPC also starts with such a higher level of cementitious product compared to normal concrete, having no coarse aggregate (instead filling its voids with replacement cementitious materials such as silica fume), may increase the pH of UHPC.

Though no studies are currently available detailing how steel rebar reacts to UHPC as a repair material, a starting place for analysis is still necessary. A study by Hansson (2006), which looked at the corrosion performance of different concrete mixes on their own. This study chose to look at three concrete mixes, one normal portland cement mix and two high performance concrete (HPC) mixes (one using 25% cement replacement of blast furnace slag and one with 25% replacement of class C fly ash) as detailed in Table 13. In this study, seven 11 in. x 6 in. x 4.5 in. (279 mm x 152 mm x 114 mm) prisms were tested for each mix, totaling to 21 specimens, each containing three 10M reinforcing bars, one with a 25 mm cover from the top and two with a 25 mm cover from the bottom. These small-scale specimens were cured with wet burlap for 7 days, stored outdoors for 5 months to prepare them for exposure to chlorides, and then tested for macrocell corrosion (Hansson 2006).

Table 13. Hansson (2006) mix designs (kg)

Material	Type 10 Portland Cement	Type 10SF Portland Cement	Slag	Fly Ash	Sand	Stone (20 mm)	Water (l)
Portland Cement	335	-	-	-	770	1070	153
HPC- Slag	-	337	113	-	718	1065	158
HPC- Fly Ash	-	337	-	113	718	1065	158

For macrocell corrosion testing, the specimens were prepared for measurements as follows: coating the vertical surfaces with epoxy resin to prevent the access of oxygen into these surfaces, mounting a ponding well onto the top surface, connecting the bottom two bars to each other and finally, connecting the two bottom bars to the top bar through a 100-ohm resistor. From there, the ponding well was filled with a 3% NaCl solution off and on for two-week periods for a total of 180 weeks, with the voltage drop across the resistor of each specimen being measured daily. The macrocell corrosion current between the top (anode) bar and the bottom (cathode) bars was determined

using the measured voltage drops and Ohm's law for conversion. Overall, this study showed the HPC's as performing significantly better at protecting the steel rebar from macrocell corrosion than normal portland concrete, having no active corrosion after 180 weeks in either HPC mix. In comparison, the portland cement concrete mix experienced corrosion initiation as soon as 35 days into testing. This is almost certainly due to the fact that HPC, like UHPC, has a high level of impermeability, and if no chloride ions can penetrate into the HPC specimens, there can be no electrical difference across the different levels steel reinforcing (Hansson 2006).

This result does not, however, guarantee that UHPC will still produce such a satisfactory result when used as a repair material. The impenetrability of UHPC may in fact cause more chloride ion build up in the base concrete, creating a large macrocell current across any steel rebar that goes through both materials.

2.10 Summary

Proprietary UHPC mixes have been extensively studied and implemented for use in precast applications and new construction. Its material properties, overall behavior, and placement techniques are fairly well known and have been tested time and again. However, less information is available on UHPC formulations using local materials. This is specifically true for bond behavior with base concrete and steel, use as a joint material, and durability. There is limited information about UHPC used for repairs at all, save for the few studies done to explore UHPC as an overlay material or as a beam end repair. A limited number of studies exist focused on determining the behavior of a UHPC joint in a slab under static and cyclic loading in flexure, and these considered specific joint reinforcing details for new construction, not retrofits. Moreover, while these properties have been demonstrated in UHPC's testing in slab connections, mid-span beam splices, and complete girders, but has not been considered in continuity joints for live load distribution. Continuity joints would greatly benefit from the advanced mechanical properties UHPC has to offer in place of normal concrete. The joint would be able to utilize the short development length and high-tension strength to make the connection less susceptible to cracking when subjected to the moments caused by time

dependent effects such as creep and shrinkage and improve the overall capacity of the joint for the negative moment from live loading.

3.0 UHPC Material Evaluation

3.1 Overview

The applicability of available proprietary UHPC products, primarily the Lafarge product Ductal®, was evaluated, and mix designs were developed using local materials for bridge repair and rehabilitation in Oklahoma. Performance requirements were identified, and each mix design was compared to these performance requirements to provide the basis for applicability. These requirements initially included a target flow (ASTM C1437) of 9 in. and a target 1-day compressive strength of 10.8 ksi.

Initially, a review of methods for proportioning UHPC using local materials and of performance requirements was conducted. The availability of cements, supplementary cementitious materials, steel fibers, and chemical admixtures in Oklahoma was investigated. Silica fume, ground granulated blast furnace slag (GGBFS), Class C fly ash, steel fibers, silica sand, masonry sand, Type I portland cement, and Type III portland cement were identified as candidate materials available in Oklahoma and sufficient quantities for evaluating potential mix designs were obtained. Particle size analyses were conducted for the Type III cement, supplementary cementitious materials, silica sand, and masonry sand to provide necessary information for optimizing the packing density of the dry constituents for mix development. The properties of the mix constituents are provided in Table 14, including their relative effect on compressive strength. A collaboration was formed with Lafarge in order to obtain a sufficient quantity of Ductal® for use in mix evaluation and small-scale specimen testing.

Table 14. Properties of UHPC mix design constituents

Property	Type I Cement	Type III Cement	Class C Fly Ash	Silica Fume	GGBFS	VCAS	Masonry Sand
Shape	Angular	Angular	Spherical	Spherical	Angular	Angular	Angular
Specific Gravity	3.15	3.15	2.38	2.22	2.97	2.6	2.63
Early Strength	-	↑	↓	↑	↓	↓	-
Long-Term Strength	-	-	↑	↑	↑	↑	-
D10 (μm)	0.86	0.71	0.82	2.08	0.92	0.94	128.71
D50 (μm)	9.94	5.51	10.6	18.75	8.25	11.13	222.12
D90 (μm)	32.25	20.4	75.17	63.13	24.96	44.13	364.98

3.2 UHPC Mix Design Using Local Materials

Nine series of mix design trials were conducted examining various parameters identified in the initial review as potentially affecting UHPC composition and properties. A complete discussion of the individual series can be found in McDaniel (2017) and Looney et al. (2019). These mixes were made using the small mortar mixer available at Fears Lab and evaluated the mortar flow test described by ASTM C1437 and using compression tests of 2 in. cubes based on the methods of ASTM C109. The first series of mortar mixes (A) consisted of cement, fly ash, silica fume, and masonry sand with water/cementitious material ratios of 0.35 to 0.30 and cement/binder ratios of 0.73 to 0.60. These mixes were based on successful mix designs from previous research. Several candidate mixes achieved the desired flowability and compressive strength requirements. The main purpose of this initial series of mixes was to verify the efficacy of the mixing methods available in the lab for UHPC.

The next iteration cycles (Series B and Series C) were conducted to increase the compressive strength of UHPC mortars. A UHPC mix design produced by FHWA served as the baseline condition. The first iteration of Series B evaluated the effect of the water-cement ratio and cement-binder ratio using only fly ash replacement of the cement. The second iteration of Series B varied the combination of water and high-

range water reducer (HRWR) against a baseline of constant dry constituents. Series C investigated the effect of supplementary cementitious materials including silica fume, fly ash, vitreous calcium aluminosilicate (VCAS), and GGBFS, along with Type I cement. Different ratios of replacement and interaction between cementitious materials were evaluated for flow as well as 1-day and 7-day compressive strengths. The effect of packing density on the behavior of UHPC mixes was also investigated. Initial results revealed that higher packing densities increased flowability but did not generally increase compressive strength. These mixes included binary, ternary, and quaternary mixes using the various supplementary cementitious materials mentioned previously. The results of Series B and Series C were used to identify the effect of the tested variables and guide subsequent iterations.

After these iterations were completed the mortar flow and compressive strength targets for developing UHPC mixes were revised. The minimum mortar flow was reduced from 9 in. to 7 in., as the 7 in. value appeared to be the demarcation line where the material transitioned to a pourable state. The 1-day compressive strength target was increased from 10.8 ksi to 14.3 ksi, primarily due to the significant initial strength gain provided by the Type III portland cement used in these mixes.

A full analysis of the particle packing potential of the available constituents was conducted prior to the next two iteration cycles (Series D) since earlier iterations were not reaching the target compressive strengths. Particle packing for over 3400 potential mixes was analyzed at 5% rates of change to find the most optimally packed combinations of fine aggregate, cement, and SCMs. This matrix found the difference between the optimal particle packing curve defined by the modified Andersen and Andreasen equation (Funk and Dinger 1994) (which uses both the maximum and minimum particle size in the mix to define the curve) and the gradation of the mix being investigated. The lower the residual sum of squares (RSS) value, the closer the particular mix is to the ideal curve. For this investigation, the slope factor of the Andersen and Andreasen curve used was 0.22, which the literature suggests is a number which a) will produce the highest strengths with exclusively fine particles and b) should produce a mix that will flow without high-range water reducer (HRWR) (Kim et al. 2016; Sbia et al. 2016; Ye et al. 2012).

The most optimally packed mixes and the most optimally packed mixes with an amount of cement found to predict high strength made up the first iteration of Series D. This research did not confirm that low RSS values will lead to either of the above properties stated in the literature. However, mixes with higher amounts of SCMs than previously explored performed better than expected. The knowledge obtained through these mixes was combined with the most successful mixes of the previous iterations to make up the second iteration of Series D. Early strengths of these mixes were comparable to the best mixes of the previous iterations. Results of the 28-day compressive strength tests on Series D (particle packing and small variations on the optimized particle packing combination) indicated that in terms of strength, the optimum silica fume dosage was 12-15%. Dosages above 15% resulted in very minimal strength gains but significantly reduced mortar flow. Variations in quantity of Type I cement from the optimum particle packing combination of 5-10% increased the mortar flow by 2 in. to 3 in. without negatively impacting strength. Specific effects of fly ash were not as clear, and further optimizations without fly ash were the next step.

Series E and F consisted of variations amounting to a total of 35 individual mixes. Series E investigated the interaction between Type I and Type III portland cements, which cure and gain strength at different rates. This investigation showed that at 7 days, combinations of Type I and Type III cement exhibited compressive strengths varying by less than 10%. As expected, mixes with a higher proportion of Type I cement resulted in greater mortar flow values, primarily due to the higher surface area of the more finely ground Type III cement, which requires more water available for wetting the cement grains. Series F studied the effect of the aggregate to cementitious material ratio. While this parameter had been investigated earlier in the research, it warranted a second look as the strength of the paste had increased dramatically since the prior investigation. Early data showed that a sand-to-cementitious material ratio of 0.8 provided a 5% increase in compressive strength. The previous mixes used a sand-to-cementitious material ratio of 1.0.

Series G, H, and J included a total of 54 mixture combinations. Series G, the first 32 mixes, investigated the effect of GGBFS at replacement rates varying from 10% to 40% in conjunction with silica fume replacements varying from 5% to 20%. The

proportion of Type I to Type III cement was varied in the latter half of this series. The mixes with the highest compressive strengths had 10-20% GGBFS paired with 5% silica fume. The mixes with higher proportions of Type I cement (thus lower proportions of Type III cement) were slightly (around 5%) higher in strength, but this may simply be due to typical variations in concrete compressive strength testing. Type I cement does have a lower specific surface than Type III cement, leaving more “free water” during mixing before curing begins. These mixes thus had higher mortar flows, and the entrapped air bubbles escaped out of the top more readily when the specimens were tapped than for mixes with a higher proportion of Type III cement. Entrapped air was a consistent issue during high shear mixing of the UHPC material, which is why it is customary to pour UHPC higher than required and grind the surface down to the desired elevations. Series H investigated potential mix combinations from a recent UHPC study (Ibrahim 2013) found in the literature. These mixes underperformed in testing compared to results presented in the previous work. Finally, Series J investigated small changes in the highest performing mixes to date. The changes included using a larger proportion of Type I cement and changing the ratio of cementitious material to aggregate.

The 28-day strengths of Series G, H, and J were evaluated to determine the candidate mixes to move forward to the next stage of development involving the addition of steel fibers and heat curing. The “best” mixes were chosen based on a combination of properties including 28-day compressive strength, sufficient mortar flow, and materials used (i.e., mixes representing a variety of SCMs). Additional information on the relative effects of different SCMs on compressive strength is provided in Table 14. Mixes J3, J8, and J13 were chosen to move forward. Mixes J3 and J13 use GGBFS as the primary SCM at 30% and 40% replacement, respectively. Mix J8 uses fly ash as the primary SCM and, although there were other mixes with higher compressive strengths, this mix was selected for the third option as it was the highest performing mix that incorporated fly ash as the primary SCM. In general, fly ash is a more easily obtainable SCM, and the compressive strengths of the highest performing fly ash mixtures differed by only 3%. The three mix designs – J3, J8, and J13 – are shown in Table 15 and represent a balance between workability, strength, and cost.

Table 15. UHPC mix designs with local materials

Material	J3	J8	J13
Type I Cement (lb/yd^3)	1179.6	1179.6	786.4
Type III Cement (lb/yd^3)	0	0	196.6
Silica Fume (lb/yd^3)	196.6	196.6	196.6
VCAS (lb/yd^3)	0	294.9	0
Class C Fly Ash (lb/yd^3)	0	294.9	0
GGBFS (lb/yd^3)	589.8	0	786.4
Masonry Sand (lb/yd^3)	1966.0	1966.0	1966.0
w/c	0.2	0.2	0.2
HRWR (oz/yd^3)	15.77	15.77	14.88

Table 16 contains a summary of the heat curing and fiber study series. With 10 variations for each of the 3 compositions shown in Table 15, a total of 30 batches were processed. The heat curing temperature was set at 180°F to coincide with the temperature achievable with the heat lamps used for the slab joint specimens described in Section 5. Heat curing of small test specimens was conducted using the aggregate drying oven with specimens placed in pans filled with water and covered in plastic as shown in Figure 39. A 2% fiber dosage rate by weight was selected based on a thorough review of previous research. In general, beyond 2%, the hardened property gains are minimal while the decrease in workability is significant.

Table 16. Heat curing and fiber study series

Cylinder Test Date	Mix Variation
1 Day	Control
1 Day	Carbon steel 1” crimped fibers
1 Day	Grade 430 steel 1” crimped fibers
3 Days	Control
3 Days	12 hours heat curing
3 Days	36 hours heat curing
3 Days	48 hours heat curing
28 Days	Control
28 Days	Carbon steel 1” crimped fibers
28 Days	Grade 430 steel 1” crimped fibers

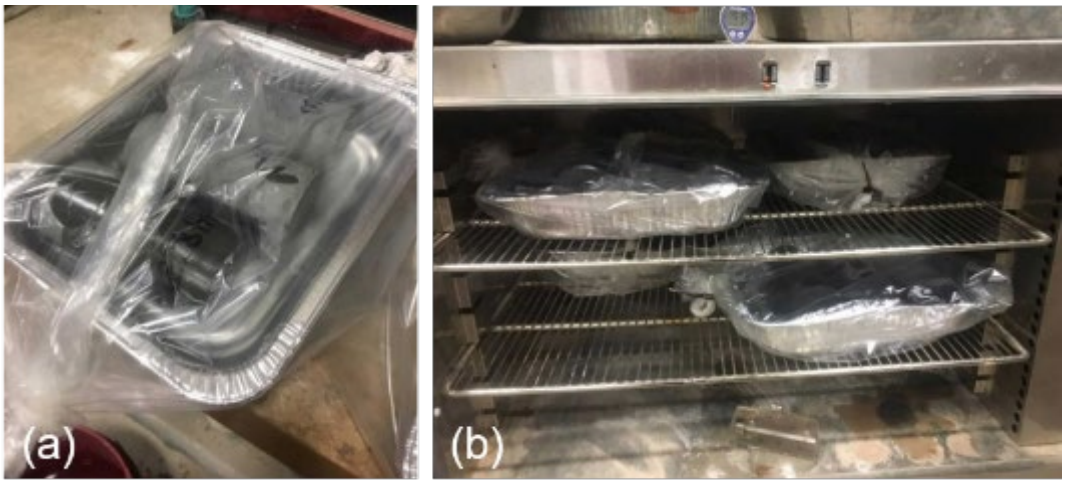

Figure 39. (a) Close-up of test specimen pan (b) overall heat curing environment of test specimens

The initial mix designs including fibers did not perform favorably. The transition of the mixes from the small planetary mortar mixer to the larger 4.25 ft^3 high-shear mortar mixer resulted in an increase in mortar flow. Furthermore, even though the mortar flow was still within the 8 in. to 10 in. target, this amount of fluidity resulted in settlement of the fibers. A series of trials was conducted with the small planetary mortar mixer to adjust the amount of HRWR, with a target flow of 7 in. The heat curing and fiber study series outlined in Table 16 were then completed using the larger high-shear mixer with the adjusted dosages. The flows for material mixed with the larger high-shear mixer using the adjusted HRWR dosages ranged from 7.5 in. to 8 in. and resulted in proper suspension of both types of fibers.

As anticipated, heat curing resulted in significant short-term strength gains. In general, the most significant strength gains occurred within the first 12 hours of heat curing. With additional heat curing, the fly ash mixes showed the largest gains, with compressive strengths increasing approximately 15% from 12 hours to 36 hours but then showed only minimal gains from 36 hours to 48 hours. Conversely, the GGBFS mixes showed very modest compressive strength gains beyond 12 hours of heat curing. It is also important to note that all three mixes reached 3-day compressive strengths of 20 ksi with 36 hours of heat curing. Also, as anticipated, the addition of fibers had limited effect on compressive strength, with increases of only 5 to 10%.

The final step in the mix development was to complete a combined heat cured/fiber-reinforced series for Mixes J3, J8, and J13, including tests for shrinkage, modulus of rupture, modulus of elasticity, abrasion resistance, and tensile strength. Stainless steel, Grade 430, Flex-Ten® steel fibers produced by D&C Supply Co., Inc. were selected for use in these tests and in the joint testing portion of this study. The properties of these fibers are shown in Table 17. At 28-days, the fibers did not produce a significant increase in compressive strength. However, the specimens that were fiber reinforced did retain continuity whereas the unreinforced specimens shattered during compressive strength testing, as shown in Figure 40.

Table 17. Properties of Flex-Ten® steel fibers used for comparative testing

Material	Thickness (in.)	Width (in)	Length (in.)	Aspect Ratio	Weight (g)
ASTM A176 Stainless Steel	0.02	0.033	1	47	0.09

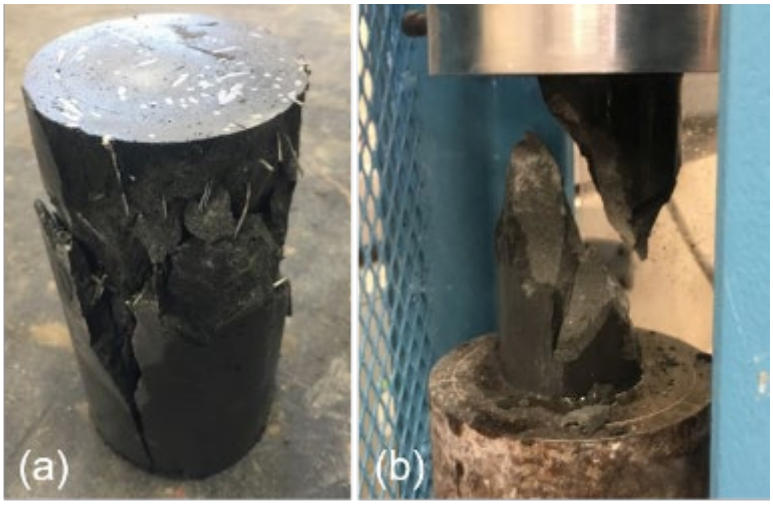

Figure 40. Fiber reinforced (a) and unreinforced specimens after compression testing

These 28-day specimens were also compared to the specimens that were heat cured and tested at 3 days during initial mix design testing, as shown in Figure 41 (J8(1), J3(2), J13(3)). The compressive strengths of the heat-cured specimens exceeded the non-heat-cured 28-day compressive strengths by 4-11%. Additionally, the heat-cured specimens failed more consistently than the non-heat-cured specimens, with about half the standard deviation between the three replicate specimens.

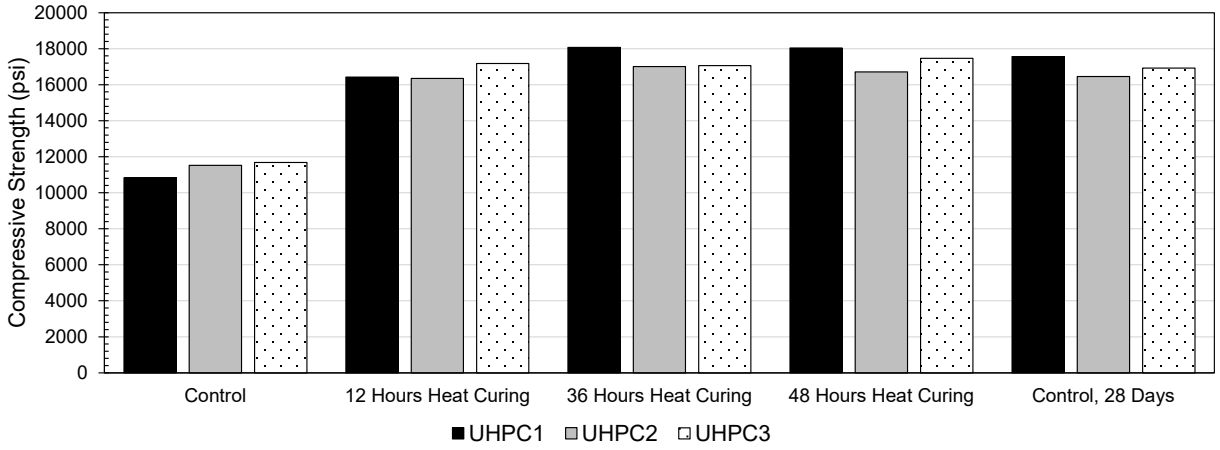

Figure 41. Compressive strengths of heat-cured (3-day) vs. non-heat-cured (28-day) for mixes J8 (1), J3 (2), and J13 (3) without fibers

The heat cured specimens that were also fiber reinforced gained strength more quickly than the heat cured specimens without fibers, as shown in Figure 42. All three mixes had improved strengths for 36 hours of heat curing with the addition of steel fibers. The metallic-based fibers possibly improved heat flow within the UHPC, which aided the curing process. There was not a large difference in the behavior between the three mixes with regard to other factors, but the GGBFS mixes (J3 (2) and J13 (3)) did see more of an improvement with the heat curing and fibers than the fly ash mix J8 (1). Mix J3 (2) exceeded 20 ksi compressive strength with mix J13 (3) close behind at 19 ksi, both with 36 hours of heat curing.

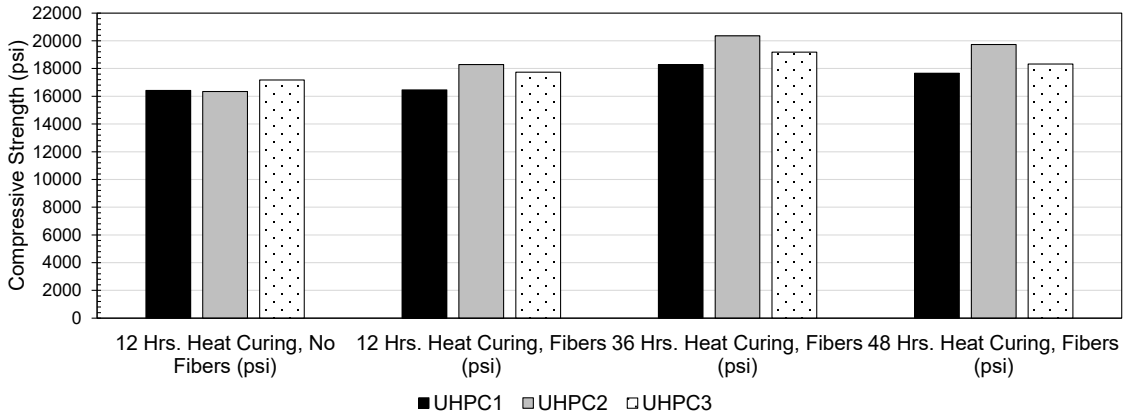

Figure 42. Compressive strengths of heat-cured UHPC mixes J8 (1), J3 (2), and J13 (3) with and without fibers

Figure 43 shows results of modulus of rupture testing for the three non-proprietary mixes at 28 days of age. The first-cracking load shown in Figure 43 is the load at which fiber reinforced MOR first cracked while the MOR value is the failure load for unreinforced specimens, which typically occurred immediately after the first crack appeared. Mixes J8 (1) and J3 (2) performed similarly with J3 (3) having higher values for both first crack and MOR. Fibers did not appear to help the first crack resistance of the UHPC for any of the mixes. The typical crack pattern for a fiber-reinforced specimen is shown in Figure 44. One item of note is the crack pattern of the unreinforced MOR shown in Figure 44. The failure crack is vertical through most of the specimen, but transitions to an angle of approximately 45 degrees near the top of the specimen. This indicates that this material may absorb more energy as the crack propagates.

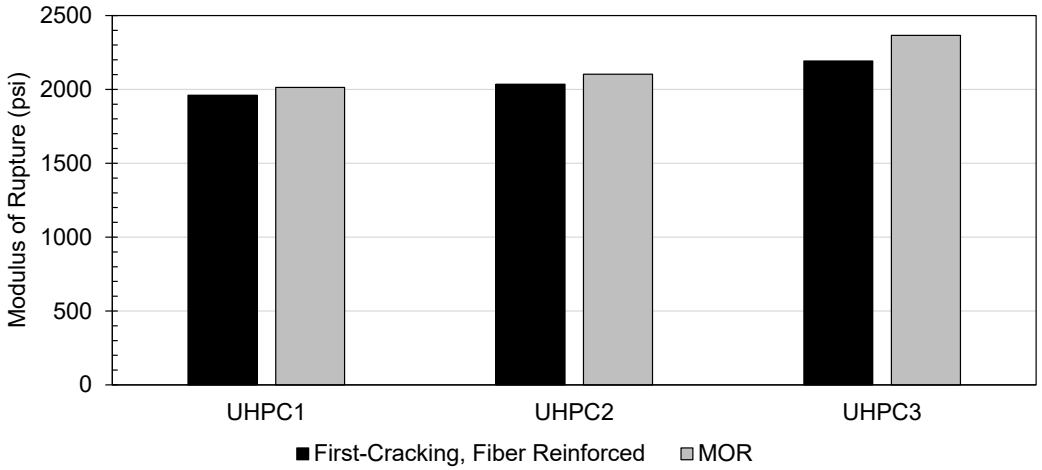

Figure 43. Modulus of rupture at 28 days for UHPC mixes (1) J8, (2) J3, and (3) J13 with and without fibers

Figure 44. Photo showing typical crack pattern for fiber reinforced (a) and unreinforced (b) modulus of rupture specimens

Modulus of elasticity values measured at 28 days for specimens without fibers are presented in Figure 45. Mixes J8 (1) and J13 (2) had very similar values of modulus of elasticity with J3 (2) having a slightly smaller value. Comparisons to the ACI (2014) equation for normal-weight concrete and the equation presented by Russel and Graybeal (2013) developed specifically for UHPC are also shown in Figure 45. The ACI equation is known to overestimate for compressive strengths greater than 6000 psi. As expected, the ACI equation greatly overestimates the measured values. The Russel and Graybeal (2013) equation (Eq. 1) produces estimates within 10% for all mix designs.

$$E_c = 46{,}200\sqrt{f_c'} \qquad \text{(Eq 1)}$$

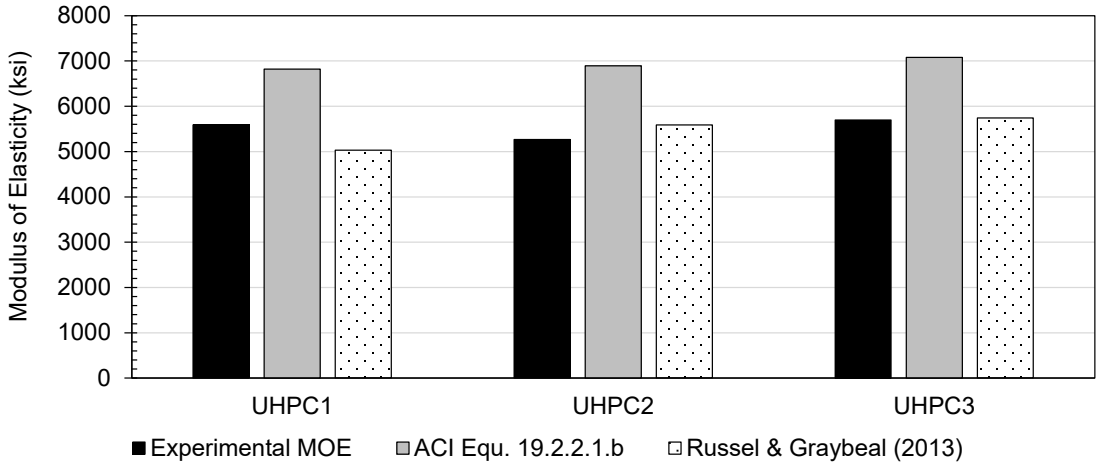

Figure 45. Modulus of elasticity at 28 days for UHPC mixes (1) J8, (2) J3, and (3) J13 with and without fibers with comparison to predicted values

In summary, UHPC mix J3 (2) with a 180 °F, 3-day heat cure produced the best overall results and was used for subsequent composite bond tests and structural joint testing.

3.3 Lafarge Ductal®

Several trial batches of Ductal® JS1000 were mixed to prepare for small scale joint testing described in Section 4.2.1. The first batch tested achieved a compressive strength in excess of the targeted 22,000 psi with the aid of heat curing. Test mixes were batched with two different high range water reducers, with and without fibers, and with two curing schemes. The final mix proportion used for Ductal® is summarized in

Table 18. The Ductal® mixes performed as anticipated, with heat cured specimens reaching the 21 ksi target compressive strength in 3 days and the 72° F moist cured specimens reaching the target compressive strength in 28 days. As anticipated, the fibers decreased mortar flow by 1 in. to 2 in. and had no effect on compressive strength. However, the fibers will increase tensile strength. Additional information regarding performance of Ductal® compared to property specifications and other materials is included in subsequent sections.

Table 18. Ductal® JS1000 mix proportion

Material	Quantity (lb/yd^3)
Premix	3700
Water	202.3
Premia 150	50.6
Steel Fiber (2%)	262.9

3.4 Mixing and Placement Method Evaluation

3.4.1 Mixer Evaluation and Mixing Procedures

The initial series of mixes described in Section 3.2 was used to verify the efficacy of the mixing methods available for UHPC at Fears Lab and additional testing was conducted before casting the joint specimens described in Section 5. Discussions were held with a project manager from Lafarge related to mixing Ductal® specifically, but these methods were considered applicable to any UHPC. Two different small planetary mortar mixers were available at Fears Lab for mixing up to approximately 5 lb to 15 lb of material and a large horizontal axis paddle mixer was available that could mix up to approximately 1700 lb of material. A decision was made to purchase an additional high-shear mixer (Imer Mortarman 120 Plus) with capacity (4.25 ft^3) between those already available to be used in evaluating UHPC mix designs based on recommendations by individuals at Lafarge. This mixer could mix between 100 lb and 150 lb of material per batch due to the high shearing forces required.

The three different small mixers were utilized for making small trial batches at Fears Lab depending on the size required. Although both the small planetary mixer and larger rotary mixer are characterized as high shear mixers, each imparts a different amount of energy into the mix. This effect is important to recognize with regard to

proper use of UHPC in the field in that different high shear mixers can result in different flowability based on the specific amount of energy imparted on the mix. In each case the mixing procedures followed were based on recommendations from Lafarge and based on previous research (Graybeal 2006). The mixing procedure for the small batches made as part of the mix design process described in Section 3.2 followed the following general procedure with variations based on the particular mixture composition. These mixing procedures resulted in material sufficient for evaluating material properties and material meeting the specified targets.

1. Blend dry constituents for 10 minutes.
2. Add water mixed with ½ of the required HRWR gradually over the course of 2 minutes.
3. Mix for 1 minute followed by scraping any material from the sides of the mixer bowl.
4. Add the second ½ of the HRWR over the course of 1 minute.
5. Mix for 3 minutes followed by scraping any material from the sides of the mixer bowl.
6. Mix for an additional two minutes.
7. Decide whether additional mixing time is required.
8. Average total mixing time was approximately 20 minutes.

The mixing procedure used for the batches of Ductal® followed the following general procedure based on recommendations provided by Lafarge. These mixing procedures resulted in material meeting the target properties specified by Lafarge for Ductal®.

1. Weigh all materials and add ½ of the HRWR to mixing water.
2. Mix premix dry for 2 minutes.
3. Add water (with ½ HRWR) slowly over the course of 2 minutes.
4. Continue mixing for one minute.
5. Add the remaining HRWR over the course of 1 minute.
6. Mix will turn from powder to paste to flowable material (time for this varies but can potentially take up to 30 minutes).

7. Once the mix turns to flowable material, add steel fibers over the course of 2 minutes.
8. Mix for an additional 1 minute after fibers are dispersed.
9. Average total mixing time is approximately 20 minutes.

The 4.25 ft^3 Imer Mortarman high-shear mixer was used for casting the full depth Ductal® slab joints Ductal® described in Section 5 using the mixing procedures described previously and placement procedures described in Section 3.4.2. The joints were placed successfully even though four batches were required for each joint. Two larger high shear mixers similar to the Imer Mortarman were used for the joint replacement described in Section 8.2. These mixers were able to produce the required quantities of material at the required rates for the replacement.

A large test batch of Ductal® was conducted using the large rotary mixer to evaluate the effectiveness of this mixer and the procedures used for smaller mixers when mixing large quantities of Ductal®. A slight increase in mixing time was required to achieve sufficient workability, but no major changes in procedures from those used for much smaller batches were required. The large rotary mixer and the mixing procedures identified from the test batch were used to mix the Ductal® material used for the demonstration joint described in Section 8.3. This mixer was also used with the mixing procedures identified from previous test batches and the demonstration described in Section 8 to cast the continuity joint specimens described in Section 6. A longer mixing time was required than typical for the first set of joints, which was determined to be due to the preparation of the mixer before batching. Another large batch of Ductal® was conducted to cast the second set of continuity joint specimens. Dampening the mixer with wet towels before batching successfully corrected the problem of longer mixing time encountered during the first continuity joint batch, as expected.

The large horizontal axis rotary mixer available at Fears lab was used to mix the J3 non-proprietary UHPC for casting the second set of slab joint specimens. Mixing procedures were selected for this mixer based on performance of all other mixers examined, but in general followed those described for the smaller mixer. Several differences in performance during mixing and placement of the material were observed

compared to the smaller mixers. The UHPC material lost flowability more quickly than expected during transport and placement, but the cause could not be definitively linked to the mixing or transporting procedures. A second batch of the J3 non-proprietary UHPC was mixed using the large rotary mixer at Fears Lab for casting the J3 composite MOR specimens. A similar loss of workability was observed during placement of the material in the specimen molds. Time in the transportation bucket was determined to be the primary cause of loss in workability based on the results of this batch. As long as the material was kept moving or quickly transported, no problems were observed.

Several small batches of the J3 non-proprietary UHPC mix were then conducted to identify any additional cause of and correct the workability loss during mixing in the large rotary mixer. The admixture dosages were adjusted to achieve proper flow without loss of strength, and a different steel fiber (the same as used for Ductal®) was examined. An additional batch of the J3 UHPC was cast using the large rotary mixer as part of the training and demonstration described in Section 8.3. This mix exhibited excellent workability immediately after mixing and during placement in the formwork.

The UHPC portion of the second set of J3 composite MOR specimens was cast using the revised J3 UHPC mixed in the large rotary mixer, shown in Figure 46. The revised mix design again performed very well, similar to its performance during the slab joint demonstration. Improved flowability resulted in all 36 composite MOR specimens fabricated in less than a quarter of the time compared to the original J3 mix design specimens.

An approximately 1 ft^3 batch of Ductal® was mixed in an 8 ft^3 capacity typical mortar mixer, shown in Figure 47, during a demonstration at Coreslab structures in Oklahoma City. The same mixing procedure used for the other mixers was followed and resulted a similar mixing time to the high shear mortar mixer of approximately 20 minutes. The measured flow of 8.5 in. was less than what was observed in other mixes, but the drum and paddles of the mixer were coated with dry material at the beginning of the test and some pieces of the material came off during mixing, which may have resulted in the low flow. In general, all mortar mixers examined in this project were

capable of mixing the UHPC materials examined with slight changes to the mixing procedures.

Figure 46. Revised J3 UHPC mix for composite MOR specimens (a) fiber addition and (b) transporting to formwork

Figure 47. Paddles of the mortar mixer used at Coreslab demonstration

3.4.2 Placement and Consolidation Procedures

Consolidation and placement methods were evaluated throughout the project and improved where possible. The flowability of the UHPC requires watertight transport and placement equipment. Plastic buckets or wheelbarrows were typically used to transport the material and it was simply poured into the required molds. For the first set of full-depth slab specimens described in Section 5, the top of the formwork was framed to prevent moisture loss. The joint was formed high to allow for air bubbles in the top

surface, which could be removed in the field. A pour hole was placed at one end of the formwork and a vent hole at the opposite end to allow for proper movement of the UHPC through the joint. A plastic funnel was used to direct the material into the formwork. Placement of UHPC into the joint formwork is shown in Figure 48.

Figure 48. Placement of UHPC into the formwork for the first set of slab joints

For the J3 full-depth slab joint specimens, half-depth slab joint specimens, continuity joint specimens, and composite MOR specimens the material was mixed in the large rotary mixer and the material was transported using the large concrete transfer bucket available at Fears Lab. It was noted that a long wait time in the bucket had a negative impact on the first two batches transported in this fashion. For these specimens, material was poured directly into the formwork without a form top in place. The joint or specimen was then immediately covered with plastic.

The UHPC used for the field bridge joint replacement described in Section 8.2 was successfully placed using methods identified by laboratory testing. Material was transported from the mixers to the joint using plastic wheelbarrows and was placed through a funnel. Top forming was necessary due to the cross-slope of the bridge deck. The concrete transfer bucket was used to transport the material used for the demonstration joint specimens cast at Fears Lab (Section 8.3). The material was placed directly into the formed joints and the form top was immediately placed on the joint after casting.

Supplemental consolidation was shown to significantly change the compressive strength of the trial mixes described in Section 3.2, by as much as 10%. High frequency mechanical vibration for five minutes provided the greatest improvement, but hand tapping the molds provided 80% of the improvement found with high frequency mechanical vibration. Supplemental consolidation removed potentially large air bubbles that tended to form within the UHPC mortar, which were most likely the result of the high amount of HRWR. Alternative admixtures were investigated to reduce the potential for forming large air bubbles. No supplemental consolidation was used for specimens cast using Ductal®.

3.4.3 Curing Procedures

Several curing regimens were evaluated including curing at 73° F in a sealed condition, curing in water at 73° F, curing at 50% relative humidity at 73° F, curing in water in an oven at 180° F, and curing under a radiant heat lamp. For each curing regimen, various times for curing were also examined. The radiant heat curing apparatus was constructed using an electric heat lamp suspended from a metal frame and a companion reflective surface surrounding the specimens or slab joint. Initial tests of the system to determine its capabilities for applying heat to the concrete were conducted using a plain concrete dummy specimen. The top and bottom of the test specimen reached temperatures in excess of 140 °F during these initial tests. Two tests were then conducted on groups of 3 in. x 6 in. Ductal® cylinders heat cured for 12 hours immediately after casting; left in ambient conditions for 4 hours, then heat cured for 8 hours; and left in ambient conditions for 12 hours then heat cured for 12 hours. For the second test the 4 hours ambient and 8 hours heat curing was exchanged for a specimen set with 12 hours heat curing and 12 hours ambient to compare strengths at 24 hours of age. All specimens for each test were cast using a single batch of UHPC corresponding to that test. The curing apparatus during one of the tests is shown in Figure 49.

Figure 49. Heat curing apparatus and Ductal® specimens during heat curing test

A thermocouple was embedded in a companion cylinder for each set of heat curing conditions to monitor internal concrete temperature. The targeted maximum temperature, including heat of hydration, was 190 °F. Cylinders in the first test exceeded this temperature so the lamp was raised higher for the second test. An example temperature history from the second heat curing test is shown in Figure 50 which shows a maximum temperature of approximately 170° F or 190° F depending on the curing time. Comparison was made to specimens without heat treatment cured at 73° F for 3 days as recommended by Lafarge. A summary of the results is provided in Table 19. Each curing regimen produced strengths in excess of 12,000 psi at the time of testing, but those left at ambient temperature for 12 hours and heat cured for 12 hours exhibited the highest compressive strengths at the end of curing. Specimens from the initial heat curing tests were tested at 28 days of age. The heat cured specimens had smaller compressive strengths than those with no heat curing. However, the compressive strengths of all heat cured specimens were in excess of 21,000 psi at 28 days.

Table 19. Compressive strengths from heat curing tests

Curing	12 hr Heat (psi)	12 hr Heat 12 hr Ambient (psi)	4 hr Ambient 8 hr Heat (psi)	12 hr Ambient 12 hr Heat (psi)	3 day, 72 °F (psi)
Test 1	16,240	NA	12,570	22,300	14,380
Test 2	14,050	16,110	NA	19,400	15,250

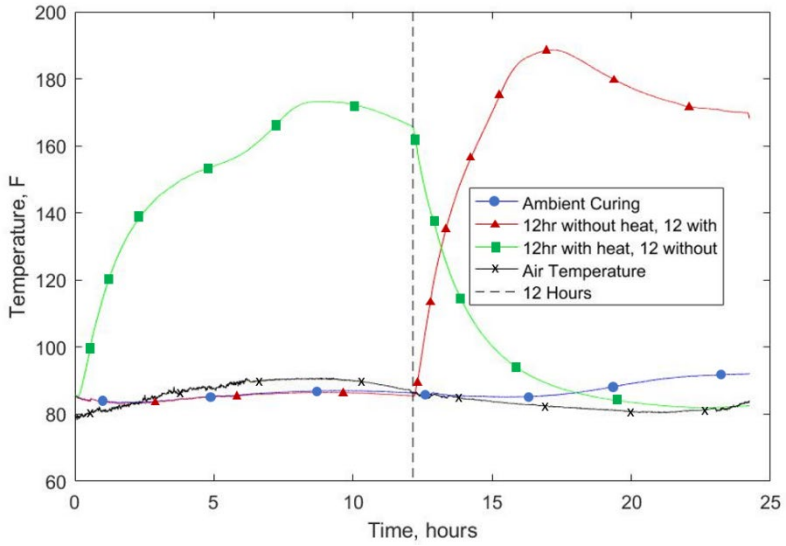

Figure 50. Temperature time history for second heat curing test

Additional compressive strength tests of heat cured cylinder specimens were conducted as part of casting the slab joints described in Section 5. All compressive strength specimens exhibited compressive strengths in excess of 12,000 psi at the end of 12 hours of heat curing.

The radiant heat lamps were used for curing the field deck slab joint replacement described in Section 8.2. This application resulted in very poor performance compared to the results obtained in the laboratory. The measured temperature history showed only a very small temperature rise over the course of the 12 hours of heat curing. It should be noted that the outside ambient temperature during the joint replacement was approximately 50 °F cooler than the temperatures in the laboratory during initial testing of the method. Forced air heaters or heating mats may be a better option if heat curing is needed in the field.

3.5 Specification Development

3.5.1 Overview

Specifications from other DOTs, FHWA, and the UHPC supplier Lafarge were investigated to focused on developing new draft specifications. An initial draft of procedures and specifications were used in casting the SH-3E bridge joint replacement described in Section 8. A number of areas were identified during the replacement where

additional information and detail were required, primarily related to material preparation before mixing, procedures required for cold-weather conditions, and quality control during mixing. The developed procedures resulted in satisfactory mixing, placement, and performance of the UHPC used for two demonstration joints cast at the end of June 2018, the continuity joint test specimens, and the half-depth slab joints.

The need for standard plan notes for UHPC repair projects was identified as part of another project, SPR 2284. Draft standard plan notes for UHPC repair projects were completed for proposed repairs to the U.S. 412 bridge over Wolf Creek in Woodward County and the finalized version was included in the project plans.

3.5.2 Specification Development

UHPC is a relatively new material with limited application in common transportation structures. It is therefore not included in the typical ODOT Standard Specifications (2009). Its composition, mixing requirements, fresh properties, material properties, and required quality control testing methods are significantly different from those of conventional concrete materials. Recommendations developed as part of this project are summarized in the following sections.

3.5.2.1 Material Selection and Preparation

- The Lafarge product Ductal® is an acceptable proprietary material when UHPC is specified.
- Certification of proprietary UHPC performance shall be provided by the manufacturer in the form of test data for the material tests listed in Table 20. Specific proprietary materials may be specified by the engineer.
- Certification of non-proprietary UHPC performance shall be provided in the form of independent test data for the material tests listed in Table 20.
- When a non-proprietary mix design is specified mixture constituents from the exact same supplier (i.e. cement, supplementary cementitious materials, aggregates, admixtures, fillers) used when certifying the mix design as UHPC shall be used in the field unless the new mixture is subjected to the same tests used to certify the original mix design and is approved by the engineer.

- Water used for mixing UHPC shall meet the requirements for conventional concrete.
- Chemical admixtures shall meet the existing requirements for admixtures and as specified by the UHPC manufacturer.
- Steel fibers shall have a tensile strength greater than 300 ksi or as specified by the UHPC manufacturer to meet the properties listed in Table 20. Steel fiber percentage shall be sufficient to meet the properties listed in Table 20.
- All materials including but not limited to cement, aggregate, steel fibers, and admixtures, shall be stored according to the UHPC manufacturer's recommendations or in such a way to protect the materials against deterioration of physical and mechanical properties.

Table 20. UHPC material property requirements

Property	Test Method	Requirement
Flow, (in.)	ASTM C1856	7 - 10
Minimum 28-Day Compressive Strength[1,2], (ksi)	ASTM C1856 ASTM C39	17.00
Minimum 4-Day Compressive Strength, (ksi)	ASTM C1856 ASTM C39	12.00
Minimum Prism Flexural Cracking Strength[1,2], (ksi)	ASTM C1856 ASTM C1609	1.3
Maximum 28-Day Shrinkage, (microstrain)	ASTM C157	1000
Maximum Rapid Chloride Ion Permeability[2], (coulombs)	ASTM C1202	250
Scaling Resistance	ASTM C672	y < 3
Alkali Silica Reactivity, % Maximum Expansion at 14 days	ASTM C1260	0.1

[1]Use 3 in. x 6 in. cylinders. [2]Ends of cylinders must be ground, saw cutting, capping or use of neoprene pads are not permitted. [3]Material should be tested without steel fibers. [4]Testing shall be after 7 day standard cure and 21 days of water curing at 100 °F.

3.5.2.2 Mixing Procedure

- Wear PPE as recommended by the UHPC manufacturer.
- Equipment sufficient to mix the UHPC material shall be identified based on the recommendations of the UHPC manufacturer. High shear mixers shall be utilized. For non-proprietary UHPC data shall be provided showing flow meeting the requirement in Table 20 using that material.

- The starting temperature of the UHPC constituent materials shall be above 60 °F.
- Perform trial batches, at least one day prior to the expected UHPC placement using the UHPC materials and equipment proposed for construction to demonstration the UHPC can be mixed and placed properly. Conduct a flow test to ensure the material meets the requirement in Table 20.
- UHPC shall be mixed according to the UHPC manufacturer's recommendations.
- The following procedures may be used for mixing UHPC:
    - Weigh all materials and add ½ of the required HRWR to mixing water.
    - Mix premix or dry components dry for 2 minutes for proprietary UHPC, 10 minutes for non-proprietary UHPC.
    - Add water (with ½ HRWR) slowly over the course of 2 minutes.
    - Continue mixing for 1 minute.
    - Add the remaining HRWR over the course of 1 minute.
    - Mix will turn from powder to paste to flowable material (time for this varies but can take up to 30 minutes).
    - Once mix turns to flowable material, add steel fibers over the course of 2 minutes.
    - Mix for an additional 1 minute after fibers are dispersed.
    - Typical average total mixing time is approximately 20 minutes.
    - Discharge an amount sufficient for temperature and flow measurements.
    - Add additional HRWR if flow is insufficient.
    - Retest temperature and flow if adjustments were made.

3.5.2.3 Quality Control

- Perform all testing based on recommendations of ASTM C1856 "Standard Practice for Fabricating and Testing Specimens of Ultra-High Performance Concrete" when applicable. At a minimum, the tests listed in Table 21 should be conducted.
- Conduct flow and temperature measurements at completion of mixing. Measure ambient temperature in addition to fresh concrete temperature.

Table 21. UHPC quality control testing requirements

Property	Test Method	Frequency
Flow	ASTM C1856	Every Batch
Temperature	ASTM C1064	Every Batch
Compressive Strength (3 in. x 6 in. cylinders)	ASTM C1856 ASTM C39	At least 3 sets per production day[1,2]

[1]Each set consists of 3 cylinders, [2]make sets of cylinders at intervals throughout the UHPC pour

- At a minimum, test a set of 3 cylinders at end of any heat curing, 4 days after casting, 14 days after casting, and 28 days after casting. Cylinders shall be cured using the same method of curing as in the field.
- Record and report the following for each batch of UHPC:
    - Batch time
    - Testing time
    - Ambient temperature
    - Mix temperature
    - Flow
    - Premix lot (if applicable)
    - Location of placement
    - Notes on weather conditions, deviation from these instructions, and any other issues encountered

3.5.2.4 Formwork and Surface Preparation

- Consult the UHPC material manufacturer (if applicable) for recommendations for formwork design and fabrication.
- Provide impermeable watertight formwork constructed at least ¼ in. higher than required to allow for grinding to the final surface elevation. This extra ¼ in. may be omitted if testing for that particular mix design shows it is unnecessary and results are approved by the engineer.
- Provide formwork with an impermeable rigid top to prevent moisture loss. Provide a minimum of two holes in the formwork top, one for placement and one to vent at the opposite end. As an alternative, material may be placed directly into the forms and the formwork top placed when the forms have been filled.

- Use a funnel or equivalent apparatus to place the UHPC in order to provide elevation head pressure on the material within the formwork.
- Prepare concrete adjacent to the section to be cast by roughening with an air chisel or sandblasting. Concrete surfaces UHPC will be cast against should be saturated surface dry at the time of concrete casting.
- The temperature of formwork and concrete substrate shall be above 60 °F at the time of casting. Portable heaters may be used to raise the temperature of the formwork and concrete substrate.
- Do not remove formwork until the UHPC has reached a compressive strength of 12 ksi.

3.5.2.5 Placement

- Prior to the initial placement of UHPC, arrange for an onsite pre-pour meeting with the UHPC manufacturer's representative (if applicable), and the engineer. The objective of the meeting is to clearly outline the procedures for mixing, transporting, placing, and curing the UHPC material.
- Only place UHPC if the outside ambient temperature is above 40 °F and below 100 °F.
- Place UHPC following the manufacturer's instructions, if applicable, and as discussed in the pre-pour meeting.
- Transport material from the mixer to joint using plastic buckets, wheelbarrows, or other watertight transport container.
- Pour material into funnel end (or directly into open formwork) and allow to flow with no external consolidation.
- New material shall be placed into already placed material to produce a single flow direction within the formwork. No cold joints shall be permitted between layers of UHPC.
- Do not finish UHPC.
- Fill joint formwork until material comes out of the vent hole and comes to equilibrium with fill hole if using the top formed and vent method. If placing directly into the forms, fill until concrete reaches the top of the forms, then place a

section of formwork top on the downhill side of the pour leaving space open to continue placement into already placed material. A hole should be cut into the final section of formwork for placement under pressure head.

- Leave joint under head for curing if possible.
- The UHPC shall be cured according to the manufacturer's recommendations at a minimum of 60 °F to attain the desired strength.
- Heat curing is acceptable if the method is shown to produce the desired curing temperature, does not result in moisture loss in the UHPC, and is approved by the engineer. Curing temperature shall not exceed 190 °F.

4.0 Bond Testing

4.1 Overview

Multiple bond tests were conducted between UHPC and conventional concrete and to assess the bonding capabilities of UHPC to mild steel reinforcement. Composite modulus of rupture (MOR) specimens, slant shear tests, and direct pull-off tests were used to examine UHPC to concrete bond. Comparative pullout tests and beam splice tests were used to assess bonding capability of reinforcing bars cast in UHPC.

4.2 Bond to Concrete Substrate

4.2.1 Composite MOR Specimens

Small-scale interface bond modulus of rupture (MOR) specimens were designed for evaluating the effect of different concrete surface preparations and orientation of saw cut on UHPC joints. The dimensions of these specimens (6 in. x 6 in. x 20 in.) were based on ASTM C78, the methods of which were used for testing the composite joints. Twenty-four small-scale modulus of rupture (MOR) style specimens with dimensions based on ASTM C 78 (6 in. x 6 in. x 20 in.) were cast for evaluating the effect of different concrete surface preparations and orientation of saw cut on bond between both Ductal® and the J3 UHPC and the base concrete. Twelve full-length specimens were cast, which were cut in half at angles of 90°, 60°, and 30° from the horizontal after 28 days of curing. The cut surfaces of the half specimens were then prepared using two different surface preparations, wire brushing and sandblasting. The remaining twelve

specimens were cast as half-specimens to allow sugar (a natural set retarder for concrete curing) to be placed on the mold prior to casting to create the exposed aggregate surface. These were simply power washed to remove the loose paste on the exterior of the specimen. A set of exposed aggregate specimens was cast for each angle, and one set was cast with a shear key. The different surface preparations and configurations resulted in a total of 36 composite specimens for each UHPC. The different variables examined for each UHPC are summarized in Table 22. The first set of MOR specimens (used with Ductal®) were cast in groups based on surface configuration. For example, all 90-degree specimens were cast at the same time with one batch of concrete, all the 45-degree specimens were cast at the same time, and so on. The subsequent sets of MOR specimens were all cast at the same time using concrete from a ready-mix supplier. A set of forms prepared for casting is shown in Figure 51. Concrete cylinders were cast with each batch of concrete to measure compressive strength over time. Completed specimens and companion cylinders were cured wrapped in wet burlap and plastic sheeting at 72° F.

Table 22. Summary of small-scale joint specimens

Qty.	Configuration	Surface Preparation	Casting Type
2	90 degrees	Sand-Blasted	2 Full specimens to be cut
2	90 degrees	Wire-Brushed	2 Full specimens to be cut
3	90 degrees	Exposed	3 half specimens
2	60 degrees	Sand-Blasted	2 Full specimens to be cut
2	60 degrees	Wire-Brushed	2 Full specimens to be cut
3	60 degrees	Exposed	3 half specimens
2	45 degrees	Sand-Blasted	2 Full specimens to be cut
2	45 degrees	Wire-Brushed	2 Full specimens to be cut
3	45 degrees	Exposed	3 half specimens
3	Shear Key	Exposed	3 half specimens

Figure 51. Formwork prepared for small-scale MOR specimens to be cast. Three half specimens for exposed aggregate finish are visible in the right of the photo

All specimens that required cutting were cut with a diamond blade concrete saw, as seen in Figure 52. Specimens were then either sand-blasted until a uniform surface roughness was visually observed, or wire-brushing was performed on the smooth cut surface to clean away any debris depending on the specified variable combination. All exposed aggregate specimens were pre-prepared. Wooden inserts were placed in the standard MOR beam forms to create the proper surface orientation, as shown in Figure 51. The faces of the wooden inserts were sprayed with adhesive and then coated with sugar. This prevented the concrete in contact with the sugar from curing, allowing extra chunks of cement paste to be power washed off the face of the concrete when the forms were removed, thereby exposing the aggregate. The exposed aggregate surface after power washing is shown in Figure 53.

Figure 52. Cutting small-scale specimen at 90° angle to the horizontal

Figure 53. Exposed aggregate surface after power washing

UHPC was cast against the prepared surface of each half specimen to create a composite specimen with approximately the same dimensions as the original MOR beam. Completed composite specimens and companion cylinders were cured for 28 days wrapped in wet burlap and plastic sheeting at 72° F. Completed specimens before and after curing are shown in Figure 54.

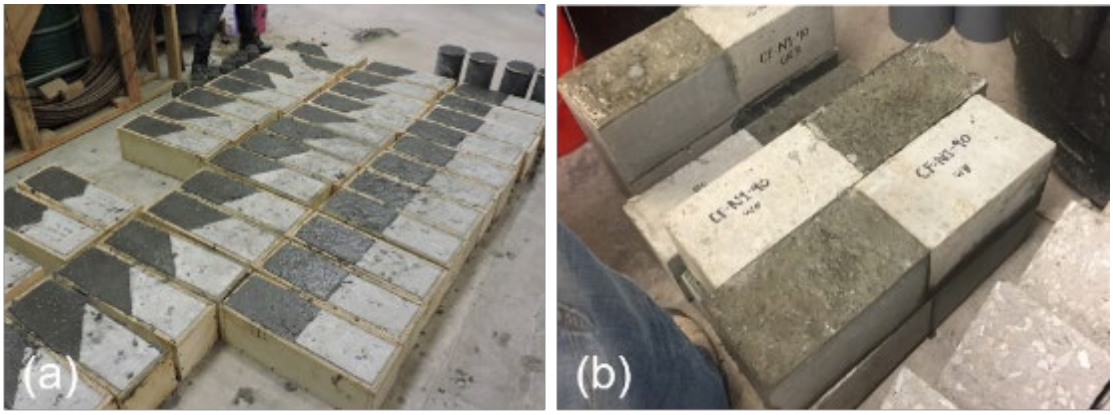

Figure 54. Composite specimens after casting (a) and after curing (b)

All composite specimens were tested in flexure using third point loading with the procedures of ASTM C78 when the UHPC portion of the specimen reached an age of 28 days. The test setup is shown in Figure 55. The thirty-six specimens were tested broken into ten groups. Four specimens were tested for each combination of wire brushed or sand blasted surface and angle of cut with the horizontal (90°, 60°, and 45°). Three exposed aggregate finish specimens were tested for each angle and three

specimens were tested with a shear key cast into the plain concrete portion of the specimen. Several the specimens required capping with gypsum cement (HydroStone) to obtain an acceptable surface condition.

Figure 55. Composite MOR specimen testing apparatus

A summary of the results for composite specimens cast with Ductal® is shown in Figure 56. Only the specimens cut at 90° with a wire brushed surface failed at the base concrete/UHPC interface. All other specimens failed in the base concrete, but within the middle third of the span. An example of the failure pattern for one of the 60° specimens is shown in Figure 57. The compressive strength of the UHPC for each specimen group was in excess of 21,500 psi at 28 days with no heat curing. Results indicate that all surface preparations create a joint stronger than the value calculated for the base concrete for the 90° and 45° specimens. The exposed aggregate finish provided the best results for these two orientations with the sandblasted and wire brushed preparations producing very similar results. The 60° specimens did not exceed the calculated flexural strength based on the base concrete compressive strength even though all specimens failed in the base concrete.

Figure 56. Summary of small-scale specimen testing results

Figure 57. Example of failure pattern for one of the 60° joint specimens

The results of the first set of composite MOR specimens cast using the non-proprietary J3 UHPC material are shown in Table 23. Unfortunately, the wire brushed specimens performed very poorly, with many of the specimens separating during the demolding process. The sand blasted specimens performed much better, with increasing bond strength as the interface angle sloped away from vertical. However, the exposed aggregate specimens showed lower bond strength than the sand blasted

specimens, whereas they should have been higher. The exposed aggregate shear key resulted in the highest bond strength. The MOR for the base concrete measured 609 psi, indicating low bond strength for the specimens.

Table 23. Summary of first set of J3 composite MOR test results (psi)

Interface	Wire brushed	Sand Blasted	Exposed Aggregate
90°	0	234	73
60°	0	301	158
45°	74	326	132
Shear Key	--	--	419

One of the reasons for the low bond strength is likely due to the effort of mixing a large quantity of the non-proprietary UHPC. These small-scale specimens required approximately 10 ft^3 of material, which was mixed in the lab's large scale, high shear rotary mixer. During mixing and placement, it was noted that the mix started to stiffen due to the time lag between mixing, placement into the concrete bucket, and then placement into the formwork. UHPC is very thixotropic, which means that when it is at rest for any lengthy period of time, it needs considerable energy to regain flowability. Subsequent large mixes of the UHPC employed a continuous mixing operation and staggered placement into the formwork, which improved flowability at the point of placement.

A second set of composite MOR specimens was cast using the non-proprietary J3 mix design due to the poor flowability of the material used for the first set. This second series of composite J3 MORs were demolded 7 days after placement. Initial inspection of the specimens indicated improved bond compared to the original J3 mix, where some specimens debonded during the process of formwork removal. Results of testing the second set of J3 MOR specimens are shown in Figure 58 as a comparison to those measured for the Ductal® specimens. In general, the 45° and sandblasted J3 specimens exhibited the best performance. In all cases the exposed aggregate specimens had the lowest bond strength, which was attributed to the surface preparation method. None of the specimens were prewetted in order to create a worst-case scenario, and evidence of desiccation at the interface was observed.

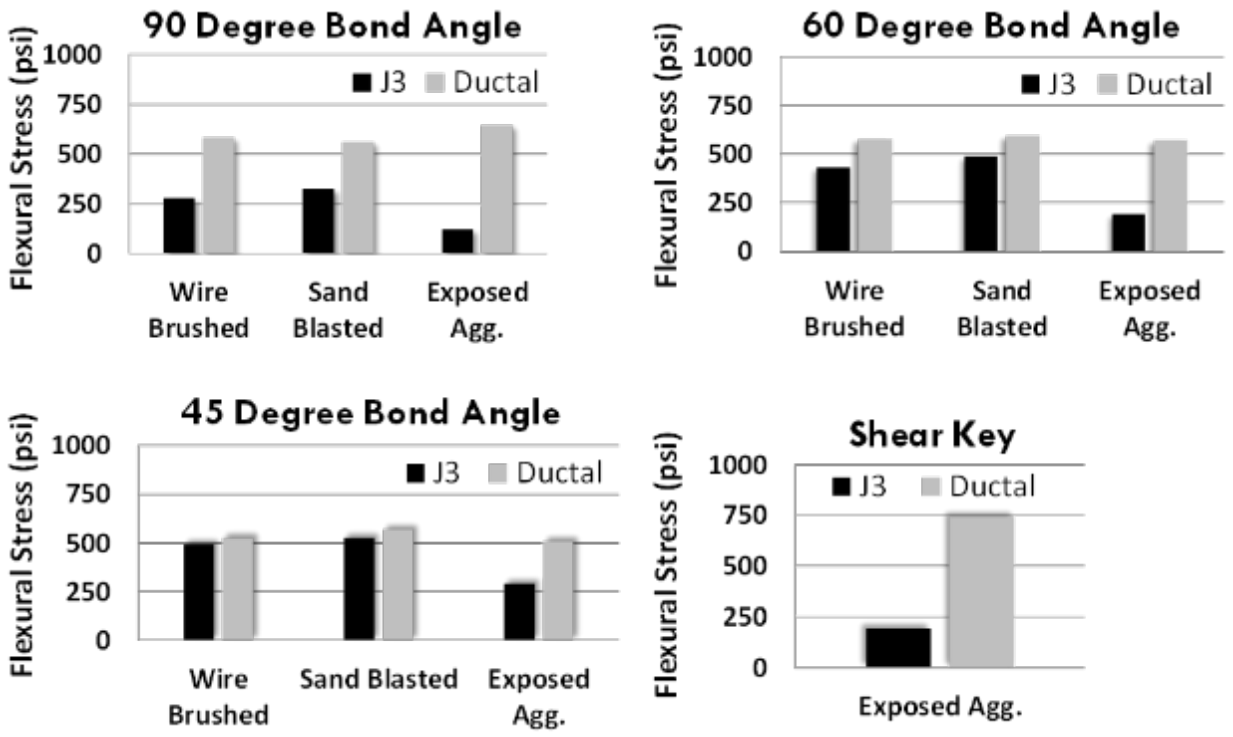

Figure 58. Comparison of the composite MOR specimen test results

4.2.2 Slant Shear Specimens

Slant shear specimens were cast in the form of 6 in. x 12 in. cylinders based on an adaptation of ASTM C882. A completed slant shear specimen before and after testing is shown in Figure 59.

Figure 59. Composite slant shear specimen prior to testing (left) and after testing (right)

Slant shear tests were first conducted with a generally finished conventional concrete surfaced. The normal strength concrete and UHPC casting occurred during the same timeframe as casting for the composite MOR specimens. Slant shear tests were carried out after both portions of the specimen were allowed to cure for 28 days. The results from these tests with Ductal® are shown in Table 24 and for the J3 specimens in Table 25. The 28-day compressive strength of the base concrete was 5850 psi for the Ductal® Specimens and was 5750 for the J3 specimens. So, the Ductal® bond strength nearly developed the full strength of the concrete in all cases, while the J3 bond strength resulted in a load about 20 percent less than the concrete compressive strength. However, the bond strengths of both materials were within 10 percent of one another.

Table 24. Maximum load and bond strength for Ductal® slant shear specimens

Specimen	Maximum Load (lb)	Bond Strength (psi)	Corresponding Compressive Strength (psi)
Cylinder 1	122,670	2170	4340
Cylinder 2	146,840	2600	5190
Cylinder 3	177,245	3130	6270
Cylinder 4	154,800	2740	5480
Cylinder 5	153,430	2710	5430
Average	150,997	2670	5340
Std. Deviation	17,487	308	619

Table 25. Maximum load and bond strength for J3 slant shear specimens

Specimen	Maximum Load (lb)	Bond Strength (psi)	Corresponding Compressive Strength (psi)
Cylinder 1	123,670	2280	4370
Cylinder 2	110,130	2230	3900
Cylinder 3	152,010	2870	5380
Cylinder 4	123,290	2380	4360
Average	127,275	2440	4500
Std. Deviation	15,286	254	541

Additional slant shear tests were conducted for both Ductal® and J3 specimens using three different surface preparations: wire brushed, sand blasted, and chipped. The base concrete was allowed to cure for 28 days before testing. Slant shear test results are shown in Table 26. With the revised surface preparation and improved flowability of the mix design, the J3 results being within approximately 5 percent of the Ductal® results.

Table 26. Slant shear test results (psi)

Surface Preparation	Ductal®	J3
Wire brushed	2873	2989
Chipped	2982	3204
Sand blasted	3380	3276

4.2.3 Pull-off testing

The research team constructed Class AA substrate specimens for direct pull-off testing and the surfaces of these specimens were prepared for overlay casting with different surface preparations: wire brushed, sand blasted, and chipped, shown in Figure 60. These specimens were allowed to cure for 28 days before Ductal® and J3 overlay placement, which was then allowed to cure 28 days before testing. Completed specimens are shown in Figure 61.

Figure 60. Sandblasted (left) and chipped (right) surface preparations

Figure 61. Pull-off test specimens for Ductal® (left) and J3 (right)

Pull-off tests were conducted for both Ductal® and J3 specimens using the methods of ASTM C1583 as shown in Figure 62. The results of the pull-off tests are shown in Table 27. The Ductal® UHPC performed better than the J3 in the direct pull-off tests.

Figure 62. Pull-off tests for J3 with overall layout (left) and test setup (right)

Table 27. Direct pull-off test results (psi)

Surface Preparation	Ductal®	J3
Wire brushed	267	160
Chipped	291	183
Sand blasted	311	226

A control set of pull-off specimens were cast consisting of a Class AA substrate and Class AA overlay. Pull-off tests were completed on the control specimens, and results indicated bond strengths of 439 psi for the sandblasted surface preparation and 382 psi for the chipped surface preparation. These results are consistent with the UHPC bond tests, which indicated noticeably better performance with a sandblasted surface.

Additional J3 UHPC pull-off specimens were cast to evaluate alternative substrate saturation levels. Previous testing of the J3 mix indicated improved performance with higher substrate saturation prior to placement of the overlay. Pull-off tests were conducted on the revised J3 overlay specimens, and results indicated bond strengths of 318 psi for the sandblasted surface preparation and 255 psi for the chipped surface preparation. These results represent an improvement over the previous test results and are likely due to maintaining a saturated surface dry condition of the substrate prior to installation of the overlay. For comparison, the results for the Ductal® overlay bond tests indicated 408 psi for the sandblasted surface preparation and 291 psi for the chipped surface preparation.

4.3 Reinforcing Bar Development Length in UHPC

4.3.1 Overview

Reinforcing bar development length was examined using a comparative pullout test to identify the difference between required embedment for No. 3, No. 5, and No. 8 reinforcing bars cast in OU J3 mix design with varying fiber contents and in the proprietary UHPC Ductal®. Beam splice tests representing a more realistic stress state were also examined using the splice length determined from the pullout tests.

4.3.2 Pullout Testing

Details for the pullout test specimens and setup used in previous research are shown in Figure 63 (RILEM 1994). Bond between the reinforcing bar and the concrete occurs only in the upper half of the concrete block, through the addition of a PVC or foam tube in the lower portion, significantly reducing the effect of any confinement pressure generated as a result of friction between the specimen and reaction plate. Data recorded during the test included load and free end slip at each end of the reinforcing bar.

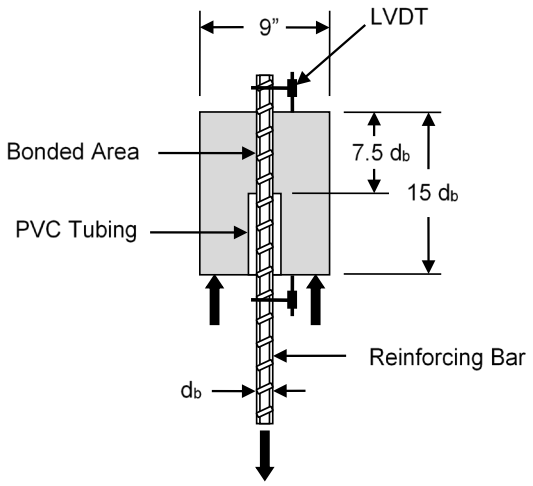

Figure 63. Direct reinforcing bar pullout test setup used in previous research (RILEM 1994)

A trial series of pullout test specimens based on the specimen shown in Figure 63 and using No. 5 bars was cast and tested to evaluate the best embedment to produce a bond failure. The circular specimens had a nominal 8 in. diameter to obtain a minimum cover of $3d_b$ for all bar diameters to be tested. Embedments examined included $2d_b$, $4d_b$, $6d_b$, $8d_b$, and $10d_b$ with a debonded length equal to the embedment length resulting in a specimen height dependent on the embedment. All specimens except the $2d_b$ embedment specimen exhibited signs of reinforcing bar yielding and the $2d_b$ embedment specimen exhibited a splitting failure, as shown in Figure 64. A set of revised specimens were cast having a $2d_b$ embedment but larger overall specimen depth and resulting debonded length in an attempt to prevent splitting failure. The revised specimens had the same 8 in. diameter, but total depths of 2.5 in. ($2d_b$ debonded), 3.5 in. ($3.6d_b$ debonded), and 5 in. ($6d_b$ debonded). Two specimens were cast and tested for each variable combination. All of these tests resulted in pullout failures, so the final dimensions chosen for the pullout test were an 8 in. diameter specimen with $2d_b$ embedment and $4d_b$ debonded length for a total depth of $6d_b$, shown in Figure 65. This resulted in a 3.75 in. thick specimen for the No. 5 bar tests, a 2.25 in. thick specimen for the No. 3 bar tests, and a 6 in. thick specimen for the No. 8 bar tests.

Figure 64. Splitting failure of $2d_b$ embedment bond test specimen

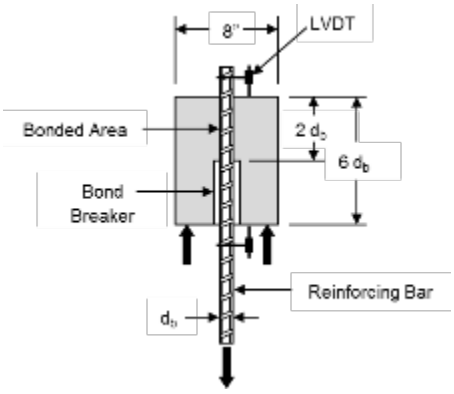

Figure 65. Final dimensions of comparative bond pullout specimens based on preliminary testing

Pullout specimens for the J3 mix with No. 3, No. 5, and No. 8 bar and 0%, 1%, 2%, 4%, and 6% fiber mixes were cast and tested at 28 days of age. Ductal® specimens with 2% steel fibers were also cast and tested. The specimens were tested in a Baldwin universal testing machine with a neoprene pad placed under the specimen to ensure uniform bearing. Load was applied constantly until failure and bar slip was measured with an LVDT on each side of the specimen. The pullout test setup is shown in Figure 66.

The No. 5 bar specimens with no fibers failed due to splitting of the concrete, but all No. 5 bar specimens containing fibers failed due to pullout of the reinforcing bars. Pullout test results for the No. 5 bar specimens are shown in Figure 67. The results indicate a significant increase in pullout capacity with the addition of fibers to prevent a splitting failure, but only modest gains in strength as the fiber content is increased beyond 1%.

Figure 66. Pullout test of No. 5 bar specimen with 1% fiber mix showing the overall setup (left) and a closeup view of the as tested top of the specimen (right)

The results of the No. 8 and No. 3 bar specimen tests are presented in Figures 68 and 69. The results were similar to those observed for the No. 5 bar specimens. The very small embedment length used for the No. 3 bar specimens (0.75 in.) may have contributed to the difference in results obtained for those specimens based only on load since even small variations in the embedded length would have represented a large percentage of the total.

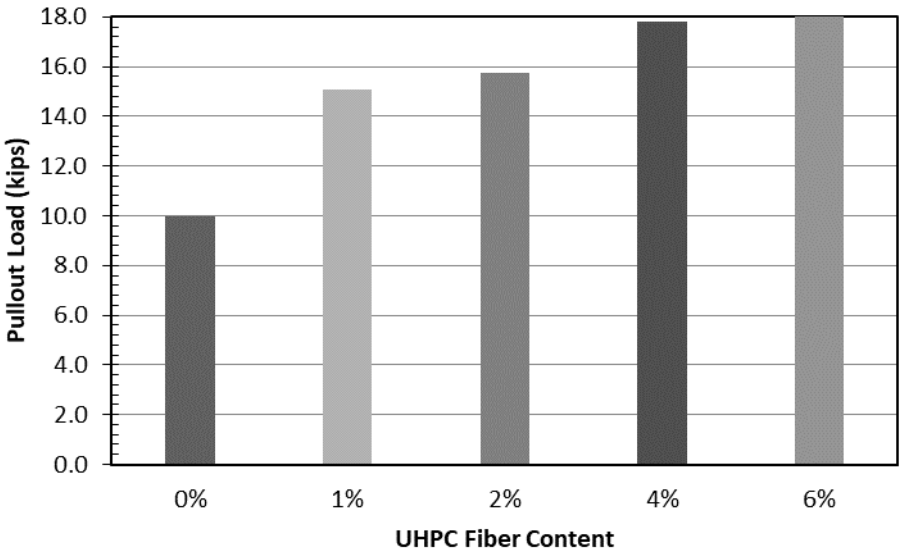

Figure 67. J3 pullout loads for No. 5 bar specimens with all fiber contents tested

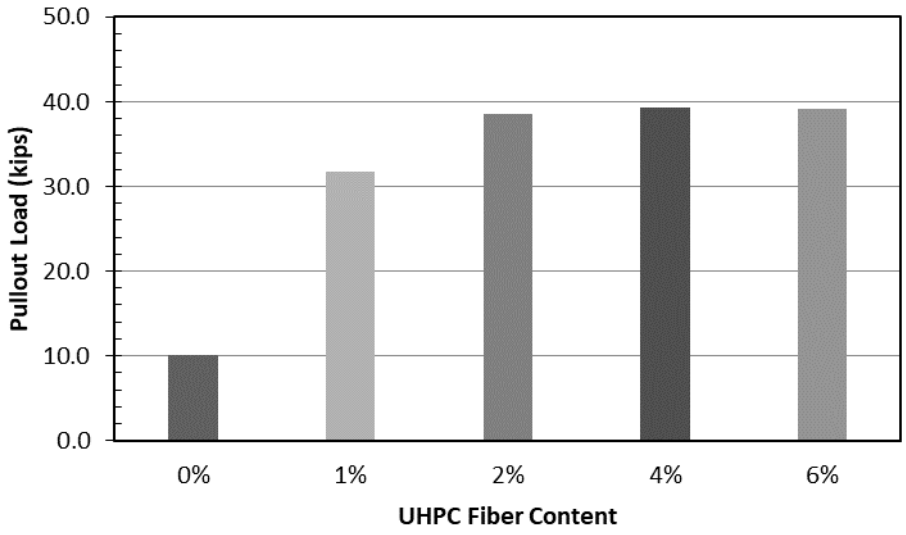

Figure 68. J3 pullout loads for No. 8 bar specimens with all fiber contents tested

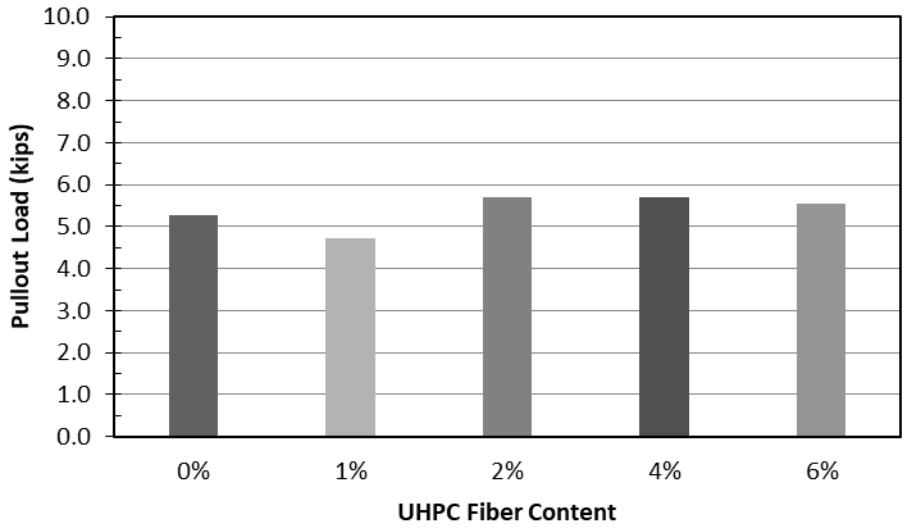

Figure 69. J3 pullout loads for No. 3 bar specimens with all fiber contents tested

A comparison of the average pullout load for the 2% steel fiber J3 mix and the proprietary UHPC Ductal® is shown in Figure 70. In all cases, the J3 mix specimens had a lower pullout load at failure. However, a similar comparison for the bond stress normalized by compressive strength is shown in Figure 71. In this figure, if the effect of compressive strength (which indirectly relates to splitting strength) is accounted for, the J3 and Ductal® specimens exhibited very similar bond stress.

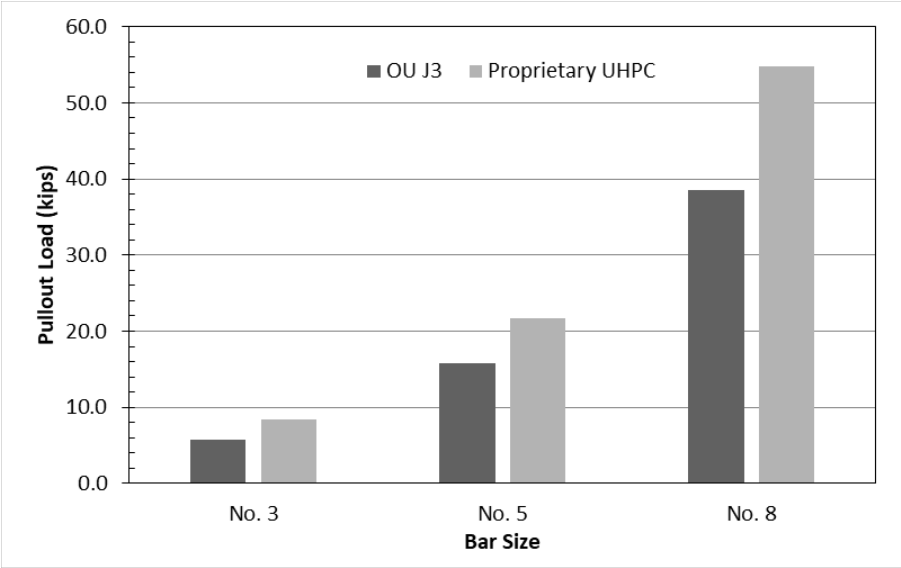

Figure 70. Average pullout load for J3 and Ductal® specimens with 2% steel fibers by volume

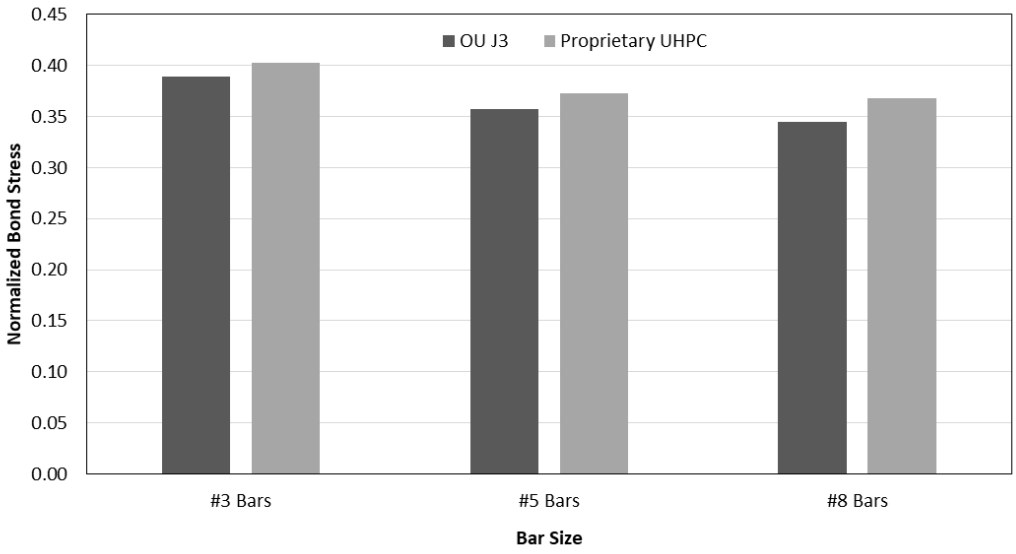

Figure 71. Bond stress normalized by compressive strength for J3 and Ductal® specimens with 2% steel fibers by volume

4.3.3 Beam Splice Testing

In order to further evaluate the reinforcing bar development length in UHPC, several sets of beam specimens were designed for flexural bond testing. Although there are a variety of bond and development length testing protocols available, the beam splice test is generally regarded as the most realistic test method (ACI 408 2003,

Ramirez and Russell 2008). The current AASHTO LRFD design provisions for development length and splice length are based primarily on data from this type of test setup (AASHTO 2017). The design of these beam specimens, which utilized a bar splice at midspan in order to isolate the bond behavior in flexure under a third point loading condition, was based upon the results obtained from the comparative direct pullout tests. Since the pullout tests showed that embedded lengths longer than 2 bar diameters tended to cause bar yielding, a splice length of $2d_b$ was chosen for the splice beam specimens. In the direct pullout tests, a minimum cover of $3d_b$ was provided for all specimens. For the splice beams, however, minimum cover and clear spacing considerations had to be weighed against required material quantities, constructability concerns, and proportioning of the section to prevent a shear failure outside of the constant moment region. Analysis concluded that for the splice beams reinforced with No. 5 bar, a bottom cover of 1.5 in., a minimum clear spacing of $2d_b$, and a minimum side cover of $2.6d_b$ would result in a pure flexural failure without shear influences, while minimizing required materials and still generally paralleling the parameters used for the direct pullout tests. These cover parameters resulted in a 7 in. square beam cross section, with a length of 10 ft. Figure 72 shows the beam dimensions, reinforcing layout, and splice configuration which was chosen for this testing.

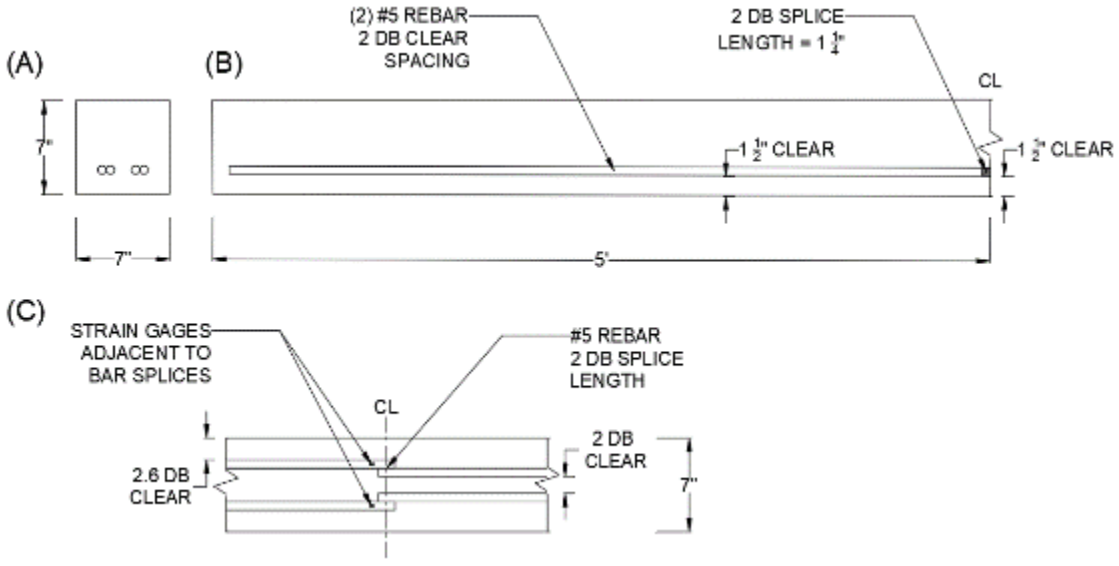

Figure 72. Section (A), profile (B), and plan (C) views of typical splice beam design with No. 5 reinforcing bars

As shown in Figure 72, two strain gages were placed on the reinforcing bars directly adjacent to the splice location, in order to estimate the bond stress developed by the splice. Cover depths could have been increased, and required materials further decreased, by designing the beams with only a single bar spliced at midspan, but a two-bar splice was chosen to reduce variability in the results due to the very short bonded length and obtain a reasonable average for the resulting bond stress.

The beam splice test considered only No. 5 reinforcing bars and three sets of beams were cast, with each set consisting of 2 otherwise identical specimens. This included 2 sets of beams cast with OU's non-proprietary J3 UHPC mix design; one set used 2% steel fibers by volume, and the other set used 1% fibers. The third set of beams were cast with the same proprietary UHPC mix design with 2% fibers which was used in the direct pullout tests.

Once each splice beam had been cast and cured for at least 28 days in the ambient temperature and humidity conditions of the Fears Lab high bay, it was tested to failure in a third point bending configuration as shown in Figure 73.

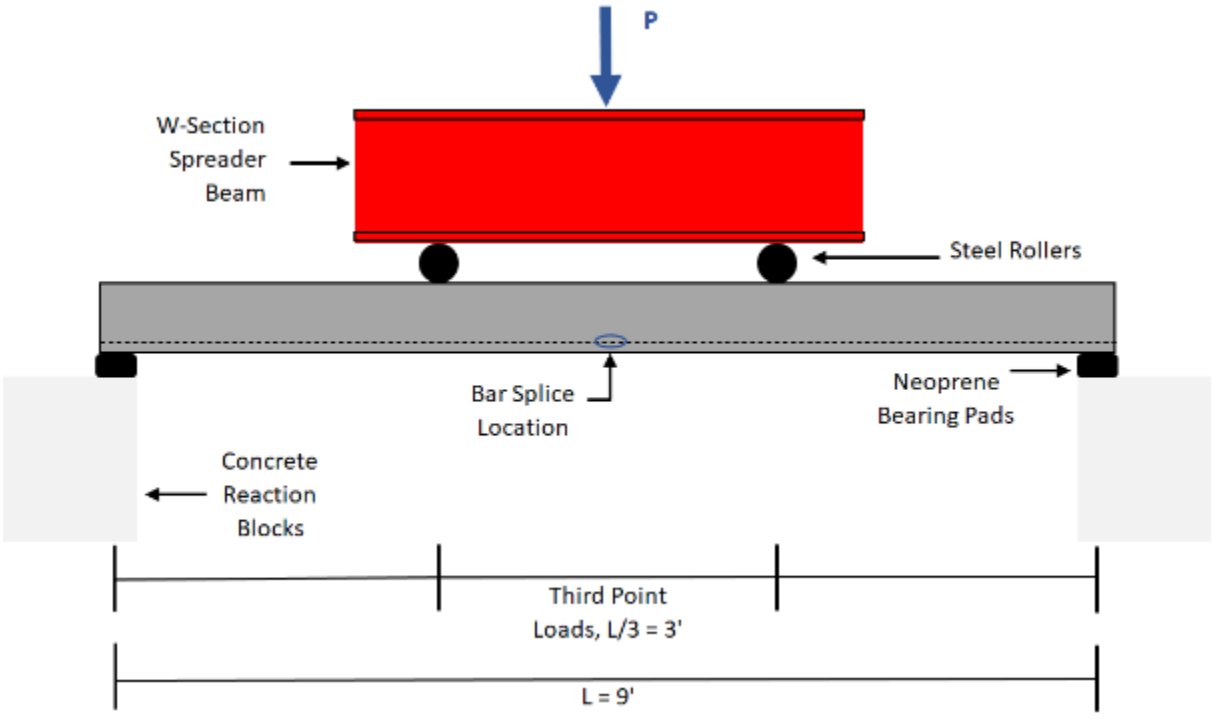

Figure 73. Third point bending test setup for UHPC splice beams

In addition to the strain gages located adjacent to the splice location on the reinforcing bars, a load cell was placed between the hydraulic ram and the spreader beam, and a pair of wire potentiometers were placed on either side of the beam at its midspan to measure deflection throughout the tests. Companion 3 in. by 6 in. cylinders were cast along with each set of splice beams in sufficient quantity to obtain an average concrete compressive strength of at least 3 cylinders for each beam. Table 28 summarizes the testing designations and concrete compressive strengths for the splice beam material at the time that each beam was tested.

Table 28. Splice beam designations and material property data

UHPC Mix	Specimen Designation	Testing Age (days)	Compressive Strength (psi)
Proprietary (2% Fibers)	SB-D5-1	67	26,100
Proprietary (2% Fibers)	SB-D5-2	69	26,800
J3 (2% Fibers)	SB-J5-1(2P)	28	17,400
J3 (2% Fibers)	SB-J5-2(2P)	29	16,300
J3 (1% Fibers)	SB-J5-1(1P)	28	15,800
J3 (1% Fibers)	SB-J5-2(1P)	28	16,400

The mix designations shown in Table 28 show the specimen (SB = splice beam) followed by the type of UHPC (D = proprietary brand, J = non-proprietary mix), the bar size (No. 5 for each beam in this series), and lastly the beam number within each set (1 = first beam cast, 2 = second beam cast). For the non-proprietary mixes, the designation is also appended with the fiber volume of the mix (2P = 2% fibers, 1P = 1% fibers). This was not added for the proprietary mix since it only utilized 2% fibers by volume.

Table 28 shows that, as expected, the compressive strength of the proprietary UHPC was significantly higher than the non-proprietary mixes, in this case by about 60%. In addition, the compressive strength of the 2% non-proprietary mix was not significantly higher than that of the 1% mix, a trend which agrees with previous testing on the effects of fiber volume on compressive strength. One other point worth noting in Table 28 is that the SB-D5 series beams were close to 40 days older when tested than the other series. This is because the SB-D5 series was cast first and had to wait for

instruments and equipment to be freed up for testing. Once the SB-J5 series were cast, the testing apparatus was already fully assembled and ready for use.

Figure 74 shows the load deflection curves for each of the six beams that made up the series of splice beams tested with No. 5 reinforcement.

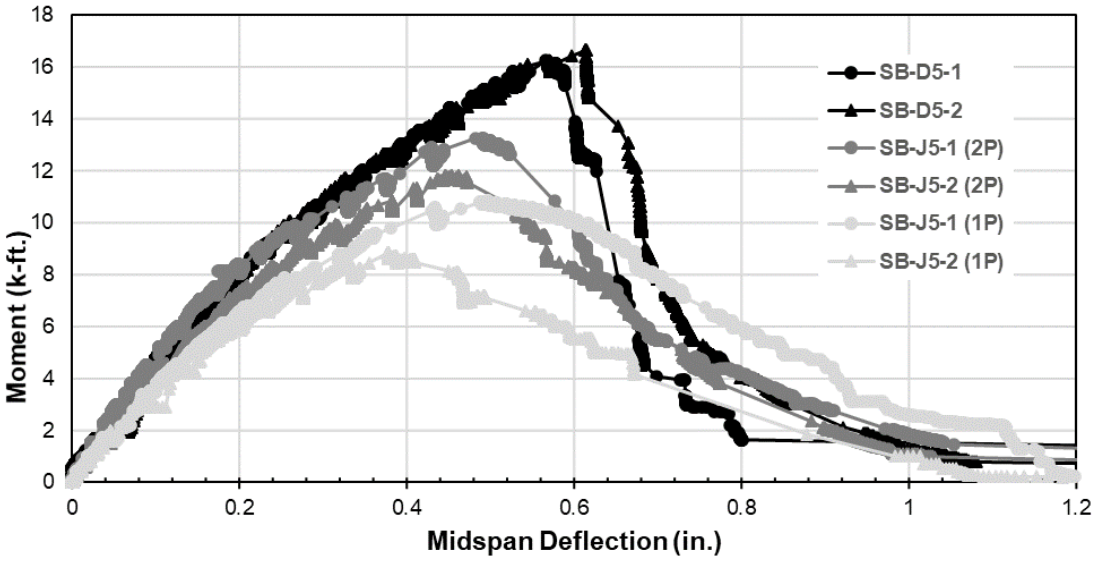

Figure 74. Load Deflection Behavior of Splice Beams with #5 Reinforcement

First, it is apparent from Figure 74 that the SB-D5 beams reach the highest peak loads, both attaining moments greater than 16 kip-ft. The 2% SB-J5 beams reached between 12 and 13 kip-ft, and the 1% SB-J5 beams reached the lowest peak moments of between 8 and 11 kip-ft. It is also interesting to note the shape of the ascending curves towards the peak moments; the SB-D5 curves are steepest, indicating the stiffest response, while the 2% and 1% SB-J5 are progressively less steep, indicating that they were less stiff, or more compliant to the applied load. Also of interest are the descending branches of the load deflection curves moving away from the peaks. The SB-D5 beams shed load quickly after the bond failure at the peak, which indicates an abrupt bond failure, while the SB-J5 curves roll over more gently after reaching their maximum capacity. This may indicate that the bars in the SB-J5 splices experienced more of a gradual bond slip instead of a sudden failure. This behavior was noted in the direct pullout testing; whereas the No. 5 bars tended to pull out suddenly from the proprietary and non-proprietary 2% fiber mixes with an audible sound and jolt, the non-

proprietary 1% fiber mix resulted in gradual pullout for all three specimens with no audible signs of sudden failure.

In addition to the load deflection data, the observed cracking pattern from these splice beam tests offer insights into the comparative performance of the mixes. In between the application of load increments using hand-pumped hydraulics, which were applied in 1 kip increments up to first observed cracking and 0.5 kip increments thereafter, the beams were examined closely using hand-held flashlights and any visible cracks were noted in permanent marker along with the load level when the crack was observed or was noted to expand. It is important to note that the presence of steel fibers and the very dense microstructure of the UHPC made it very difficult to see cracks early in the test, and that internal micro-cracking likely began before this behavior was apparent. Even considering this, there were several trends that were consistent between tests regarding the propagation of macroscopic crack patterns.

The SB-D5 tests both exhibited minimal visible cracking throughout the tests; in each test, a few small vertical cracks appeared near or just outside the load points (which bracketed the constant moment region) at loads between 6 and 7 kips. Subsequently, a few more vertical cracks began to propagate between the load points, near midspan of the beam at the splice location. These cracks appeared at around 7 to 7.5 kips, and a few more such cracks appeared and propagated from bottom to top of the section as load was increased towards ultimate, which was around 11 kips for both SB-D5 beams. In both cases, at loads of around 9 to 9.5 kips, the crack nearest the splice location began to widen and lengthen considerably as the beam neared ultimate load; then, after the peak load was reached, the load began to fall rapidly as the midspan crack opened very wide. After that point, continuing to pump the hydraulics still resulted in falling load levels, until eventually the last fibers holding the beam together near the top were pulled out, and the beam collapsed onto wooden fall supports, in two more or less separate halves. Figures 75 and 76 show the relatively minimal and discrete cracking patterns that were observed in beams SB-D5-1 and 2 respectively. In both Figures 75 and 76, it is clear that the cracks were confined to a few at or just outside the load points, and a few clustered near the beam midspan, although test SB-D5-2 had more cracks between midspan and the load points.

Figure 75. Crack pattern for test SB-D5-1

Figure 76. Crack pattern for test SB-D5-2

The SB-J5 tests, however, exhibited significantly more visible cracking throughout the tests, and this cracking was substantially more distributed along the span. In addition, the cracking began to appear at substantially lower loads, as low as around 4 kips for the 2% beams and as low as 2 kips for the 1% beams. Once the beams approached their ultimate failure loads, however, the cracking behavior closely mirrored the SB-D5 beams, in that the vertical cracks near midspan began to propagate more quickly, while the smaller distributed cracks away from midspan mostly stopped growing. Figures 77 and 78 show the typical cracking pattern for 2% and 1% SB-J5 beams respectively.

Figure 77. Crack pattern typical of SB-J5 with 2% fibers

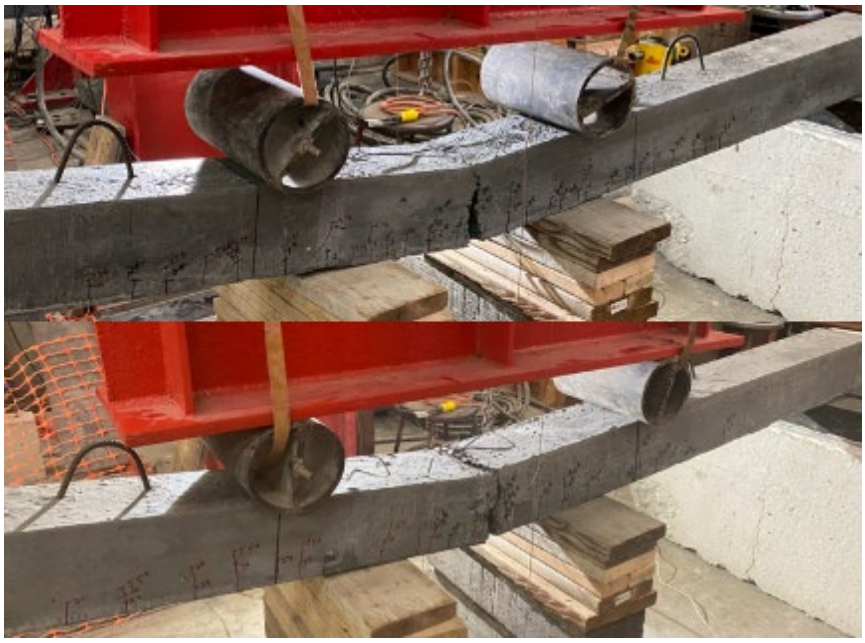

Figure 78. Crack patterns typical of SB-J5 with 1% fibers

Figures 77 and 78 clearly show that the crack patterns for the SB-J5 beams were significantly more numerous and widely distributed along the spans than those of the SB-D5 beams. In addition, they appeared at loads of 2 to 4 kips as opposed to around 7 kips for the SB-D5 beams. Both the slope of the ascending branches of the load deflection curves and the observed cracking patterns both indicate a stiffer response by the proprietary material compared to the non-proprietary, as well as a stiffer response by the 2% fiber mixes compared to the 1% fiber mix.

Figure 79 displays a comparison of the average deflections for each series of splice beams, at the first observed crack appearance, at the peak load, and at the end of the test immediately before the beams collapsed.

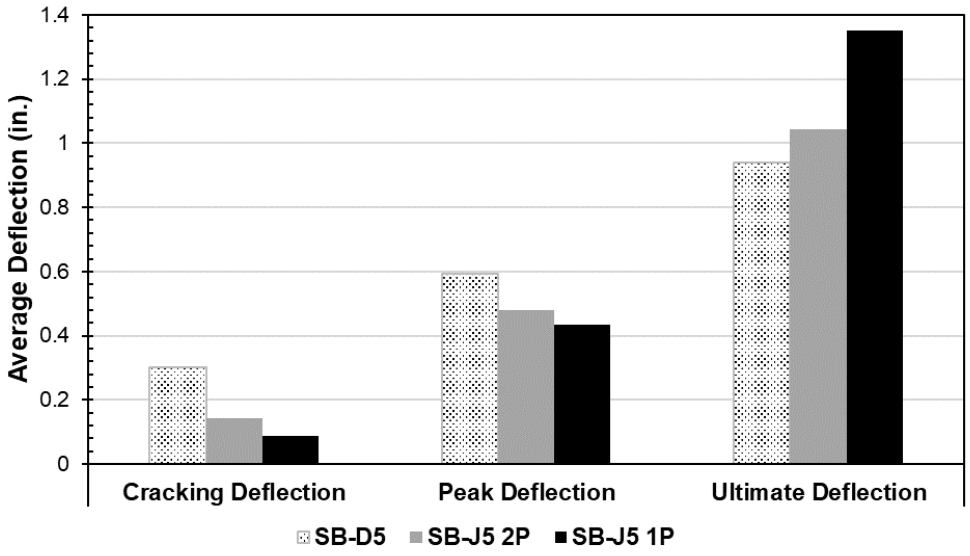

Figure 79. Comparison of average deflections for splice beams

There are several important trends which are visible in Figure 79. First, however, it is important to understand the way in which the deflections are categorized. First, each deflection measurement shown is an average; since each mix series included 2 beam tests, and each beam test was instrumented with 2 wire potentiometers, each value in Figure 79 is the average of 4 independent measurements. The “cracking deflection” represents the average deflection measurement which corresponded to the load on the beam when the first visible crack was marked. Although microcracking might have occurred sooner, cracks visible to the naked eye under a flashlight were used to estimate initial cracking consistently across all splice beam series. The “peak deflection” refers to the deflection measurement when the peak force on the beam was registered by the load cell. The “ultimate deflection” refers to the final measured deflection the instant before the beam collapsed onto the fall protection system beneath the beam. This deflection was straightforward to identify graphically from load deflection data, because as soon as the beam collapsed, the deflection increased immediately by several inches.

Figure 79 shows that the SB-D5 beams had the highest average deflection at both first apparent cracking and at the peak load, the SB-J5 beams with 2% fibers had the next highest deflection, and the SB-J5 beams with 1% fibers had the lowest deflections at these stages. This observation is reasonable, because as seen in the load deflection curves and cracking patterns, the proprietary UHPC mix seemed to have the highest overall load carrying capacity. As a result, the SB-D5 beams exhibited apparent cracking at significantly higher loads than the SB-J5 beams and were therefore able to sustain more deflection, both at first cracking and at the peak load after cracking. Both these phenomena may be due to the significantly higher compressive strength of the SB-D5 material (~60% more than the SB-J5 material). Before cracking, the SB-D5 beams could sustain more deflection because the high compressive strength UHPC likely also had a correspondingly higher modulus of rupture (MOR). After cracking, however, the SB-D5 beams still could sustain higher deflections because the high compressive strength likely also resulted in enhanced bond with the individual steel fibers which helped bridge both microcracks and visible cracks.

This ordered trend of deflections was reversed, however, at ultimate, with the 1% fiber SB-J5 beams exhibiting the highest deflections, and the SB-D5 beams at the lowest deflections. This is also reasonable, because at impending failure, the mix with 1% fibers had the least connectivity across a substantial crack and was therefore free to hinge and fall rapidly at midspan. For the SB-D5 and J5 mixes with 2% fibers, there was substantially more reserve resistance after the spliced bars had been pulled apart, and with twice as many fibers these beams better supported themselves for a time before collapsing.

5.0 Slab Joint Testing

5.1 Overview

Initially a review of joint details recommended by FHWA and available in the literature was conducted in preparation for designing the joint specimens. Joints connecting 4 ft by 4 ft slab specimens were used to test joint details including reinforcement across the joints. Initially, full-depth joints with vertical interfaces were examined for both the proprietary and non-proprietary UHPC. A half-depth joint detail

representing what would more likely be done in the field was then tested for both materials. Both sets of slab joint specimens were tested statically and under a fatigue loading to evaluate overall performance of the joint detail and provide an indication of required bar development length. More detail on the full-depth slab joint testing can be found in Coleman (2018), Funderburg (2018), and Looney et al. (2020). More detail on the half-depth slab joint testing can be found in Chea (2020).

5.2 Conventional Concrete Mix Design

A suitable mix design that met ODOT Standard Specifications (2009) for Class AA concrete was designed first using a mix design available from Dolese Bros. as the baseline case. Several trial batches were necessary to determine the correct proportions of materials and concrete properties to satisfy the specifications listed in Table 29. Five trial batches were conducted with varying water-cement ratios, amount of high-range water reducer, and amount of chemical air-entrainer. The first three trials were conducted to determine a mix design that was appropriate, changing one variable each time. The fourth and fifth batches were conducted to verify the properties of the chosen mix design. The final chosen mix designs used to cast the small-scale bond test specimens and slab joint specimens are shown in Table 30.

Table 29. ODOT Standard Specifications (2009) for concrete related to bridge repair

Concrete Class	Min. Cement Content, lb/yd^3 (kg/m^3)	Air Content, %	w/cm, lb/lb (kg/kg)	Slump, in. (mm)	Min. 28-day Strength (f'_c), psi (MPa)
AA	564 (335)	6.5 ± 1.5	0.25 – 0.44	2 ± 1 (50 ± 25)	4000 (27.6)
A	517 (307)	6.0 ± 1.5	0.25 – 0.48	2 ± 1 (50 ± 25)	3000 (20.7)
HDC	825 (490)	6.5 ± 1.0	<0.35	½ – 1.0 (12 – 25)	4000 (27.6)
VES I	900 (535)	6.0 ± 1.5	<0.30	1 – 8 (25 – 203)	3000 (20.7)
VES III	600 (423)	6.0 ± 1.5	<0.35	1 – 8 (25 – 203)	3000 (20.7)

Note: VES I includes Type I cement and VES III includes Type III cement.

Table 30. Concrete mix designs Used to cast joint specimens

Material	Initial MOR Specimens	Slab Joints and Remaining MOR
Type I Cement (lb/yd^3)	588	470
Fly Ash (lb/yd^3)	0	118
Coarse Aggregate (lb/yd^3)	1855	1859
Fine Aggregate (lb/yd^3)	1282	1340
Water (lb/yd^3)	218	153.3
w/c	0.37	0.26
HRWR (oz/yd^3)	17.6	17.6
AEA (oz/yd^3)	4.1	3.3

5.3 Slab Joint Specimens

5.3.1 Overview

Three large-scale slab joint specimens were cast and tested for both the full-depth and half-depth joint detail using both the proprietary UHPC Ductal® and the non-proprietary J3 UHPC to examine structural behavior of the UHPC slab joint detail resulting in a total of six specimens for each joint detail. Six 4 ft x 4 ft by 8 in. thick slab specimens were first cast using a reinforcing bar arrangement based on the slab reinforcement in the SH-3 bridge over the N. Canadian River in Pottawatomie Co. (NBI No. 19276) for use with each UHPC. The slab specimens were reinforced to allow the testing to examine development length, bond strength, and flexural capacity.

5.3.2 Full-Depth Joints

The formwork and reinforcement for three of the slab specimens immediately before casting are shown in Figure 80. Approximately 5 in. of each bar was left exposed to provide dowels into the 12 in. UHPC joint. This bar extension is based on the short anticipated development length of $8d_b$ (5 in. for this case) embedment recommended by FHWA for mild steel reinforcing bars cast in UHPC (Graybeal 2014). This arrangement was intended to represent the steel that will be exposed in the field after an existing joint is sawn out to be replaced.

Class AA concrete supplied by Dolese Bros. was used to cast the slabs due to the large quantity needed for this portion of the study, and the mix design is shown in Table 30. It was similar to the mix used to cast the first set of small-scale MOR specimens except that it contained 20% fly ash by weight as cement replacement and had a lower *w*/*c*. The same curing regimen used for the small-scale MOR specimens was applied to the slabs. For the first 7 days of curing, the concrete was covered with burlap and kept damp (Figure 81). The slabs were then cured in the ambient conditions inside the lab until 28 days of age, after which the UHPC joints were poured between slab pairs. The slabs were arranged end to end and formwork was built around the joint as shown in Figure 82. A 10 in. splice bar was tied to the protruding rebar to ensure proper development of forces between the slabs. Rebar splices had an average lap of 5.5 in. in each direction.

Figure 80. Formwork and reinforcement for slab specimens immediately before casting

Figure 81. Conventional concrete slabs curing under wet burlap

Figure 82. UHPC slab joint formwork and reinforcement before placing the formwork top

The joint was formed ¼ in. high along the entire width of the slab and formwork was placed for the joint ends and top. Copper tubes for embedding thermocouples were placed at approximately the levels of the two rebar mats near the joint end and near the center of the joint thickness at the joint center. A 4 in. diameter hole was cut near each end of the formwork top to allow placement of the UHPC and an air vent. A large funnel was placed in one of the holes to direct the UHPC into the formwork for the Ductal® specimens and first J3 specimen. The funnel is visible in Figure 83.

Figure 83. Placement of UHPC into the slab joint formwork

Four batches were required using the 4.25 ft^3 high-shear mixer available at Fears Lab for the Ductal® UHPC joints. This mixer was used to examine the effect of placing multiple batches as would be required in the field. The batches were mixed

consecutively with a time between placements of 20 min to 30 min. The material was very flowable, as shown in Figure 83Figure and was all placed from the same location and allowed to flow across the joint. Material was placed until it began to run out of the vent hole on the opposite end of the formwork. The J3 joints were cast using a single batch of UHPC mixed in the larger rotary mixer. The funnel placement method was abandoned after the first J3 specimen and the UHPC was poured directly into the forms and then topped due to the extremely thixotropic behavior of that that batch. Once casting of all specimens was complete, the top of the formwork was removed, the thermocouples were inserted, and the top of the joint was covered with heat resistant plastic. The heat lamp was moved into place and heat curing was conducted on both the joint and companion compressive strength specimens for 12 hours using the regimen identified during previous testing for the Ductal® specimens and 36 hours for the J3 specimens. When the heat curing duration was reached, the heat lamp was removed, and the joint was allowed to cure in ambient conditions for the remainder of 28 days. The heat curing setup is shown in Figure 84 and the temperature history for the first slab is shown in Figure 85. Compressive strength tests were conducted on heat cured cylinders at the end of curing. Companion cylinders cured in ambient conditions were tested at 24 hours and 3 days of age for comparison.

Figure 84. Heat curing for Ductal® slab joint 1

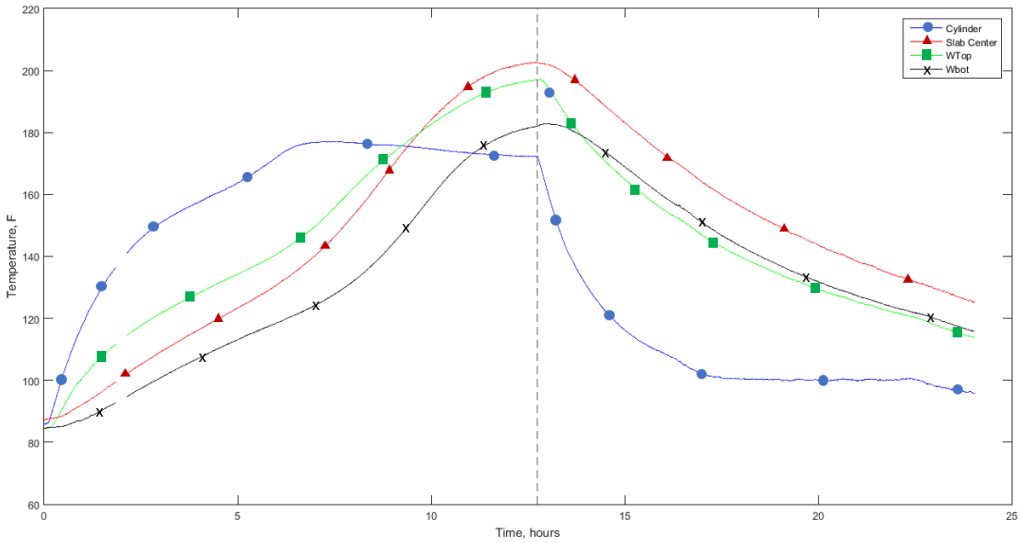

Figure 85. Temperature history during heat curing for Ductal® slab joint 1

Formwork was removed from the joint the day following the end of heat curing. A completed Ductal® joint after removal of the formwork is shown in Figure 86. Faint lines were visible between the placement layers but no indication of poor consolidation or poor bond between layers was observed.

Figure 86. Completed Ductal® slab joint after formwork removal

Two of the composite slab joint specimens in each group were tested in static flexure and the third was set up to be loaded cyclically for 5,000,000 cycles. All tests were conducted using an 8 ft span with neoprene bearing supports and a single point load placed immediately next to the slab joint. Load was applied using a 22-kip capacity

MTS servo hydraulic cylinder and corresponding load frame. The point load was distributed over a 10 in. by 20 in. area using a steel plate and neoprene pad designed to mimic the wheel patch area specified in AASHTO LRFD Chapter 3 (2017). A photo of the load test setup is shown in Figure 87. For all tests, deflection was monitored on both sides of the joint using linear voltage differential transformers (LVDTs) or wire potentiometers (pots). Deflection was also monitored near the supports using LVDTs in order to remove the effects of support deflection from the results. Applied load was measured using a load cell placed at the load point. External strain gages were placed on the base concrete on either side of the joint and in the center of the UHPC joint material on the south side of each specimen and one strain gage was placed at the center of the UHPC joint material on the north side of the specimen. A photo showing the strain gauges and LVDTs on the south side of the slab is provided in Figure 88. After testing the Ductal® joints it was determined that strain gages on the reinforcing bars would provide additional useful information. For the three J3 joints foil strain gages were placed on two of the bottom reinforcing bars extending from the slab nearest the load point and on the corresponding splice bars.

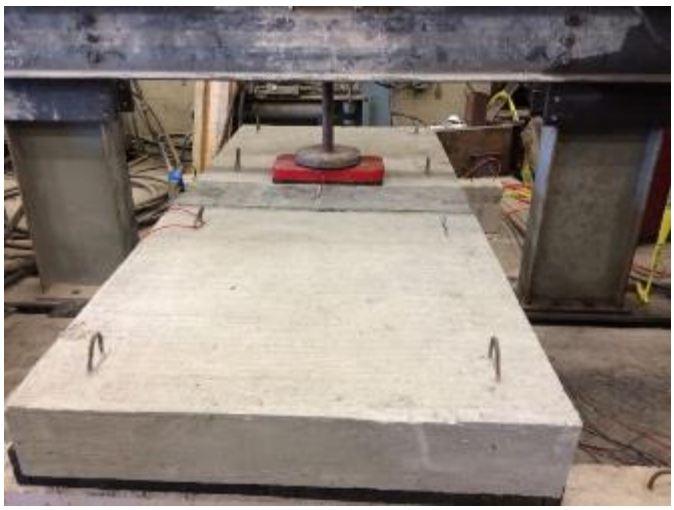

Figure 87. Full-depth UHPC slab joint load test setup

Figure 88. Placement of external strain gauges and LVDTs on the south side of the slab specimen

The load for the static tests was applied in 1 kip increments with a pause between load increments to investigate for any cracking resulting from that load increment. Loading was continued for the first slab until the load capacity of the MTS hydraulic cylinder was reached. At this point the load was removed and the LVDTs used to measure deflection near the load point were removed and replaced with wire pots to allow for a greater range of deflection. A hydraulic cylinder with greater capacity was then attached to the load frame and the slab was then reloaded in 1 kip increments to failure. The same loading process was used for the subsequent slabs to provide more precise deflection measurements at low load levels and to be comparable to the first test.

5.3.3 Half-Depth Joints

5.3.3.1 Slab Specimen Construction

Three slab joint specimens in total were constructed for each UHPC material and each was fabricated from two normal strength concrete panels with dimensions of 4 ft x 4 ft x 8 in. and a cut-off dimension of 4 ft x 8 in. x 4 in. Six wooden forms were fabricated with interior dimensions of 4 ft x 4 ft x 8 in. However, the forms included an insert to allow the specimens to have a cut-off section dimension at one end of 4 ft x 8 in. x 4 in. for joint connections as shown in Figures 89 and 90. Slab reinforcement was spaced to match the deck reinforcement for the same existing bridge in Oklahoma as

used for the full depth joints. No. 5 steel reinforcing steel bars were used for all slab reinforcement, which is shown in Figures 90 to 92. The reinforcing bars protrude 7 in. from one end in the cut-off portion to allow for bar splices between the slabs, as shown in Figures 90 and 91.

Figure 89. Formwork prepared for concrete casting

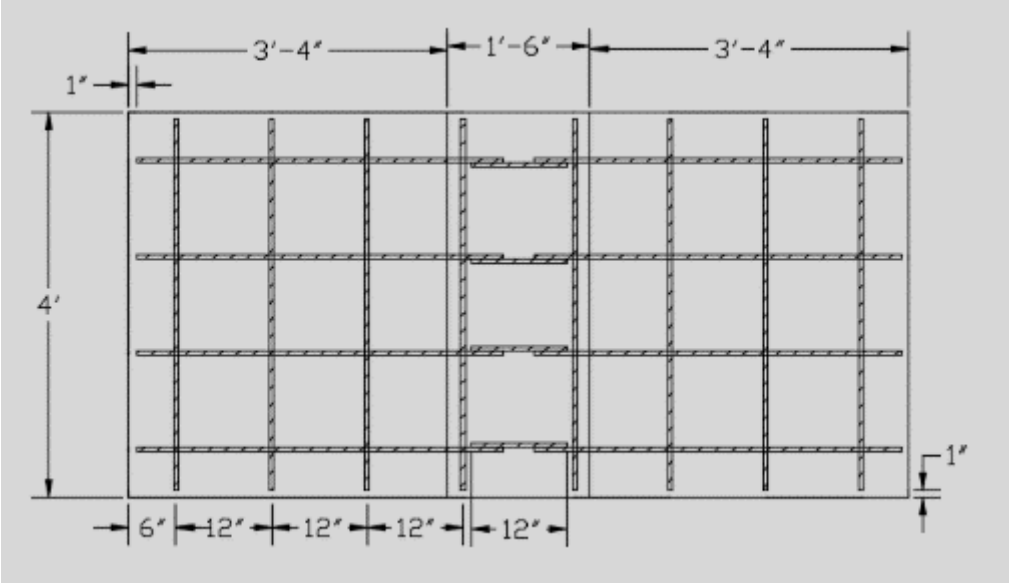

Figure 90. Plan view of reinforcement of slab specimens

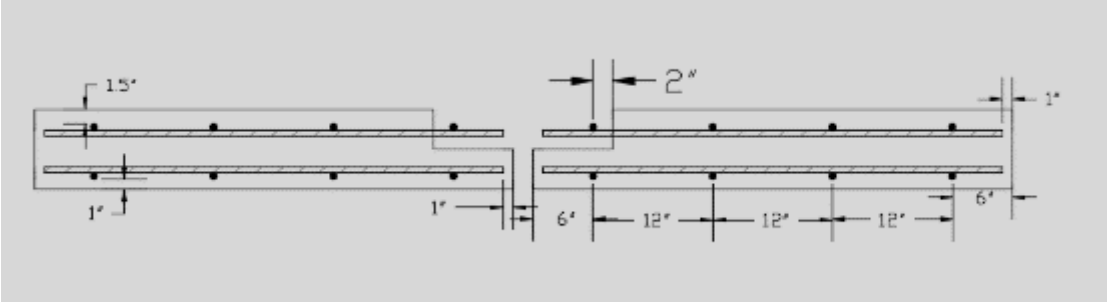

Figure 91. Elevation view of reinforcement excluding splice bar between slab specimens

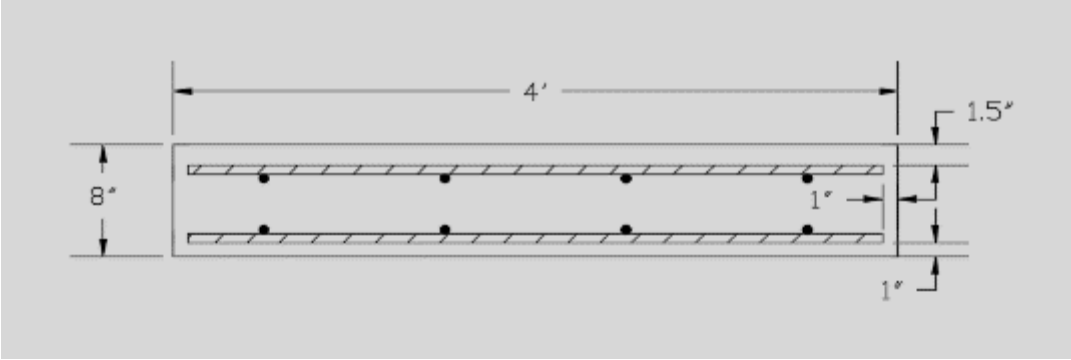

Figure 92. Cross-sectional view of reinforcement for slab specimens

The twelve base slabs required for the joints were cast in two sets of six using the same Class AA concrete mix from Table 30 obtained from Dolese Bros. Finishing work was required at the top surface as shown in Figure 93 before a final broom finish was applied. Completed slabs are shown in Figure 94. A total of 24 4 in. x 8 in. cylinders were also cast from the same conventional concrete mixture. A group of 12 cylinders were used for testing compressive strength of conventional concrete for non- proprietary UHPC joint connections. The other 12 cylinders were used for testing compressive strength of conventional concrete for proprietary UHPC joint connections.

Next, the concrete slabs were covered with wet burlap and a plastic tarp for seven days to allow for moisture retention when the concrete was curing. Figures 95 and 96 show the slabs covered in burlap and a plastic tarp. After the seven-day curing period was completed, the slabs were stacked and allowed to cure in the ambient laboratory conditions until they reached an age of 28 days. A completed slab specimen after curing and is shown in Figure 97. The half-depth portions of the slab were roughened using an impact hammer in preparation for casting of the UHPC.

Figure 93. Finishing the top surface of the base concrete slabs

Figure 94. Side-by-side slabs after finishing applied

Figure 95. Concrete slabs curing covered by wet burlap

Figure 96. Plastic tarp covering curing concrete slabs

Figure 97. Completed half-depth slab specimens showing protruding rebar

5.3.3.2 Joint Casting

After the conventional concrete reached adequate strength (taken as 28 days of age), the conventional concrete panels were positioned 2 in. apart so that splice bars could be placed across the exposed bars on each slab to connect the two panels as shown in Figures 98 and 99. The formwork was constructed spanning across the two panels to create the 18 in. wide joint and allow for UHPC to be poured in. Next, foil strain gauges were installed on the protruding bars and splice bars to observe the changes in reinforcing bar strain during testing as shown in Figures 98 and 99.

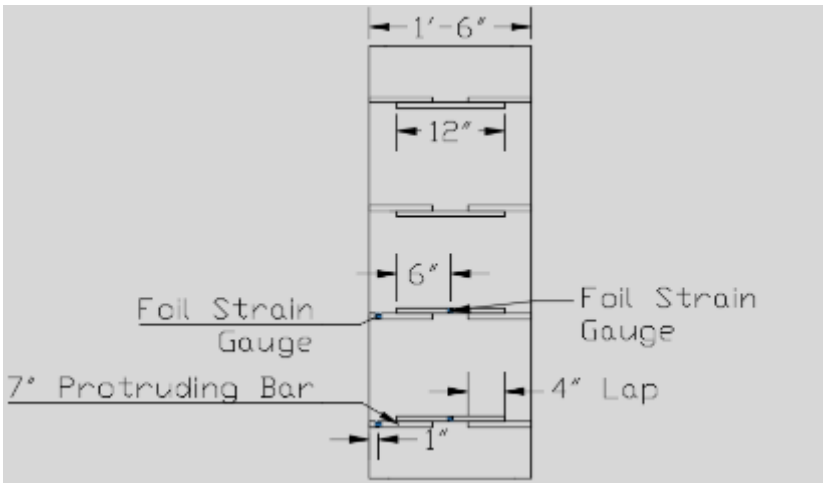

Figure 98. Plan view of UHPC joints with foil strain gauge locations shown

Figure 991. Two slab panels with formwork in place and strain gauges installed

The UHPC (both J3 and Ductal®) was mixed using a large horizontal axis high-shear mixer available at Donald G. Fears Structural Engineering Laboratory. UHPC was transported from the mixer to the joint formwork using a concrete transfer bucket and overhead crane. UHPC was poured into the forms and allowed to self-level, as shown in Figures 100 and 101. No consolidation was applied to the UHPC material. The width of the top half of the UHPC joint (the half-depth portion) was 18 in. and UHPC was allowed to fill the 2 in. between the bottom halves of the slabs. No reinforcement was placed to connect the bottom halves of the slab. The slab joints were slightly over-poured (approximately 0.25 in.) so air bubble formation on the top of the joints occurred in the over-poured surface and not in the main part of the joints. Two sets of 12 3 in. x 6 in.

cylinders were cast for testing compressive strength of UHPC. A total of 12 cylinders were cast from the same J3 non-proprietary UHPC mixture, and the other 12 cylinders were cast from the same Ductal® proprietary UHPC mixture.

Figure 100. Placement of UHPC connecting two slab panels

Figure 101. Self-consolidating UHPC filling the joints

Copper tubing was embedded in the UHPC joints and thermocouples were installed to monitor the temperature of the joints during heat curing. The non-proprietary UHPC joints were heat-cured for 36 hours with heat lamps installed at 16 in. above the top surface of the joints to ensure constant heat was provided throughout the joints as determined by Coleman (2018) and the internal temperature was approximately 200°F. The proprietary UHPC joints were cured using the same setup but for a duration of 12 hours and the internal temperature was approximately 180°F. Heat resistant plastic

sheeting was placed over the UHPC joints to retain moisture during. Companion cylinder specimens were placed alongside the joints to be subjected to heat curing as well. Figure 102 shows the setup of the heat lamps and the UHPC joints being cured. At the end of the 36- or 12-hour curing period, the heat lamps were removed, and the joints were allowed to cure under ambient laboratory conditions for at least 28 days before testing. Figure 103 shows a completed UHPC joint.

Figure 102. Heat curing of OU J3 half-depth slab joint specimens

Figure 103. Completed half-depth slab joint cast using OU J3 mix

5.3.3.3 Slab Joint Testing

Once the UHPC joint material reached 28 days of curing, the slab joints were ready to be tested. The same general methods used for testing the full-depth slabs were used with some modification. Each slab was flipped with its orientation for testing as shown in Figure 104 to represent negative moment occurring over a bridge pier. Each slab was positioned within a steel portal frame supported by concrete beams and 6 in. wide rubber pads at each end. Each specimen was tested using a hydraulic ram and

pump. Deflection was measured on both sides of the joint and at the rubber pad supports using 7 linear variable differential transformers (LVDTs) or using a combination of LVDTs and wire potentiometers (pots). These LVDTs were placed underneath the slab in different positions as shown in Figure 105, except for LVDT 1 which was included inside the MTS hydraulic cylinder. The strain gauges described in Section 5.3.2.2 were also used to measure strain in the reinforcing bars within the joint during the test. These gauges were installed on two of the splice bars and two of the protruding bars on the load side of the joint. The difference in overhang on each end of the slab as shown in Figure 106 is due to the location of the support pads and LVDT 1. The support pads' location was based on the full depth slab test and those specimens were 10 in. longer.

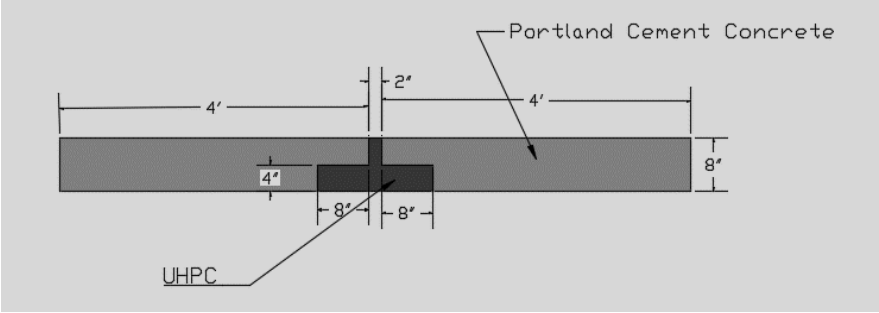

Figure 104. Elevation view of slab orientation during testing

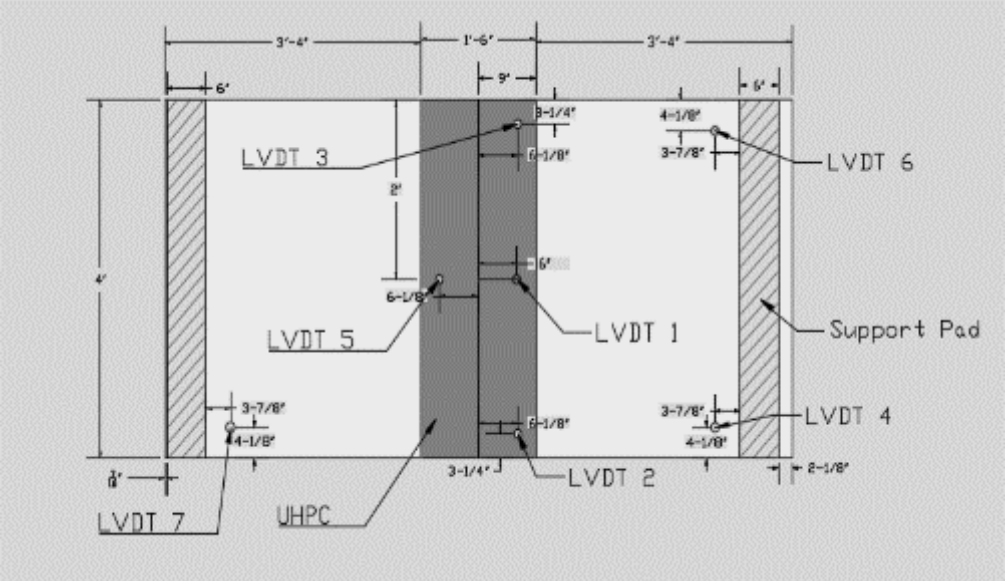

Figure 105. LVDT layout for slab testing

Slabs 1 and 2 for non-proprietary UHPC joints were tested using an MTS hydraulic ram with a maximum capacity of 22 kips as shown in Figure 106. A load cell was used to measure the load, and the load was applied through a 10 in. by 20 in. metal plate on top of a rubber pad. Both slabs were loaded in 1-kip increments up to the maximum capacity of the MTS. Once the MTS capacity was reached, the slab was unloaded and the MTS was replaced with a manually controlled hydraulic cylinder and pump with a capacity of 50 kips, shown in Figure 107. The slabs were then reloaded again to failure. In addition, the three LVDTs around the joint were replaced with wire pots to provide more deflection measurement capacity and prevent damage to the LVDTs. The slabs were then loaded until flexural failure using 1-kip load increments. The results of the static tests were used to plan the cyclic loading used for slab 3.

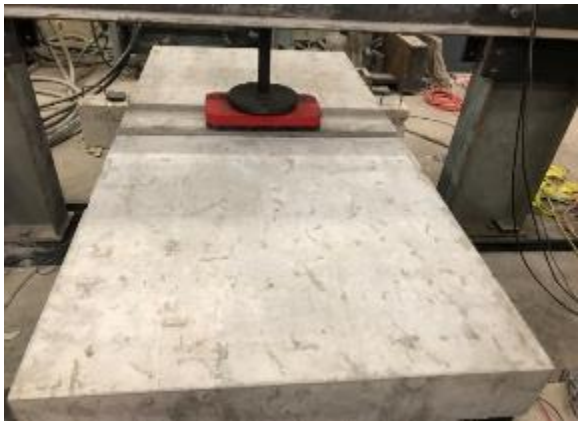

Figure 106. Test setup for slabs using the MTS hydraulic ram

Figure 107. Test setup for slabs using the manually controlled hydraulic cylinder and pump

Slab 3 with the non-proprietary UHPC joint was cyclically loaded using the MTS hydraulic ram. The 7 LVDTs were installed in the same positions as used for slabs 1 and 2. A total of 3 million cycles were applied to this slab with minimum cyclic load of 500 lb and maximum cyclic load of 90% of the cracking load (which was 5.3 kips) observed during the slab 1 and 2 tests. After 3 million cycles were completed, the maximum cyclic load was increased to 110% of the cracking load (which was 6.5 kips) observed during the Slab 1 and 2 tests. This test was run for 850,950 cycles without slab failure. The decision was made to increase the maximum cyclic load to 8.7 kips, which was loosely based on the maximum load for cyclic test performed on the full-depth joints The test was then run for another 473,425 cycles without failure at which point the test was stopped due to equipment problems.

The same set of slab tests was repeated for the proprietary UHPC slab joints. Slabs 1 and 2 for the proprietary UHPC joints were tested using a manual hydraulic pump to failure without the initial loading done for the non-proprietary joint specimens due to equipment problems with the MTS system. They were loaded in 1-kip increments up to the deflection capacity of the manual hydraulic pump. The slabs were then unloaded, the ram repositioned to gain additional stroke, and the slabs were reloaded with 3-kip increments instead of 1-kip increment until failure. This reloading is referred to as Part 2 in the results.

Slab 3 with proprietary UHPC joint was cyclically loaded using the MTS hydraulic ram. The cyclic test was performed the same way as slab 3 with non-proprietary UHPC joints. However, the slab was tested cyclically for only 3 million cycles, and the results were analyzed over a representative period of time to compare stiffness between the slab joints.

5.4 Full-Depth Slab Joint Test Results

5.4.1 Ductal® Slab Joint Results

For both statically loaded Ductal® joints, the first crack was observed directly beneath the point load (approximately 5 in. from the joint) after the 14-kip load increment. Failure of slab specimen 1 occurred at a load of approximately 36.4 kips and slab specimen 2 at a load of 37.7 kips, which was substantially greater than the

estimated capacity considering the slab to be completely monolithic using the base concrete. The load deflection relationships for the two tests are shown in Figure 108. Both failures occurred due to crushing of the concrete directly below the load point after substantial deflection was measured. The slab concrete did separate from the UHPC on both sides of the joint, but not until after a crack formed in the base concrete. Figure 109 shows cracks near the applied load for Ductal® specimen 2 at failure. Based on the experimental capacity being greater than the estimated capacity, it was concluded that the reinforcing bars were able to develop their full strength across the joint.

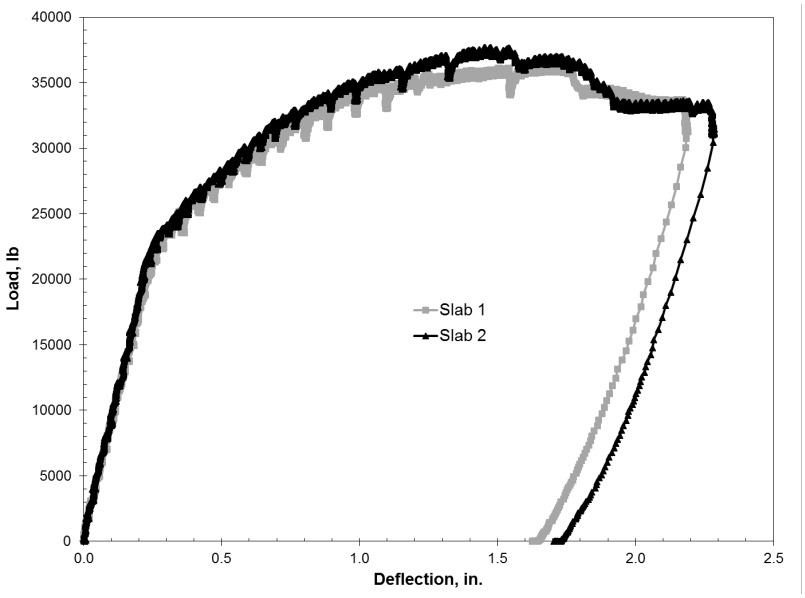

Figure 108. Load-deflection relationships for the static tests of Ductal® slab joints 1 and 2

Figure 109. Cracking near the load point at failure for Ductal® slab joint 2

Ductal® slab specimen 3 was set up for cyclic load testing to a load just below the calculated cracking load, which was confirmed by observations during the static load tests. A haversine load curve was programmed into the MTS system to cycle between 500 lb. and 12,500 lb (90% of the expected cracking moment) at a rate of 1 Hz. However, during cycles at a load of 12,500 lb, cracks were observed directly below the load point and at the slab to UHPC interface. The maximum load was then reduced to 9,000 lb. Data were collected from the load cell, LVDTs and strain gauges at a rate of 20 Hz. An example of load application for a 5 second window of the test is shown in Figure 110. Plots of load-deflection behavior for single cycles at various points during testing are shown in Figures 111 and 112. Figure 112 shows the residual deflection and change in stiffness observed as the magnitude of the applied load was increased up to the initial 12,500 lb target then reduced to 9000 lb. Load cycles taken from every second day of testing were examined for change in stiffness over time. Figure 112 shows load-deflection curves for different days of testing up to approximately 3,000,000 load cycles. A linear trend line was considered for each load cycle examined, since the slab was expected to have a linear response at the applied load level. The slope of the equation shown is a measure of the stiffness of the slab, which generally decreased throughout the first 3 million cycles as shown in Figure 113. This could be due to the fact that the slab was cracked prematurely during the initial cyclic loading.

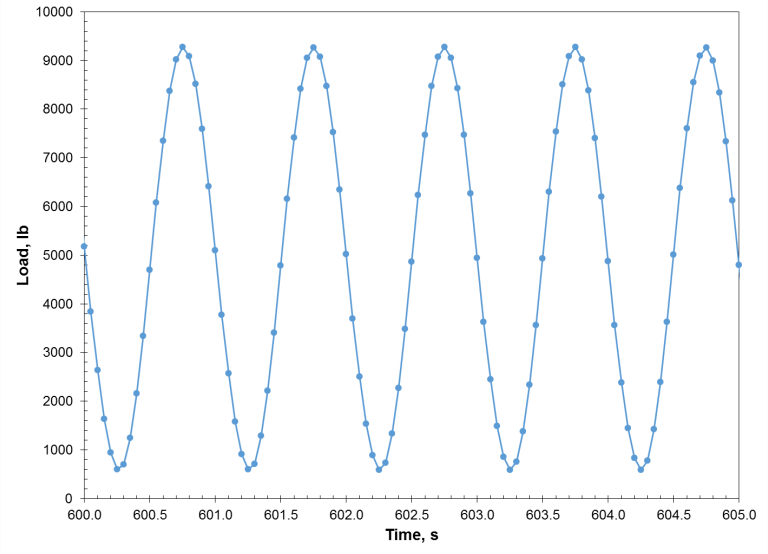

Figure 110. Sample load time history for cyclic testing of Ductal® slab joint 3

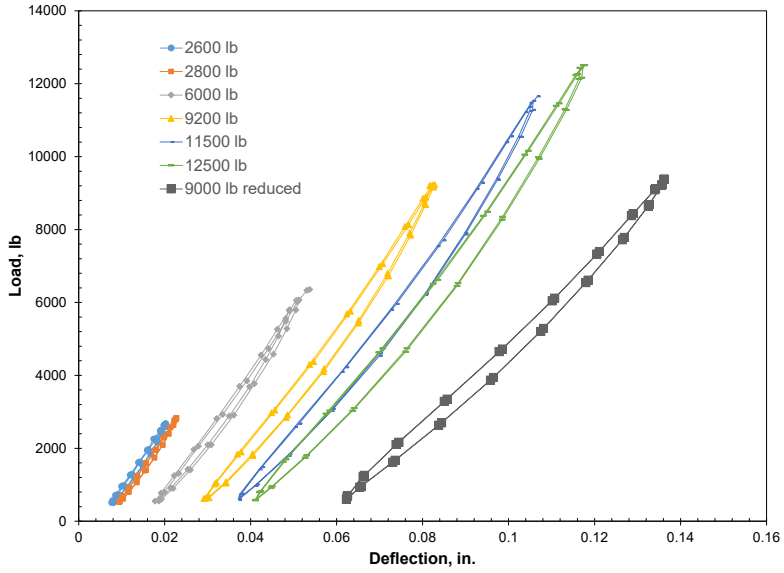

Figure 111. Load deflection relationship for first few cycles showing progression of applied load and residual deflection

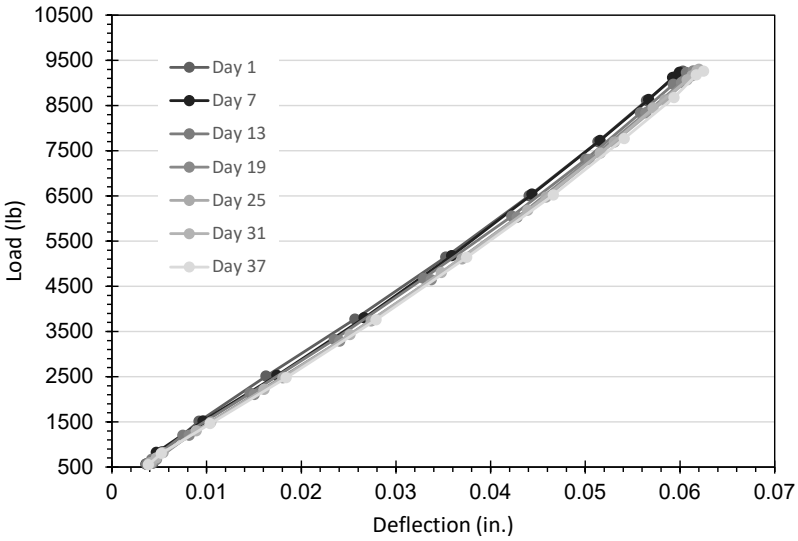

Figure 112. Sample load deflection relationships from cyclic testing of Ductal® slab joint 3

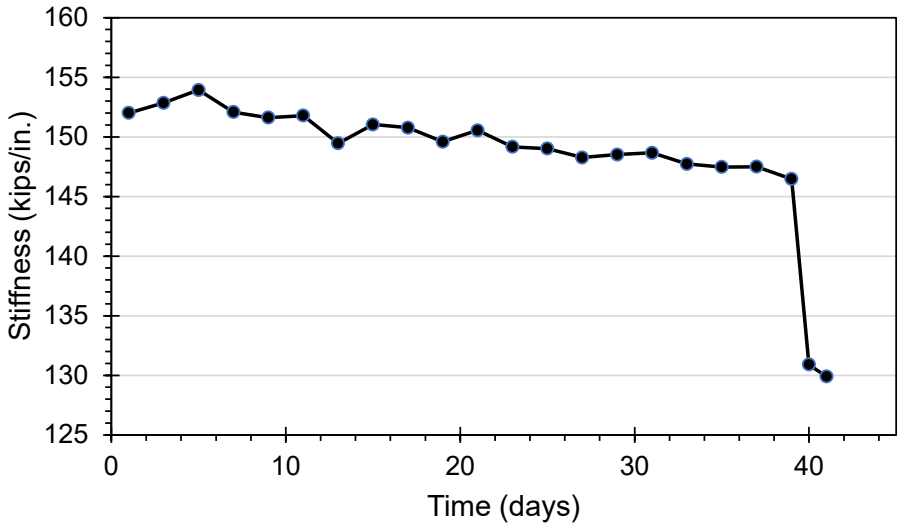

Figure 113. Ductal® slab joint 3 stiffness over loading period

Very little change in behavior was observed over time for the first 3,000,000 load cycles. The load was then increased to a load greater than the cracking load and loading continued until specimen failure after approximately 244,000 additional load cycles. There was significant visible cracking and a residual deflection of 0.38 inches. The major failure crack on the bottom of the slab began on the south side 5.9 inches away from the joint interface closest to the load. Halfway across the slab (in the north-south direction) the crack migrated westward toward the joint and continued along the interface to the north edge. The slab was then statically loaded to complete failure at an ultimate load of approximately 17.7 kips, significantly less than the other two slabs and less than the expected capacity. It was determined that the steel stress for the increased loading beyond 3,000,000 cycles exceeded the fatigue stress limit for the reinforcing steel and that at least one of the reinforcing bars fractured during fatigue testing. The slab joint after completion of testing is shown in Figure 114.

Figure 114. Ductal® slab joint 3 after completion of testing showing concrete crushing and separation at joint indicative of rebar failure

5.4.2 J3 Slab Joint Results

Failure of the first two non-proprietary J3 UHPC slab joints tested statically initiated due to yielding of the lapped reinforcing steel within the joint, as indicated by both a plateau in the load-deflection plot (Figure 115 and Figure 116) and through strain gage readings from sensors installed on the reinforcing steel. The lap lengths measured only 5 in. for the No. 5 reinforcing steel, indicating exceptional bond strength within the UHPC joint. Cracking occurred exclusively within the base concrete and not within the UHPC joint, although the interface did begin to open as the stresses exceeded the bond strength between the UHPC and base concrete and the reinforcing steel yielded, as shown in Figure 117.

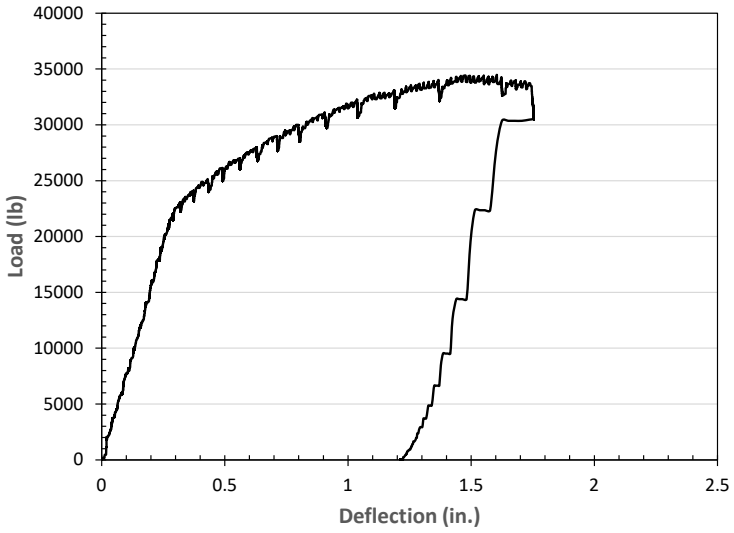

Figure 115. Load-deflection relationship for J3 slab joint 1

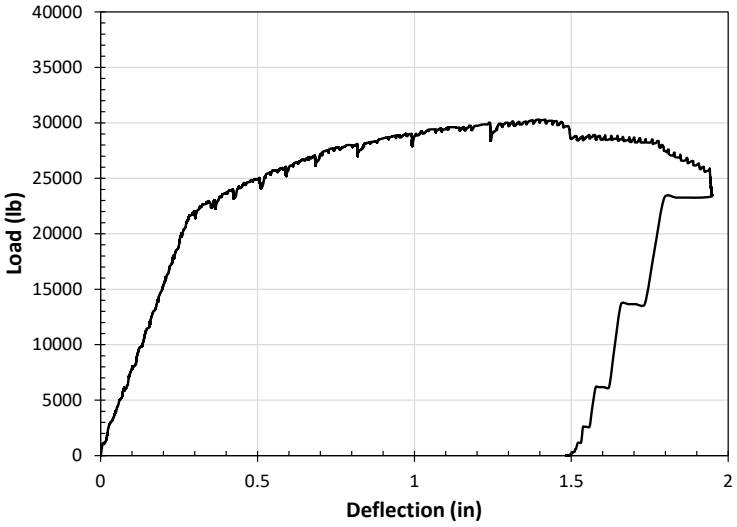

Figure 116. Load-deflection relationship for J3 slab joint 2

Figure 117. Slab joint at failure showing concrete crushing on the compression face, cracking in base concrete, and opening at joint interface

The third non-proprietary J3 UHPC slab joint specimen was tested under fatigue loading using the same loading regimen used for the third Ductal® joint tested with the exception that the maximum applied load was only 8000 lb due to differences in observed cracking moment. Three million cycles at a load less than the cracking moment were completed with minimal observed loss of stiffness. The load was then increased to 10% over the cracking moment and cyclic loading was restarted. The specimen exhibited a fatigue failure after approximately 420,000 cycles of loading greater than the cracking moment. The slab was then loaded statically to flexural failure

to determine residual capacity. The J3 specimen exhibited similar performance to the previously tested Ductal® specimen. After testing the concrete on the load side of the joint was removed to expose the reinforcement, shown in Figure 118. Two fractured reinforcing bars resulting from fatigue failure were observed, but no evidence of bar pullout from the UHPC was visible.

Figure 118. Fractured tension reinforcing bars after fatigue failure of slab joint (note that the slab has been flipped relative to the testing orientation)

Concrete cores were removed from one of the statically tested J3 slab joint specimens to examine the upper surface of the non-proprietary UHPC. It was noted previously that the non-proprietary UHPC did not experience a very friable upper portion as what normally occurs with the Ductal® material. Ductal® tends to experience a very high degree of bubbles and thus weak, friable material near the top surface and typically requires grinding/removal of that poor material. As such, the manufacturers of Ductal® require the material to be cast at least ¼ in. higher than finished grade. However, the non-proprietary UHPC does not show a comparable weakened upper surface, as shown in Figure 119. As a result, it may be possible to cast the non-proprietary material at the finished grade and eliminate the need for grinding the top surface, saving considerable cost in a bridge joint replacement or other application.

Figure 119. Non-proprietary UHPC slab joint core indicating uniform consistency

5.4.3 Comparison of Full-Depth Slab Joint Results

Comparisons of the load-deflection behavior for static tests of the slab joints using Ductal® and the non-proprietary J3 mix are shown in Figures 120 and 121 and for the cyclic test in Figure 122. In general, the stiffness and ultimate load capacity were less for the J3 specimens, most likely due to earlier separation of the joint interface. However, in general behavior of joints cast with the two different UHPC materials was very similar.

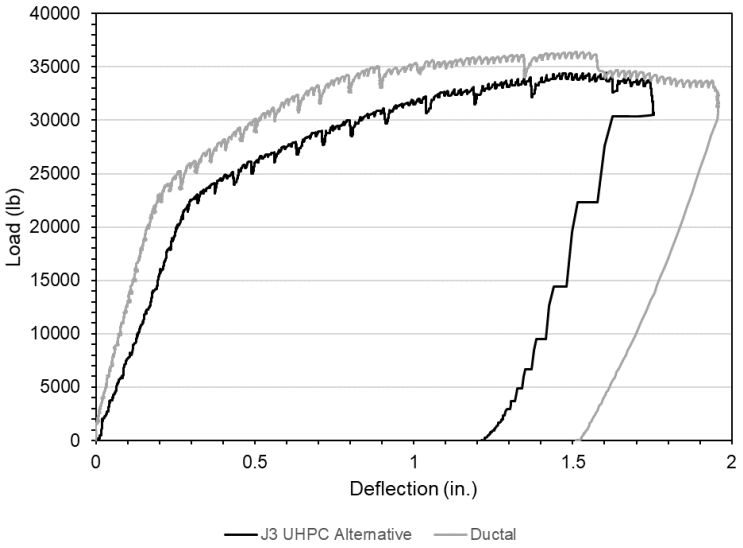

Figure 120. Comparison of load-deflection behavior for static test of slab joint 1 cast with each UHPC

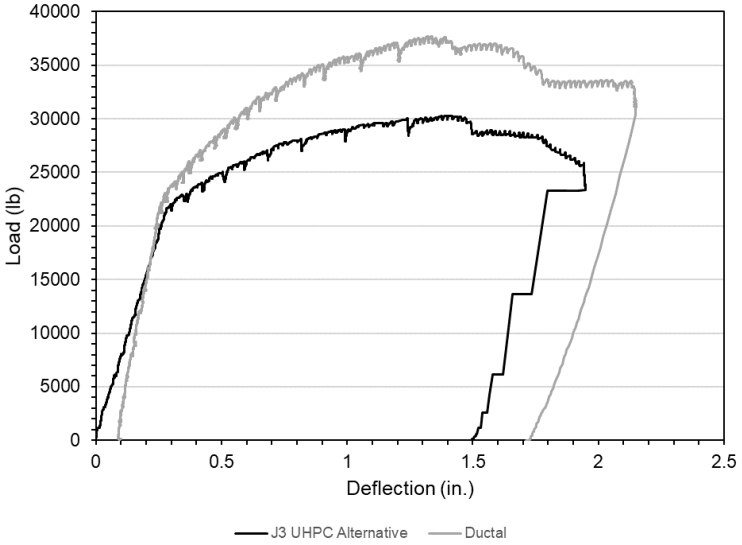

Figure 121. Comparison of load-deflection behavior for static test of slab joint 2 cast with each UHPC

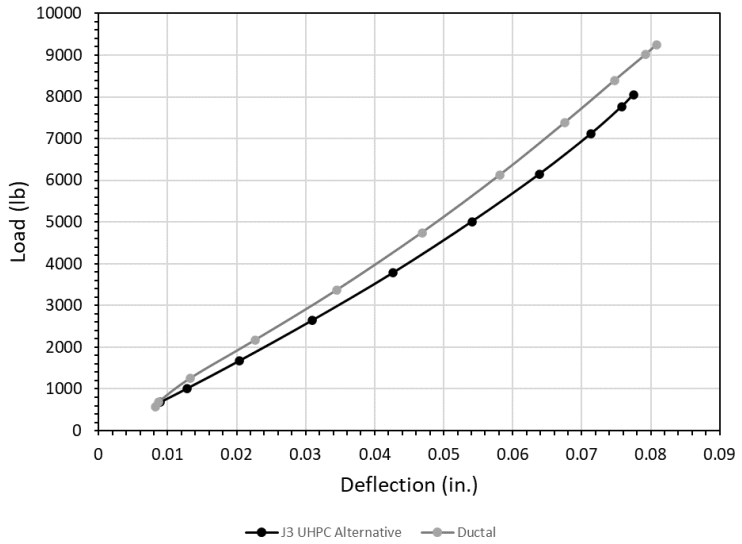

Figure 122. Comparison of load-deflection behavior for slab 3 cast with each UHPC for single load cycle during day three of cyclic load test

5.5 Half-Depth Slab Joint Test Results

5.5.1 Compressive Strength Results

Average compressive strengths for the concrete used in the half-depth slab joints are presented in Tables 31 and 32. The six slab panels for each series of joints were poured at the same time using the same mix that was batched and delivered to Fears

Lab by Dolese Bros. Co. The compressive strength of the slabs for the three J3 specimens exceeded the desired 4000 psi at 28 days. The compressive strength of the conventional concrete slab panels for the Ductal® joints did not exceed the desired 4000 psi at 28 days and showed reduced values at time of testing. The lower than desired compressive strength could be caused by high water to cement ratio due to water added during casting. In Table 31 test day is defined as the day that the cyclic test began for this study, which applies to other compressive strength results in the following tables. All the J3 UHPC joints were cast at the same time using the same batch and all the Ductal® UHPC joints were cast at the same time using the same batch.

Table 31. Compressive strength (psi) of the conventional concrete for half-depth joints

Age	J3 Joint Slabs	Ductal® Slabs
1-Day	1380	1950
7-Day	3330	3700
28-Day	4690	3930
Test Day	4220	3370

Table 32. Compressive strength (psi) of the UHPC for half-depth joints

Age	J3 UHPC	Ductal® UHPC
3-Day	14,310	13,170
7-Day	14,030	18,370
28-Day	15,870	20,990
Test Day	17,000	24,710

5.5.2 J3 Slab Joint Static Test Results

The maximum load applied to J3 slab 1 in part 1 was approximately 20 kips. Due to the limitations of the MTS system loading capacity, the test was stopped at this point before switching to the manual hydraulic pump for part 2. The first cracks appeared at the conventional concrete and UHPC interface at an approximate load of 6 kips. This cracking load was determined from when the first crack became visible to the observing eyes. Additional graphical analysis using the change in stiffness at the point of cracking indicates that the first crack appeared at approximately 5.9 kips, which is almost the same as the cracking load observed by naked eye. Figure 123 shows the load vs. deflection curve for J3 slab 1 part 1. The curve showed the crack appears at

approximately 5.9 kips. This cracking load was determined graphically by observing the point of the curve where there was an increase in deflection but no increase in load since the MTS loading was load controlled. Once the cracking load was reached, there was a slightly less steep slope which demonstrated a reduction in stiffness. The load corresponding to the cracking moment of a monolithic conventional concrete slab was calculated as 11.1 kips. This calculation assumed a monolithic normal-strength (4000 psi) concrete slab and was determined based on the span and loading configuration of the specimen set up. The graphically calculated cracking load of this slab specimen was considerably less than that of a monolithic normal-strength concrete slab, which was potentially due to a cold joint between the conventional concrete and the UHPC.

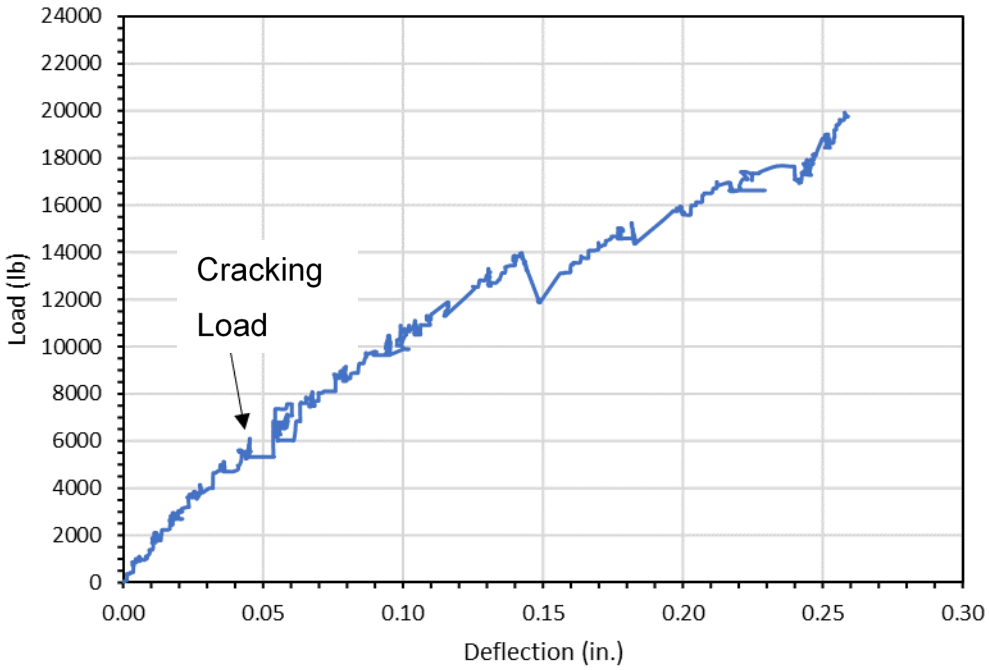

Figure 123. Load vs. deflection curve for J3 slab joint 1, part 1

Figure 124 shows the load vs. deflection curve for part 2 of J3 slab 1 testing. This testing was performed using a manual hydraulic pump, which caused more variability in the load application that the digital MTS system. Load increments of 1 kip were applied, and the slab was observed for cracks using a flashlight and marker to highlight and label where and when each crack appeared. The load dropped slightly within that timeframe due to fluid being pushed back through the pump; this drop in load can be

observed from the trend of the curve. The ultimate load achieved for slab 1 was approximately 35 kips. The calculated failure load for a monolithic normal-strength concrete slab with the same reinforcement and dimensions was calculated to be 27.3 kips. The actual failure load of the specimen exceeded the calculated failure load by 28%. Failure was defined as the point when the specimen could not sustain any additional load, produced yielding behavior, and concrete crushing was observed at the top of the slab specimen in the conventional concrete. The load vs. deflection curve plateaued and there was concrete crushing at the top of the slab. This suggested that the slab had failed.

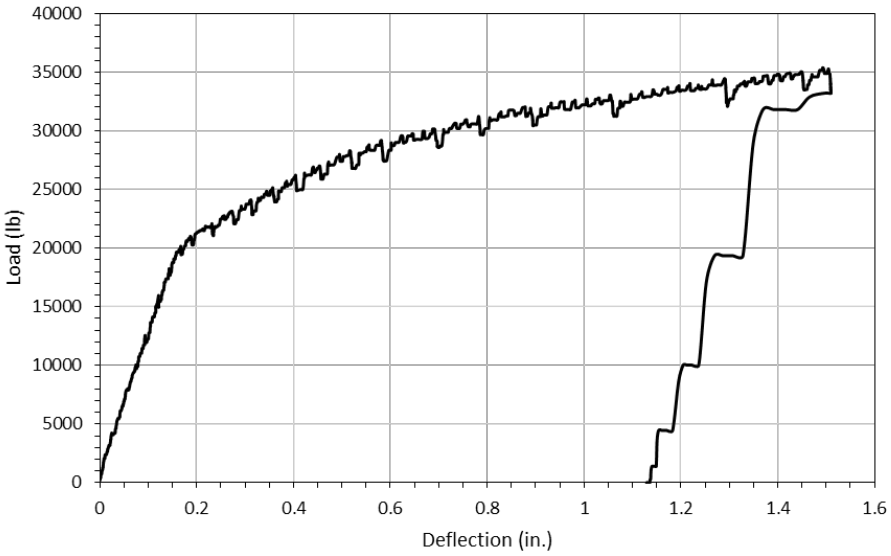

Figure 124. Load vs. deflection curve for J3 slab joint 1, part 2

Figure 125 shows a comparison for J3 slab 1 part 1 and part 2 load vs. deflection curves. The part 2 curve started at the residual deflection of the part 1 curve. Because there was not enough data for residual deflection in part 1 curve, the starting point of part 2 curve is based on slope and pattern of both curves. The slope of each curve is similar up until the cracking load after which the slope of the part 1 curve decreases. This result is unexpected as the part 2 curve was expected to have a lower slope than part 1 since the slab had already been cracked.

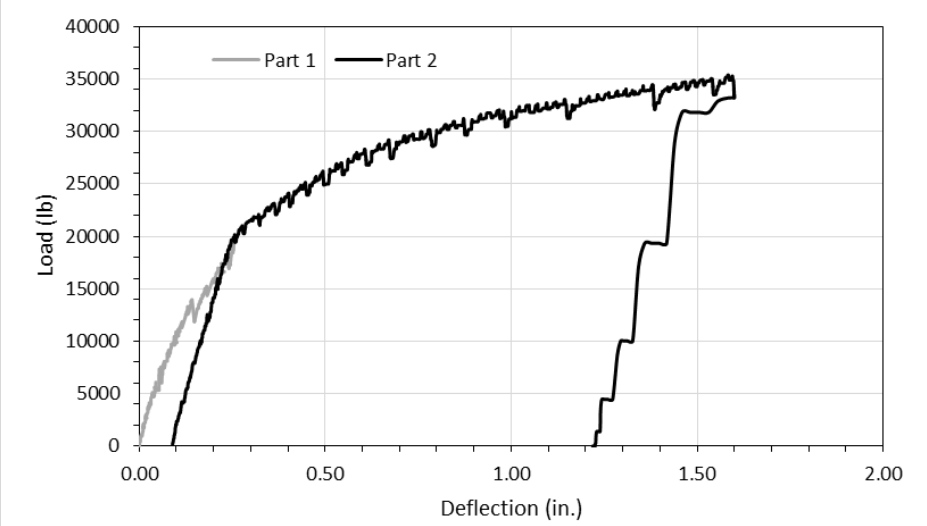

Figure 125. Load vs. deflection curve for J3 slab 1, part 1 and 2

At failure, the cracks were mainly at the interface between the conventional concrete and UHPC, with some cracks in the conventional concrete. Figures 126 and 127 show cracks on the slab after failure. The majority of the cracks at failure appeared to be evenly distributed on both sides of the joint. Significant cracks appeared at the interface between the UHPC and conventional concrete. Additional cracks were located approximately 3 in., 4 in., and 5 in. away from the interface. There was also substantial separation at the conventional concrete to UHPC interface at the as-tested bottom of the slab, which was visible while loading, but could not be seen once the load was removed from the slab. Figures 128 and 129 show images of cracks and deformation of the slab after failure.

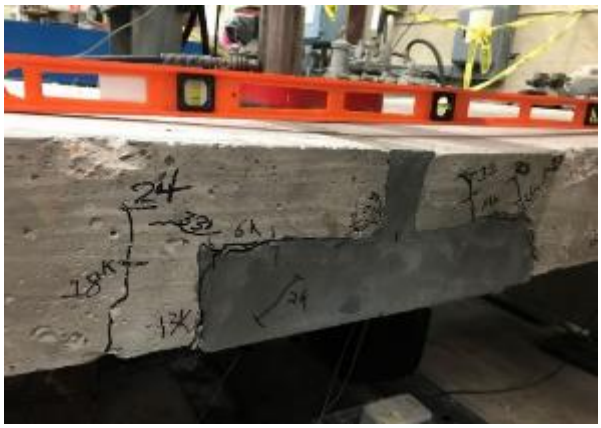

Figure 126. Cracks formed at interface between UHPC and conventional concrete and underneath the load point on the south side of J3 slab joint 1

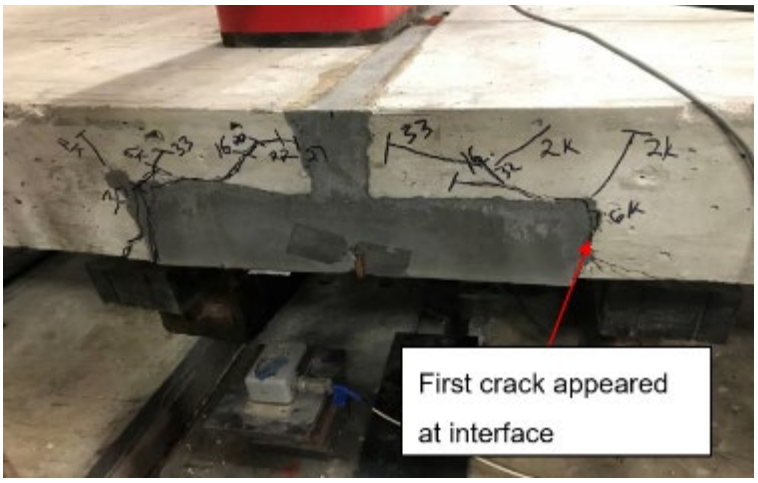

Figure 127. Cracks propagating from the bottom of the slab to the top at failure on the north side of J3 slab joint 1

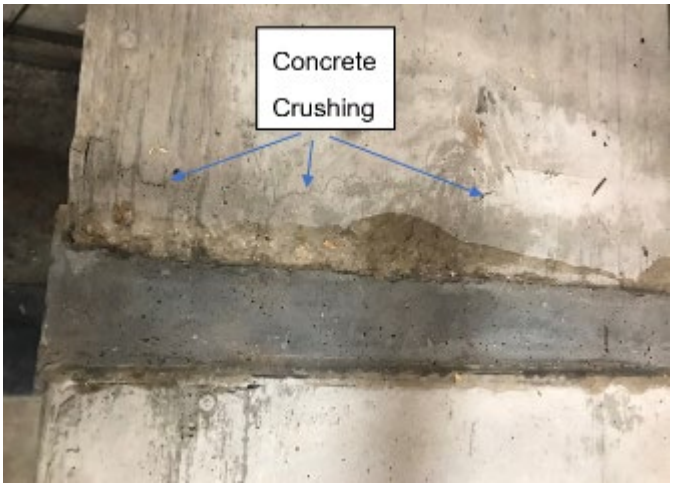

Figure 128. Concrete crushing at the top surface of J3 slab joint 1 indicating failure

Figure 129. J3 Slab joint 1 curvature after failure

The initial plan was to test J3 slab joint 2 cyclically and test slab joint 3 statically. Slab 2 was loaded cyclically with loads ranging from 0.5 kips to 7.8 kips for 397 cycles. Load vs. deflection behavior for one of these load cycles is shown in Figure 130. Realizing that the slab showed cracks, the test was stopped and switched to a static test instead. The maximum load applied to J3 slab 2 during the subsequent part 1 of static testing was approximately 20 kips as shown in Figure 131. The slope did not change much because the slab may have already cracked. The first visible crack was observed at approximately 8 kips using the naked eye with the help of flashlight. Graphical analysis revealed the crack could potentially happened at a load of approximately 4 kips. This is a smaller load compared to slab 1, which could be caused by cracks that took place during the cyclic load cycles. Hence, this may not accurately represent the actual cracking load. Once the cracking load was reached, there was a slightly less steep slope which demonstrated a slight reduction in stiffness. Similar to slab 1, the cracking load of a monolithic conventional concrete was calculated as 11.1 kips. Again, the lower cracking load observed graphically is considerably less than that of a monolithic normal-strength concrete slab is potentially due to a cold joint between the conventional concrete and the UHPC. For part 1, there are enough data to show the returned deflection value of 0.055 in. when the slab specimen was unloaded.

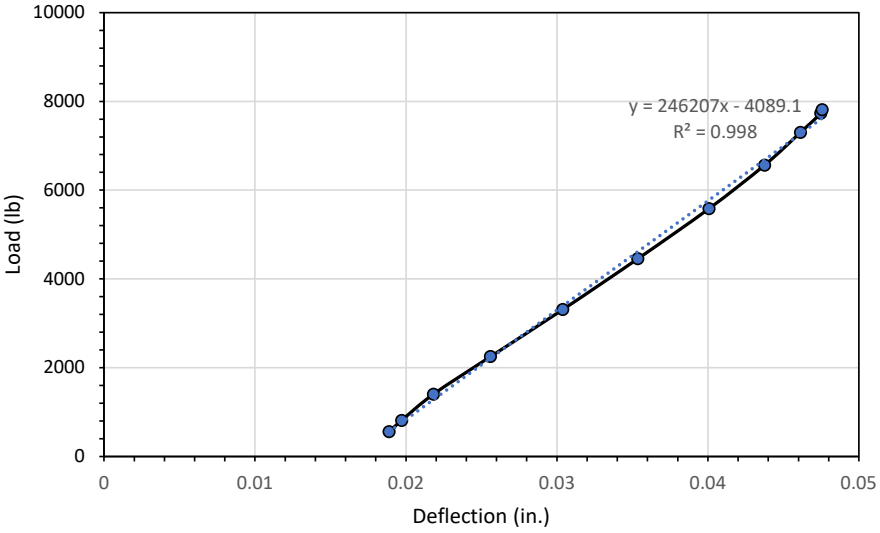

Figure 130. Load vs. deflection curve for J3 slab joint 2, single load cycle

The load vs. deflection curves for the part 1 tests of slabs 1 and 2 are shown together in Figure 132. Slab 1 has a shallower loading slope than slab 2. This may have been caused by different interaction between conventional concrete and the UHPC for the two slab specimens. There was not enough data to show the unloading slope for slab 1 for comparison of the residual deflections. The different slope could be attributed to the impact of cyclic loads on slab 2 before switching to static loads.

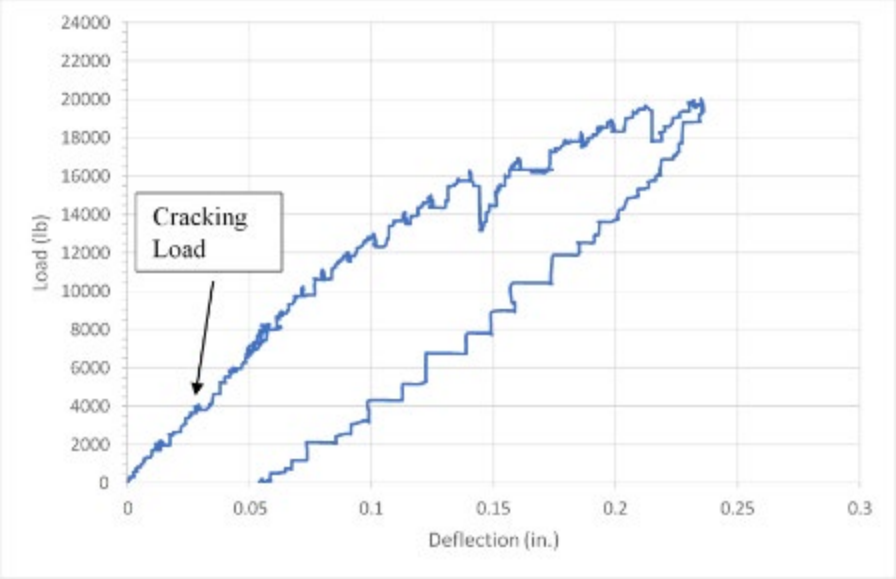

Figure 131. Load vs. deflection curve for J3 slab joint 2, part 1

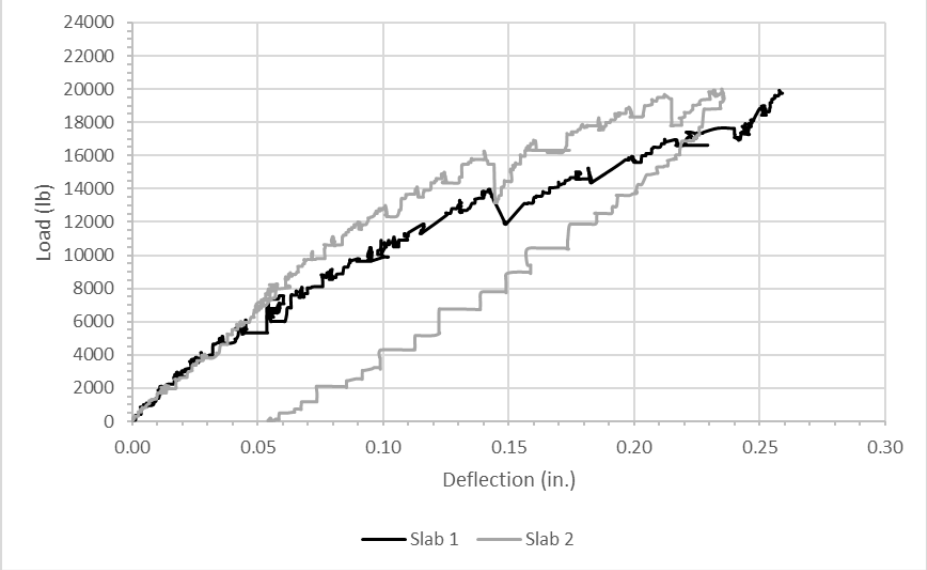

Figure 132. Load vs. deflection curve for J3 slabs 1 and 2, part 1

Figure 133 shows the load vs. deflection for J3 slab 2 part 2. Like J3 slab 1 part 2, the load was applied using a manual hydraulic pump instead of the MTS system. The calculated failure load for a monolithic normal-strength concrete slab is 27.3 kips, the same as for J3 slab 1. The ultimate load achieved for J3 slab 2 was approximately 32.5 kips. The actual failure load of J3 slab 2 exceeded the calculated failure load by 19%. The plateau visible on the load vs. deflection curve indicates that the steel reinforcement yielded and concrete crushing at the top of the slab indicated that the slab had failed.

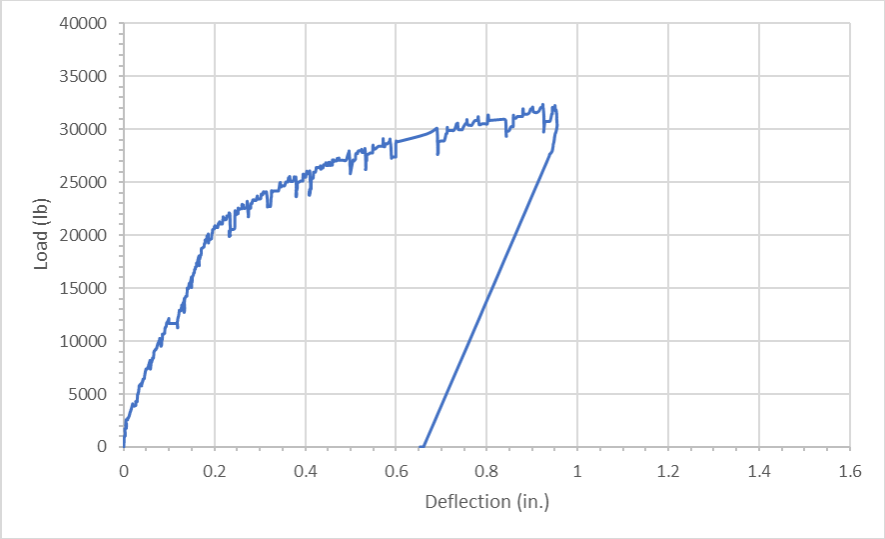

Figure 133. Load vs. deflection curve for J3 slab joint 2, part 2

Figure 134 shows a comparison of part 1 and part 2 of the load vs. deflection curves for J3 slab joint 2. The part 2 curve started at the residual deflection of the part 1 curve. The part 2 curve has a lower slope than part 1, which was the expected result since the slab was already cracked in part 1.

Similar to slab 1, multiple cracks appeared at the interface between the conventional concrete and UHPC. Some cracks also appeared in the conventional concrete. Figures 135 and 136 show cracks in the slab after failure for the north and south sides of the slabs. The majority of the cracks at failure appeared below the load point and there was a large separation between the conventional concrete and UHPC. A gap of approximately 0.25 in. was visible. Figure 137 shows concrete crushing at the top of the slab indicating failure.

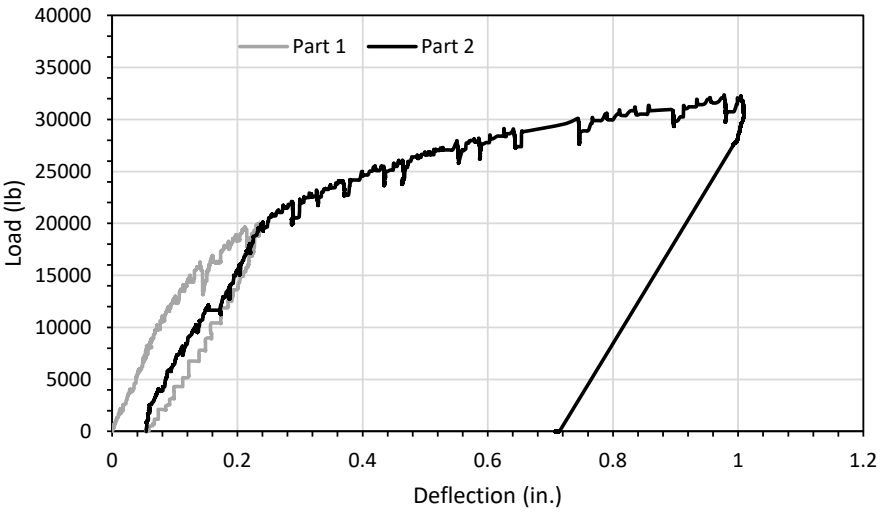

Figure 134. Load vs. deflection curves for J3 slab joint 2, parts 1 and 2

Figure 135. Cracks formed at the conventional concrete to UHPC interface on the north side of J3 slab joint 2

Figure 136. Cracks formed at the conventional concrete to UHPC interface and propagating upward on the south side of J3 slab joint 2

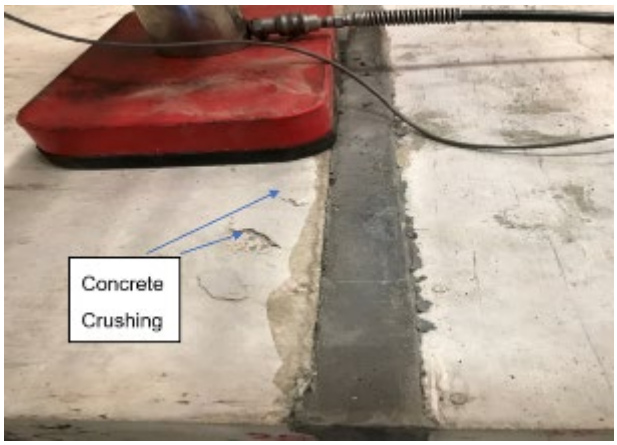

Figure 137. Concrete crushing at the top of the slab for J3 slab 2 at failure

5.5.3 Ductal® Slab Joint Static Test Results

The test for Ductal® slab joint 1 was performed using the manual hydraulic pump for parts 1 and 2. Part 1 of testing was completed when the hydraulic cylinder reached its maximum extended length. Before part 2 of testing was conducted, the hydraulic cylinder was adjusted to provide additional extended length. The first crack observed with the naked eye appeared at the intersection between the conventional concrete and UHPC at 6 kips. The graphical analysis of the load vs. deflection curve did not provide enough indication of where the crack appeared if the deflection range was set to 0 in. to 1.6 in., as in Figure 138. However, if the range of the load and deflection is set to the same as the J3 UHPC slab 1, part 1 curve, as shown in Figure 139, the cracking load appeared to be at 7.5 kips. Figure 140 shows the load vs. deflection for slab 1 part 1. As the 1-kip load increments were applied, the slab was examined for cracks using a flashlight and marker to label where the crack appeared. Once the cracking load was reached, the slope became less steep indicating a slight reduction in stiffness. The load corresponding to the cracking moment of a monolithic conventional concrete slab was calculated as 11.1 kips. This calculation assumed for a monolithic normal strength (4000 psi) concrete slab and was determined based on the span and loading configuration of the test specimen set up. The graphically calculated cracking load for this slab specimen is considerably less than that of a monolithic normal-strength concrete slab, which is potentially due to the presence of a cold joint between the conventional concrete and UHPC.

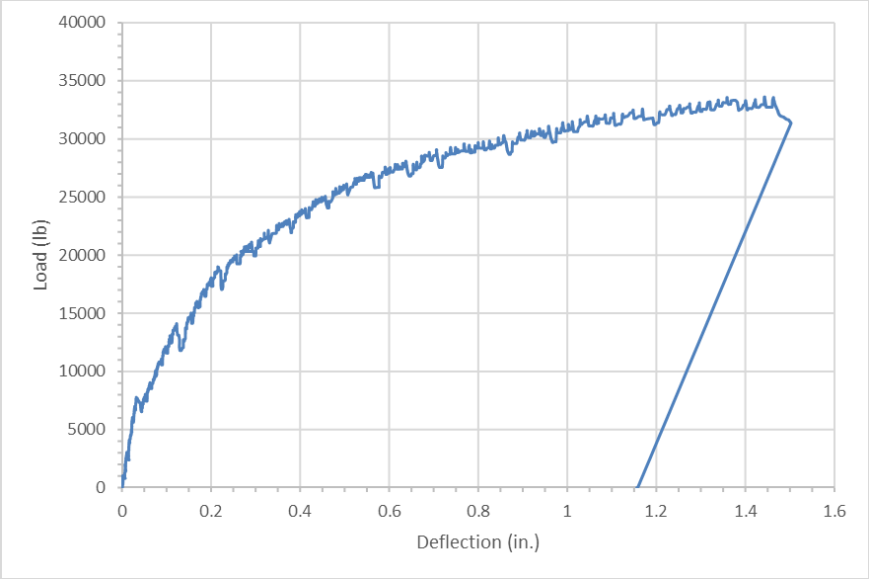

Figure 138. Load vs. deflection curve for Ductal® slab joint 1, part 1

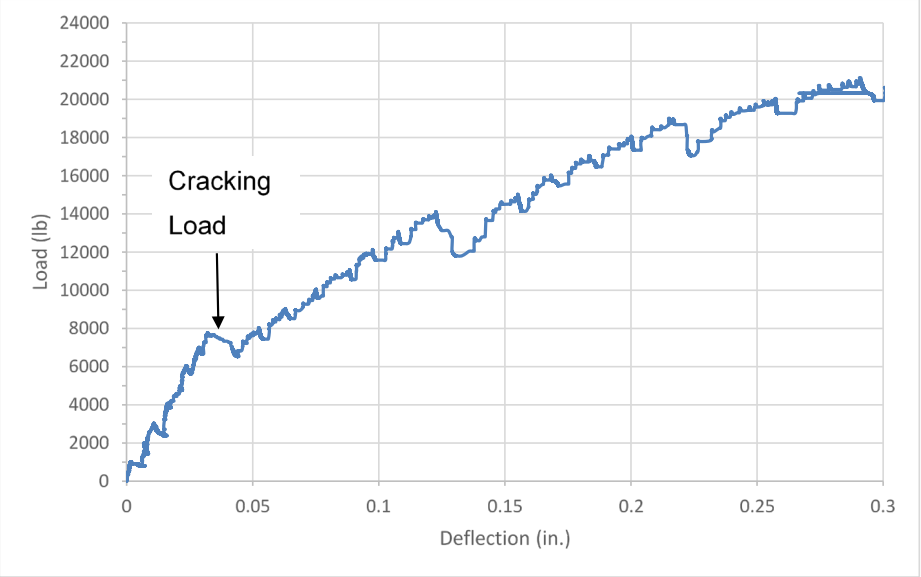

Figure 139. Load vs. deflection curve for Ductal® slab 1, part 1 after adjusting load and deflection range to the anticipated elastic portion

Figure 140 shows cracks after part 1 of testing where the maximum load was 33.3 kips. The primary cracks occurred at the interface between the conventional concrete and UHPC. The gap grew larger as higher loads were applied. Cracks started at the bottom of the slab and propagated toward the top of the slab. In addition, cracks appeared at 2.25 in. away from the interface.

Figure 140. Large cracks at the conventional concrete to UHPC interface after part 1 of testing for Ductal® slab joint 1

Figure 141 shows the load vs. deflection curve for part 2 of the Ductal® slab 1 testing. Similar to part 1, this testing was performed using a manual hydraulic pump. However, 3-kip load increments were applied instead of 1-kip load increments until the maximum load from part 1 was applied, and the slab was inspected for cracks between load increments using a flashlight and marker to label when and where the cracks appeared. The ultimate load for Ductal® slab 1, part 2 was approximately 35.8 kips. The maximum load from part 2 was 8% greater than the maximum load of part 1. For comparison, the calculated failure load for a monolithic normal-strength concrete slab was 27.3 kips. The actual failure load of the specimen exceeded the calculated failure load by 31%. The curve plateaued, which suggests yielding of the steel reinforcement within the joint. Failure was evident due to the concrete crushing at the top surface.

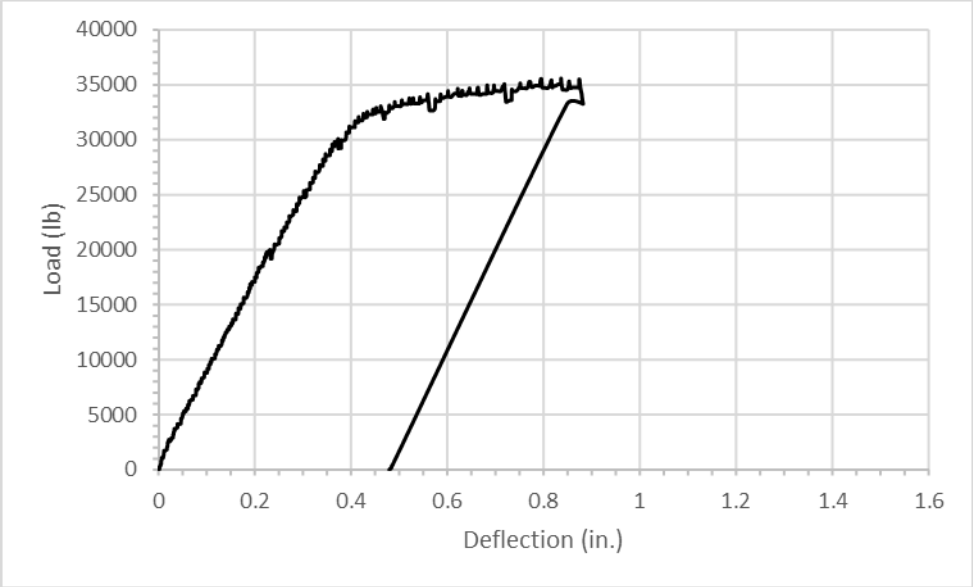

Figure 141. Load vs. deflection curve for Ductal® slab joint 1, part 2

Figure 142 shows a comparison of the part 1 and part 2 load vs. deflection curves for Ductal® slab 1. The part 2 curve started at the residual deflection of the part 1 curve. The part 2 curve has a lower slope than part 1 up until 20 kips. This was expected as the slab already cracked in part 1. From about 20 kips to 32 kips, it shows a much higher slope.

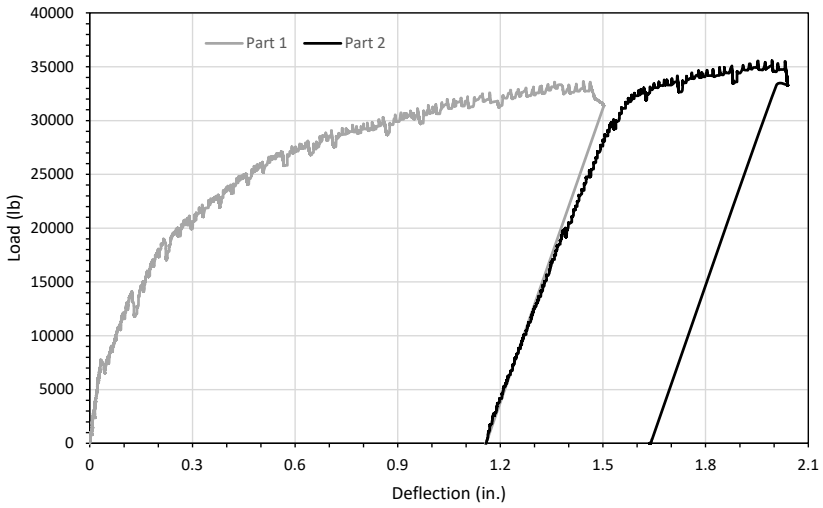

Figure 142. Load vs. deflection curve for Ductal® slab joint 1, part 1 and part 2

After the completion of part 2 of testing, more cracks were observed at the interface between the conventional concrete and UHPC. Additional cracks also

appeared in the conventional concrete. Figure 143 shows cracks on the north side of the slab after failure, on the as-tested underside of the slab, and concrete crushing on the as-tested top of the slab. The majority of the cracks at failure appeared below the load point. From the bottom surface of the slab, it was evident that cracks extended across the entire width of the slab at the interface and approximately 3 in. away from the interface as shown in Figure 144. Large separation between the conventional concrete and the UHPC joint was visible. Figure 145 shows concrete crushing at the top of the slab indicating failure.

Figure 143. Ductal® slab 1 after part 2 of testing

Figure 144. Cracks extending across the entire width of the slab at the joint and in the conventional concrete

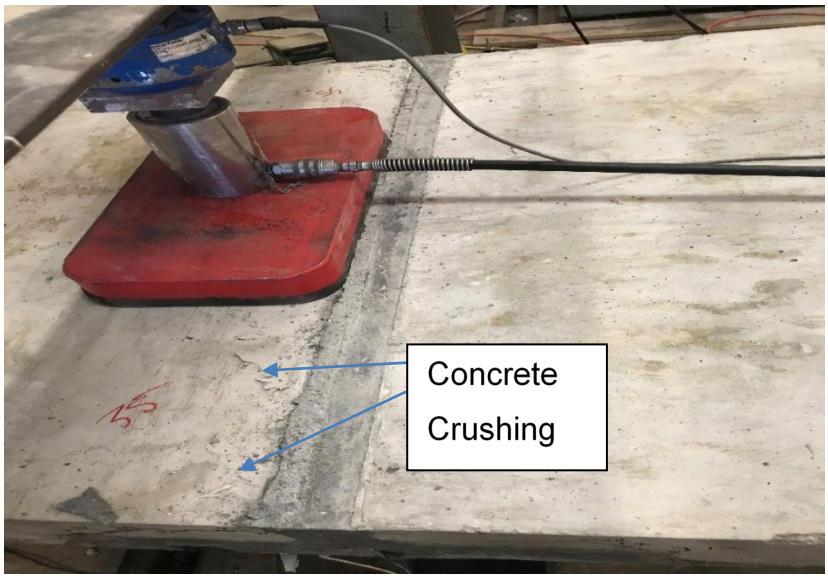

Figure 145. Concrete crushing at the top of Ductal® slab 1 indicating failure

Part 1 of Ductal® slab joint 2 testing was completed when the hydraulic cylinder reached its maximum extended length. The part 2 test was performed using the same manual hydraulic pump used for part 1. Load was applied in 1-kip increments and between increments a flashlight was used to observe cracks and a marker was used to mark out where cracks occurred and how they propagated. The first crack observed by the naked eye appeared at the intersection between the conventional concrete and UHPC at a load of 9 kips. The load vs. deflection curve was plotted to determine the cracking load. During testing, one wire pot fell off the slab at approximately 1.6 inches deflection causing error in measurement deflection. Hence, the data were neglected for deflection greater than 1.6 inches. By adjusting the range of the load and deflection, the cracking load appeared to be at 7 kips. Figures 146 and 147 show the load vs. deflection curve for Ductal® slab 2 part 1 before and after adjustment of the deflection range. The slope of the curve became less steep as more load was applied. This indicated that the stiffness of the slab had been reduced. The cracking load of a monolithic conventional concrete slab was determined to be 11.1 kips. The graphically calculated cracking load is 37% less than the calculated value.

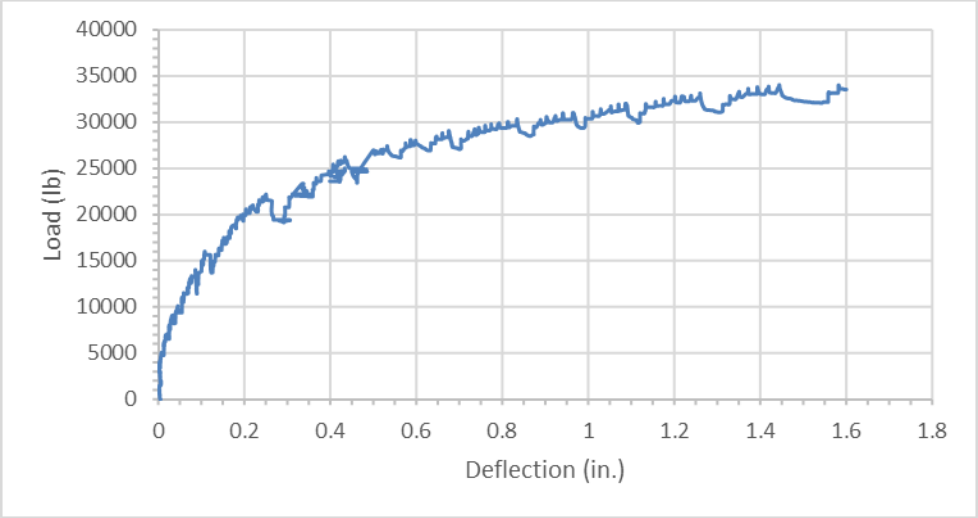

Figure 146. Load vs. deflection curve for Ductal® slab joint 2, part 1

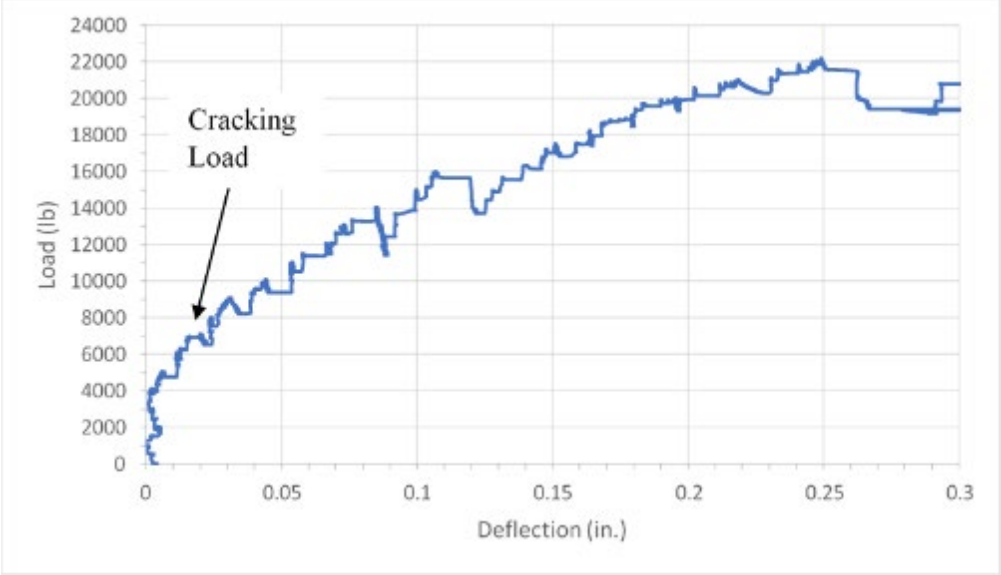

Figure 147. Load vs. deflection curve for Ductal® slab joint 2, part 1 after adjusting load and deflection range

Figures 148 and 149 show cracks after part 1 of testing on the north and south sides of the slab. Cracks occurred at the interface between the conventional concrete and UHPC and within the conventional concrete away from the joint. The gap between the UHPC and conventional concrete grew larger as higher loads were applied. All cracks started at the bottom of the slab and propagated toward the top of the slab while curving toward the load point.

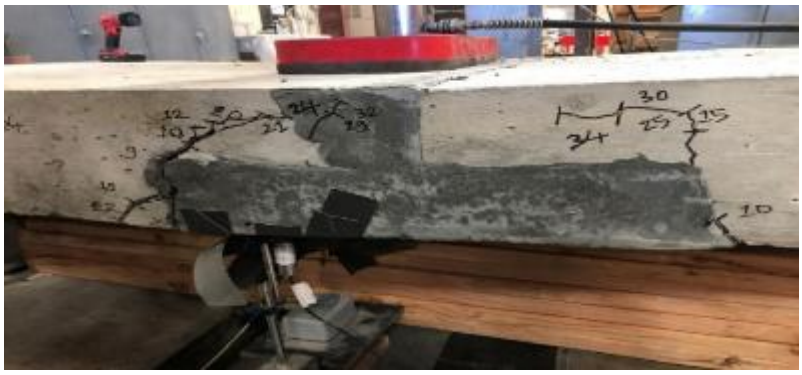

Figure 148. Cracks on the north side of Ductal® slab joint 2 after part 1 testing

Figure 149. Cracks on the south side of Ductal® slab joint 2 after part 1 testing

Figure 150 shows the load vs. deflection curve for part 2 of Ductal® slab 2 testing. Part 1 of testing was completed when the hydraulic cylinder reached its maximum extended length. Before part 2 of testing was conducted, the hydraulic cylinder was adjusted to provide additional extended length. Similar to part 1, this testing was performed using a manual hydraulic pump. However, larger load increments of approximately 3 kips were applied instead of 1-kip load increments because the slab was loaded almost to failure in part 1 and to substantially reduce testing time. The slab was inspected for cracks using a flashlight between load increments and a marker was used to label when and where the crack appeared. The ultimate load for Ductal® slab 2, part 2 was approximately 36 kips. In comparison, the calculated failure load for a monolithic normal-strength concrete slab was 27.3 kips. The actual failure load of the specimen exceeded the calculated failure load by 32%. The curve plateaued near the ultimate load and concrete crushing on the top surface indicated failure. There were not enough data to plot the unloading curve.

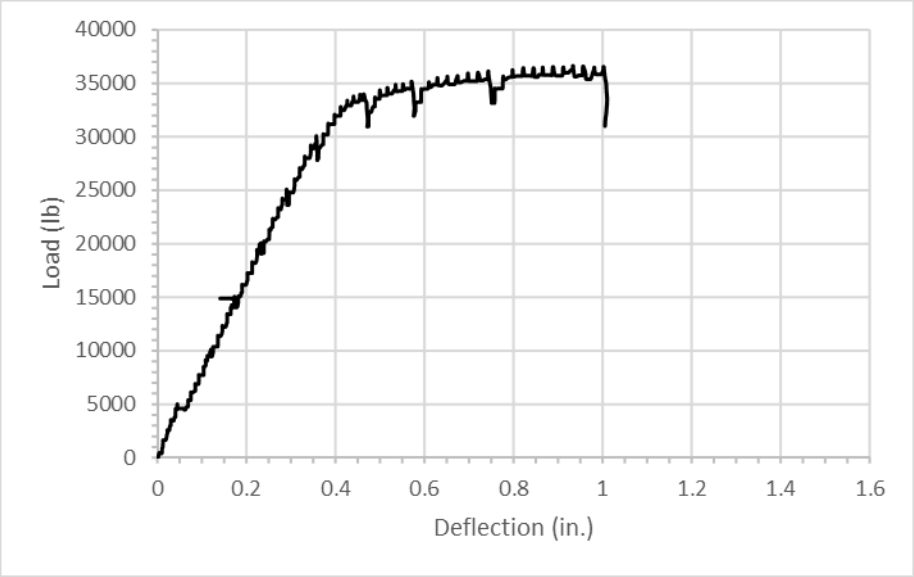

Figure 150. Load vs. deflection curve for Ductal® slab 2, part 2

Figure 151 shows a comparison for slab 2 by plotting the part 1 and part 2 load vs. deflection curves on the same graph. The part 2 curve started at the residual deflection of the part 1 curve. Because there was not enough data from the part 1 test to determine residual deflection, the starting point of the part 2 curve is based on the slope and pattern of both curves. The part 2 curve has a lower slope than part 1. This was expected as the slab already cracked in part 1.

Additional cracks were observed at the conventional concrete to UHPC interface during part 2 of testing. These cracks also propagated from the bottom of the slab to the top and curved toward the load point. Figures 152-154 show cracks on the slab after failure on the north side of the slab, cracks on the as-tested underside the slab, and concrete crushing on the as-tested top of the slab, respectively. The majority of the cracks occurred below the load point. There was significant separation between the conventional concrete and UHPC at the interface, which Figure 152 illustrates. Similar to previous static tests, concrete crushing at the top of the slab indicated that the slab failed.

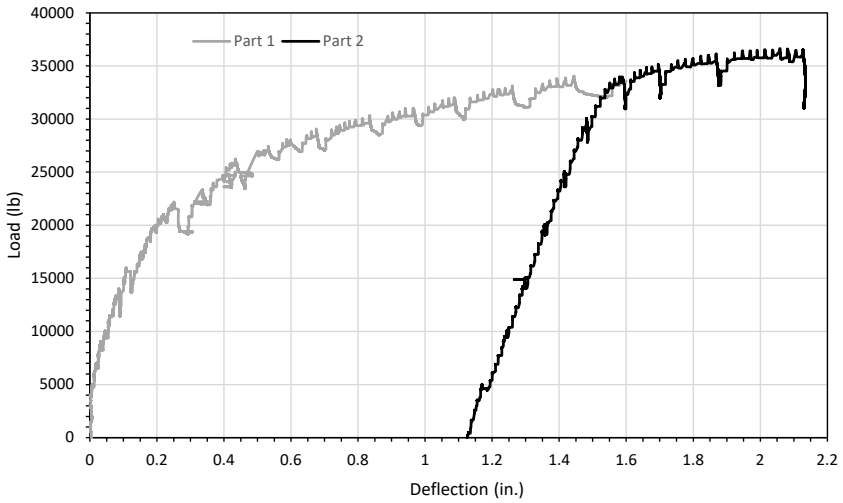

Figure 151. Load vs. deflection curve for Ductal® slab 2, part 1 and part 2

Figure 152. Cracks on the north side of Ductal® slab joint 2 after part 2 testing

Figure 153. Cracks on the as-tested underside of Ductal® slab joint 2 after testing

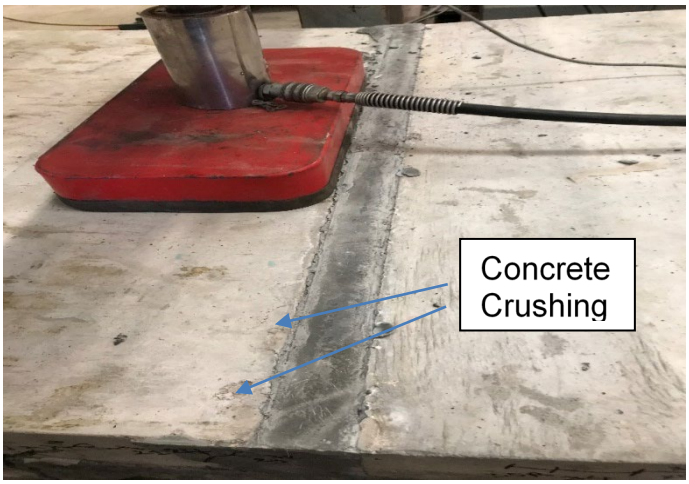

Figure 154. Concrete crushing at the top of the slab indicating failure

5.5.4 Comparison of J3 and Ductal® UHPC Slab Static Test Results

This section provides analysis and comparison between the J3 and Ductal® UHPC static test results. The focus will be on the comparison between part 1 of the slab 1 test for both UHPC's, and part 1 of the slab 2 test for both UHPCs. The same also applies for part 2 comparisons. Finally, part 1 curves of all slabs are plotted on the same graph, and the same procedure is applied to part 2.

Figure 155 shows the J3 UHPC and Ductal® UHPC slab 1, part 1 curves together on the same graph. Both curves had similar patterns, the main difference was the cracking load. The Ductal® slab had a higher stiffness and a cracking load of 7.5 kips, whereas the J3 slab had a cracking of load of 5.9 kips. Figure 156 shows the J3 UHPC and Ductal® UHPC slab 2, part 1 curves together on the same graph. Both curves possessed some similarity in pattern, but substantial difference in cracking load was apparent. This is primarily because the J3 slab 2 was tested cyclically with 397 cycles of load that caused cracking before the static load test was performed. The cracking load for the J3 slab 2 was approximately 4 kips. However, this may not have represented actual cracking load as the slab cracked during the cyclic testing. The cracking load for the Ductal® slab 2 was approximately 7 kips. The plot for J3 slab 2 did not include the unloading part to help compare behavior of the two slabs. Figure 157 shows part 1 curves for all four slabs plotted on the same graph. All the curves displayed similar patterns and excluded the unloading parts for comparison.

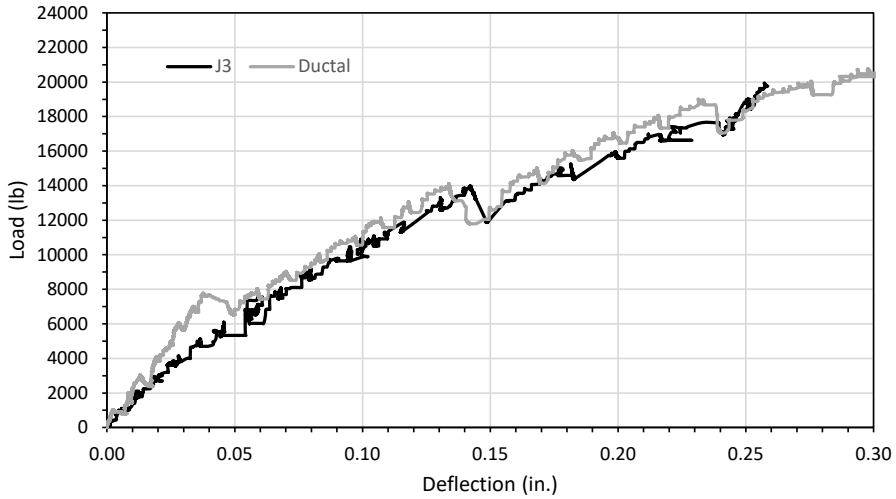

Figure 155. Load vs. deflection curves for J3 and Ductal® slab 1, part 1

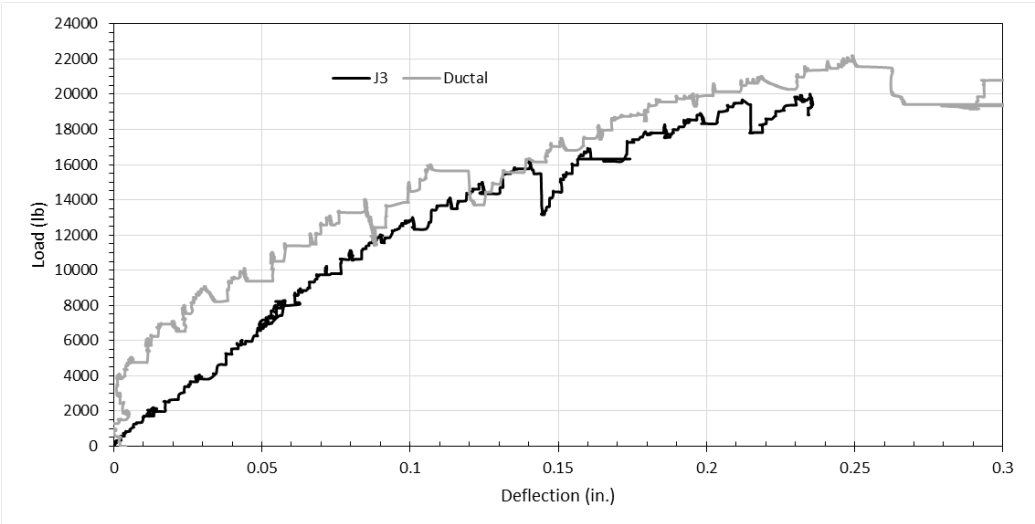

Figure 156. Load vs. deflection curves for J3 and Ductal® slab 2, part 1

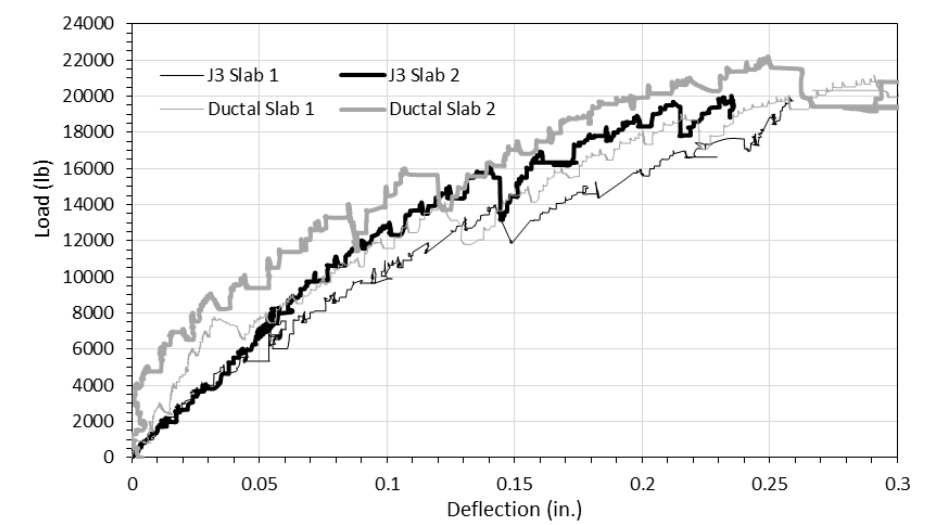

Figure157. Load vs. deflection curves for J3 and Ductal® part 1 static tests

Figure 158 shows the J3 UHPC and Ductal® UHPC slab 1, part 2 curves together on the same graph. The J3 slab had a higher stiffness compared to the Ductal® slab, but the Ductal® slab displayed a more linear behavior before yielding compared to J3. At the same deflection of approximately 0.9 in., the Ductal® slab had reached the ultimate load of approximately 35 kips compared to approximately 32 kips for the J3 slab. Figure 159 shows the J3 UHPC and Ductal® UHPC slab 2, part 2 curves together on the same graph. Both curves possess some similarity in pattern. The ultimate load for the Ductal® slab was approximately 36 kips, whereas the J3 slab had approximately 33 kips ultimate load. The plot for the Ductal® slab 2 did not include the unloading curve as there was not enough data to be analyzed. The overall stiffness that the Ductal® slabs reached a higher load at a smaller deflection because of the higher initial stiffness compared to J3 slabs. This is possibly because part 1 for the Ductal® slabs went to a significantly higher load. Therefore, the load vs. deflection curves for Ductal® slabs part 1 and J3 part 2 were plotted on the same graph for comparison. Figure 160 shows curves for Ductal® slabs part 1 and J3 part 2. All four curves show very similar patterns. Figure 161 shows the part 2 curves for all four slabs plotted on the same graph. All the curves displayed similar patterns and excluded the unloaded parts for comparison.

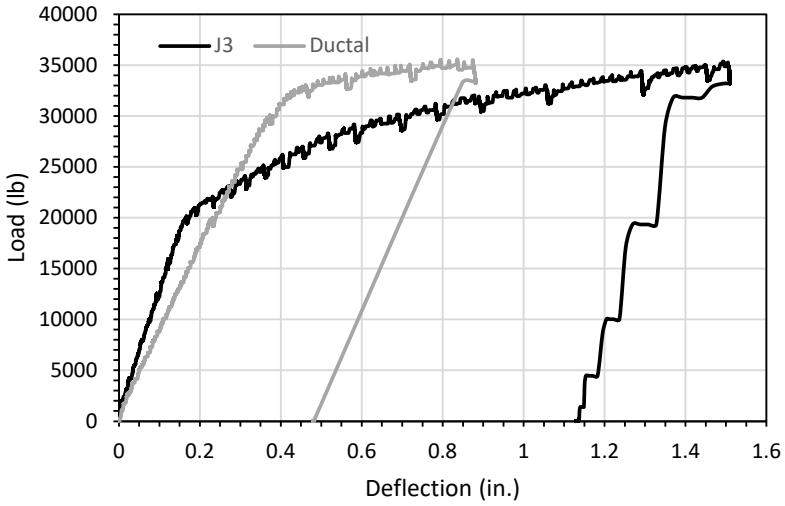

Figure 158. Load vs. deflection curves for J3 and Ductal® slab 1, part 2

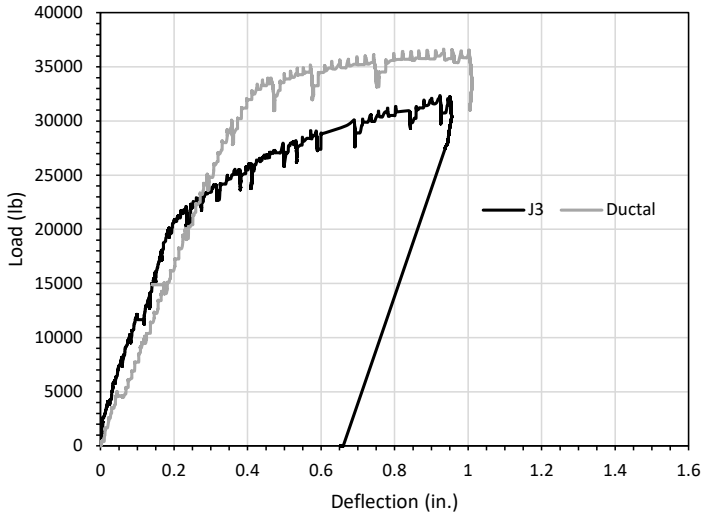

Figure 159. Load vs. deflection curves for J3 and Ductal® slab 2, part 2

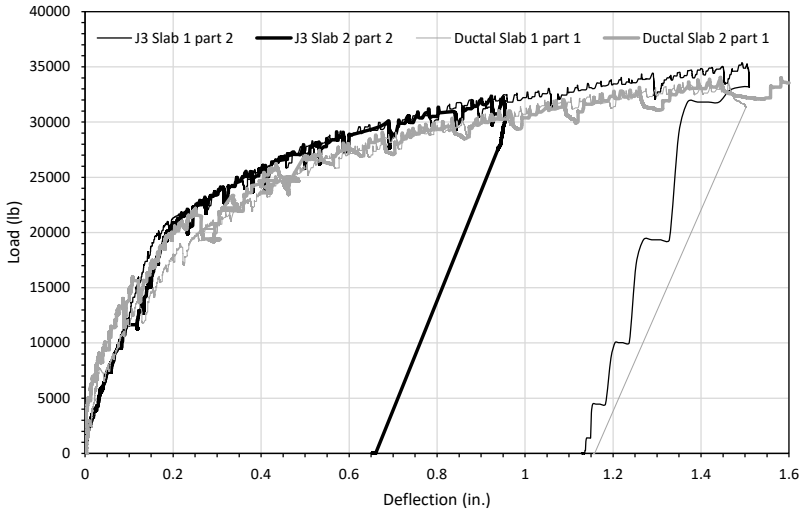

Figure 160. Load vs. deflection curves for J3 part 2 and Ductal® part 1

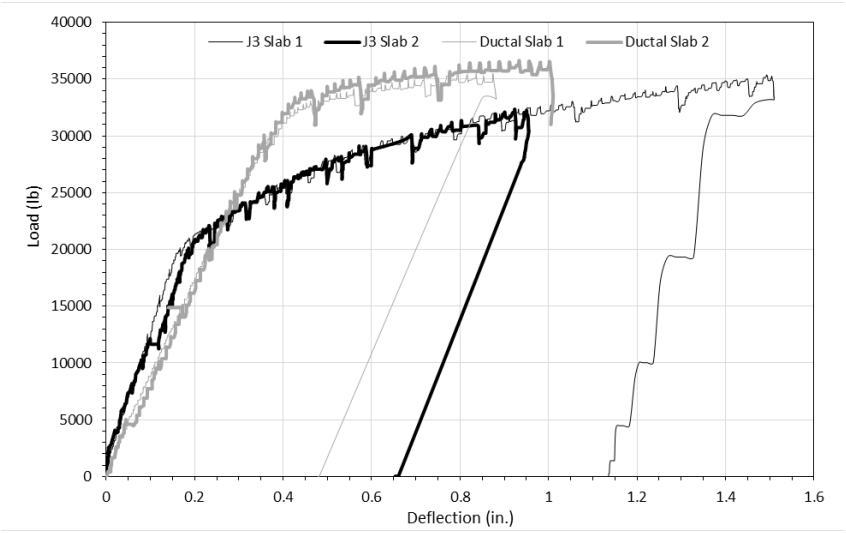

Figure 161. Load vs. deflection curves for J3 and Ductal® slab static tests, part 2

5.5.5 J3 Slab Joint 3 Cyclic Test Results

J3 Slab 3 was tested cyclically under fatigue loading. For the first 3 million cycles, the slab was to be loaded cyclically to a maximum value of 90% of the cracking load. The cracking load for J3 slab 1 was determined to be 5.9 kips. The cracking load for J3 slab 2 was lower due to having been initially tested cyclically. Therefore, the maximum value of the cyclic load for the slab was chosen to be 90% of 5.9 kips. In addition, the cracking loads determined from Ductal® slab 1 and slab 2 were more than the 5.9 kips determined for J3 slab 1. Therefore, a maximum load of 5.3 kips was applied for cyclic

loading of the J3 and Ductal® slabs. Using the MTS system, a 1 hertz cyclic load was applied to J3 slab 3 with a maximum value of 5.3 kips. Approximately 86,400 cycles were run each day. Figure 162 depicts a typical cyclic loading over a period of 10 seconds. A 500-pound preload was set to prevent the load from coming up off the slab, so the curves did not begin at zero. This preload is not intended to represent moments of the dead load of the bridge deck. The stiffness of the slab could be determined from the slope in the equation shown on the graph. The slope generally decreased throughout the first 3 million cycles. The reason the stiffness gradually decreased over time is due to additional cracking and fatigue. Figure 163 shows load cycles from different days for comparison. The unloading portion of the curves are not displayed but were similar to the loading portion. On certain days such as days 23 and 25, there were negative deflections. This may have been caused by the correction made with the support deflections. There was possibly more support deflection than slab deflection.

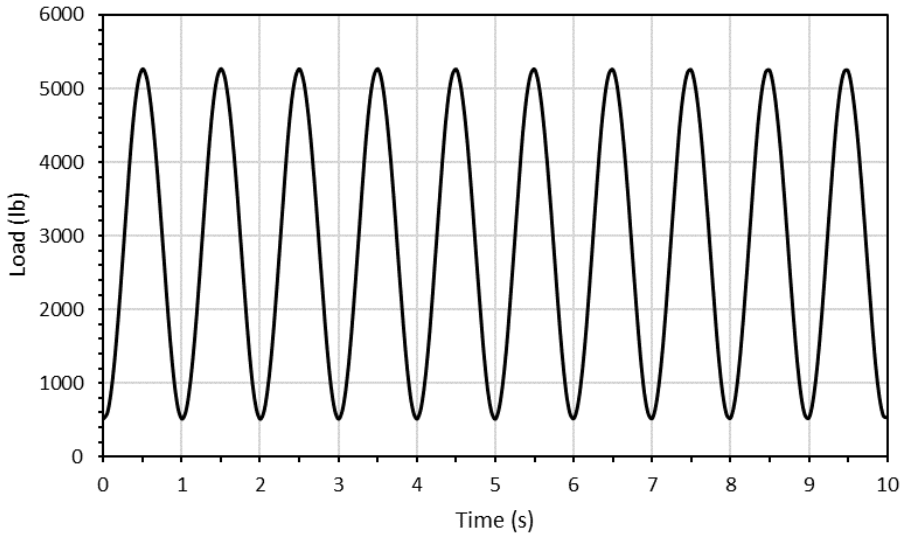

Figure 162. Typical cyclic loading over a period of 10 seconds

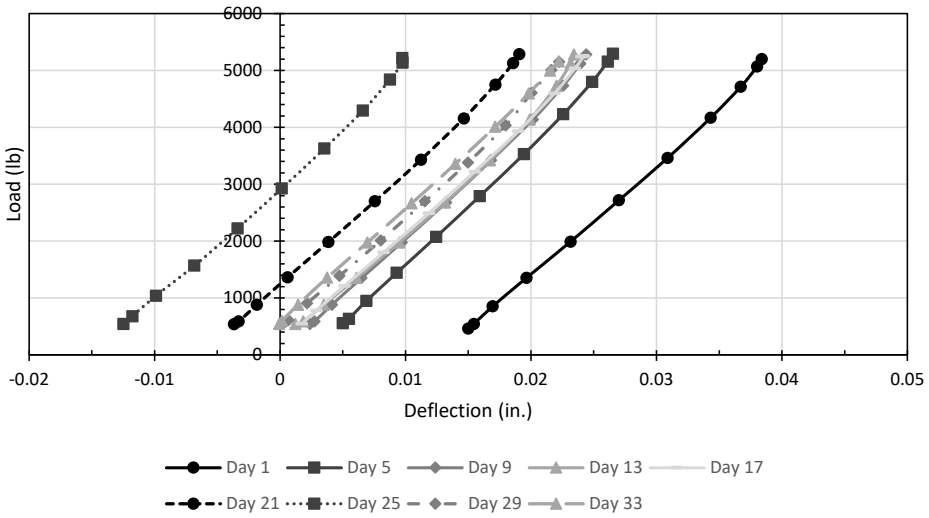

Figure 163. Comparison of load vs. deflection curves for J3 slab 3 for multiple days

After the specimen had been subjected to 3 million load cycles, the load was increased to 6.5 kips and applied cyclically with a frequency of 1 hertz. This was 10% more than the expected cracking load. The test program demanded for the specimen to be loaded at this rate for 2 million cycles more, or until failure, which is triggered if the slab had excessive deflection (beyond 1.5 in.) or if the reinforcement failed due to fatigue. Figure 164 shows multiple cycles from different days after maximum cyclic load was increased to 6.5 kips for comparison. Data did not overlap but they display very similar slopes. On certain days such as days 36 and 38, there were negative deflections. This may have been caused by the correction made with the support deflections. There was possibly more support deflection than slab deflection.

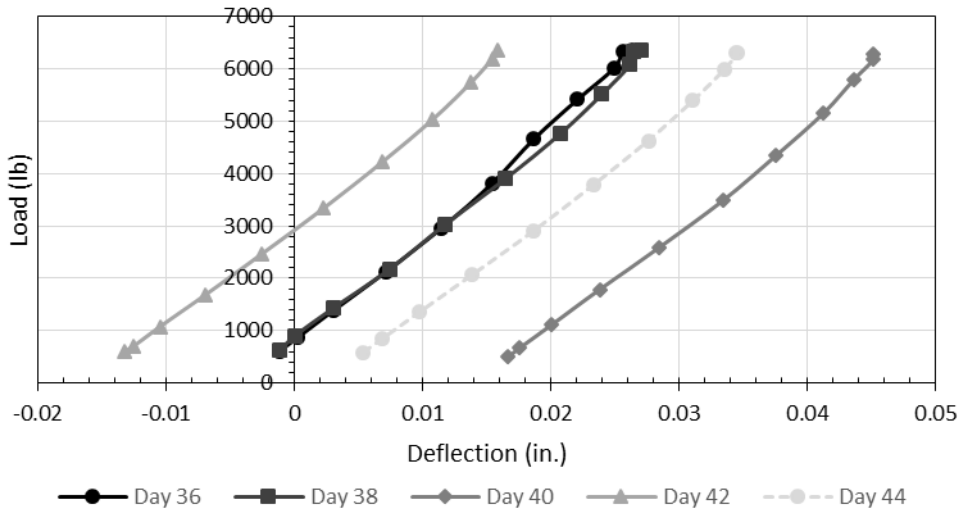

Figure 164. Comparison of load vs. deflection curves for J3 slab 3 for multiple days after maximum cyclic load was increased to 6.5 kips

The slab was cyclically loaded for 850,950 cycles but it did not deflect enough to consider failure and the reinforcing steel did not fail in fatigue. The decision was made to increase to maximum load to 8.7 kips and cyclically loaded a further 1,149,050 cycles or until failure. The 8.7 kips maximum load was loosely based on the maximum load for the cyclic testing for the full-depth slabs even though it was slightly less than the 9-kip maximum load from that previous research. The test was run for 473,425 cycles with the 8.7 kips load. Figure 165 shows multiple cycles from different days for comparison. All those data overlap each other indicating that the stiffness did not decrease much during period. The curves looked non-linear compared to curves plotted in the first 35 days. There were also negative deflections that may have been caused by the correction made with the support deflections if there was more support deflection than slab deflection.

Figure 166 shows the slab stiffness vs. time for the 50-day period of cyclic testing. There was a general steady decrease in stiffness over time. From day 2 to day 35, the trend was generally very similar. However, the stiffness decreased by approximately 12.8% between day 35 and 46. The maximum cyclic load was increased on day 36 from 5.3 kips to 6.5 kips. The subsequent days, the trend was similar again starting from day 37-45 and from day 46-50. Day 46 was when the maximum cyclic load was increased from 6.5 kips to 8.7 kips.

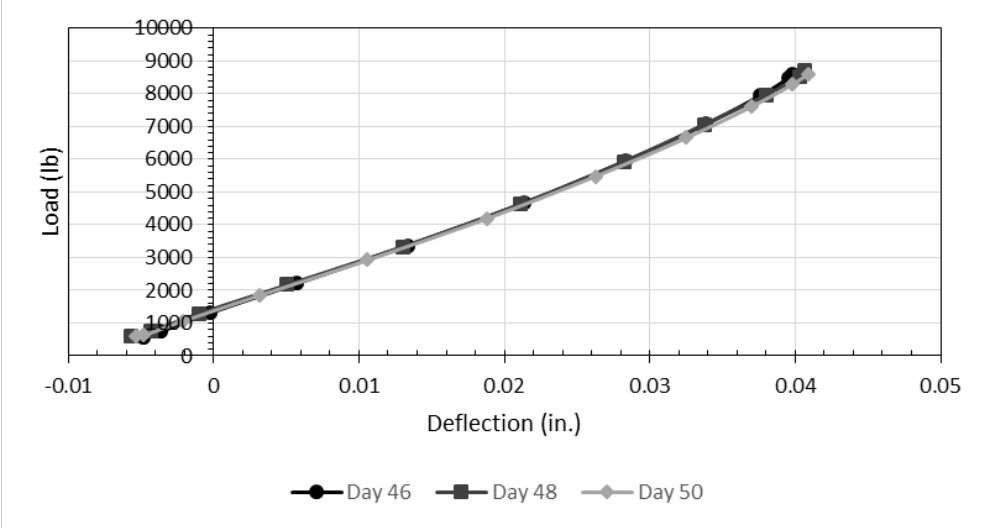

Figure 165. Comparison of load vs. deflection curves for J3 slab 3 for multiple days after maximum cyclic load was increased to 8.7 kips

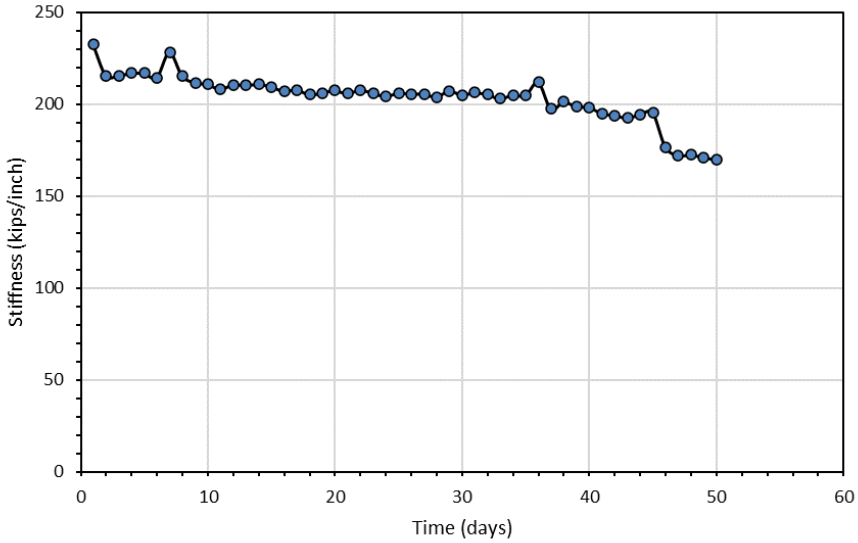

Figure 166. J3 slab 3 stiffness over 50-day loading period

5.5.6 Ductal® Slab Joint 3 Cyclic Test Results

The cyclic test for Ductal® slab 3 essentially followed the same procedure as the cyclic test for J3 slab 3. Ductal® slab 3 was tested cyclically for 3 million cycles with the maximum load of 5.3 kips. Using the MTS system, a 1 hertz cyclic load was applied to Ductal® slab 3 with a maximum load of 5.3 kips. Figure 167 shows multiple load cycles from different days for comparison. The unloading portion of the curves were not displayed but was similar to the loading portion. A 500-pound preload was set similar to

the J3 slab, which resulted in the plots not starting at zero. Figure 168 shows the stiffness vs. time plot for the 35 days period of cyclic testing. There was a general steady decrease in stiffness over time.

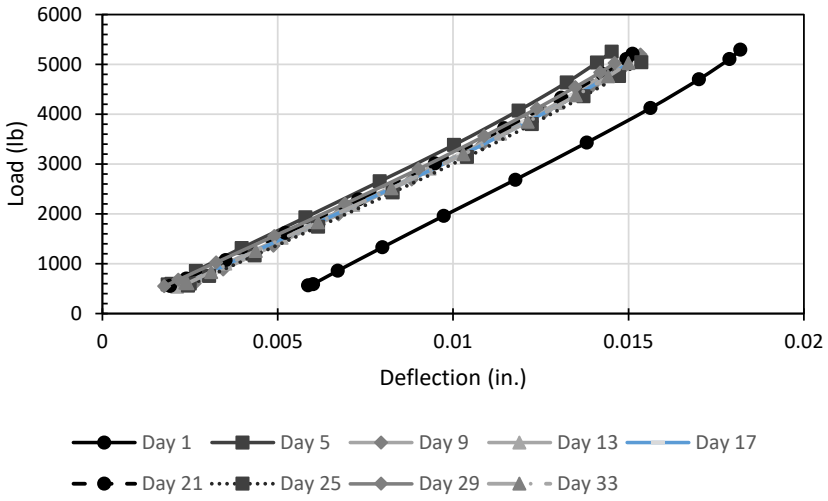

Figure 167. Comparison of load vs. deflection curves for Ductal® slab 3 for multiple days

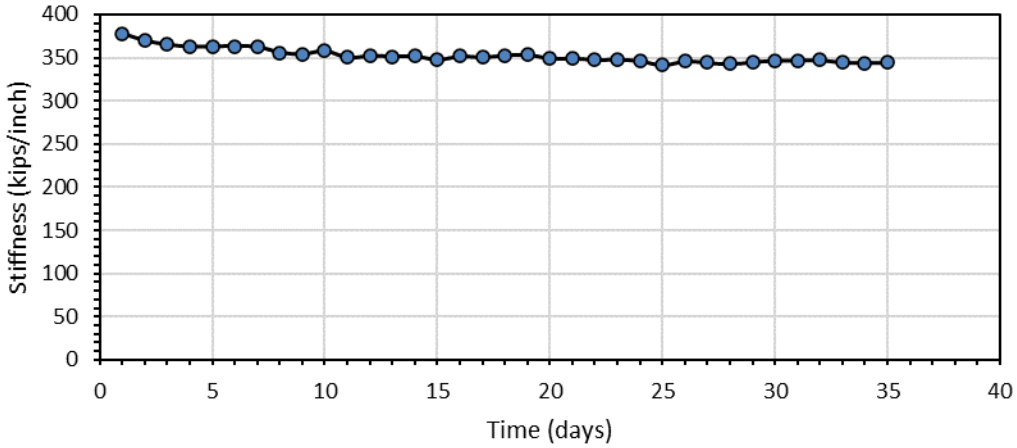

Figure 168. Ductal® slab 3 stiffness over the 35-day loading period

5.5.7 Comparison of Slabs 1, 2, and 3

Figure 169 shows the J3 UHPC load vs. deflection for the initial loading from the static tests of slabs 1 and 2 and one cyclic load from slab 3. The slab 3 curve has a steeper slope compared to slabs 1 and 2. Slabs 1 and 2 have very similar slope, which demonstrates that they have similar flexural behavior. Slab 3 has a slightly steeper

slope than slabs 1 and 2, but the trends of all three slabs are similar. Figure 170 shows the Ductal® UHPC load vs. deflection for the initial loading from the static tests of slabs 1 and 2 and one cyclic load from slab 3. Slab 3 has steeper slope compared to slabs 1 and 2. Slabs 1 and 2 have very similar slopes, which demonstrates that they have similar flexural behavior. The slab 3 curve is sandwiched between slabs 1 and 2, but the trends for all three slabs are similar.

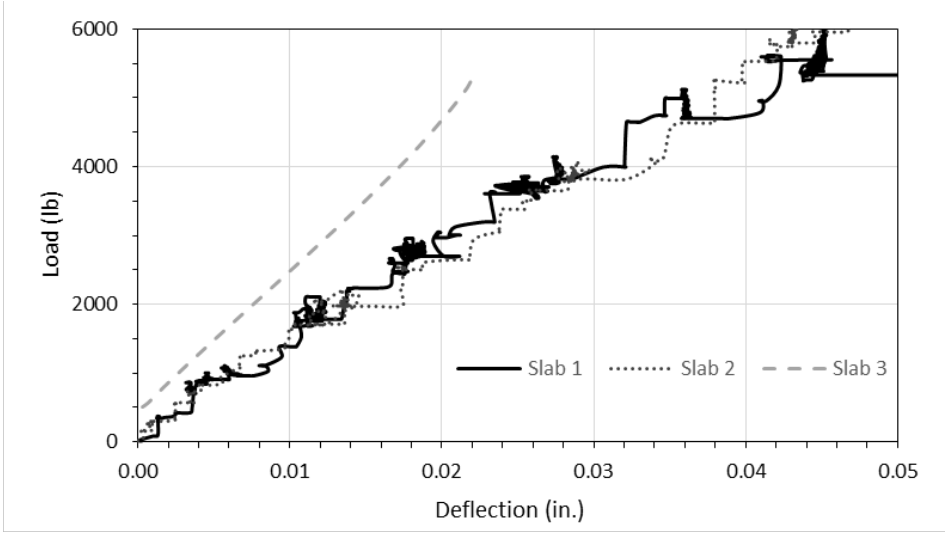

Figure 169. Load vs. deflection curves for initial portion of loading for the J3 slab joints

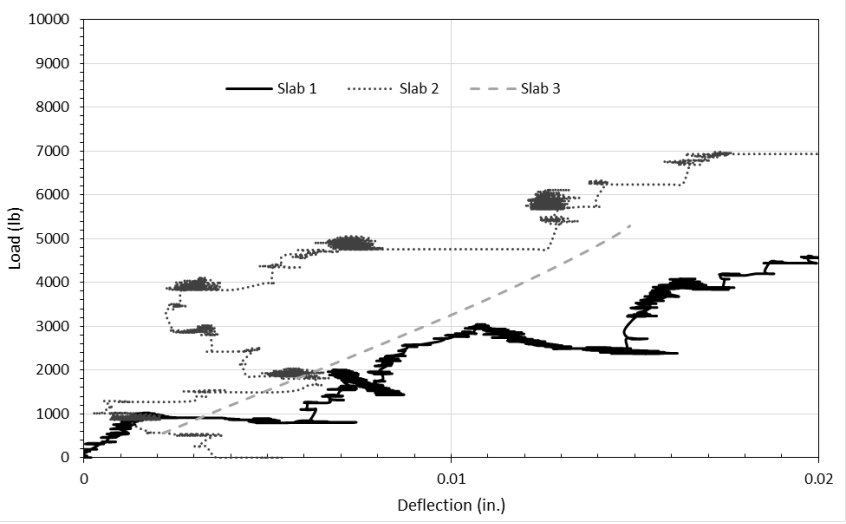

Figure 170. Load vs. deflection curve for initial portion of loading for the Ductal® slab joints

5.6 Comparison of Full-Depth and Half-Depth Slab Joint Results

Table 33 shows a comparison of cracking and ultimate loads between half-depth and full-depth J3 slab joints. The cracking load for slab 2 in both cases are less than values for slab 1, however slabs 1 and 2 for each material share the same design and construction. For the half-depth joint, slab 2 may have cracked due to applying cyclic load before switching to static load. For the full-depth joints, slab 2 was inaccurately loaded initially as it was mistakenly loaded constantly instead of being loaded in 1-kip increments. The cracking load for the half-depth joints is approximately half that of full-depth joints. The larger cracking load for the full-depth joints could be attributed to greater volume of UHPC providing additional strength along with the smaller total interface between the conventional concrete and UHPC. The ultimate load for slab 1 has similar values. For slab 2, the half-depth joint has 7% more ultimate load than the full-depth joint, which may have been caused by inaccurate loading on the slab 2 full-depth joint. However, the average ultimate load for the half-depth J3 joints (33.8 kips) is only 4% greater than ultimate load of full-depth J3 joints (32.3 kips).

Table 33. Comparison of cracking and ultimate loads (kips) between half-depth and full depth J3 joints

Value	Half-depth J3 Joints	Full-depth J3 Joints
Slab 1 Cracking Load	5.9	10.5
Slab 2 Cracking Load	4.0	8.2
Average Cracking Load	5.0	9.4
Slab 1 Ultimate Load	35.0	34.3
Slab 2 Ultimate Load	32.5	30.3
Average Ultimate Load	33.8	32.3

Table 34 shows a comparison of cracking and flexural moments between the half-depth and full-depth J3 joints since the span length of the half-depth and full-depth tests differed slightly. The average cracking moment for the full-depth J3 joints (19.0 kip-ft) is 53% greater than the average cracking moment for the half-depth J3 joints (8.9 kip-ft). The average maximum flexural moment for the full-depth J3 joints (65.4 kip-ft) is 7% greater than the average maximum moment for the half-depth J3 joints (60.6 kip-ft).

Table 34. Comparison of cracking and flexural moments (kip-ft) between half-depth and full depth J3 joints

Value	Half-depth J3 Joints	Full-depth J3 Joints
Slab 1 Cracking Moment	10.6	21.3
Slab 2 Cracking Moment	7.2	16.6
Average Cracking Moment	8.9	19.0
Slab 1 Flexural Moment	62.8	69.5
Slab 2 Flexural Moment	58.3	61.4
Average Flexural Moment	60.6	65.4

Table 35 shows a comparison between the half-depth and full-depth Ductal® joints. The cracking loads for the half-depth joints are greater than half of the cracking loads of the full-depth joints. The larger cracking load for the full-depth joints could be attributed to greater volume of UHPC providing additional strength and the smaller total area of interface between the conventional concrete and the UHPC. There is not much difference in the ultimate loads for both cases. The average ultimate load of the half-depth Ductal® joints (35.9 kips) is only 2% less than ultimate load of the full-depth Ductal® joints (36.7 kips).

Table 35. Comparison of cracking and ultimate loads (kips) between half-depth and full depth Ductal® joints

Value	Half-depth Ductal® Joints	Full-depth Ductal® Joints
Slab 1 Cracking Load	7.5	10.9
Slab 2 Cracking Load	7.0	13.1
Average Cracking Load	7.3	12.0
Slab 1 Ultimate Load	35.8	36.2
Slab 2 Ultimate Load	36.0	37.2
Average Ultimate Load	35.9	36.7

Table 36 shows a comparison of cracking and flexural moments between the half-depth and full-depth Ductal® joints since the span length of the half-depth and full-depth tests differed slightly. The average cracking moment for the full-depth Ductal® joints (24.3 kip-ft) is 46% greater than average cracking moment for the half-depth Ductal® joints (13.1 kip-ft). The average flexural moment for the full-depth Ductal®

joints (74.4 kip-ft) is 13% greater than ultimate moment of half-depth Ductal® joints (64.4 kip-ft).

From Tables 33 and 35, the ultimate load of the half-depth J3 joints can be compared to that of half-depth Ductal® joints. The average ultimate load of the half-depth J3 joints (33.8 kips) is only 6% less than ultimate load of half-depth Ductal® joints (35.9 kips). From Tables 34 and 36, the ultimate flexural moment of the half-depth J3 joints can be compared to that of half-depth Ductal® joints. The average ultimate flexural moment of the half-depth J3 joints (60.6 kip-ft) is only 6% less than ultimate moment of the half-depth Ductal® joints (64.4 kip-ft). Overall, the cracking moment for the half-depth joints is approximately half that of full-depth joints and the ultimate load is 5% to 10% less for the half-depth joints than for the full-depth joints.

Table 36. Comparison of cracking and flexural moments (kip-ft) between half-depth and full depth Ductal® joints

Value	Half-depth Ductal® Joints	Full-depth Ductal® Joints
Slab 1 Cracking Moment	13.5	22.1
Slab 2 Cracking Moment	12.6	26.5
Average Cracking Moment	13.1	24.3
Slab 1 Flexural Moment	64.2	73.3
Slab 2 Flexural Moment	64.6	75.4
Average Flexural Moment	64.4	74.4

6.0 Continuity Joint Testing

6.1 Overview

Six continuity specimens were cast by connecting two precast, prestressed concrete beams end to end using one of two UHPC joint details, one intended to represent new construction and one intended to represent a retrofit bridge. These specimens were tested statically in the elastic range and to failure. Continuity joint details used in practice and in previous research, including information provided by ODOT, were investigated to identify potential joint details for use in testing and the joints were designed using the AASHTO LRFD Specifications (2017) requirements for conventional concrete. More detail on the continuity joint testing can be found in Casey (2019).

6.2 Beam and Joint Design and Construction

The beam design for this this task was based on the approximately ½ scale AASHTO Type II girder specimens constructed as part previous research at Fears Lab (Mayhorn 2016; Murray 2018) The prestressing arrangement was modified from what was used in the previous project to move the strands closer to the bottom of the specimen to more realistically represent actual beam specimens. The strand type selected was based on readily available 0.5 in. special grade 270 low relaxation strands. The design also required mild steel to be placed in the top portion of the girder to resist tension stress caused by the prestressing force applied to the beam. Shear reinforcement design was based on previous students' work with the same type of geometry (Mayhorn 2016, Murray 2018). The beam design is shown in Figures 171 and 172.

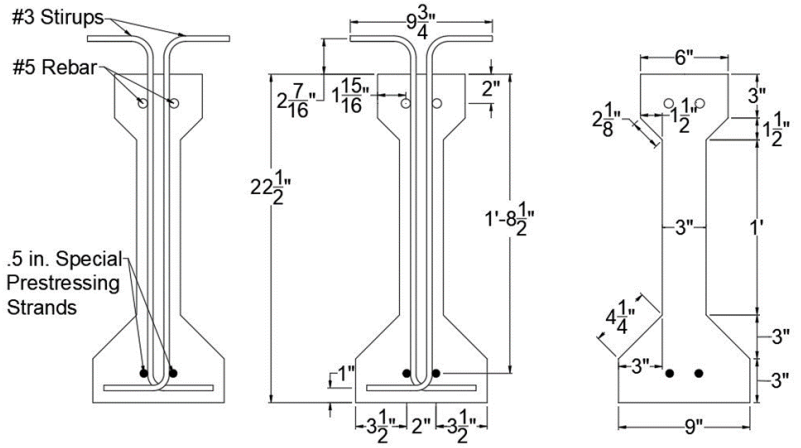

Figure 171. Prestressed beam specimen cross-section view

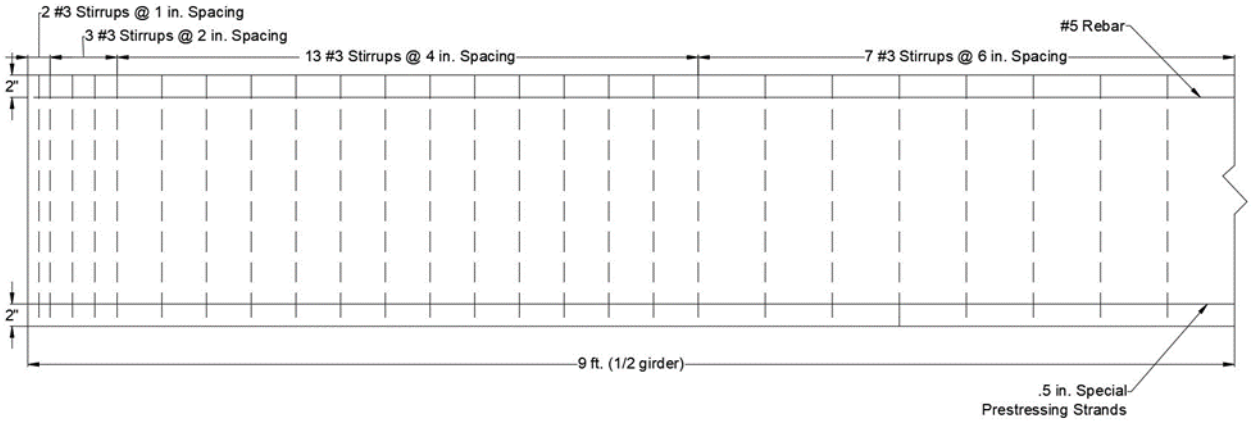

Figure 172. Prestressed beam specimen elevation view showing shear reinforcement

Twelve prestressed beam specimens were cast in sets of two specimens using the prestressing bed available at Fears Lab. The concrete mix design used for the base concrete is shown in Table 37. A minimum compressive strength at 1 day of 4 ksi, and a minimum 28-day strength of 6 ksi were required for the concrete mix design. The minimum compressive strength of 4 ksi at 24 hours was required for release of the prestressing strands. The fresh property tests conducted were the slump, air content, and temperature with a target slump of 6 in., and target air content of 2 percent. Completed formwork for a specimen set is shown in Figure 173 and the completed beams in Figure 174. Prestress release was conducted at one day of age and enough strand was left exposed at the end of each specimen to provide adequate anchorage into the proposed joint details. All beams were placed in the Fears Lab high bay for curing until placement of the composite deck section.

Table 37. Mix design per yd^3 at saturated surface dry used in prestressed girders

Material	Weight (lb/yd^3)
Cement	750
Sand	1250
Rock	1850
Water	248
w/c	0.33

Figure 173. Prestressed beam formwork immediately before casting

Figure 174. Completed set of two prestressed beam specimens

A composite deck section was designed with a width slightly larger than the beam top flange to provide the required reinforcing bars in the joint and flexural capacity at mid-span. The design of the composite concrete deck involved scaling down the geometric dimensions from a full-scale bridge to half-scale. The same bridge system considered in previous research (Murray 2017) was used as the considered case. The geometric dimensions of the full-scale tributary width over a typical beam line used was 96 in., which was scaled down to 46 in. for half-scale. The concrete deck depth at full scale was 8 in., which was scaled down to 4 in. for half-scale. The tributary width at half-scale presented some problems for construction due to restrictions in a lab setting. The restrictions include limited space for staging specimens and the amount of construction time required to build the formwork. Considering these restrictions, the tributary width was reduced by optimizing the depth of the deck relative to the tributary width. This was done by using the calculated moment capacity of the half-scale prestressed concrete beam with the half-scale concrete composite deck attached to determine the required depth to get a matching moment capacity from the half-scale beam and reduced deck width. This allowed a large reduction in the tributary width, from 46 in. to 9 in., with only a small increase to the depth of the deck, from 4 in. to 4.625 in. No flexural, temperature, or shrinkage steel was designed for the composite deck to prevent congestion from the shear steel hooks and the negative moment reinforcement for the joints due to the smaller dimensions of the revised composite deck. The final dimensions of the composite deck are shown in Figure 175.

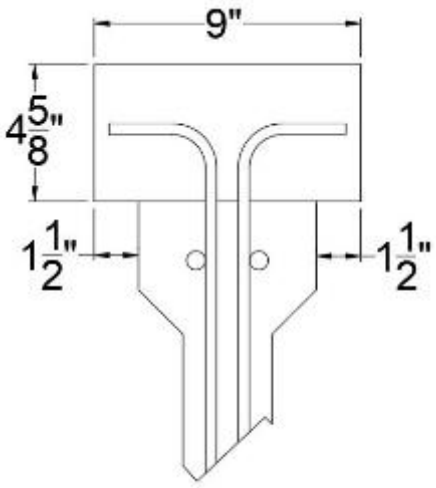

Figure 175. Composite deck dimensions

Two different joint details were designed intended to represent new construction and a retrofit joint. Designs were based on the AASHTO LRFD Bridge Design Specifications (2014), previous research, and previous ODOT practice. All joints were designed to transfer the expected negative moment required for full girder capacity in the two-span configuration, 1.2 times the cracking moment (M_{cr}) for positive moment, and all splices were designed based on the short development lengths required for UHPC. The design of the positive moment region of the continuity joint was based on AASHTO LRFD 5.14.1.4.9a. This section allows the use of section 5.14.1.4.4 to determine the magnitude of positive moment for the steel reinforcement design. Section 5.14.1.4.4 specifies a minimum precast girder age of 90 days before establishing continuity to allow restraint moments caused by creep and shrinkage to be taken as zero. The section then allows the use of M_{cr} with a factor of 1.2 for the design positive moment value. The reinforcement within the joint for the specimens representing new construction consisted of No. 5 reinforcing bars extending from each beam slab across the joint, bent up prestressing strands and two No. 3 reinforcing bars with standard hooks extending into the joint (Figures 176-180).

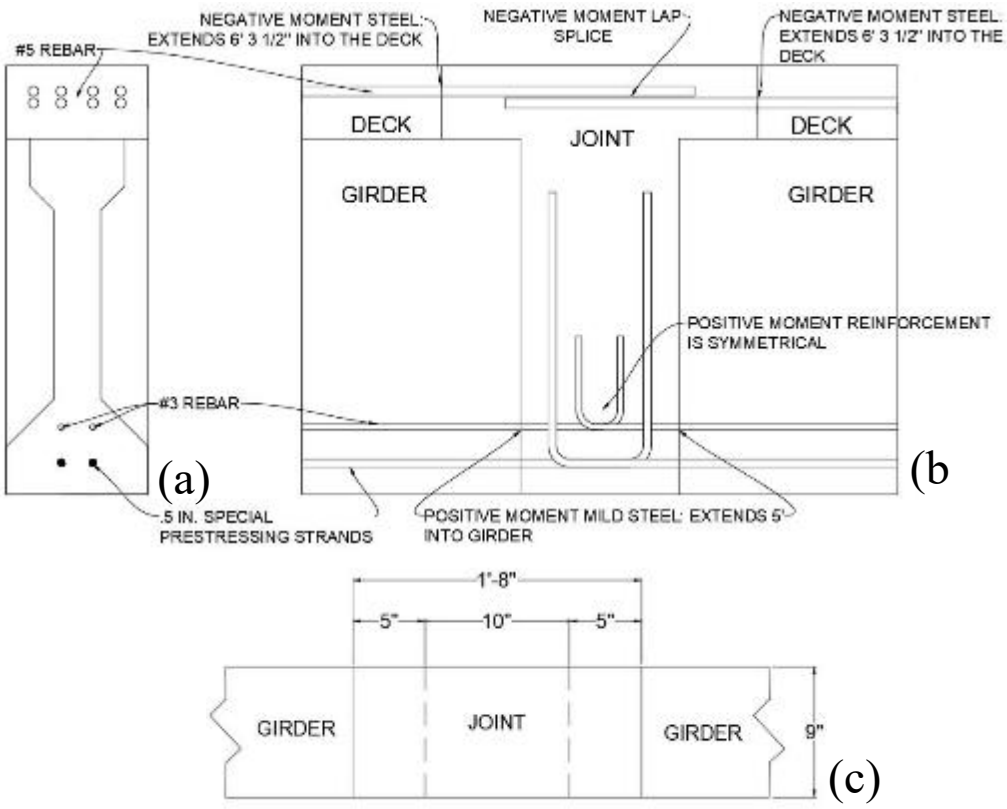

Figure 176. Newly constructed continuity joint cross-section (a), elevation view, (b), and plan view (c)

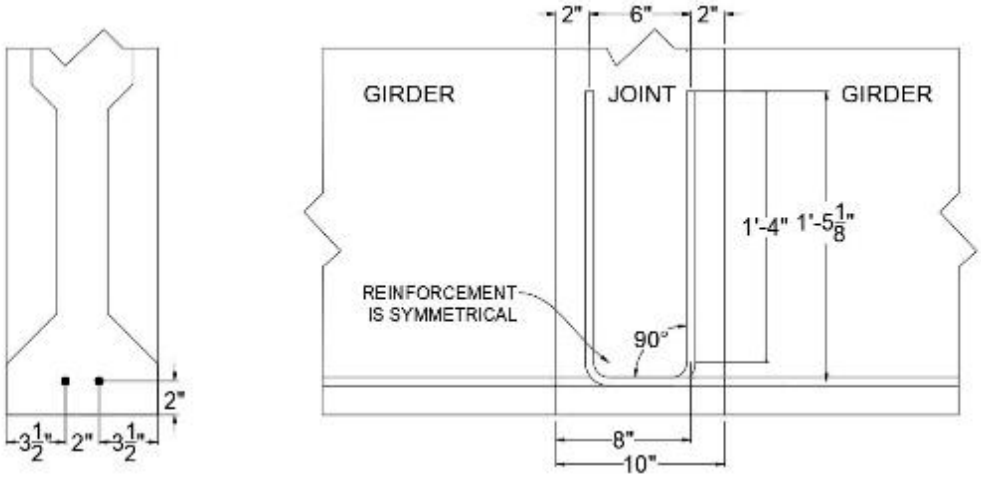

Figure 177. Newly constructed continuity joint prestressing strands detail for positive moment

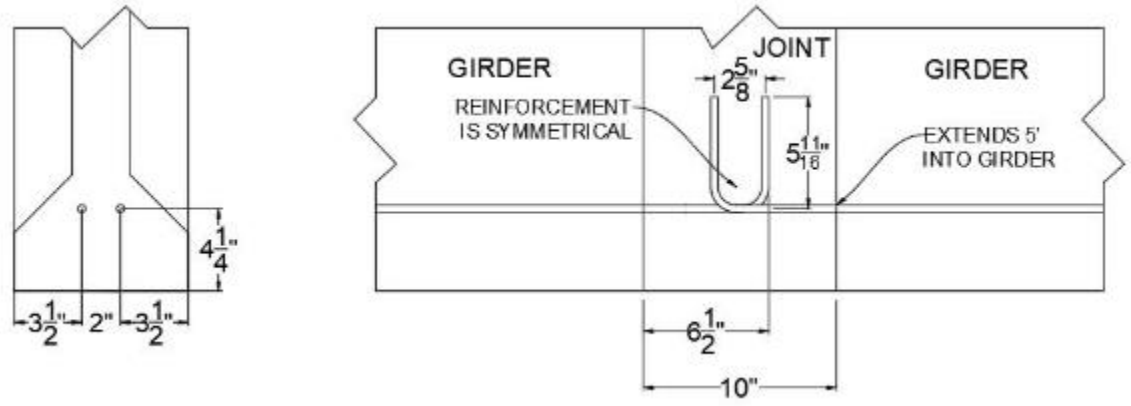

Figure 178. Newly constructed continuity joint mild steel detail for positive moment

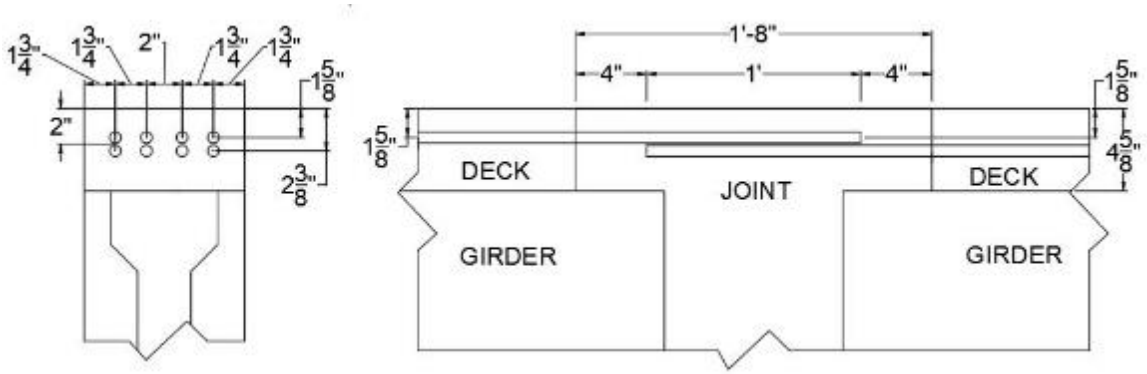

Figure 179. Newly constructed continuity joint mild steel detail for negative moment

Figure 180. Reinforcement within continuity joint specimen representing new construction

The retrofit continuity joint was designed with the intention that it could be implemented on existing bridges in service with a simple span configuration. ODOT standard detailing sheets showed a 4 in. gap between girder ends in simple span configuration, which does not allow positive moment steel to be added in the end face of the girders. A solution had to be created for attaching reinforcing steel in another location on the girder at the required elevation. The solution decided on was to attach rebar shear studs on the outside surface of each side of the flange near the end of the girder. This would allow the steel required to resist the positive moment induced at the joint to be transferred into the girders as if the steel was fully developed into the girders as in the newly constructed joint design. The positive moment value used for determination of the required reinforcing steel was based on the same method as used for the newly constructed joint design since the age of the girders would far exceed 90 days for pre-existing girders to be retrofitted in the field. Reinforcement for the retrofit specimens (Figures 181-186) consisted of dowels embedded in the beam bottom flange using Hilti concrete epoxy with standard hooks extending into the UHPC joint material, three No. 3 splice bars extending across the joint at the beam bottom flange, and No. 5 splice bars between the reinforcement in the two beam slabs.

The required tension force for $1.2M_{cr}$ was used to determine the required number of rebar shear studs to be embedded into the girder bottom flange for adequate transfer of load. The number of rebar shear studs required was determined using the HILTI epoxy adhesive HILTI HIT-RE 500 specification sheet that gave shear strength values for a No. 3 rebar embedded at multiple embedment lengths with various concrete compressive strength values. The highest compressive strength given (6 ksi) combined with the shortest embedment of 3-3/8 in. had a listed shear value of 12.2 kips. The embedment length of 3-3/8 in. was not possible, however, because a hole of this length would interfere with the location of the prestressing strands. Instead, a 2-½ in. embedment length was chosen to avoid interference with the prestressing strands and still meet the 2-3/8 in. minimum embedment length listed for the epoxy. Linear interpolation was then used to estimate the shear strength for the new embedment length as 9.09 kips. This value was then divided into the tension force of 33.74 kips to determine a required total of four rebar shear studs for each girder end, with two on

each side if using the epoxy HILTI HIT-RE 500. A 2 in. clear cover from the girder end and anchor spacing was used to satisfy the geometry of the joint and follow the minimum requirements from the epoxy specification sheet. The geometry of the joint limited the ability to include a straight rebar shear stud extending from the face of the bottom flange. To account for this and ensure proper development of the rebar shear studs, a 90-degree hook with a tail based on the recommendation of $8d_b$ (3 in.) for a No. 3 rebar (Yuan and Graybeal 2014) was applied. Figure 183 shows the positive moment rebar shear stud placement within the joint, and Figure 184 shows the rebar shear stud hook dimensions.

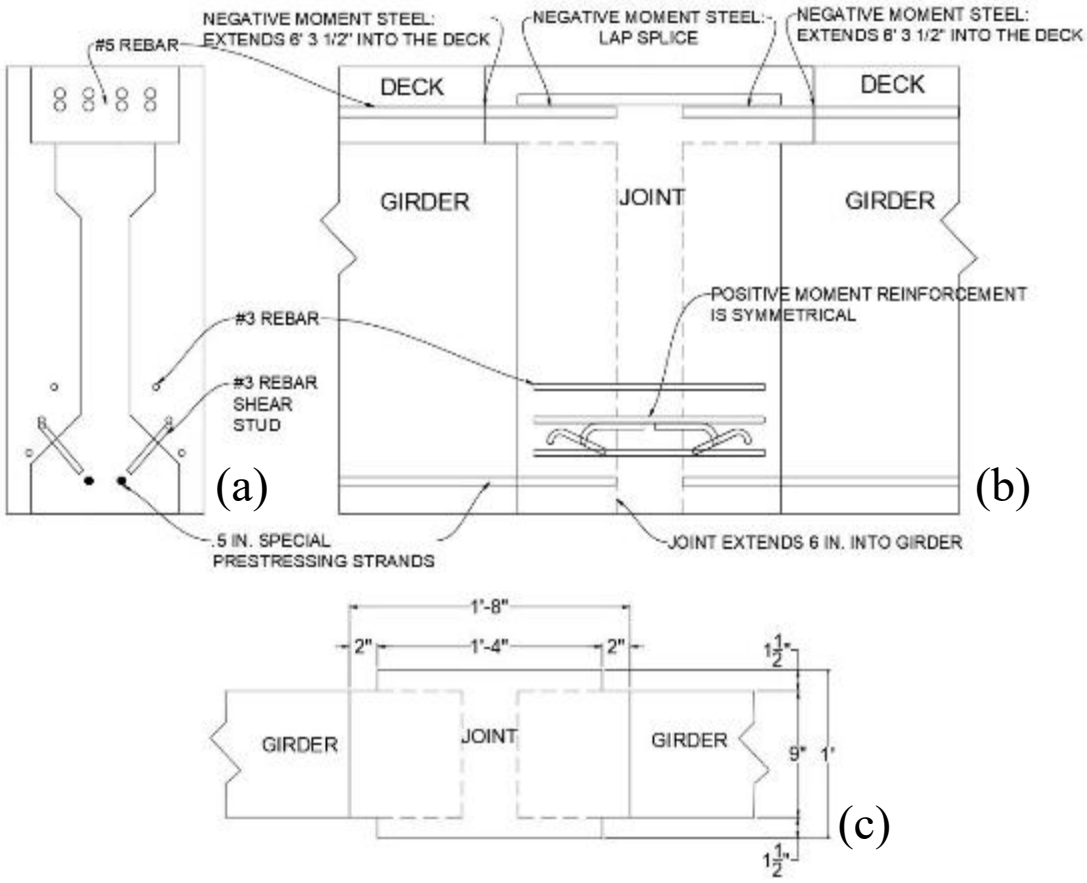

Figure 181. Retrofit continuity joint cross-section (a), elevation view (b), and plan view (c)

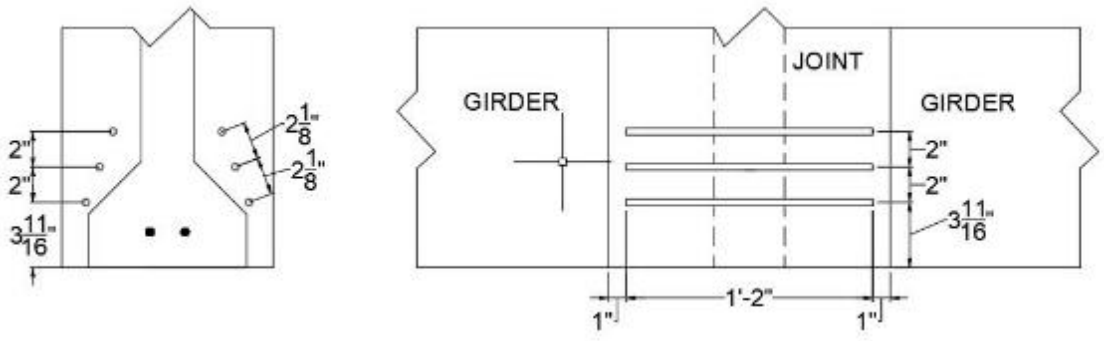

Figure 182. Retrofit continuity joint mild steel detail for positive moment

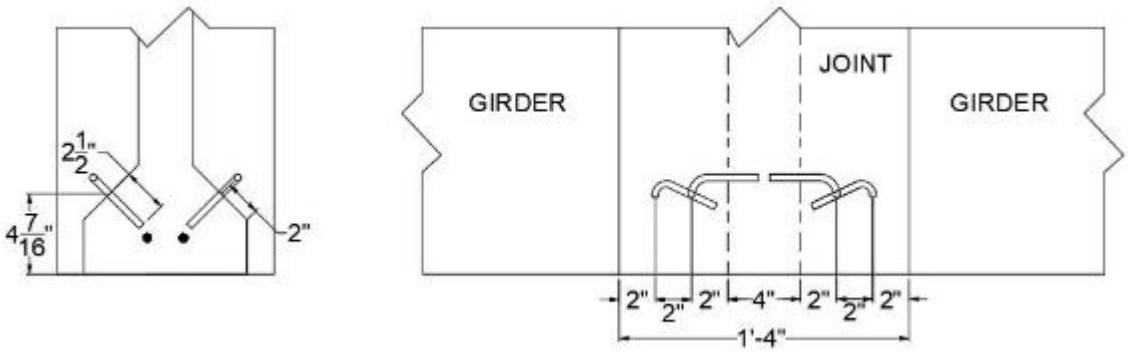

Figure 183. Retrofit continuity joint rebar shear studs detail for positive moment

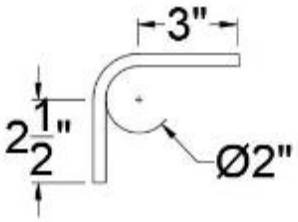

Figure 184. Rebar shear stud detail.

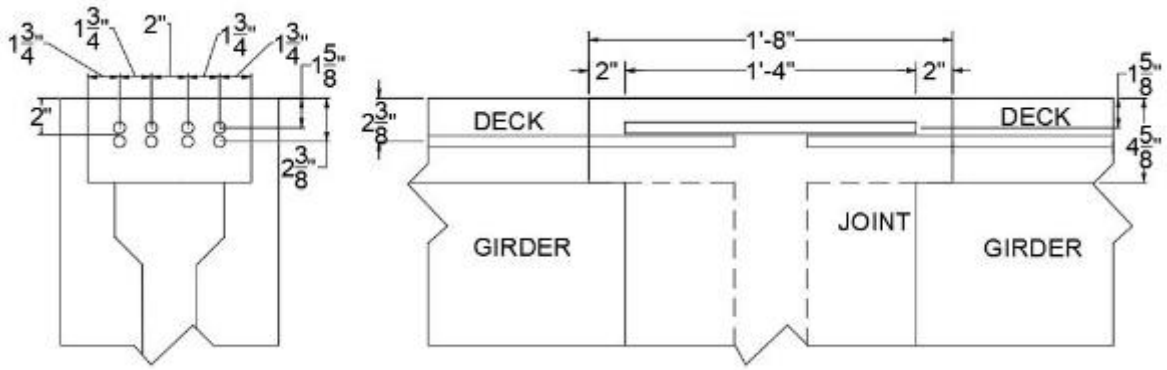

Figure 185. Retrofit continuity joint mild steel detail for negative moment

Figure 186. Reinforcement within continuity joint representing retrofit of an existing structure

The three joint specimens representing retrofit of an existing bridge were cast first followed by the three joint specimens representing new construction. Each set of joints was cast with a single batch of Ductal® UHPC mixed with the large rotary mixer. A completed retrofit joint is shown in Figure 187 and a completed joint representing new construction is shown in Figure 188.

Figure187. Completed continuity joint representing retrofit of an existing structure

Figure 188. Completed continuity joint representing new construction

6.3 Testing Methods

Two load frames available at Fears lab were used to create the individual point loads. The load frames were attached to the strong floor in the lab spaced at a distance equal to the distance between the mid-spans of each girder with the joint in the middle. Two identical hydraulic rams were attached to each load frame with hydraulic hoses running from the rams to the same pump to create a parallel system. This was done to ensure the same load would be applied to each of the girders at the same time to obtain a symmetric loading. In the case of a girder failing prematurely, a series of hydraulic valves were installed between the hydraulic pump and rams. This would allow one set

of valves to be shut off to maintain hydraulic pressure in the ram on the prematurely failed girder and allow the continuation of loading on the other girder. Figure 189 shows the hydraulic pump, and valves.

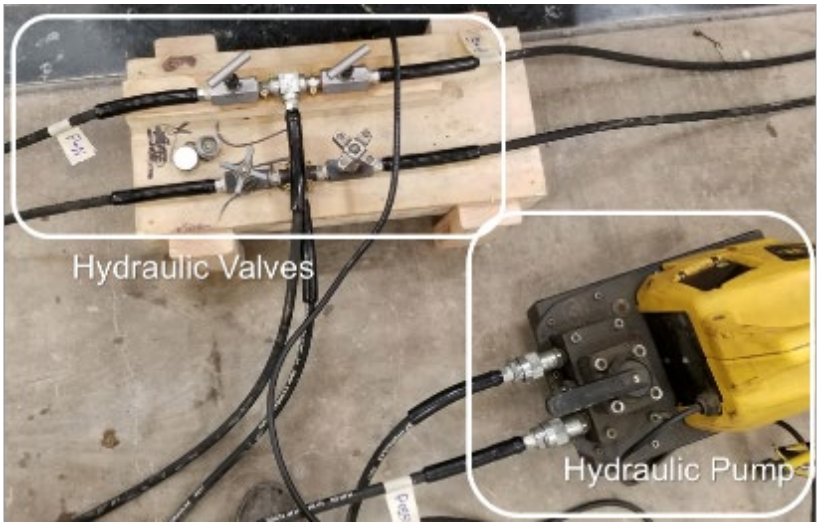

Figure 189. Hydraulic pump and valves

Cylindrical washers were used at each load point to allow for rotation during loading. Load cells were placed directly under each hydraulic ram to record the applied load and to monitor both loads during the test to verify both were within the same loading range. Figure 190 shows the load cell and hydraulic ram set up on one of the specimens on the north and south ends.

One wire potentiometer (pot) was placed directly under the beam at each load point to measure the deflection of each beam at mid-span. Linear voltage differential transformers (LVDTs) were placed under the girder center line at each of the supports. These LVDTs were used to measure the deflection of the neoprene pads supporting the girders during loading to subtract from the wire pot readings to get a true deflection of the girder at mid-span. Figure 191 shows a wire pot set up at midspan of the girder, and the LVDT set up at one of the supports.

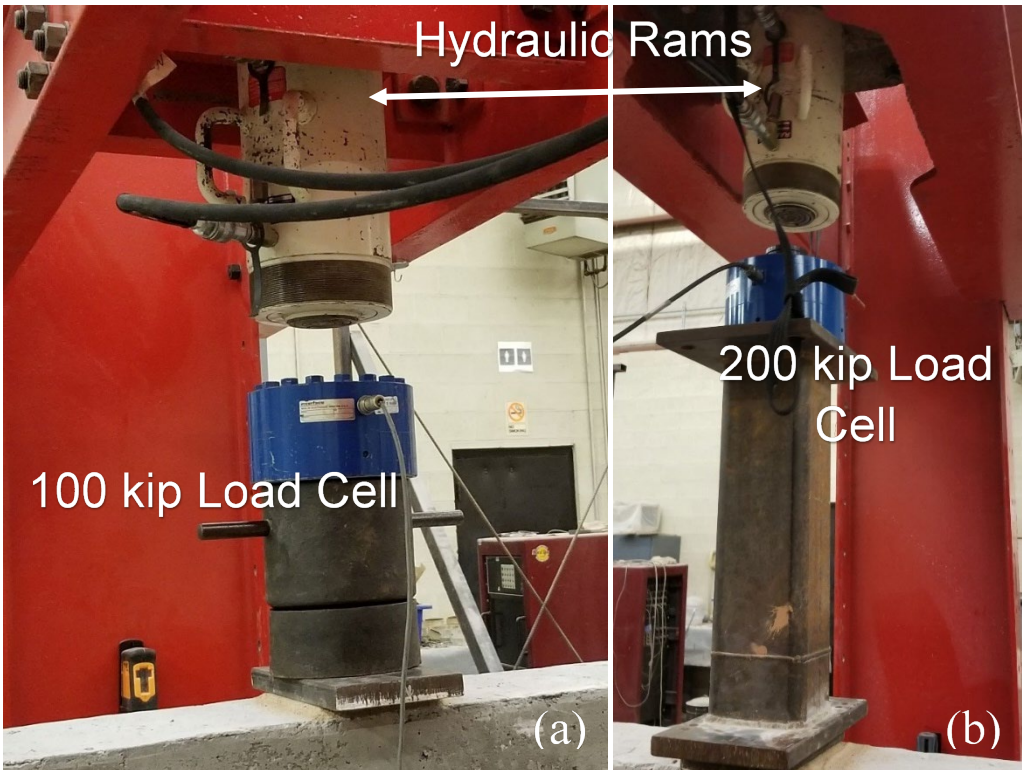

Figure 190. 100-kip load cell and hydraulic ram on the North beam (a) and 200 kip load cell and hydraulic ram on South beam (b)

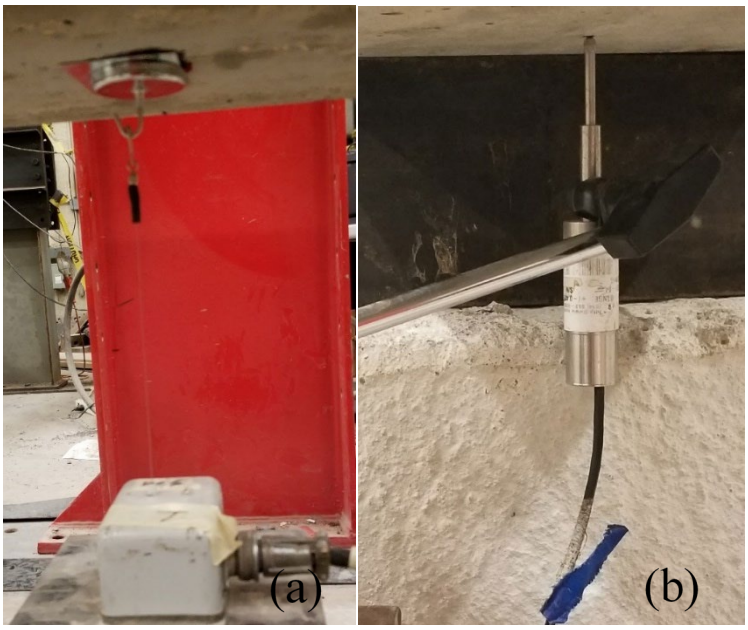

Figure 191. Wire potentiometer (pot) attached to bottom of girder at midspan (a) and linear voltage differential transformer (LVDTs) placed under girder near the support (b).

Four more LVDTs were attached around the negative moment region of the joint to measure joint separation at the interface of the connection if it occurred. One LVDT was attached directly to the concrete deck 2 in. below the top of the deck on each side of the joint on each side of the specimen using two conduit clamps and concrete screws. The LVDTs pushed against an aluminum angle attached to the UHPC joint. This allowed the LVDT to measure joint separation at the top portion of each interface on the side of the joint. Figure 192 shows two LVDTs attached to one face of the continuity joint.

Figure 192. LVDTs used to measure joint separation attached to the girder

Location of all the external sensors for the newly constructed joint is shown in Figure 193. For the retrofit connection tests, the LVDTs 3 and 5 were adjusted to 11 inches from the end of girder due to the joint length being shorter.

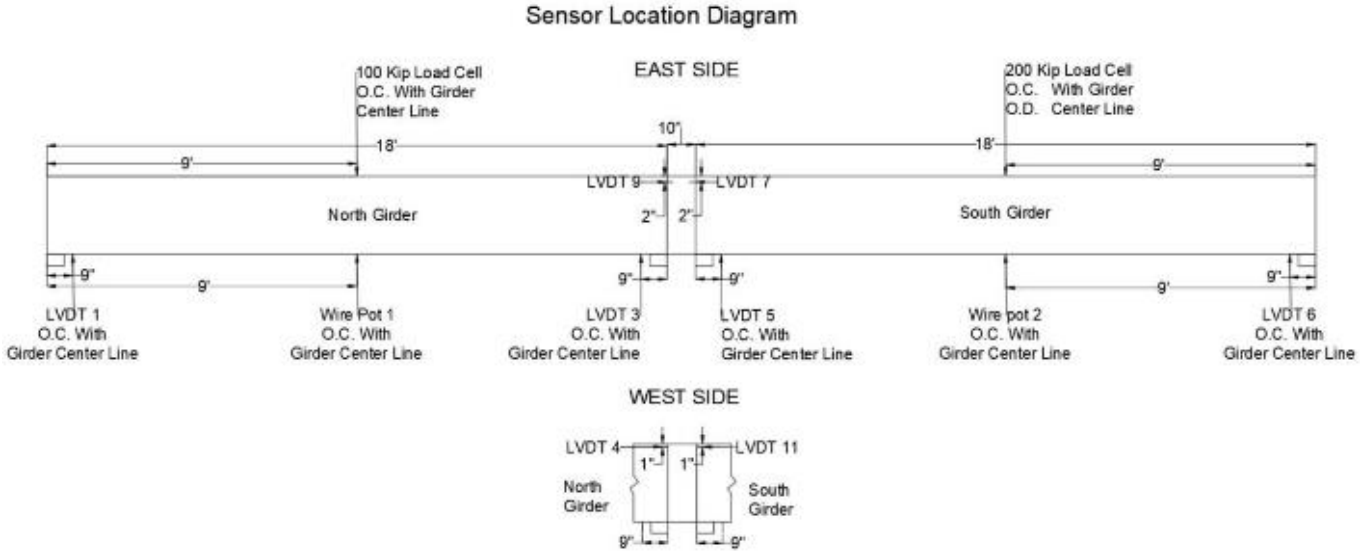

Figure 193. Sensor locations for each test

Two internal strain gauges with a 6 mm gauge length were attached to the negative moment reinforcing steel in the joint were used to measure strain in the maximum moment region and determine if the steel began to yield during the test. The strain gages were attached in the same location for the newly constructed and retrofit connection. They were attached at the middle of the joint on the rebar, with one strain gauge being attached to and interior bar, and the second gauge to the outer bar not next to the interior bar with the strain gauge. The gauges were coated in silicon to prevent them from getting damaged during concrete placement. Figure 194 shows a strain gauge attached to a reinforcing bar.

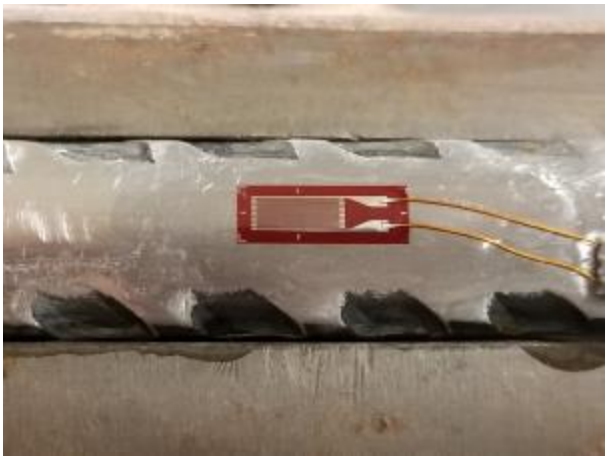

Figure 194. Strain gauge attached to a rebar

The procedure to begin testing a new specimen started with moving the specimen into the load frames and aligning the specimen on the supports to ensure each girder was in line with the hydraulic ram. After the specimen was correctly aligned, the load cells, wire pots, and LVDTs were attached/placed into the correct position based on the sensor diagram. A specimen in place and ready for testing is shown in Figure 195. Once the sensors were in place, each sensor was tested to verify a signal change was being read on the data acquisition system, and all sensors were zeroed. Load was applied to each specimen in 5 kip increments until initial cracking. The specimen was inspected for initial cracking between each load increment. Upon finding initial cracking, the cracks were traced with a black marker, and the corresponding load increment was written at the end of the crack. Loading increments were changed from 5 kips to 2 kips after initial cracking occurred to allow a more precise crack tracking on the

specimen. When the specimen was deemed failed or unsafe to continue loading the specimen was unloaded to end the test.

Figure 195. Continuity joint specimen in place for testing

6.4 Continuity Joint Testing Results

6.4.1 Compressive strengths

The concrete compressive strength data for the prestressed girders associated with the new construction (NC) joint specimens is listed in Table 38. The compressive strength data for the concrete decks associated with each NC specimen is listed in Table 39. The compressive strength data associated with each NC specimen UHPC continuity joint is listed in Table 40. It should be noted that the blanks in Table 38 are missing data that was not collected by mistake. All specimens described in Tables 39 and 40 share the same compressive strengths for 1, 7, and 28 days.

Table 38. Concrete compressive strengths for the NC prestressed girders

Age	NC1-N	NC1-S	NC2-N	NC2-S	NC1-N	NC1-S
1 Day (psi)	4670	4910	5010	5410	5360	5200
7 Day (psi)	7110	7070			7310	7090
28 Day (psi)			8730	9270	8220	8210
Day of Test (psi)	7840	8000	8650	8790	8130	8630

Table 39. Compressive strengths for the NC concrete decks

Age	NC1	NC2	NC3
1 Day (psi)	3970	3970	3970
7 Day (psi)	5090	5090	5090
28 Day (psi)	4930	4930	4930
Day of Test (psi)	4860	4740	5200

Table 40. Compressive strengths for the NC UHPC joints

Age	NC1	NC2	NC3
3 Day (psi)	12870	12870	12870
7 Day (psi)	18000	18000	18000
28 Day (psi)	23390	23390	23390
Day of Test (psi)	23790	25880	24620

The concrete compressive strength data for the prestressed girders associated with the retrofit construction (RC) joint specimens is listed in Table 41. The compressive strength data for the concrete decks associated with each RC specimen is listed in Table 42. The compressive strength data associated with each RC specimen UHPC continuity joint is listed in Table 43. All compressive strength data presented is the average between two to three specimens tested. It should be noted that the blanks in Table 41 are missing data that was not collected by mistake. All specimens described in Tables 42 and 43 share the same compressive strengths for 1, 7, and 28 days.

Table 41. Concrete compressive strengths for the RC prestressed girders

Age	RC1-N	RC1-S	RC2-N	RC2-S	RC3-N	RC3-S
1 Day (psi)	4990	4910	4660	4790	4320	4630
7 Day (psi)	6870	7230	6980	7440		
28 Day (psi)	8640	8500	7890	8320	7640	8200
Day of Test (psi)	8750	8140	7350	7500	7530	8510

Table 42. Compressive strengths for the RC concrete decks

Age	RC1	RC2	RC3
1 Day (psi)	3970	3970	3970
7 Day (psi)	5090	5090	5090
28 Day (psi)	4930	4930	4930
Day of Test (psi)	5460	5510	5160

Table 43. Compressive strengths for the RC UHPC joints

Age	RC1	RC2	RC3
3 Day (psi)	16430	16430	16430
7 Day (psi)	22100	22100	22100
28 Day (psi)	25020	25020	25020
Day of Test (psi)	24850	23980	24790

6.4.2 New Construction (NC) Specimens

6.4.2.1 Test NC1

During the loading of the NC1 specimen, the data acquisition system crashed approximately two thirds through the loading. The system crashed from over collecting data from the sensors, which resulted in the data file being too large to open with any program and deeming it unusable. The data acquisition system was adjusted to reduce the incoming data before reloading the NC1 specimen. On the second loading the file size was significantly smaller and could be opened with no difficulty. Cracks that formed during the reload test were labeled with an R with the load amount.

Initial flexural cracking was observed during the first loading near the joint interface on the NC1-S girder at a load of 35 kips, shown in Figure 197(b). The next flexural crack was observed directly under the load point on the NC1-N girder at a load of 43 kips, shown in Figure 196(a). In addition, two more cracks had developed at a load of 43 kips, a flexural crack near the joint interface on the NC1-N girder, shown in Figure 197(a), and a flexure-shear crack near the joint interface on NC1-S, shown in Figure 197(b). On the next load increment a flexural crack was observed on the NC1-S girder directly under the load point at a load of 45 kips, shown in Figure 196(b). A flexure-shear crack had also developed near the joint interface on the NC1-N girder at the same load, shown in Figure 197(a). Asymmetrical hairline flexural cracks were observed in the continuity joint at a load of 52 kips during the first loading, as indicated with dark lines in Figure 198. During the reload test a flexural crack was observed on the east face of continuity joint at a load of 44 kips, as indicated in Figure 197(b) with a dark oval. Additional flexural cracks developed during the reload test in the continuity joint at a load of 46 kips, as indicated in Figure 199 with dark ovals. These flexural cracks in the continuity joint developed at a lower load increment during the reload test

than the initial cracks observed during the first loading. This would likely be due to the cracks already existing prior to the reload, but which did not fully separate to be visually distinguishable as a crack until the reloading occurred.

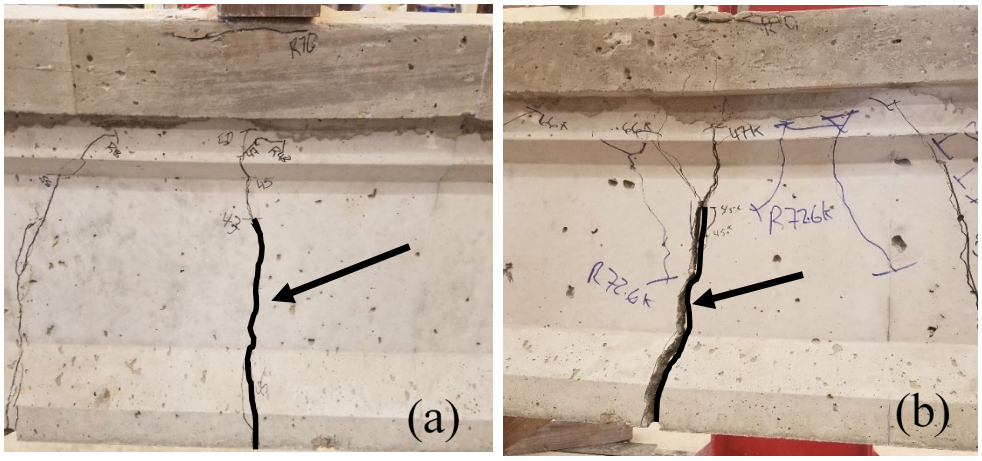

Figure 196. Initial flexural cracking under the load point on the NC1-N girder at 43 kips of load (a) and initial flexural cracking under the load point on the NC1-S girder at 45 kips of load (b). Arrows point to the dark lines that indicate the initial flexural cracks.

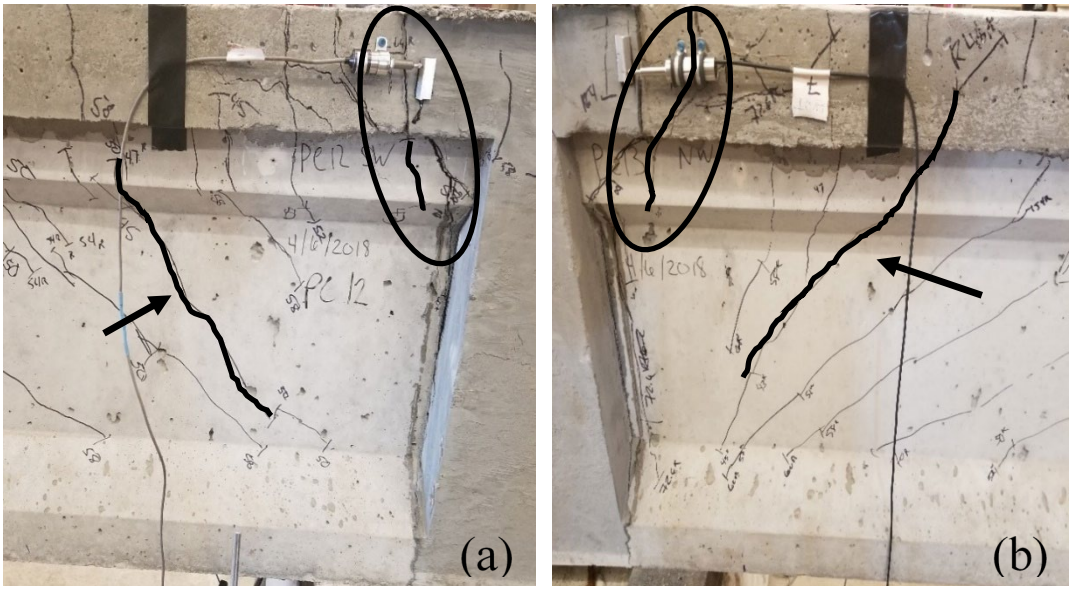

Figure 197. Initial flexural cracking on the NC1-N girder at 43 kips of load and initial flexure-shear cracking on the NC1-N girder at 45 kips of load (a) and initial flexural cracking on the NC1-S girder at 35 kips of load and initial flexure-shear cracking on the NC1-S girder at 43 kips of load (b). Dark ovals indicate the initial flexural cracking near the continuity joint, and arrows point to the dark lines that indicate the initial flexure-shear cracking.

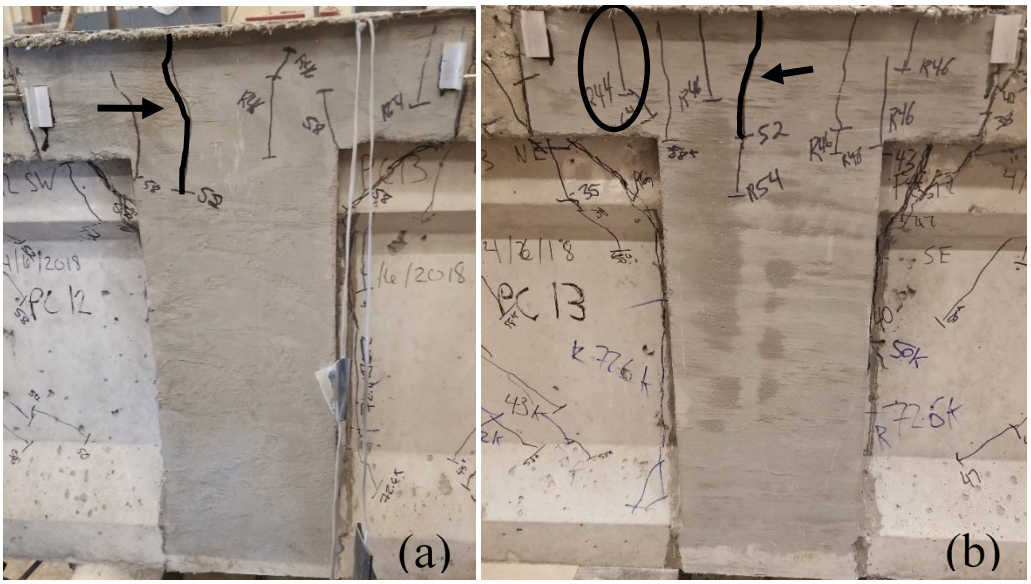

Figure 198. Initial continuity joint flexural cracking on the west face (a) and east face (b) at 52 kips of load. Arrows point to the dark lines that indicate the initial flexural cracks, and the dark oval shows the initial flexural cracks from the reload test. Other reloading cracks are indicated by an R before the load value.

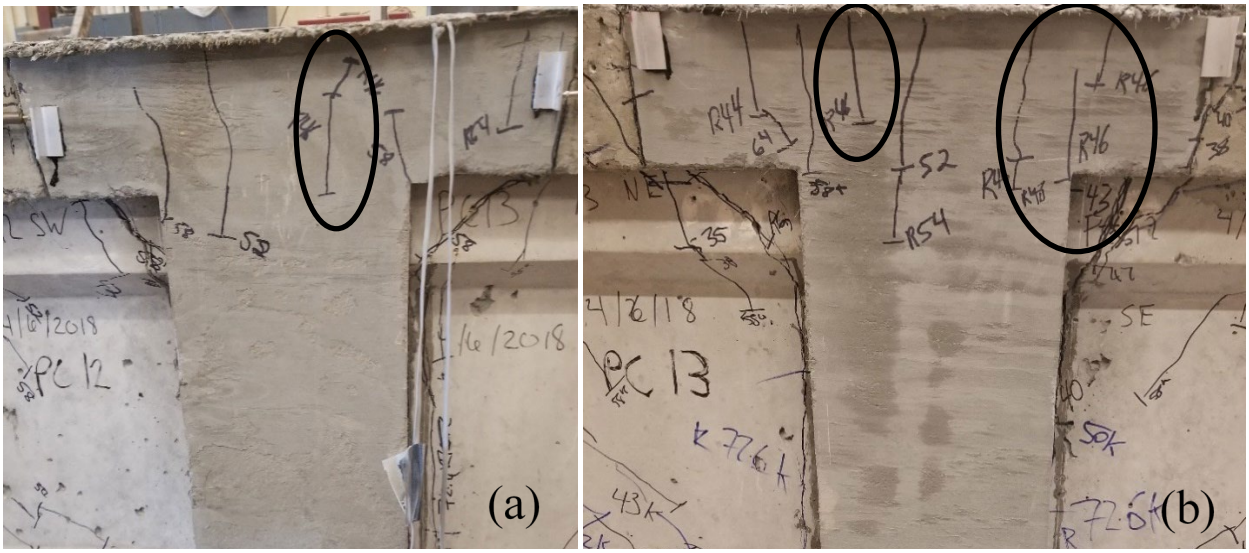

Figure 199. Continuity joint flexural cracking during the reload test on the west face (a) and east face (b) at 46 kips of load. Dark ovals show the initial flexural cracks from the reload test. Other reloading cracks are indicated by an R before the load value.

Cracks that developed between initial cracking and final failure included additional flexural cracks under the point loads, flexure-shear cracks near the joint interface, web shear cracks near the point load, and flexural cracks in the UHPC joint. Most cracks occurring on the NC1 specimen when reaching final failure were flexure-

shear and web shear cracks. These cracks developed as the load increased and the flexure-shear cracks began to move away from the joint interface towards the load point. Upon reaching approximately halfway to the load point from the joint, web shear cracks developed in place of the flexure-shear cracks. Figure 200 shows the flexural cracks and web shear cracks between the joint interface and load point for the NC1-N and NC1-S girder.

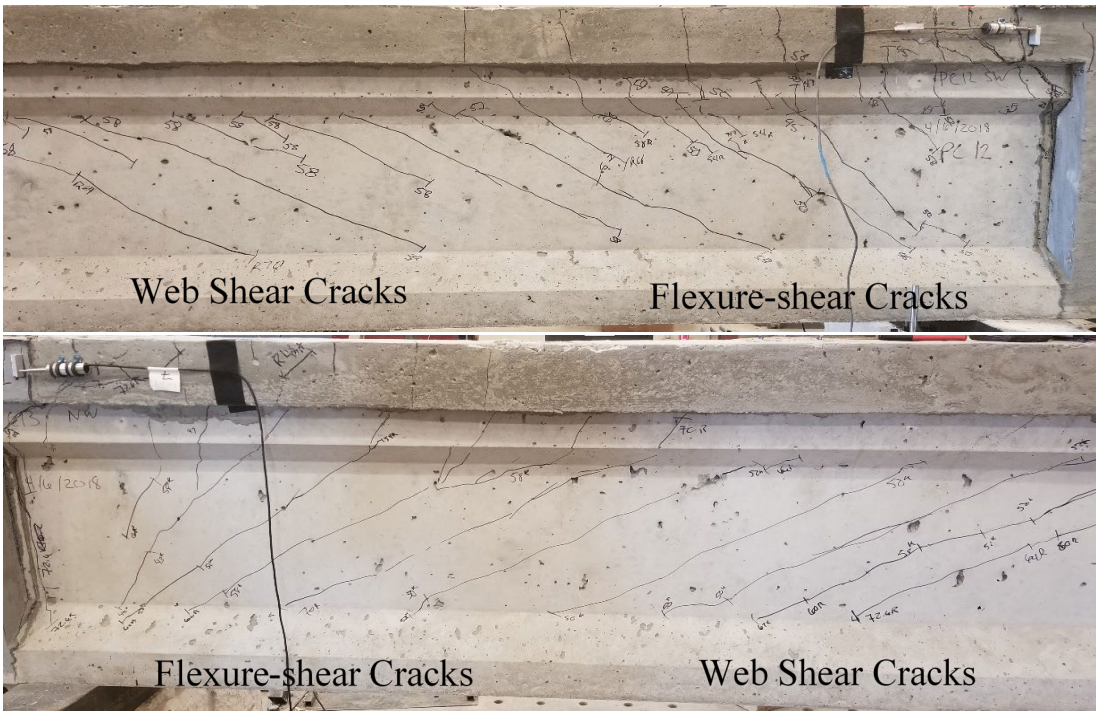

Figure 200. NC1-N girder with flexure-shear and web shear cracks (top) NC1-S girder with flexure-shear and web shear cracks (bottom)

Loading of the specimen was stopped when the prestressing strands in the NC1-S girder ruptured directly under the load point at a load of 73.8 kips. The flexural crack directly under the load point where the prestressing strands ruptured is indicated in Figure 201 with a dark oval. The concrete deck began to crush at the load point in both girders under the loading conditions immediately before the prestressing strands ruptured, as shown by the dark circles in Figure 202. In addition, there was significant widening of the flexural cracks under both load points with additional load application, as shown by dark lines in Figure 202. These conditions were taken to indicate flexural failure of the beam specimens. Allowing the prestressing strands to rupture on the first test specimen helped indicate the capacity of the prestressed concrete girders

connected to the continuity joint had been reached, and to prevent the need to take future prestressing strands all the way to rupture.

Figure 201. Flexural crack where the prestressing strands ruptured under the load point on the NC1-S girder, indicated by a dark oval

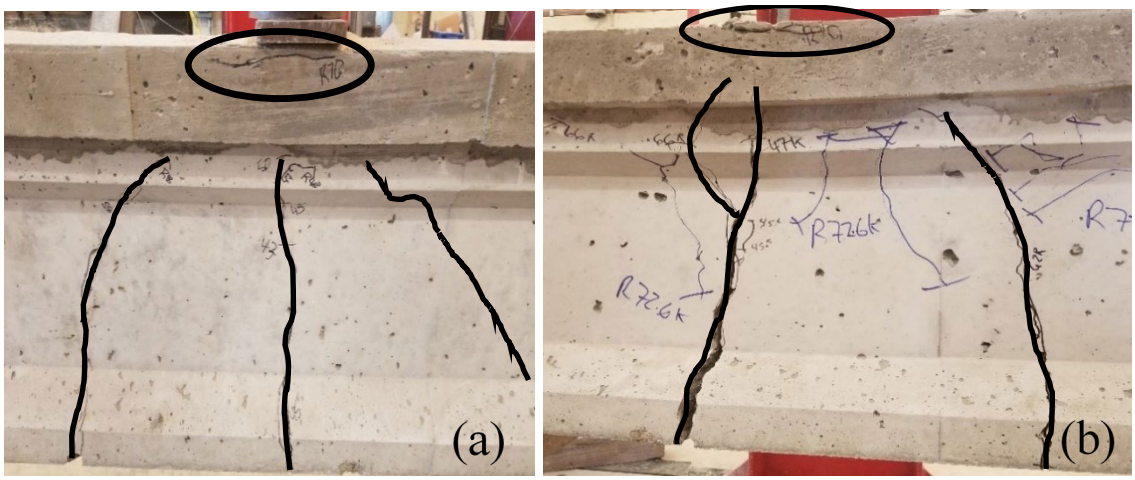

Figure 202. Crushed concrete deck in the NC1-N (a) and NC1-S (b) girder are indicated by a black oval and the final flexural cracks under the load point in the NC2-N (a) and NC2-S (b) girders are indicated by dark lines

The interface between the NC1-N girder and the UHPC joint exhibited flexural cracking along the interface, which resulted in separation of the girder from the joint material, as shown by the dark lines in Figure 203(a). Additional separation was observed at the interface between the UHPC joint and the NC1-S girder, but also

flexural cracking parallel to the interface, as shown in Figure 203(b). The term ”joint separation” will be used throughout the remainder of the document and is defined as the debonding between the concrete deck and UHPC joint interface due to flexural cracking.

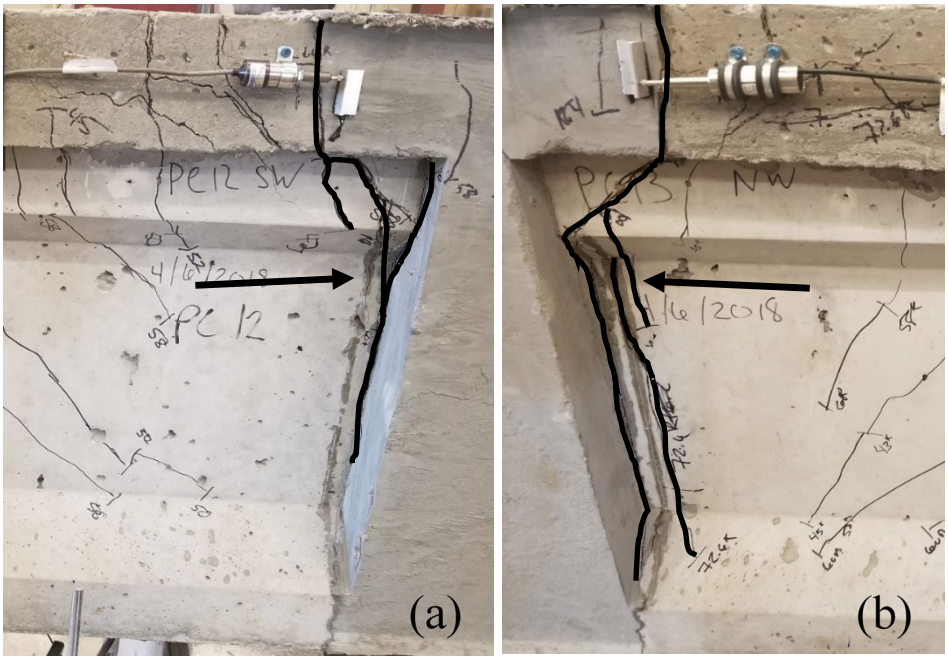

Figure 203. Joint separation at the interface between the NC1-N girder and the UHPC joint (a) and flexural cracking parallel to the interface between the UHPC joint and the NC1-S girder (b) are indicated by dark lines.

Figure 204 shows the load-deflection curve for the NC1-N girder from the reload test. The reload curve does not clearly indicate the girder having a ductile behavior due to initial cracking occurring in the first test. No sudden loss of stiffness indicating cracking is visible in the reload curve. The reload curve beginning to plateau out to 2 in. of deflection after exceeding the maximum load that was reached in the first test indicates that the prestressing strands began to yield. This supports a ductile behavior of the NC1-N prestressed girder during loading up to the ultimate load of 72.5 kips, as the graph was unable to show clear indication of the behavior. Figure 205 shows the reload-deflection curve for the NC1-S girder. The NC1-N and NC1-S girders had the same ductile behavior, but the NC1-S girder’s prestressing strands ruptured after the ultimate load of 73.8 kips was achieved. The NC1-S girder deflected an inch more than the NC1-N girder due to the strands rupturing. The noise in the data visible in both

figures comes from the wire pots measuring deflection, and for the future tests they were switched to different data acquisition channels with better signal conditioning to reduce the noise in the signals.

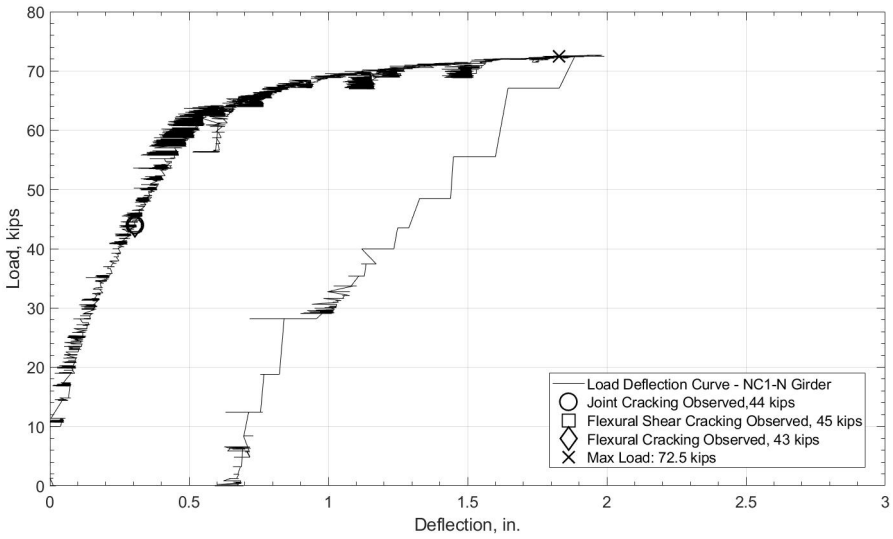

Figure 204. Load-deflection curve for the NC1-N girder, reload test.

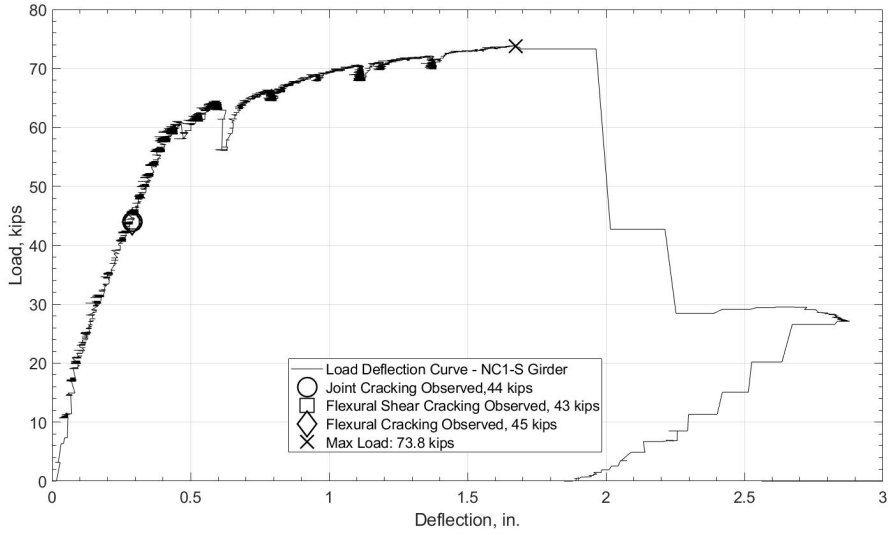

Figure 205. Load-deflection curve for the NC1-S girder, reload test.

Figure 206 shows the load-joint separation curve between the NC1-N girder's concrete deck and the UHPC joint from the reload test. The readings from the LVDTs on the east and west faces of the concrete deck were averaged to get a better

representation of the joint separation. The LVDTs on the joint interface were located 2 in. below the top of the deck. The reload curve showed a linear trend from zero back to where the final load of the initial test had stopped. Beyond the 60 kip load joint separation increased significantly with each load increment. At this point the NC1-N girder began to exhibit an increase in deflection, resulting in a less stiff member and creating a hinge at the weak point, that is the joint interface. Figure 207 shows the reload joint separation curve between the NC1-S girder's concrete deck and the UHPC joint. This figure only represents LVDT11 on the west face of the deck. LVDT 7 was not included for any of the six tests, as the data was unreliable. This load joint separation curve shows the same trends as for the average of LVDT 4 and 9 between the NC-1N girder deck and UHPC joint, but with a smaller magnitude.

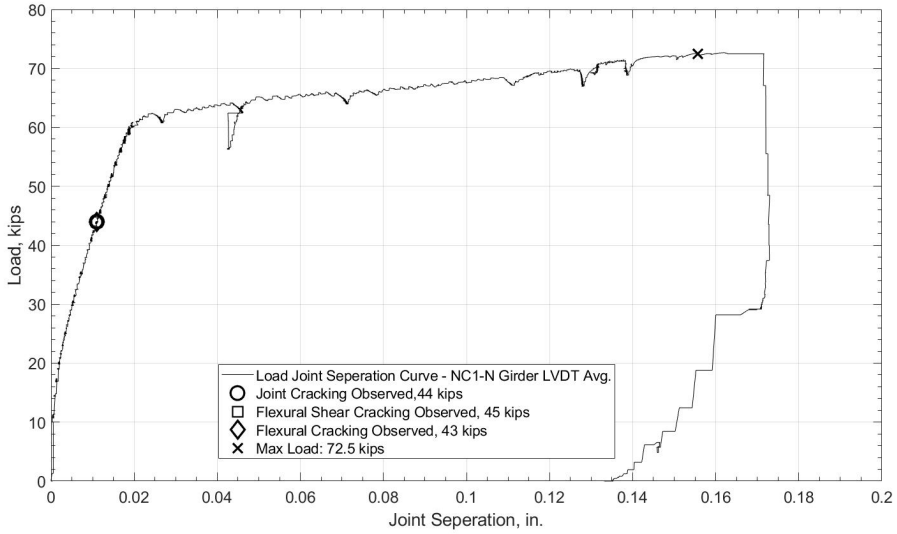

Figure 206. Load-joint separation curve at the NC1-N girder deck to joint interface

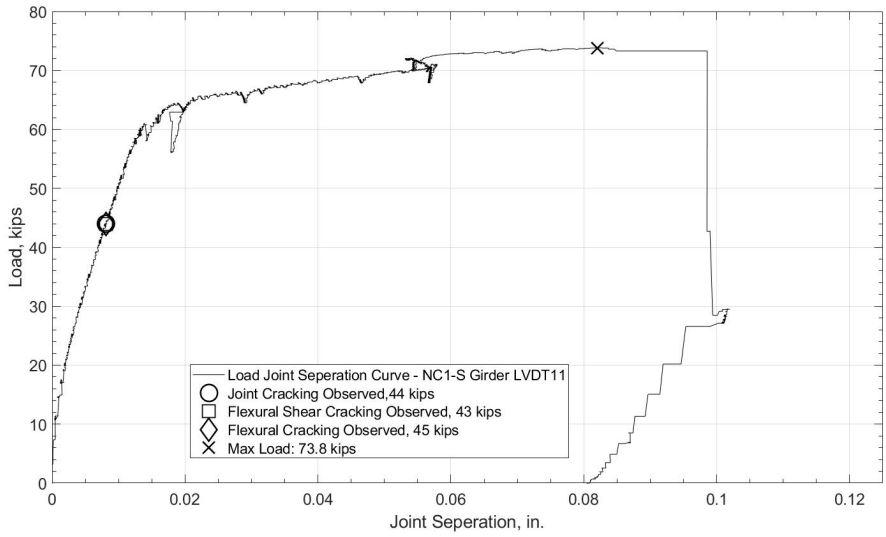

Figure 207. Load-joint separation curve at the NC1-S girder deck to joint interface west face

6.4.2.2 Test NC2

Initial flexural cracking was observed directly under the load point on the NC2-N girder at a load of 40 kips, shown in Figure 208(a). During the next 5 kip load increment a flexural crack was observed on the NC2-S girder directly under the load point, shown in Figure 208(b). In addition, flexure-shear cracks, shown in Figure 209(b), had also developed on the NC2-S girder near the continuity joint. Asymmetrical hairline flexural cracks occurred in the continuity joint at the same load increment of 45 kips as shown in Figure 210. The cracking observed on the east face of the joint did not match the west face, as the east face had irregular flexural cracking as indicated in Figure 210(b) with a dark circle. The second flexural crack did not go to the top of the joint, but instead started below and shifted from the first crack. The NC2-N girder exhibited similar flexure-shear cracks as the NC2-S girder at 47 kips near the joint as shown in Figure 209(b).

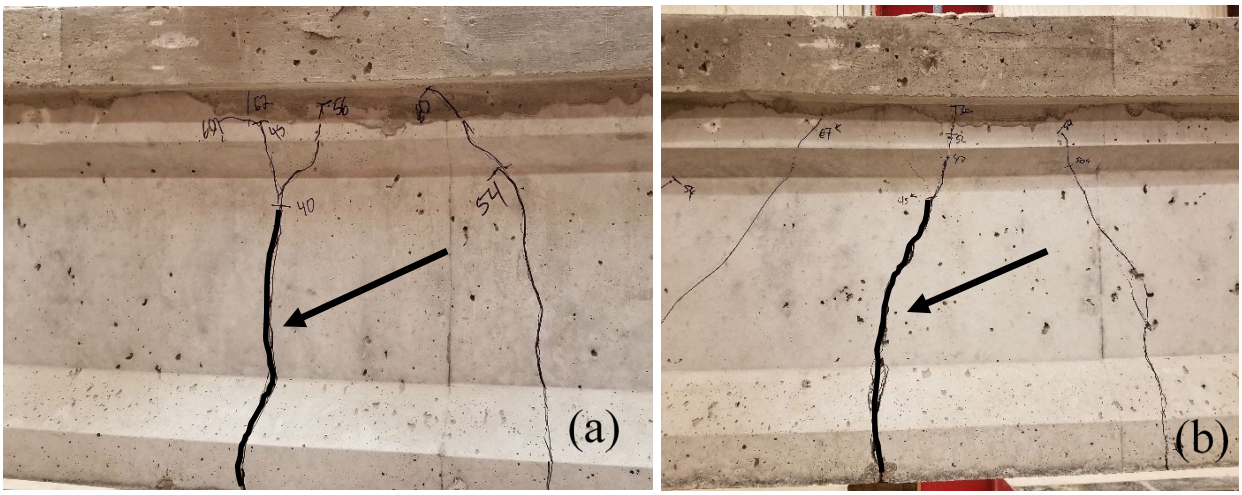

Figure 208. Initial flexural cracking under the load point on the NC2-N girder at 40 kips of load (a) and initial flexural cracking under the load point on the NC2-S girder at 45 kips of load (b). Arrows point to the dark lines that indicate the initial flexural crack.

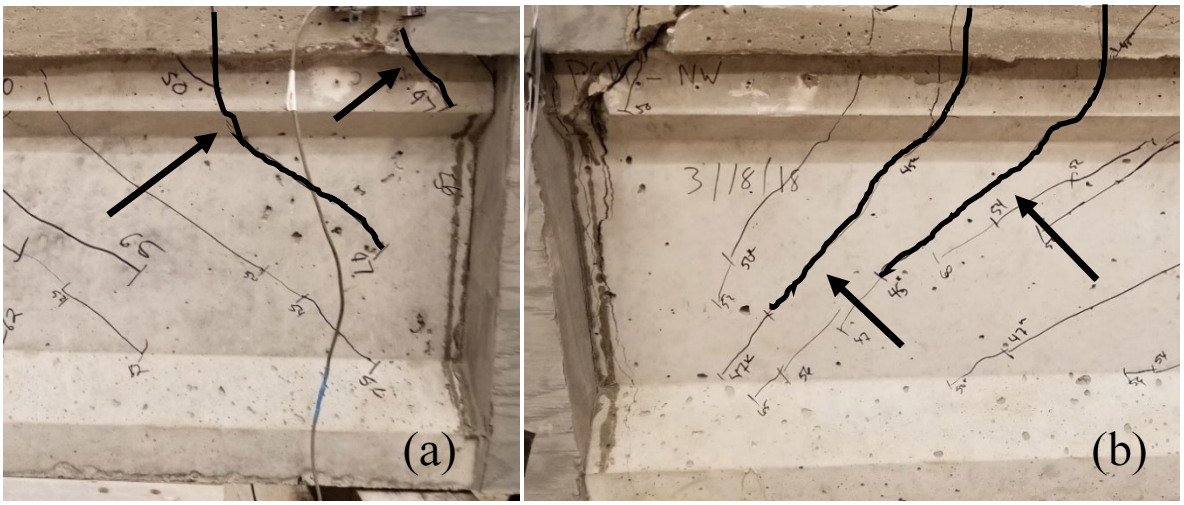

Figure 209. Flexure-shear cracking on the NC2-N girder at 47 kips of load (a) and flexure-shear cracking on the NC2-S girder at 45 kips of load (b). Arrows point to the dark lines that indicate the initial flexure-shear cracking.

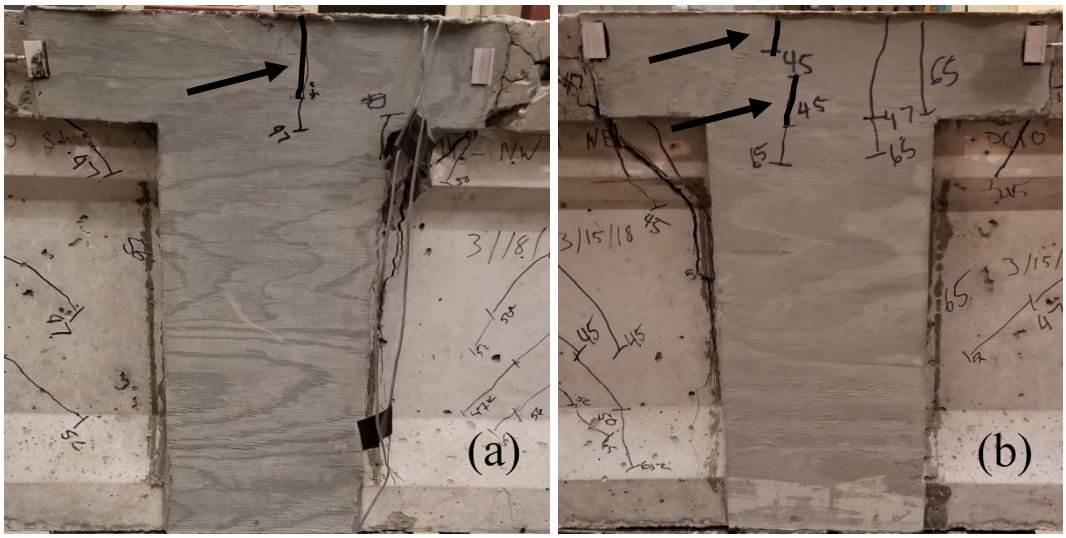

Figure 210. Initial continuity joint flexural cracking on the west face (a) and east face (b) at 45 kips of load. Arrows point to the dark lines that indicate the initial flexural cracks, and the dark circle on the east face (b) shows the irregular flexural cracking.

Cracks that developed between initial cracking and final failure included additional flexural cracks under the point load, flexure-shear cracks near the joint interface, web shear cracks near the point load, and flexural cracks in the UHPC joint. The majority of cracks observed for the NC2 specimen were at final failure were flexure-shear and web shear cracks. These cracks developed as the load increased and the flexure-shear cracks propagated away from the joint interface towards the load point. Beginning approximately halfway to the load point web shear cracks developed in place of the flexure-shear cracks. Figure 211 shows the flexural cracks and web shear cracks between the joint interface and load point for the NC2-N and NC2-S girder.

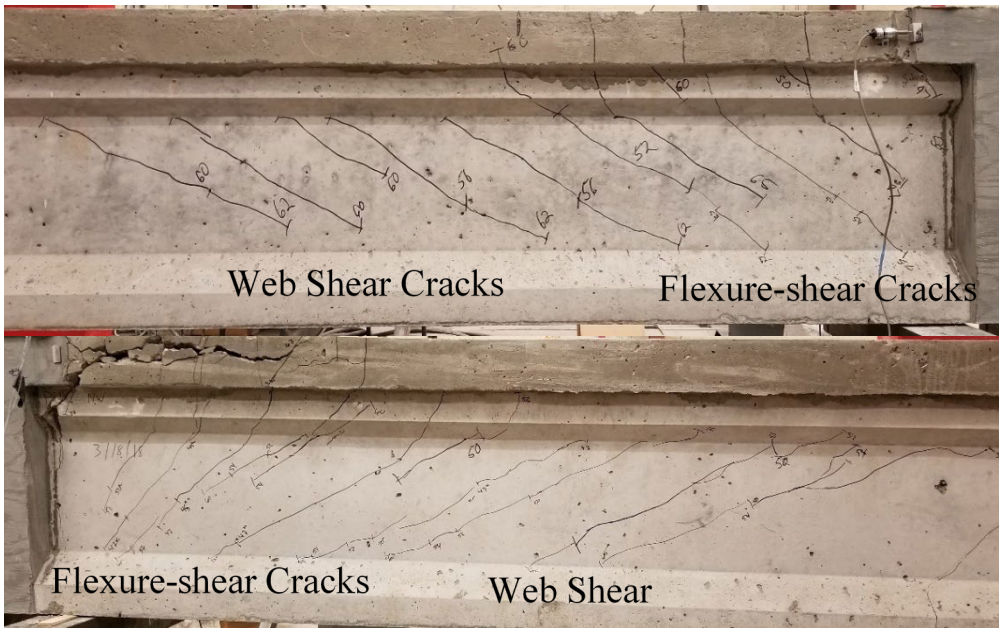

Figure 211. NC2-N girder with flexure-shear and web shear cracks (top) and NC2-S girder with flexure-shear and web shear cracks (bottom)

Loading of the specimen was stopped upon reaching an applied load of 71.5 kips on the NC2-N girder and 72 kips on the NC2-S girder. Under these loading conditions the concrete deck had begun to crush at the load point in both girders, as shown by the dark circles in Figure 212. In addition, the flexural cracks under both load points had significantly widened. These conditions were taken to indicate flexural failure of the beam specimens and testing was concluded to prevent the prestressing strands from rupturing and causing damage to the testing apparatus. Flexural cracking was observed along the interface between the NC2-N girder and the UHPC joint, which resulted in separation of the girder from the joint, as shown by the dark lines in Figure 213(a). Less separation was observed at the interface between the UHPC joint and the NC2-S girder, but more flexural cracking parallel to the interface was observed, as shown in Figure 213(b).

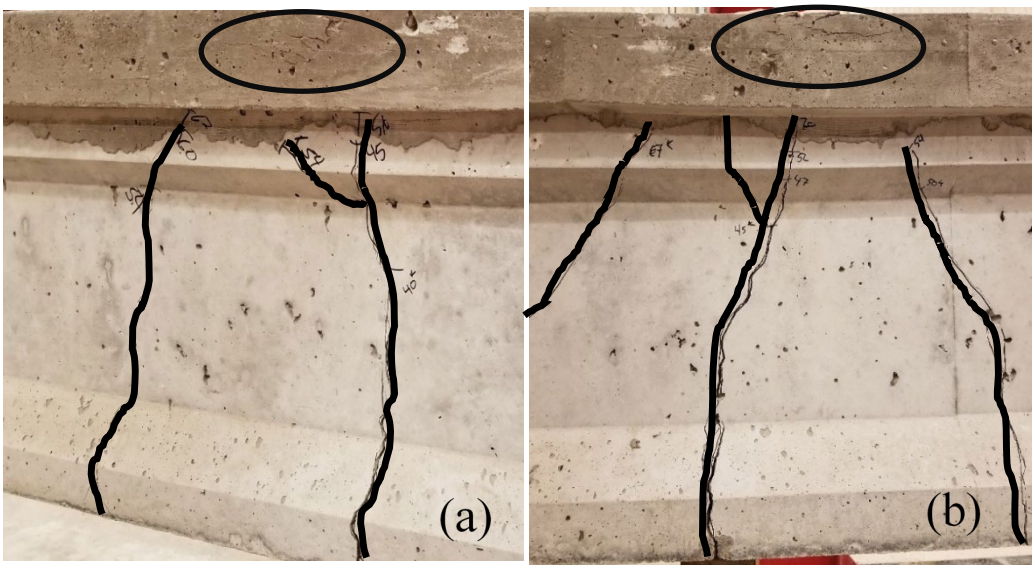

Figure 212. Crushed concrete deck in the NC2-N (a) and NC2-S (b) girders is indicated by a black oval, and the final flexural cracking under the load point in the girders are indicated by dark lines.

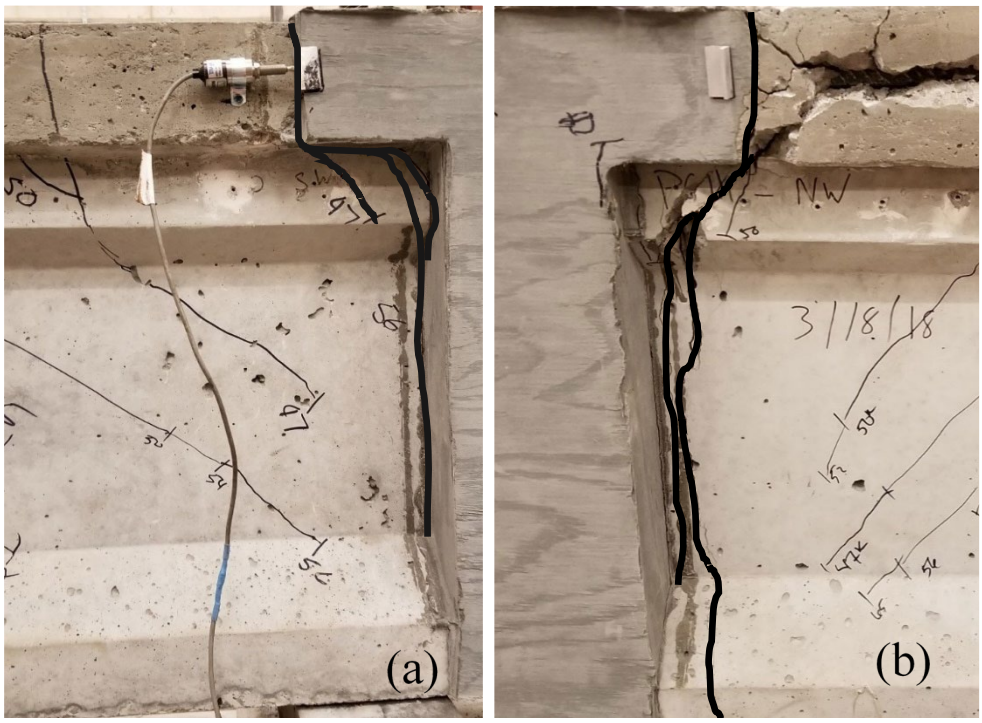

Figure 213. Joint separation at the interface between the NC2-N girder and the UHPC joint (a) and flexural cracking parallel to the interface between the UHPC joint and the NC2-S girder (b) are indicated by dark lines.

The NC2-S girder deck near the joint interface exhibited severe cracking along the side of the deck in the longitudinal direction at the level of the negative moment

reinforcement. After testing was complete, the top portion of the deck was removed to determine the cause of this behavior. After the concrete had been removed above the negative reinforcement, it was determined that the rebar had plastically deformed during loading. There was no sign of cracking around the reinforcement entering the UHPC joint, which indicated that the UHPC joint acted as a fixed end for the reinforcement. As the load increased during the test, the girder deflected more than the relatively rigid joint causing the rebar to follow the same curvature as the girder but remain fixed in the UHPC joint. This caused the rebar to bend sharply upward, and it separated the concrete along the longitudinal negative moment reinforcement in the deck. Figure 214 shows the NC2-S girder deck before and after the excavation of the concrete separation in the deck.

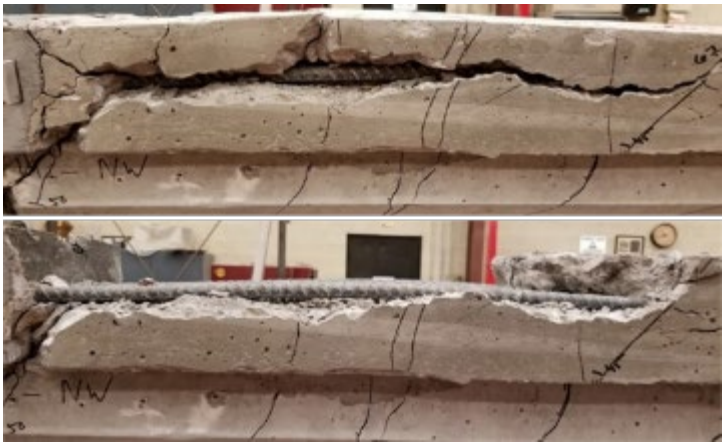

Figure 214. NC2-S girder before excavation of the concrete in the deck (top) and the deck after excavation exposing the reinforcement (bottom)

Figure 215 shows the load-deflection curve for the NC2-N girder. The curve shows a reduction in stiffness that corresponds with the initial flexural cracking observed at 40 kips. Other types of initial cracking did not reduce the stiffness of the girder. This indicates a ductile behavior of the NC2-N prestressed girder during loading up to the ultimate load of 71.5 kips. In addition, the plateau of the load-deflection curve out to 2 in. of deflection indicated the prestressing strands were yielding. Figure 216 shows the load-deflection curve for the NC2-S girder. The NC2-N and NC2-S girders had the same ductile behavior, but with the NC2-S girder having less deflection at mid-span. The varying deflection of the girders can be related to a difference in the concrete mix,

compressive strength, modulus of elasticity, and a difference in prestress loss between the girders. These variables could have caused the NC2-N girder to crack 5 kips earlier in flexure than the NC2-S girder and could have resulted in the NC2-N girder having a reduced stiffness compared to the NC2-S girder. This led to a larger downward curvature, which created more strain in the prestressing strands, and led to even larger deflection in the NC2-N girder.

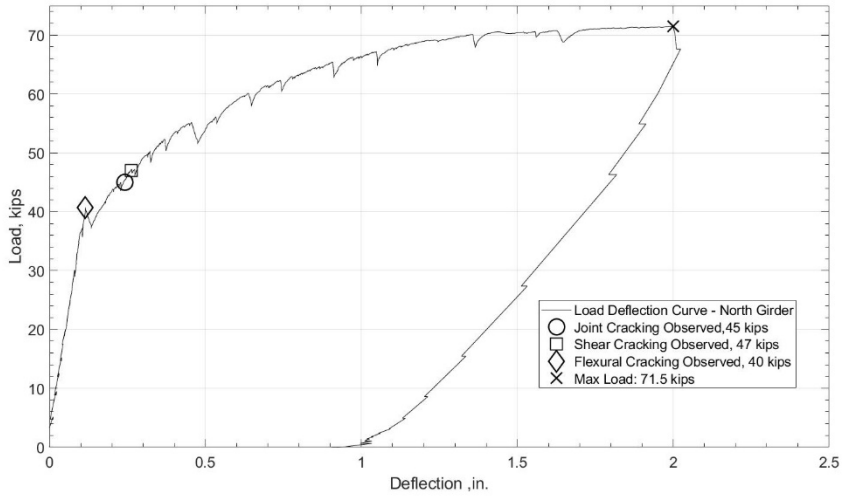

Figure 215. Load-deflection curve for the NC2-N girder

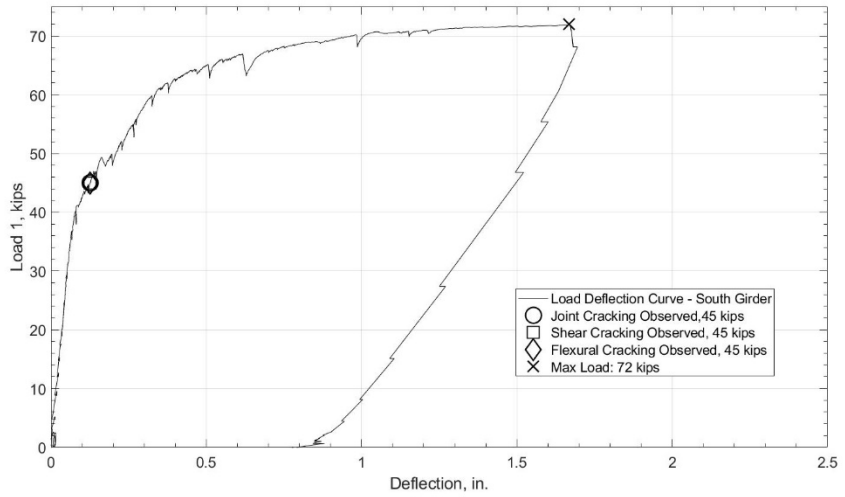

Figure 216. Load-deflection curve for the NC2-S girder

Figure 217 shows the load-joint separation curve between the NC2-N girder's concrete deck and the UHPC joint. The average of the readings from the LVDTs on the

east and west faces of the concrete deck was taken to get a better representation of the joint separation. The LVDTs on the joint interface were located 2 in. below the top of the deck. The deck joint had minor separation until reaching the initial flexural cracking of 40 kips. After that load, indicated by a diamond shape in Figure 217, the joint separation began to increase significantly with each load increment. It is reasonable that major joint separation could only occur after the girder cracked due to flexure, resulting in a less stiff member and creating a hinge at the weak point; the joint interface. Figure 218 shows the load-joint separation curve between the NC2-S girder's concrete deck and the UHPC joint. This figure only includes results from LVDT11 on the west face of the deck. This load-joint separation curve shows the opposite of what was expected. As the girder cracked in flexure, the reduction of girder stiffness appeared to have no effect on the rate of the joint separation as the load increased. No major joint separation occurred until reaching over 60 kips of load, after which the separation rapidly increased until the LVDT gave a faulty reading. The results shown only include data from before the faulty reading occurred.

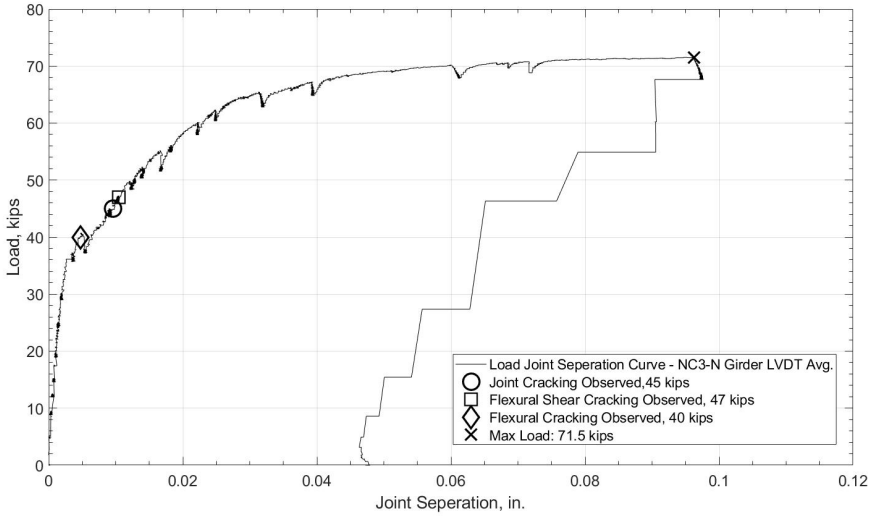

Figure 217. Load-joint separation curve at the NC2-N girder deck to joint interface

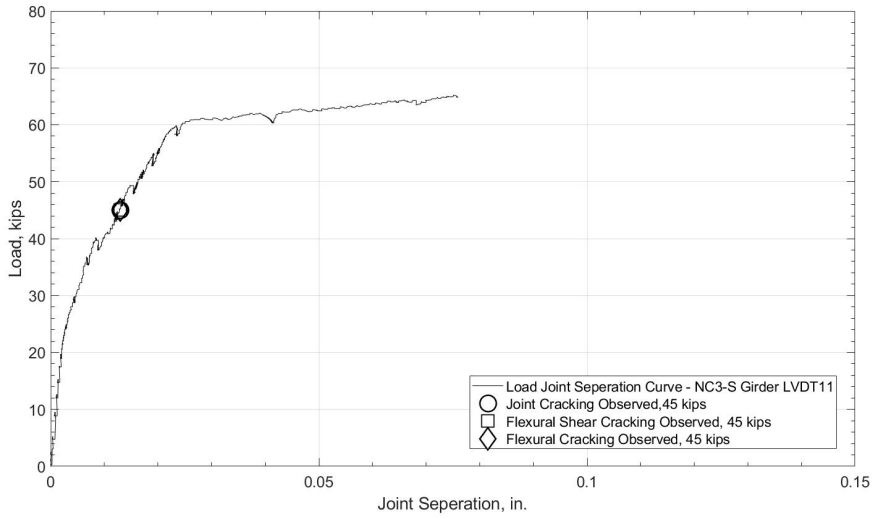

Figure 218. Load-joint separation curve at the NC2-S girder deck to joint interface west face

6.4.2.3 NC3 Positive Moment Test

A positive moment test was conducted on the NC3 specimen, in order to test the positive moment region of the UHPC continuity joint. This approach was intended to recreate the time dependent effects that are applied to the continuity joint and create the positive moment that often results in cracking. The supports were removed at the NC3-N and NC3-S joint interface to create a simply supported span with the UHPC joint at the middle of that span. The two loads were then applied in the exact location as the negative moment tests to the girders to create positive moment in the continuity joint region. Initial flexural cracking was observed along the joint interface at a load of 4.5 kips, as indicated with dark lines in Figure 219. As the load progressed, the flexural crack progressed upward along the joint causing joint separation. A flexural crack was observed at 7.2 kips near the joint interface on the NC3-S girder, as indicated in Figure 219(b) with a dark oval. Upon reaching the 7 kip mark the positive moment test was stopped to prevent any additional damage to the joint, as this test was conducted only to see the initial cracking behavior of the joint under this loading condition. No flexural cracks were observed in the UHPC joint.

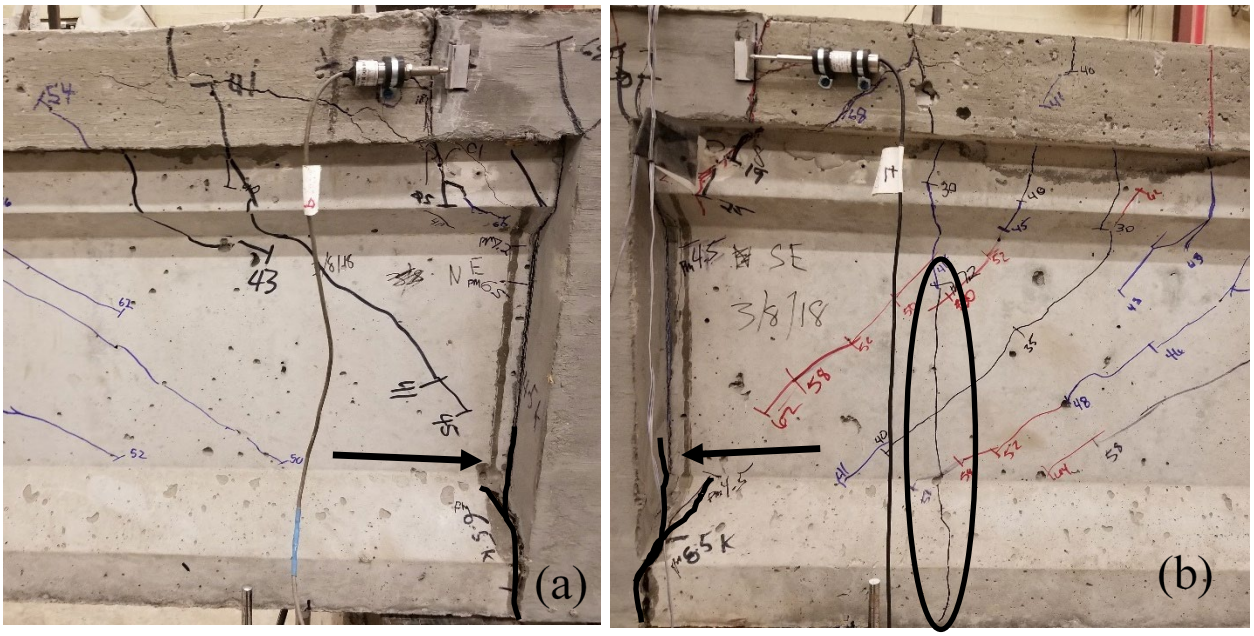

Figure 219. Joint separation at the interface between the NC3-N girder and the UHPC joint during the positive moment test (a) and joint separation at the interface between the NC3-S girder and the UHPC joint (b) are indicated by dark lines. Flexural crack near the joint interface in the NC3-S girder (b) is indicated by a dark oval.

6.4.2.4 Test NC3

Initial flexural cracking was observed near the joint interface on the NC3-S girder at a load of 19 kips, shown in Figure 220(b). After the next load increment, asymmetrical flexural cracks were observed in the continuity joint at a load of 25 kips, shown in Figure 221. In addition, a flexural crack had developed in the NC3-N girder near the joint interface, shown in Figure 220(a). Initial flexure-shear cracking was observed near the joint interface on the NC3-S glider at a load of 35 kips, shown in Figure 220(b). Two cracks were observed at a load of 41 kips, a flexural crack directly under the load point on the NC3-N girder, shown in Figure 222(a), and a flexure-shear crack near the joint interface on the NC3-N girder, shown in Figure 220(a). After the next load increment a flexural crack had developed directly under the load point on the NC3-S girder at a load of 46 kips, shown in Figure 222(b).

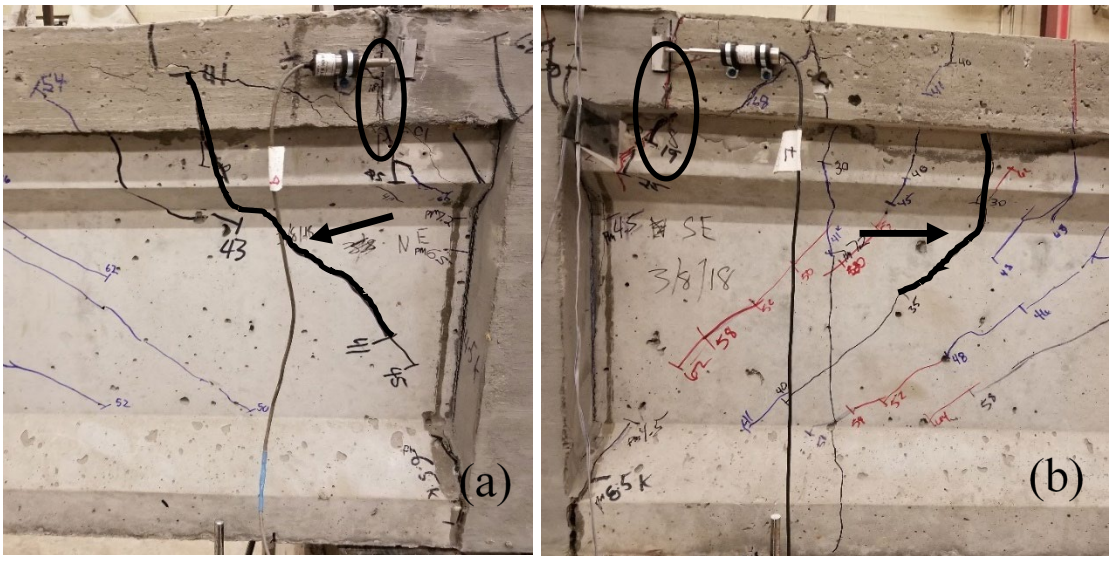

Figure 220. Initial flexural cracking on the NC3-N girder at 25 kips of load and initial flexure-shear cracking on the NC3-N girder at 41 kips of load (a) and initial flexural cracking on the NC3-S girder at 19 kips of load and flexure-shear cracking on the NC3-S girder at 35 kips of load (b). Dark circles show the initial flexural cracking near the continuity joint and arrows point to the dark lines that indicate the initial flexural shear cracking.

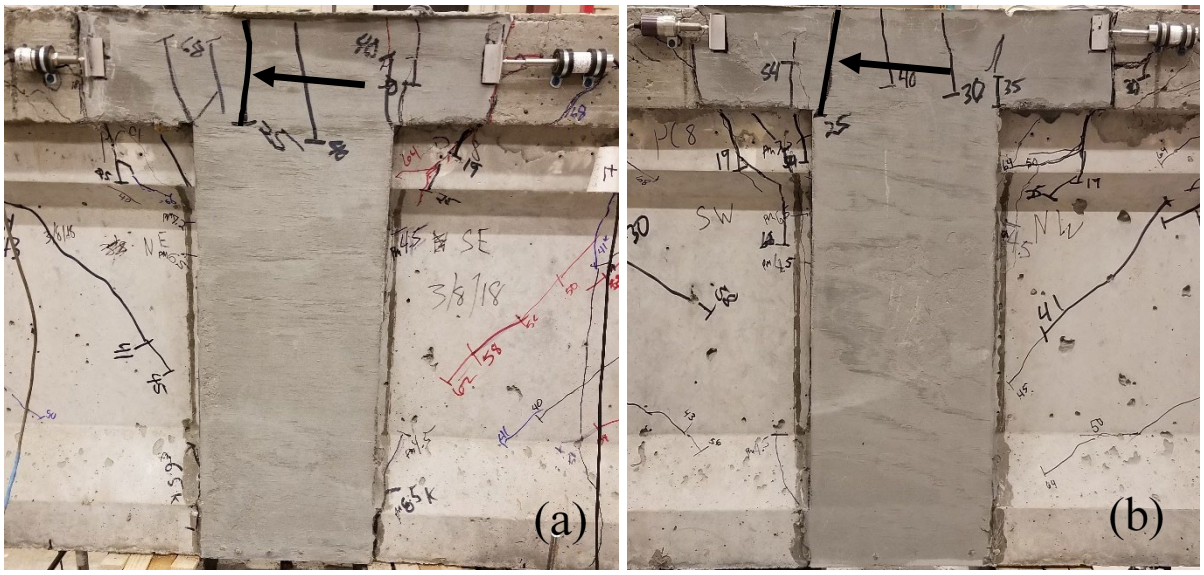

Figure 221. Initial continuity joint flexural cracking on the west face (a) and east face (b) at 25 kips of load. Arrows point to the dark lines that indicate the initial flexural cracks.

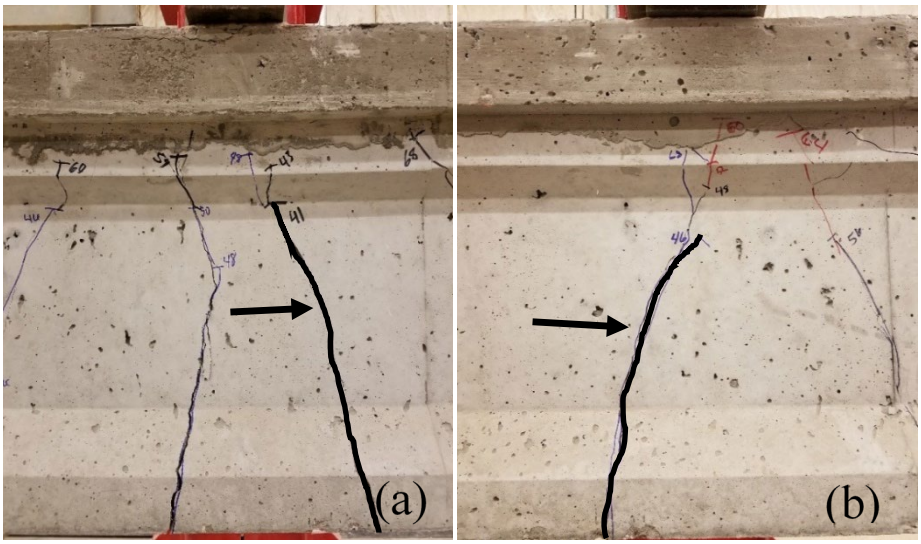

Figure 222. Initial flexural cracking under the load point on the NC3-N girder at 41 kips of load (a) and initial flexural cracking under the load point on the NC3-S girder at 46 kips of load (b). Arrows point to the dark lines that indicate the initial flexural cracks.

Cracks that developed between initial cracking and final failure included additional flexural cracks under the point load, flexure-shear cracks near the joint interface, web shear cracks near the point load, and flexural cracks in the UHPC joint. Most of the cracks observed on the NC3 specimen at final failure were flexure-shear and web shear cracks. These cracks developed as the load increased and the flexure-shear cracks propagated away from the joint interface toward the load point. At approximately halfway to the load point from the joint, web shear cracks developed in place of the flexure-shear cracks. Figure 223 shows the flexural cracks and shear cracks between the joint interface and load point for the NC3-N and NC3-S girders at failure.

Loading of the specimen was stopped upon reaching an applied load of 69.8 kips on the NC3-N girder and 70.2 kips on the NC3-S girder. Under these loading conditions the concrete deck began to crush at the load point on the NC3-N girder, as shown by the dark circle in Figure 224. There was no visual concrete crushing in the NC3-S girder. In addition, there was significant widening of the flexural cracks under both load points, as shown by dark lines in Figure 224. These conditions were taken to indicate flexural failure of the beam specimens and testing was concluded to prevent the prestressing strands from rupturing and causing damage to the testing apparatus.

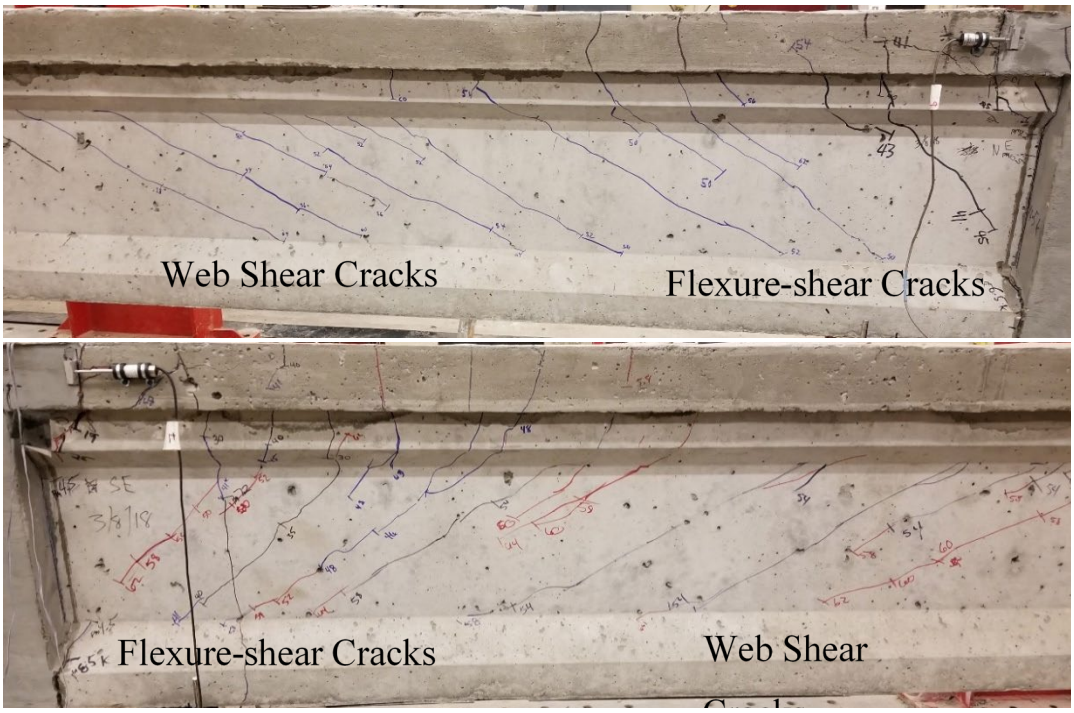

Figure 223. NC3-N girder with flexure-shear and shear cracks top and NC3-S girder with flexure-shear and shear cracks (bottom).

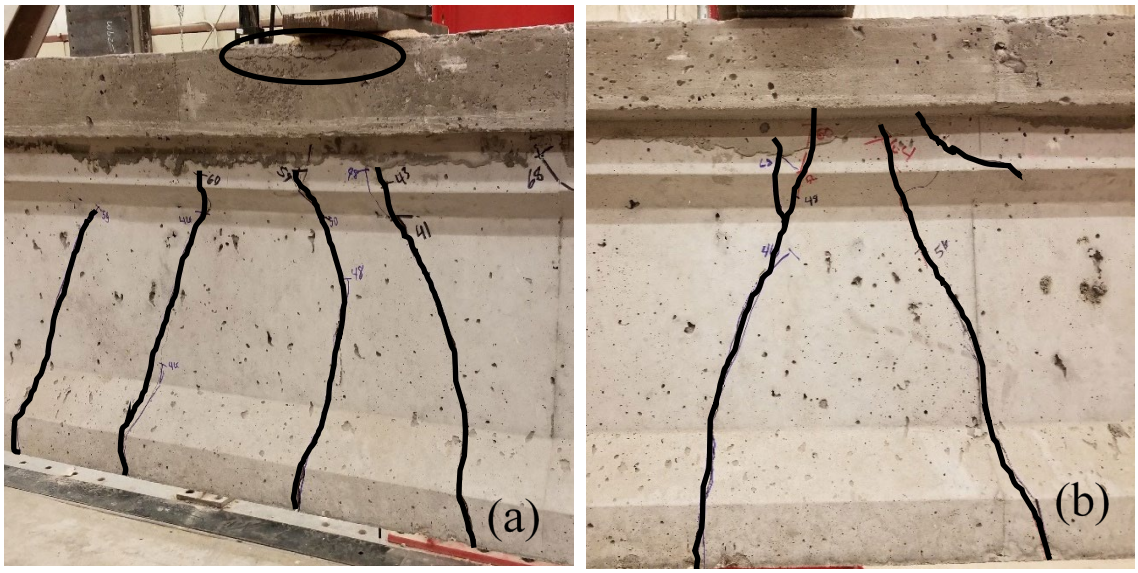

Figure 224. Crushed concrete deck in the NC3-N girder is indicated by a black oval (a) and the final flexural cracking under the load point in the NC3-N (a) and NC3-S (b) girders are indicated by dark lines.

The interface between the NC3-N girder and the UHPC joint had preexisting flexural cracking from the positive moment test, shown in Figure 220(a). Flexural

cracking occurred along the top portion of the joint interface that extended into the preexisting crack during the final load test. This resulted in separation of the girder from the joint, as shown by the dark lines in Figure 225(a). The same type of flexural cracking occurred at the NC3-S girder and UHPC joint interface, as shown by the dark lines in Figure 225(b).

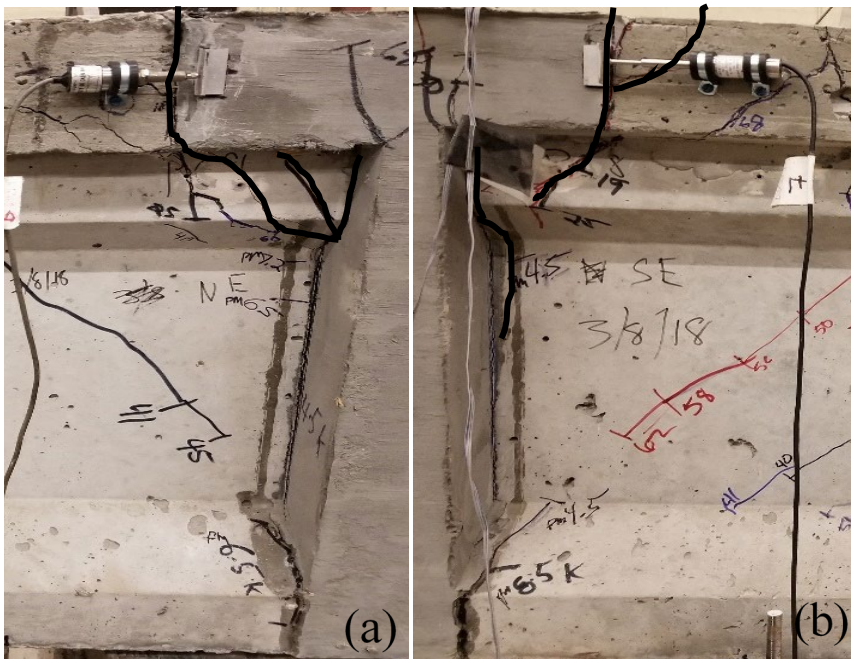

Figure 225. Joint separation at the interface between the NC3-N girder and the UHPC joint (a) and separation at the interface between the NC3-S girder and the UHPC joint (b) are indicated by dark lines.

Figure 226 shows the load-deflection curve for the NC3-N girder. The curve shows a reduction in stiffness that corresponds with the initial flexural and flexure-shear cracking observed at 41 kips. Initial cracking of the UHPC joint did not reduce the stiffness of the girder. This indicates ductile behavior of the NC2-N prestressed girder during loading up to the ultimate load of 69.8 kips. In addition, the plateau of the load-deflection curve out to 2 in. of deflection also indicated the prestressing strands were yielding. Figure 227 shows the load-deflection curve for the NC3-S girder. The NC3-N and NC3-S girders exhibited the same ductile behavior, but with the NC3-N girder having more than 1 in. more deflection at mid-span than NC3-S. The varying deflection of the girders can be related to differences in the concrete mix, compressive strength, modulus of elasticity, and a difference in prestress loss between the girders. These

variables could have caused the NC3-N girder to crack in flexure 5 kips earlier in load than the NC3-S girder and could have resulted in the NC3-N girder having a reduced stiffness compared to the NC3-S girder. This led to a larger downward curvature, which created more strain in the prestressing strands, and led to larger deflection in the NC3-N girder.

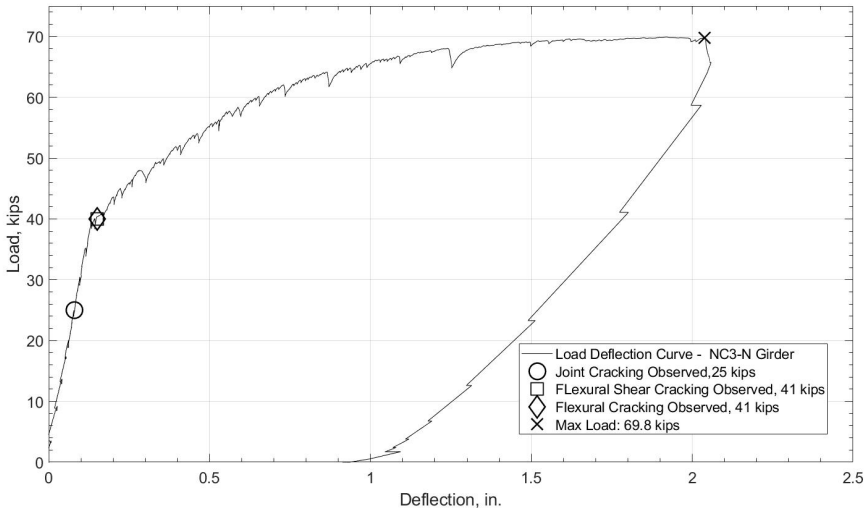

Figure 226. Load-deflection curve for the NC3-N girder

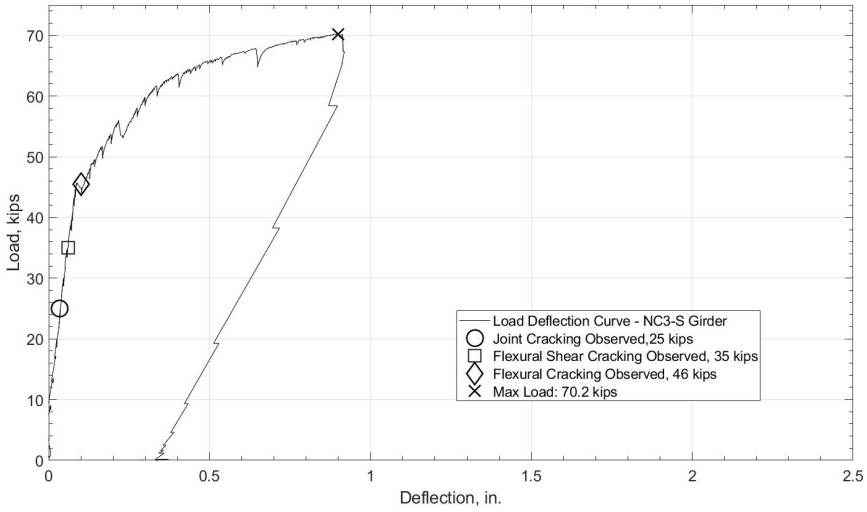

Figure 227. Load-deflection curve for the NC3-S girder

Figure 228 shows the load-joint separation curve between the NC3-N girder's concrete deck and the UHPC joint. The results from the LVDTs on the east and west

face of the concrete deck were averaged to provide a better representation of the joint separation. The LVDTs on the joint interface were located 2 in. below the top of the deck. The deck joint had minor separation until reaching the 60 kip load mark. As the girder cracked in flexure, the reduction of girder stiffness appeared to have no effect on the rate of joint separation. The joint began to separate after the 60 kip mark more significantly because the girder began to have more downward curvature, creating a hinge at the weak point; that is the joint interface. Figure 229 shows the load-joint separation curve between the NC3-S girder's concrete deck and the UHPC joint. This figure only presents data from LVDT11 on the west face of the deck. The NC3-N and NC3-S curves closely match one another in behavior expect the NC3-S separation curve shows less separation occurring. This is most likely due to the NC3-S girder having less deflection at the mid span of the girder, and the NC3-N girder having more resulting in more joint separation at the NC3-N girder to deck joint interface.

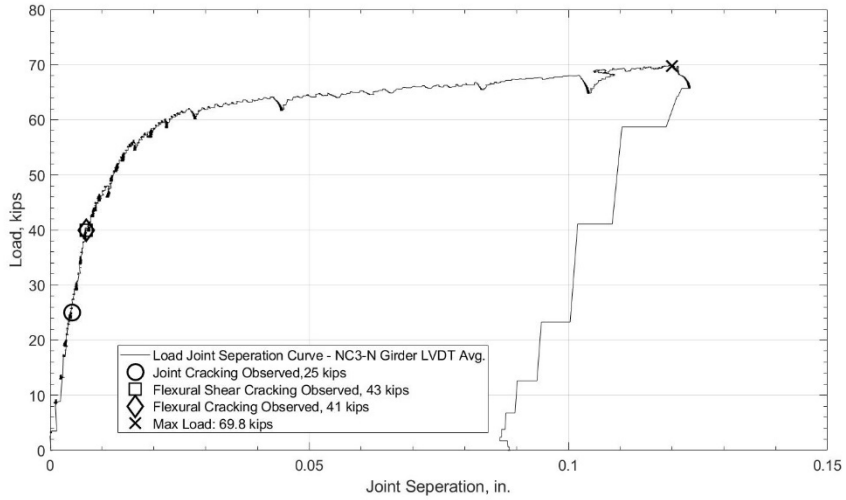

Figure 228. Load-joint separation curve at the NC3-N girder deck to UHPC joint interface.

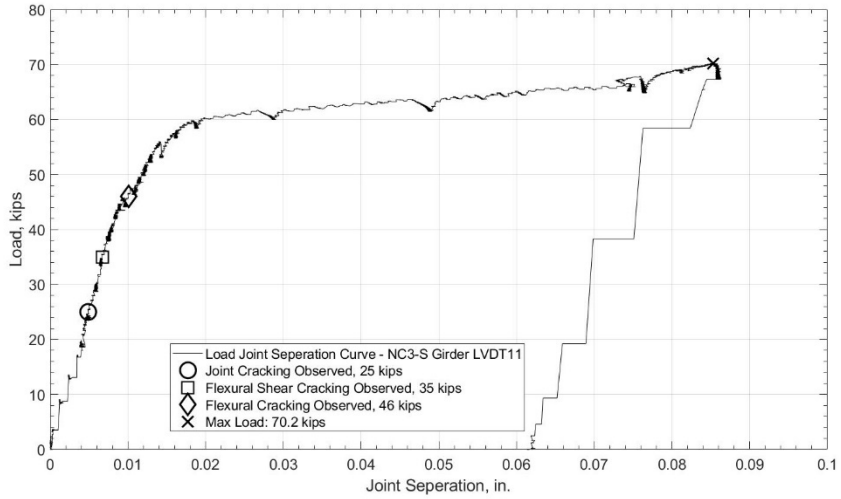

Figure 229. Load-joint separation curve at the NC3-S girder deck to UHPC joint interface

Overall, the NC3 specimen performed quite well considering the additional positive moment test done to the specimen before the negative moment test was performed. The load-deflection graphs, and the load-joint separation graphs of the NC3 compared quite well to the NC1 and NC2 graphs.

6.4.3 Retrofit Construction (RC) Specimens

6.4.3.1 Test RC1

Initial flexural cracking was observed near the joint interface on the RC1-N and RC1-S girders at a load of 20 kips, indicated in Figure 230 with dark ovals. An initial flexure-shear crack was observed after the next loading increment near the joint interface on the RC1-S specimen at a load of 25 kips, shown in Figure 230(b). A similar flexure-shear crack to that which had developed on the RC-S girder was observed on the RC1-N girder at a load of 30 kips, shown in Figure 230(a). A flexural crack was observed directly under the load point on RC1-S girder at a load of 45 kips, shown in Figure 231(b). During the following load increment a flexural crack developed directly under the load point on the RC1-N girder, shown in Figure 231(a). The first flexural crack observed in the continuity joint occurred on the east face at a load of 60 kips, shown in Figure 232(a). On the next load increment a flexural crack developed on the west face of the joint at a load of 62 kips, shown in Figure 232(b).

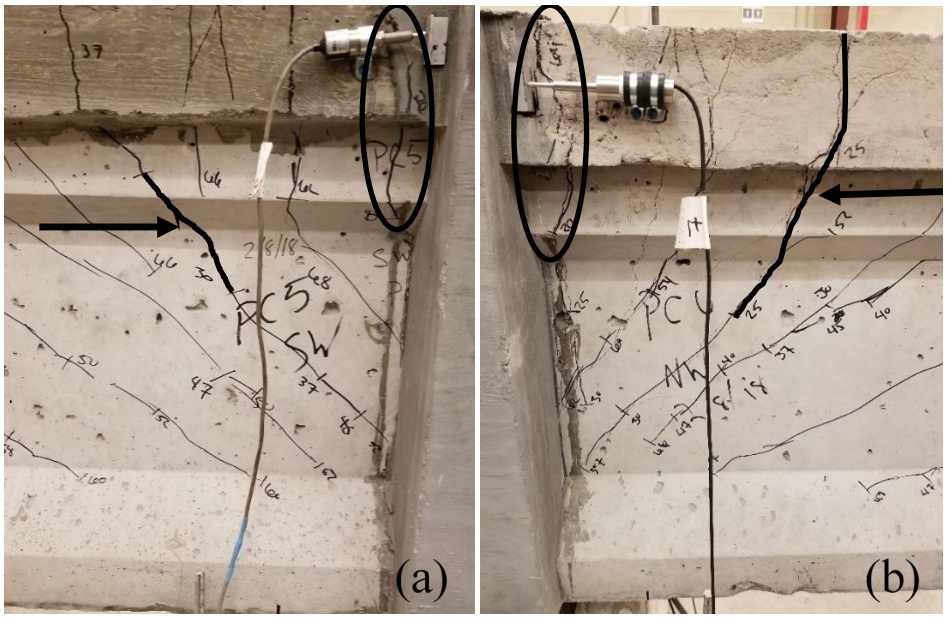

Figure 230. Initial flexural cracking on the NC1-N girder at 25 kips of load and initial flexure-shear cracking on the NC1-N girder at 41 kips of load (a) and initial flexural cracking on the NC1-S girder at 19 kips of load and flexure-shear cracking on the NC1-S girder at 35 kips of load (b). Dark ovals show the initial flexural cracking near the continuity joint, and arrows point to the dark lines that indicate the initial flexure-shear cracking.

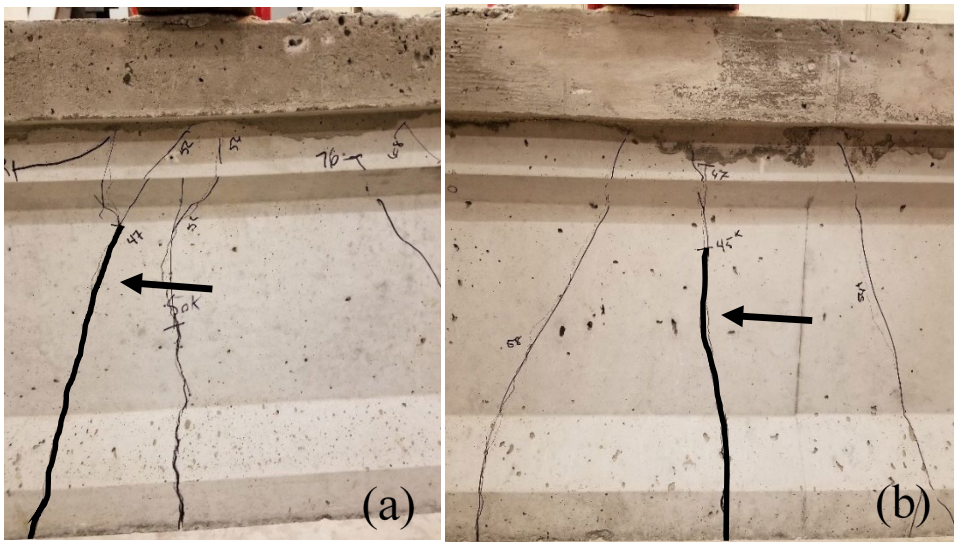

Figure 231. Initial flexural cracking under the load point on the NC2-N girder at 47 kips of load (a) and initial flexural cracking under the load point on the NC2-S girder at 45 kips of load (b). Arrows point to the dark lines that indicate the initial flexural cracks.

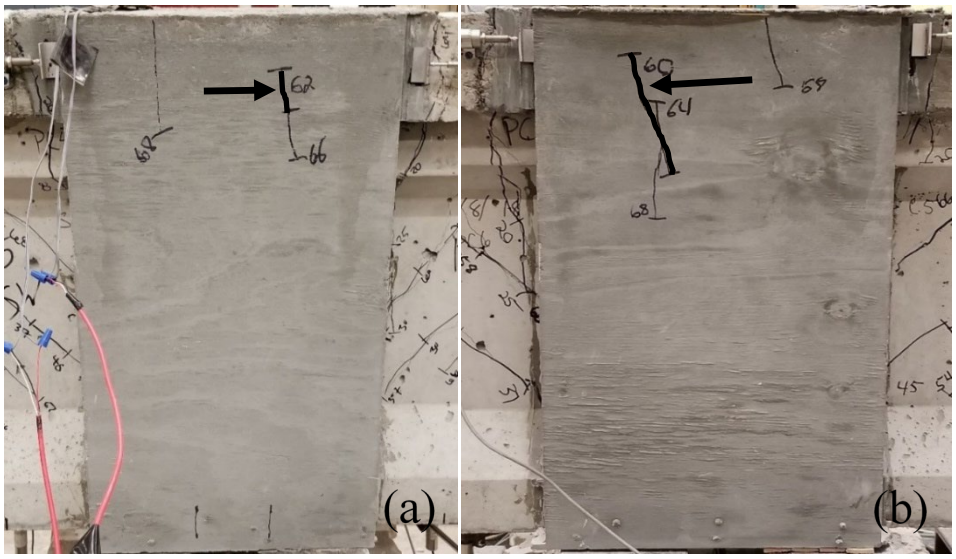

Figure 232. Initial continuity joint flexural cracking on the east face at a load of 62 kips (a) and initial continuity joint flexural cracking on the west face at a load of 60 kips (b). Arrows point to the dark lines that indicate the initial flexure cracks.

Cracks that developed between initial cracking and final failure included additional flexural cracks under the point load, flexure-shear cracks near the joint interface, web shear cracks near the point load, and flexural cracks in the UHPC joint. The majority of cracks that occurred between initial cracking and failure were flexure-shear and web shear cracks for the RC1 specimen. These cracks developed as the load increased and the flexure-shear cracks began to move away from the joint interface towards the load point. Upon reaching approximately halfway to the load point from the joint, web shear cracks developed in place of the flexure-shear cracks. Figure 233 shows the flexure-shear cracks and web shear cracks between the joint interface and load point for the RC1-N and RC1-S girders.

Loading of the specimen was stopped upon reaching an applied load of 76 kips on the RC1-N girder and 75.9 kips on the RC1-S girder. Under these loading conditions the concrete deck began to crush at the load point in both girders, as shown by the dark circles and arrows in Figure 234. In addition, there was significant widening of the flexural cracks under both loads points, as shown by dark lines and arrows in Figure 234. These conditions were taken to indicate flexural failure of the beam specimens and testing was concluded to prevent the prestressing strands from rupturing and causing damage to the testing apparatus.

Figure 233. RC1-N girder with flexure-shear cracks and web shear cracks at failure (top) and RC1-S girder with flexure-shear cracks and web shear cracks at failure (bottom)

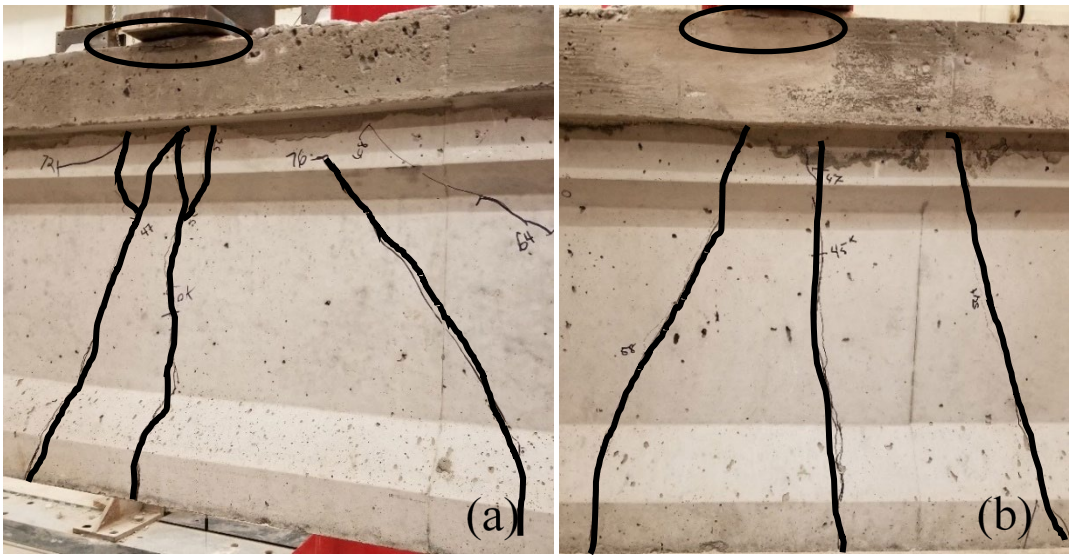

Figure 234. Crushed deck concrete in the RC1-N (a) and RC1-S (b) girders is indicated by a black oval, and the final flexural cracking under the load point in the RC1-N (a) and RC1-S (b) girders is indicated by dark lines.

Flexural cracking occurred at the interface between the RC1-N girder deck and the UHPC joint, which resulted in separation of the deck from the joint. However, the

flexural crack from the concrete deck joint interface continued vertically down into the RC1-N girder's flange and then into the web before diverting back towards the joint interface, as shown in Figure 235(a). The interface between the RC1-S girder and the UHPC joint exhibited similar flexural cracking to the RC1-N girder and joint interface, as shown in Figure 235(b).

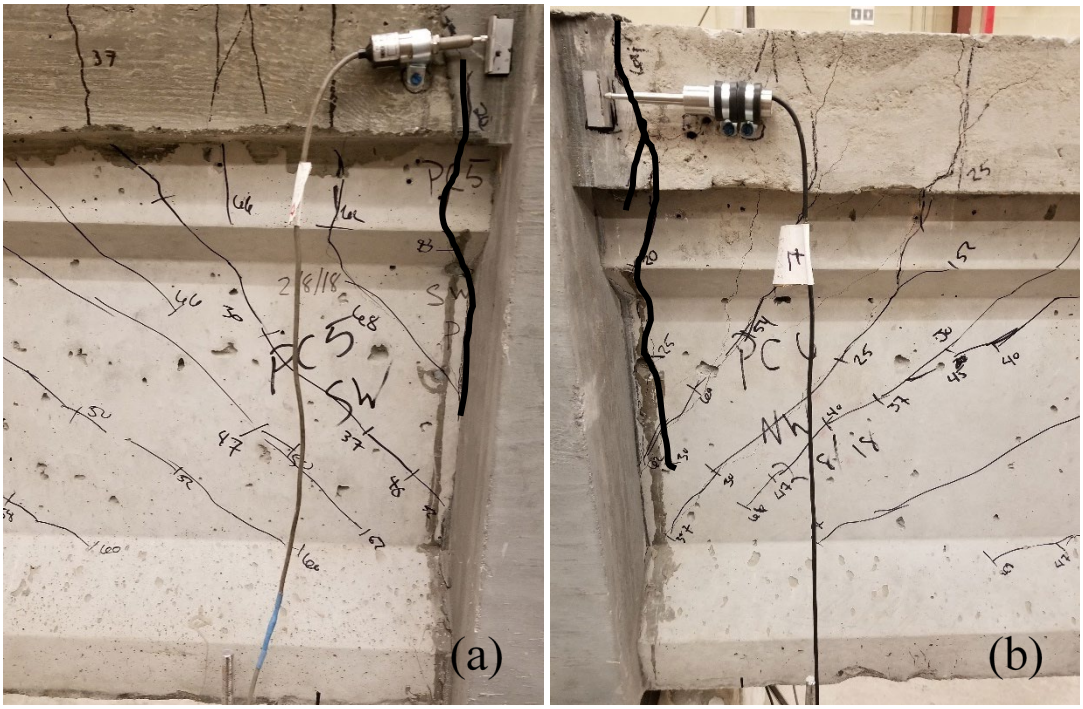

Figure 235. Joint separation at the interface between the RC1-N concrete deck and the UHPC joint with the flexural crack going vertically down in the girder (a) and joint separation at the interface between the RC1-S concrete deck and the UHPC joint with the flexural crack going vertically down in the girder (b) are indicated by dark lines.

Figure 236 shows the load-deflection curve for the RC1-N girder. The curve shows a reduction in stiffness that corresponds with the initial flexural cracking observed at 47 kips. Other types of initial cracking did not reduce the stiffness of the girder. The load-deflection curve indicates a ductile behavior of the RC1-N prestressed girder during loading up to the ultimate load of 76 kips. The plateau of the load-deflection curve out to 1.5 in. of deflection also indicated the prestressing strands were yielding. Figure 237 shows the load-deflection curve for the RC1-S girder. The RC1-N and RC1-S girders had the same ductile behavior, but with the RC1-S girder having less deflection at mid-span. The varying deflection of the girders can be related to potential

differences in the concrete mix, compressive strength, modulus of elasticity, and in prestress loss between the girders. These variables could have resulted in the RC1-N girder having a reduced stiffness compared to the RC1-S girder. This reduced stiffness led to a larger downward curvature, which created more strain in the prestressing strands, and led to larger deflection in the RC1-N girder.

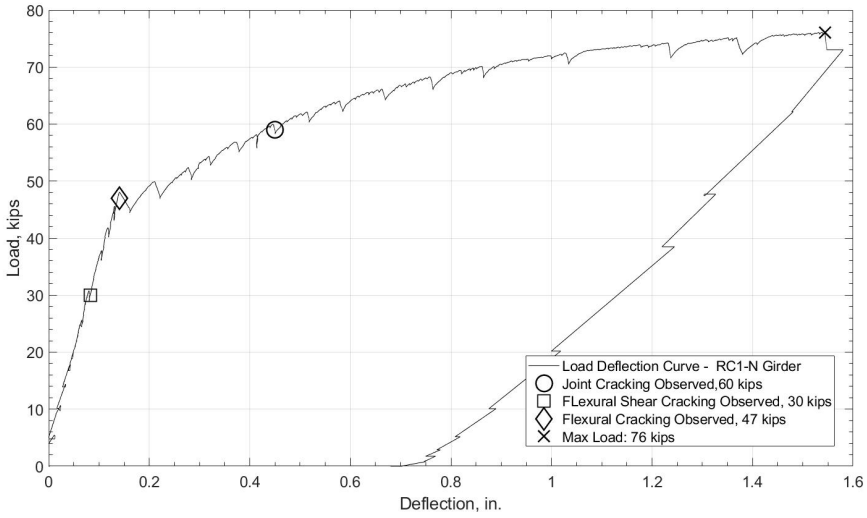

Figure 236. Load-deflection curve for the RC1-N girder

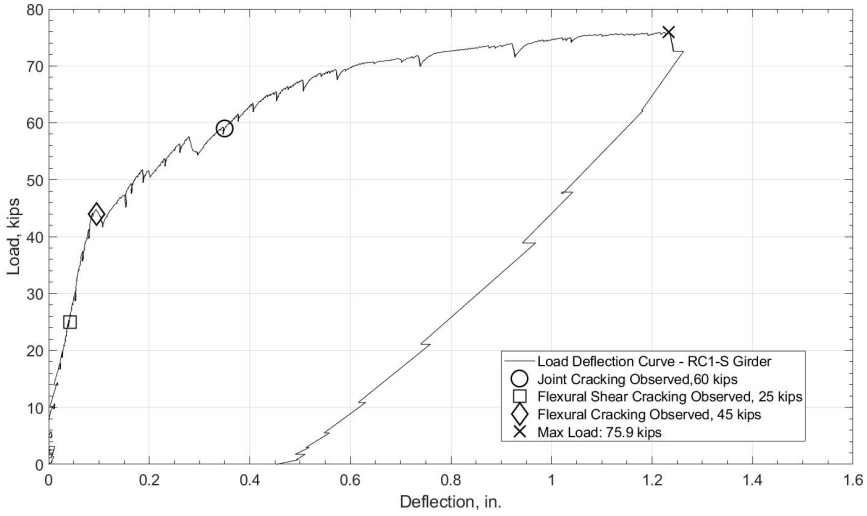

Figure 237. Load-deflection curve for the RC1-S girder

Figure 238 shows the load-joint separation curve between the RC2-N girder's concrete deck and the UHPC joint. The average of the readings from the LVDTs on the

east and west face of the concrete deck was taken to get a better representation of the joint separation. The LVDTs on the joint interface were located 2 in. below the top of the deck. The deck joint had minor separation until reaching the initial flexural cracking of 47 kips. After the 47 kip load, indicated by a diamond shape on Figure 238, the joint separation began to increase significantly with each load increment. This makes sense because major joint separation could only occur after the girder cracked due to flexure, resulting in a less stiff member and creating a hinge at the weak point being the joint interface. The LVDTs on the RC2-S girder's concrete deck did not collect reliable data and the measurements from these instruments were excluded from this section.

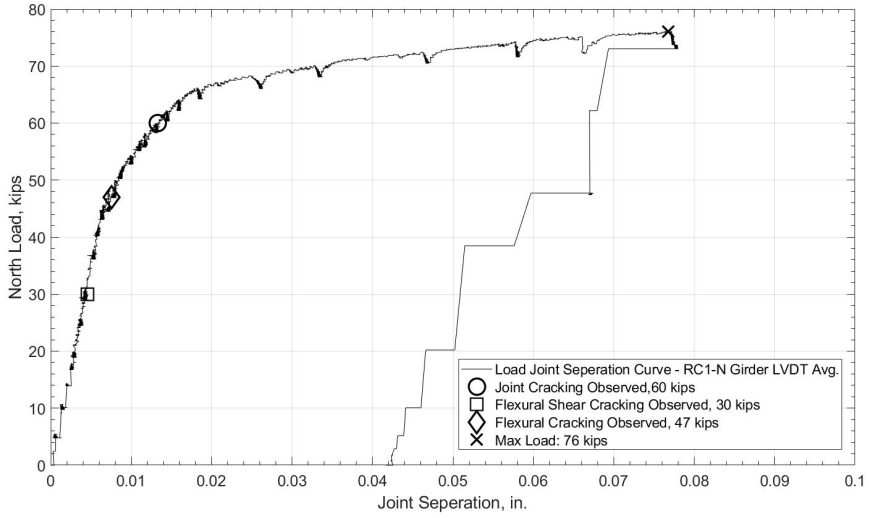

Figure 238. Load joint separation curve at the RC1-N girder deck to UHPC joint interface

6.4.3.2 Test RC2

Initial flexural cracking was observed near the joint interface on the RC1-S girder at a load of 19.5 kips, indicated in Figure 239(b) by a dark oval. Asymmetrical flexural cracks were observed on the continuity joint after the next load increment, at a load of 25 kips, as shown in Figure 240. In addition, two more cracks had developed at 25 kips of load, a flexural crack near the joint interface on the RC2-N girder, indicated in Figure 240(a) by a dark oval, and a flexure-shear crack near the joint interface on the RC2-S girder, shown in Figure 239(b). At the next load increment a flexure-shear crack developed on the RC2-N girder, shown in Figure 239(a). Flexural cracking directly

under the load point was observed on the RC2-N and RC2-S girders at a load of 44 kips, shown in Figure 241.

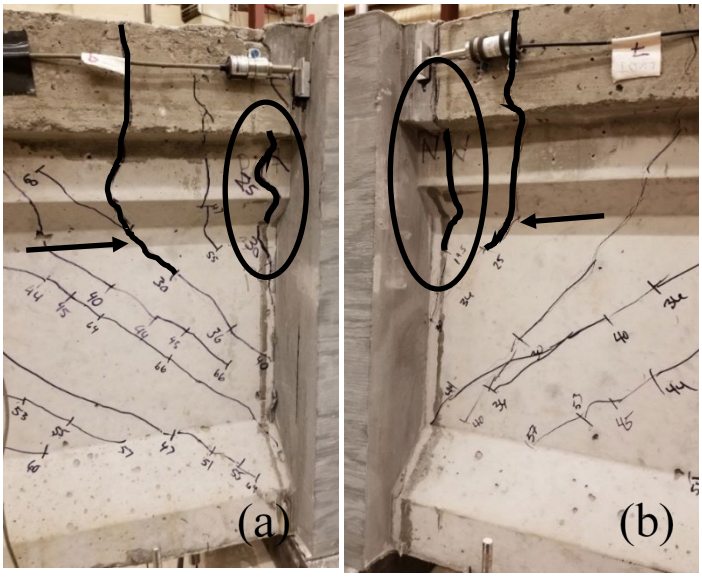

Figure 239. Initial flexural cracking on the RC2-N girder at 25 kips of load and initial flexure-shear cracking on the RC2-N girder at 30 kips of load (a) and initial flexural cracking on the RC2-S girder at 19.5 kips of load and flexure-shear cracking on the RC2-S girder at 25 kips of load (b). Dark ovals show the initial flexural cracking near the continuity joint and arrows point to the dark lines that indicate the initial flexure-shear cracking.

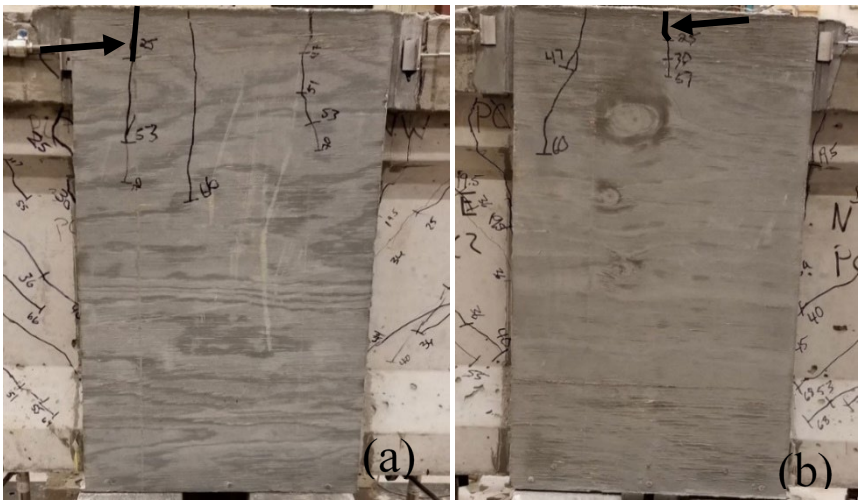

Figure 240. Initial continuity joint flexural cracking on the east face (a) and west face (b) at 25 kips of load. Arrows point to the dark lines that indicate the initial flexural cracks.

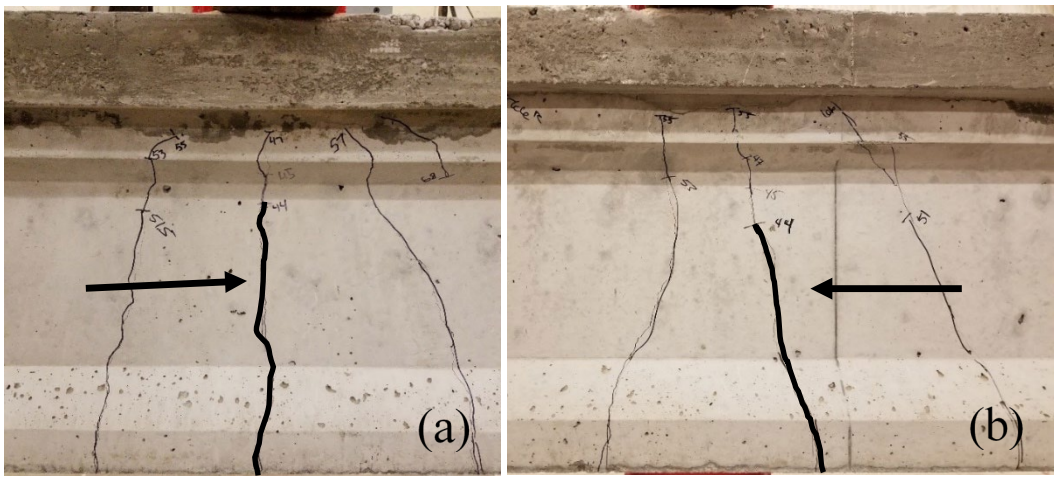

Figure 241. Initial flexural cracking under the load point on the RC2-N girder at 44 kips of load (a) and initial flexural cracking under the load point on the RC2-S girder at 44 kips of load (b). Arrows point to the dark lines that indicate the initial flexural cracks.

Cracking that developed between initial cracking and final failure included additional flexural cracks under the point load, flexure-shear cracks near the joint interface, web shear cracks near the point load, and flexural cracks in the UHPC joint. Most of the cracks that occurred in the RC2 specimen between initial cracking and failure were flexure-shear and shear cracks. These cracks developed as the load increased and the flexure-shear cracks began to move away from the joint interface toward the load point. Approximately halfway to the load point from the joint web shear cracks developed in place of flexure-shear cracks. Figure 242 shows the flexural cracks and shear cracks between the joint interface and load point for the RC2-N and RC2-S girders.

Loading of the specimen was stopped upon reaching an applied load of 74.1 kips on the NC2-N girder and 74.2 kips on the NC2-S girder. Under these loading conditions the concrete deck began to crush at the load point in both girders. This is not clear in Figure 243 due to the crushing not being significant on the east face. In addition, there was significant widening of the flexural cracks under both load points, as shown by dark lines in Figure 243. These conditions were taken to indicate flexural failure of the beam specimens and testing was concluded to prevent the prestressing strands from rupturing and causing damage to the testing apparatus.

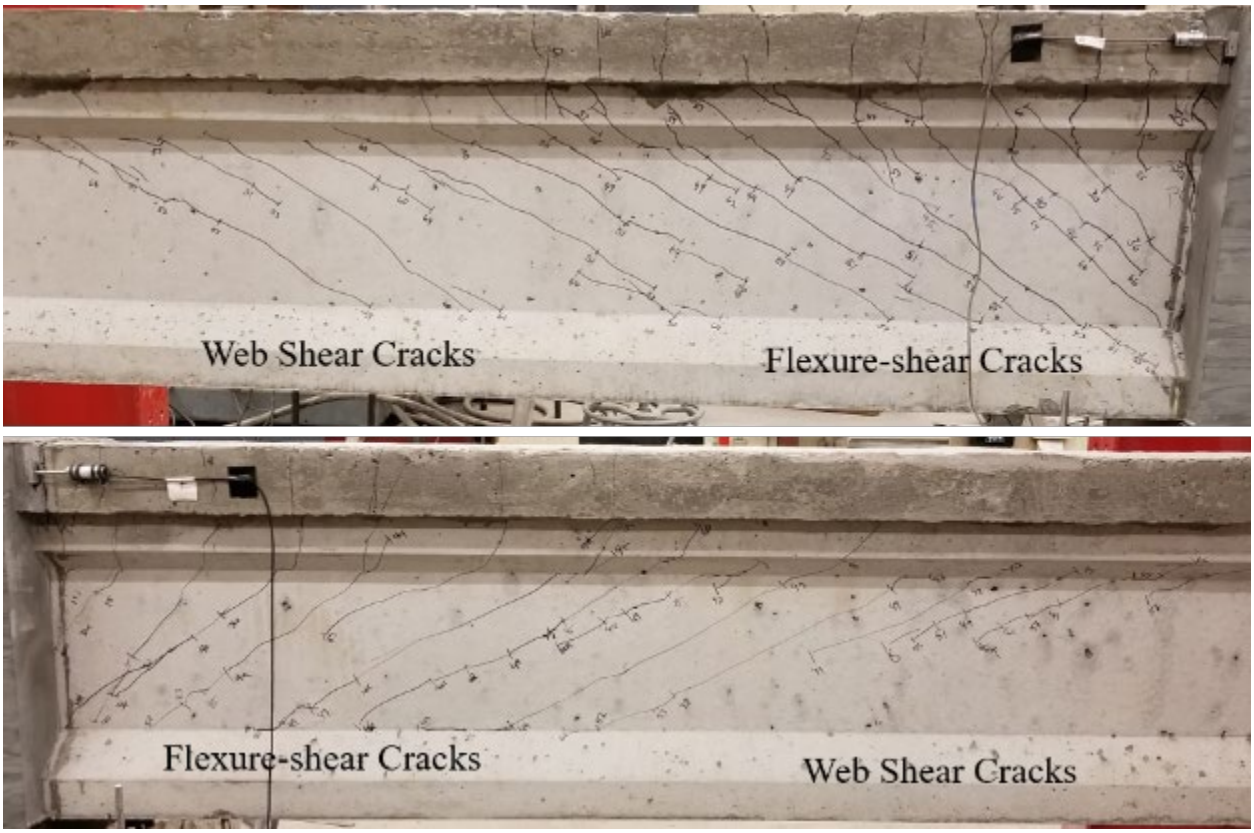

Figure 242. RC2-N girder with flexure-shear cracks and shear cracks (top) and RC2-S girder with flexure-shear cracks and shear cracks (bottom)

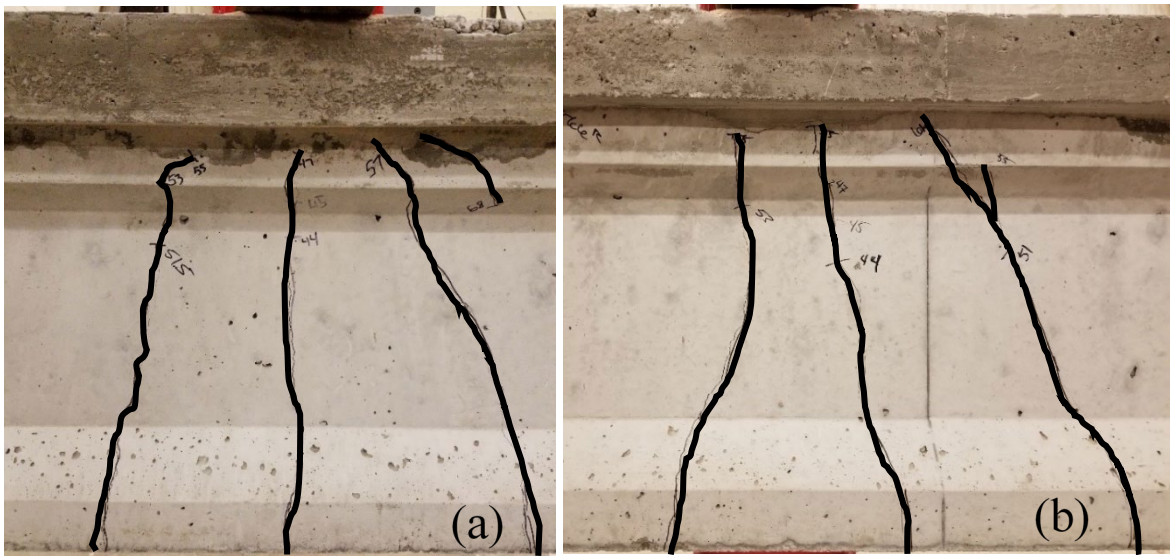

Figure 243. Final flexural cracking under the load point in the RC2-N (a) and RC2-S (b) girders are indicated by dark lines

Flexural cracking occurred between the RC2-N girder deck and the UHPC joint, which resulted in separation of the deck from the joint. However, the flexural crack from the concrete deck joint interface continued vertically down into the RC2-N girder's flange and then into the web before diverting back towards the joint interface, as shown in Figure 244(a). The interface between the RC2-S girder and the UHPC joint had similar flexural cracking to the RC1-N girder and UHPC joint interface, as shown in Figure 244(b).

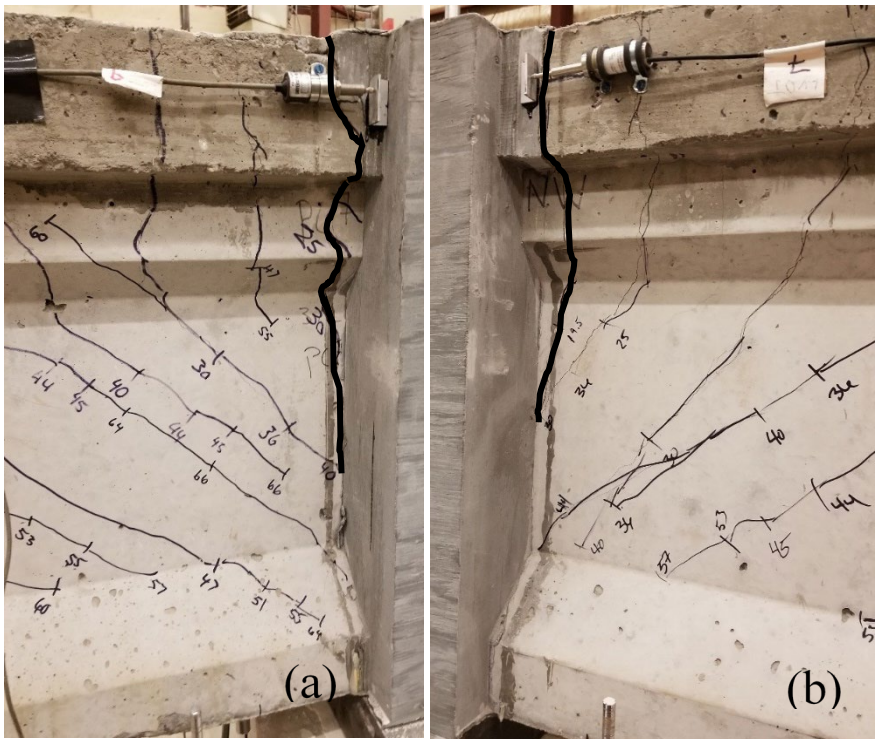

Figure 244. Joint separation at the interface between the RC2-N concrete deck and the UHPC joint with the flexural crack going vertically down in the girder (a) and joint separation at the interface between the RC2-S concrete deck and the UHPC joint with the flexural crack going vertically down in the girder (b) are indicated by dark lines.

Figure 245 shows the load-deflection curve for the RC2-N girder. The curve shows a reduction in stiffness that corresponds with the initial flexural cracking observed at 44 kips. Other types of initial cracking did not reduce the stiffness of the girder. This curve indicates a ductile behavior of the RC2-N prestressed girder during loading up to the ultimate load of 76 kips. In addition, the plateau of the load-deflection curve out to 1.4 inches of deflection also indicated the prestressing strands were yielding. Figure 246 shows the load-deflection curve for the RC2-S girder. The RC1-N and RC1-S

girders had similar ductile behavior, but with the RC1-S girder having less deflection at mid-span. The varying deflection of the girders could be related to differences in the concrete mix, compressive strength, modulus of elasticity, and in prestress loss between the girders. These variables could have resulted in the RC2-N girder having a reduced stiffness compared to the RC2-S girder. The reduced stiffness led to a larger downward curvature, which created more strain in the prestressing strands, and led to larger deflection in the RC2-N girder.

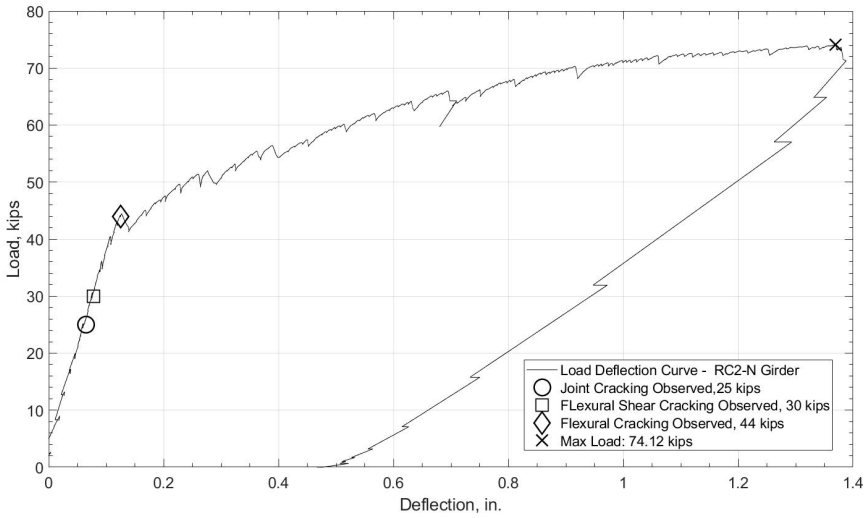

Figure 245. Load-deflection curve for the RC2-N girder

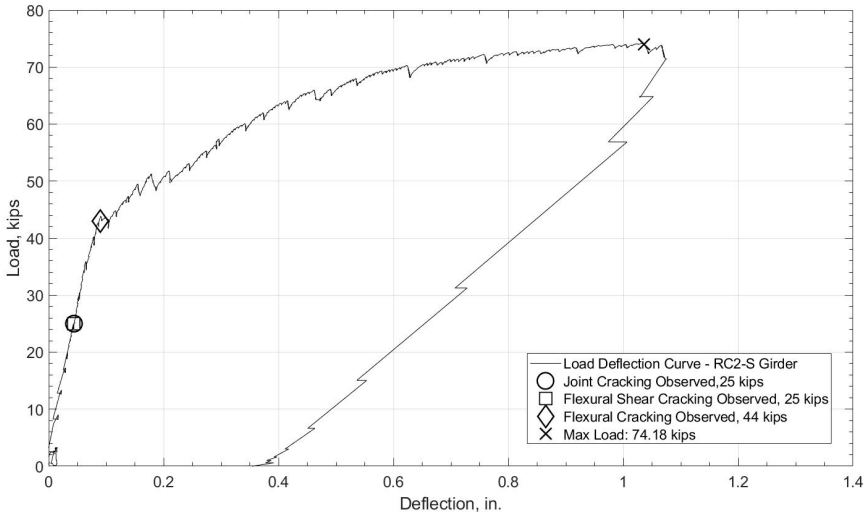

Figure 246. Load-deflection curve for the RC2-S girder

Figure 247 shows the load-joint separation curve between the RC2-N girder's concrete deck and the UHPC joint. This figure only represents LVDT4 on the west face of the deck. LVDT9 on the east face did not give accurate data for this test, and was excluded from the results. The LVDTs on the joint interface were located 2 in. below the top of the deck. The deck joint had minor separation until reaching initial flexural cracking at 44 kips of load. After that load, indicated by a diamond shape on Figure 247, the joint separation began to increase significantly with each load increment. This makes sense because major joint separation could only occur after the girder cracked to flexure, resulting in a less stiff member creating a hinge at the weak point being the joint interface. Figure 248 shows the load-joint separation curve between the RC2-S girder's concrete deck and the UHPC joint. This figure only represents LVDT11 on the west face of the deck. This load-joint separation curve shows a similar trend to the RC2-N side of the joint, but with more deflection.

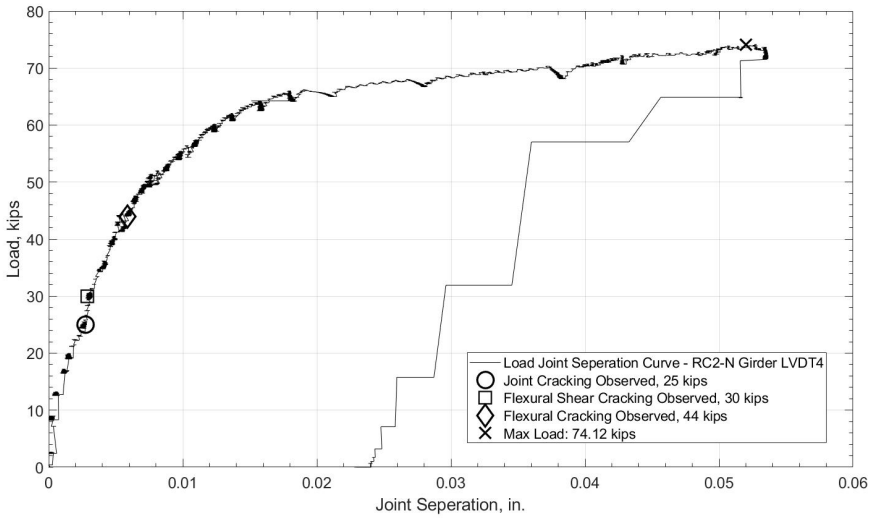

Figure 247. Load-joint separation curve at the RC2-N girder deck to joint interface west face

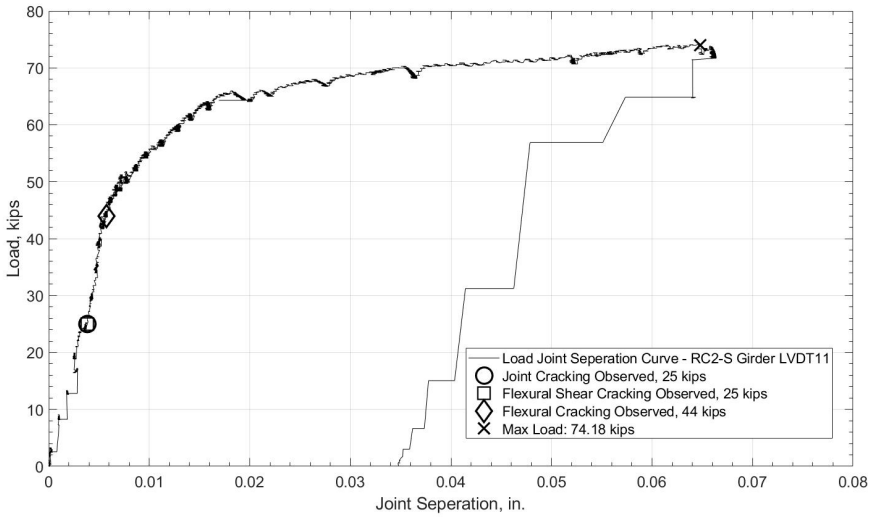

Figure 248. Load-joint separation curve at the RC2-S girder deck to joint interface west face.

6.4.3.3 RC Positive Moment Test

A positive moment test was conducted on the RC3 specimen, as conducted on the NC3 specimen. Initial flexural cracking was observed along the joint interface at a load of 4 kips, as indicated in Figure 249 with a dark oval. No additional cracks were observed up until this point, however it is possible cracks formed on the girder where the UHPC joint overlaps the girder ends, and the cracks were not visually exposed. In addition, no flexural cracks were observed in the UHPC joint. The positive moment test was concluded after the initial crack was observed to prevent additional damage around the joint interface for the negative moment test.

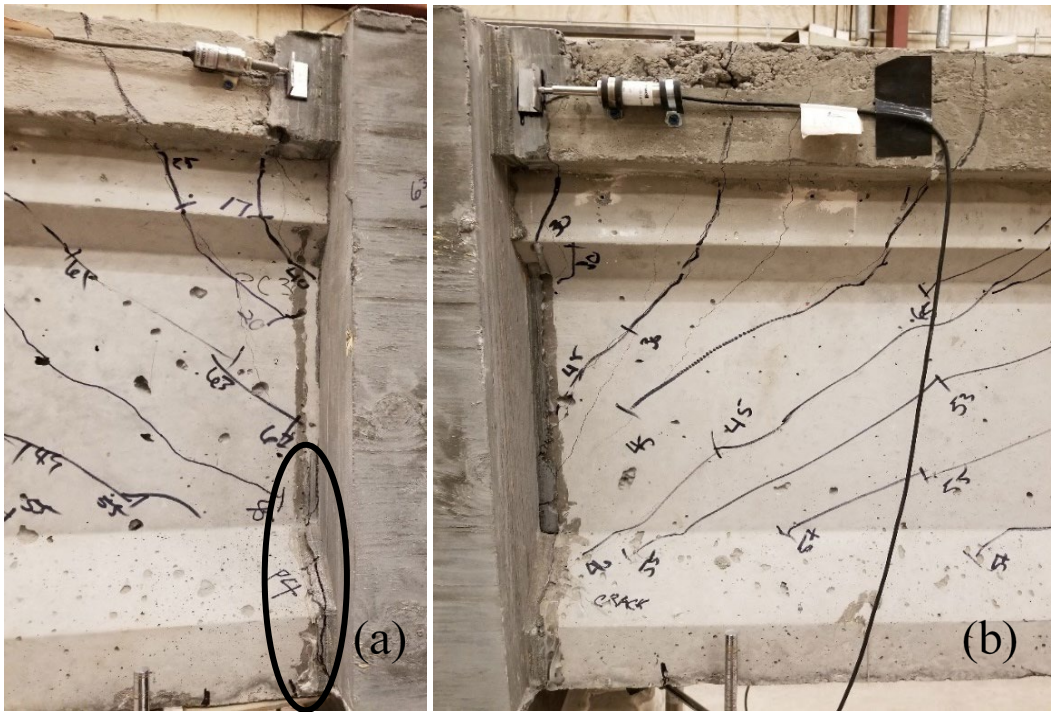

Figure 249. Positive moment joint separation at the interface between the NC3-N girder and the UHPC joint (a) indicated by a dark oval and interface between the NC3-S girder and the UHPC joint showing no visible positive moment cracking (b)

6.4.3.4 Test RC3

Initial flexural cracking was observed near the joint interface on the RC3-N girder at a load of 17 kips, indicated in Figure 250(a) with a dark oval. A flexure-shear crack developed in the same girder at a load of 20 kips, shown in Figure 251(a). Flexural cracks were observed on the east face of the continuity joint after the next load increment, at a load of 30 kips, shown in Figure 251(a). In addition, two more cracks had developed at a load of 30 kips, a flexural crack near the joint interface in the RC3-S girder, indicated in Figure 250(b) with a dark oval, and a flexure-shear crack near the joint interface in the RC3-S girder, shown in Figure 250(b). Flexural cracking directly under the load point was observed in the RC2-N at a load of 45 kips, and in the RC3-S girder at a load of 46 kips, shown in Figure 252. A flexural crack was observed on the west face of the continuity joint at a load of 51 kips, shown in Figure 251(b).

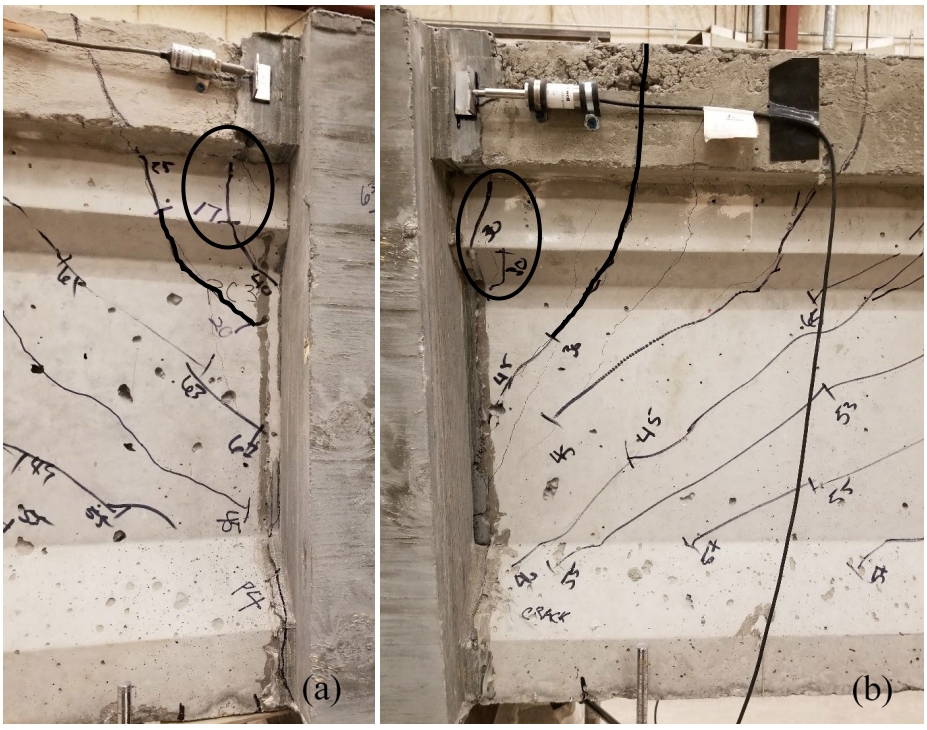

Figure 250. Initial flexural cracking on the RC3-N girder at 17 kips of load and initial flexure-shear cracking on the RC3-N girder at 20 kips of load (a) and initial flexural cracking on the RC3-S girder at 30 kips of load and flexure-shear cracking on the RC3-S girder at 30 kips of load (b). Dark ovals show the initial flexural cracking near the continuity joint and arrows point to the dark lines that indicate the initial flexure-shear cracking.

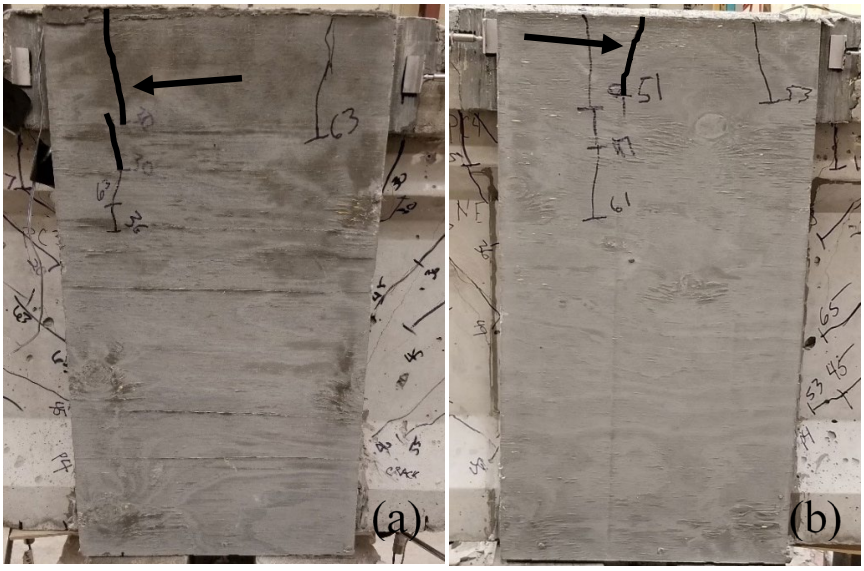

Figure 251. Initial continuity joint flexural cracking on the east face at a load of 30 kips (a) and initial continuity joint flexural cracking on the west face at a load of 51 kips (b). Arrows point to the dark lines that indicate the initial flexural cracking.

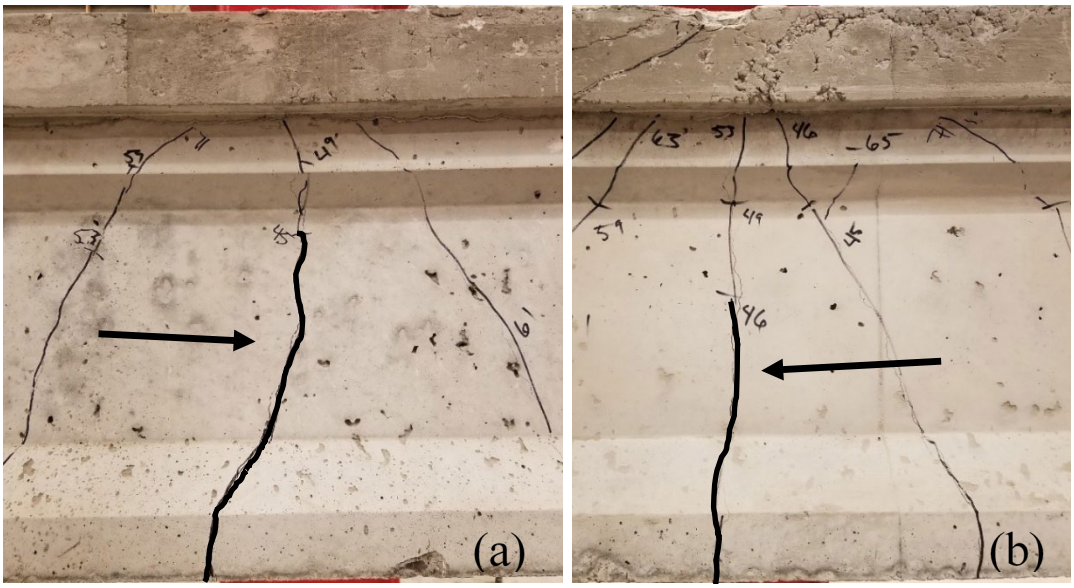

Figure 252. Initial flexural cracking under the load point on the RC3-N girder at 45 kips of load (a) and initial flexural cracking under the load point on the RC3-S girder at 46 kips of load (b). Arrows point to the dark lines that indicate the initial flexural cracks.

Cracking that developed between initial cracking and final failure included additional flexural cracks under the point load, flexure-shear cracks near the joint interface, web shear cracks near the point load, and flexural cracks in the UHPC joint. Most of the cracks that occurred in the RC3 specimen between initial cracking and failure were flexure-shear and web shear cracks. These cracks developed as the load increased and the flexure-shear cracks began to move away from the joint interface toward the load point. Upon reaching approximately halfway to the load point from the joint, web shear cracks developed in place of the flexure-shear cracks. Figure 253 shows the flexural cracks and web shear cracks between the joint interface and load point for the RC3-N and RC3-S girders.

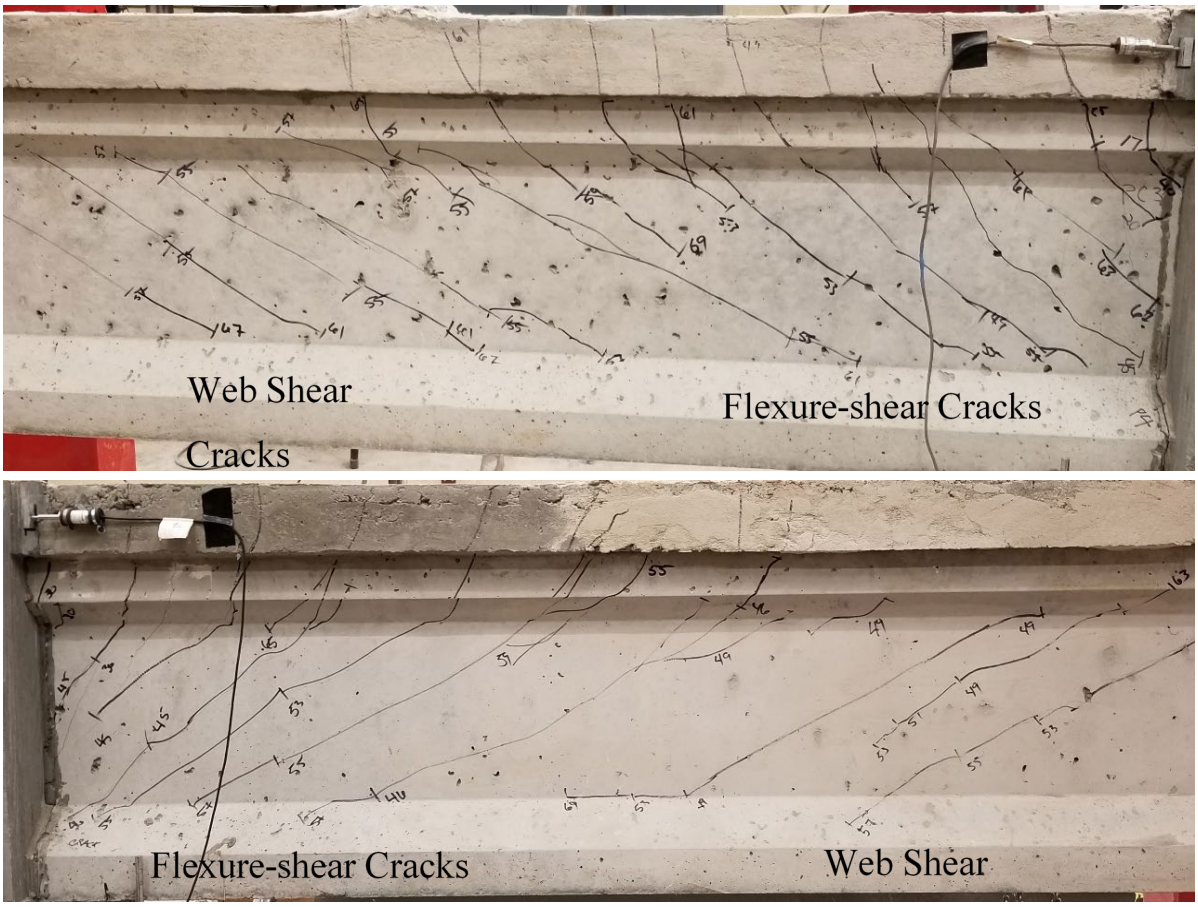

Figure 253. RC3-N girder with flexure-shear cracks and web shear cracks (top) and RC3-S girder with flexure-shear cracks and web shear cracks (bottom)

Loading of the specimen was stopped upon reaching an applied load of 76.1 kips on the RC3-N girder and 73.3 kips on the RC3-S girder. Under these loading conditions the concrete deck began to crush at the load point in both girders, as shown by the dark ovals in Figure 254. In addition, there was significant widening of the flexural cracks under both load points. These conditions were taken to indicate flexural failure of the beams and testing was concluded to prevent the prestressing strands from rupturing and causing damage to the testing apparatus.

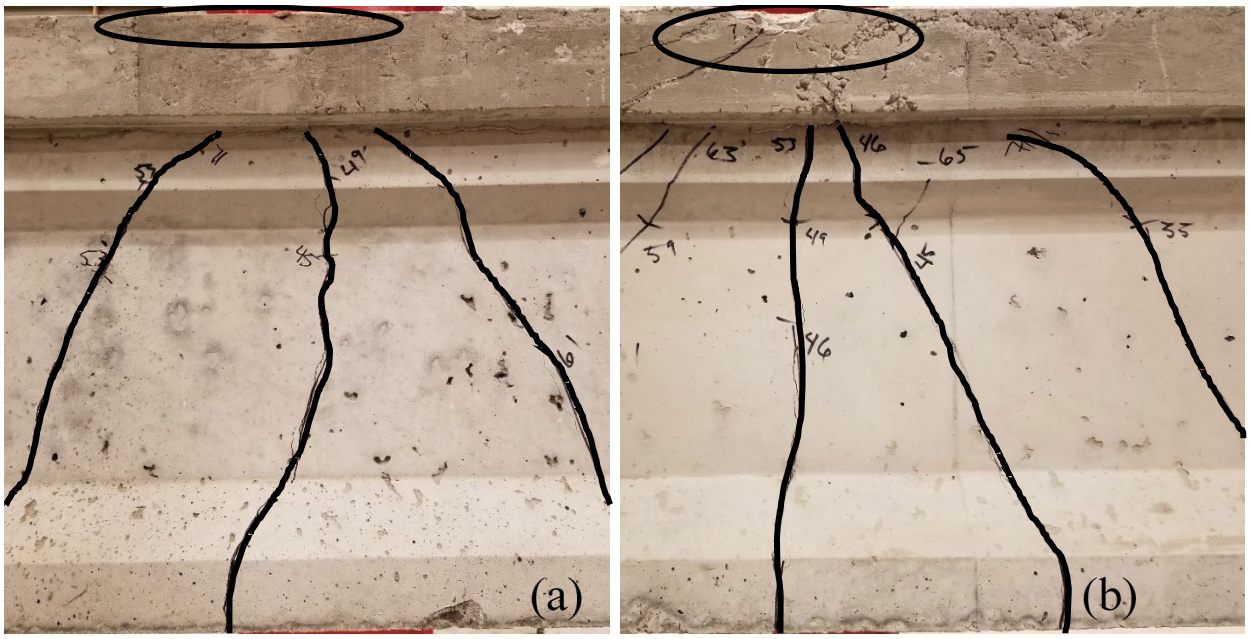

Figure 254. Final flexural cracking under the load point in the RC3-N (a) and RC3-S (b) girders are indicated by dark lines and concrete deck crushing is indicated by dark ovals.

The interface between the RC3-N girder and the UHPC joint had preexisting flexural cracking from the positive moment test. Flexural cracking occurred along the concrete deck to UHPC joint interface, which resulted in separation of the deck from the joint, and the flexural crack continued vertically down into the RC3-N girder's top flange and then into the web before going back toward the joint interface, as shown in Figure 255(a). There was no clear indication that the flexural cracks from the negative moment test continued into the flexural cracks that had developed from the positive moment test, as had happened in the NC3 specimen. The interface between the RC3-S girder and UHPC joint had similar joint separation at the concrete deck to the RC3-N girder deck joint interface, as shown in Figure 255(b). There was no clear indication of joint separation from the positive moment test, and the flexural cracks shown in Figure 256(b) did not indicate continuation into the joint interface.

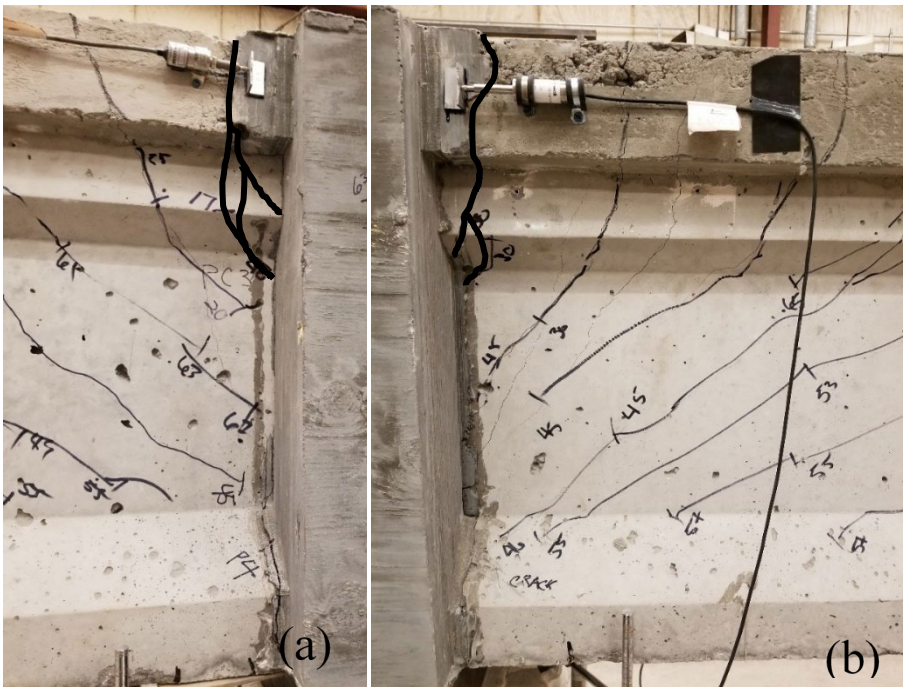

Figure 255. Joint separation at the interface between the RC3-N concrete deck and the UHPC joint with the flexural crack going vertically down in the girder (a) and joint separation at the joint interface between the RC3-S concrete deck and the UHPC joint with the flexural crack going vertically down into the girder (b) are indicated by dark lines.

Figure 256 shows the load-deflection curve for the RC3-N girder. The curve shows a reduction in stiffness that corresponds with the initial flexural cracking observed at 45 kips. Other types of initial cracking did not reduce the stiffness of the girder. This curve indicates a ductile behavior of the RC2-N prestressed girder during loading up to the ultimate load of 76.1 kips. In addition, the plateau of the load-deflection curve out to 1.4 inches of deflection also indicated the prestressing strands were yielding. Figure 257 shows the load-deflection curve for the RC3-S girder. The RC3-N and RC3-S girders had similar ductile behavior, and similar deflection at mid-span.

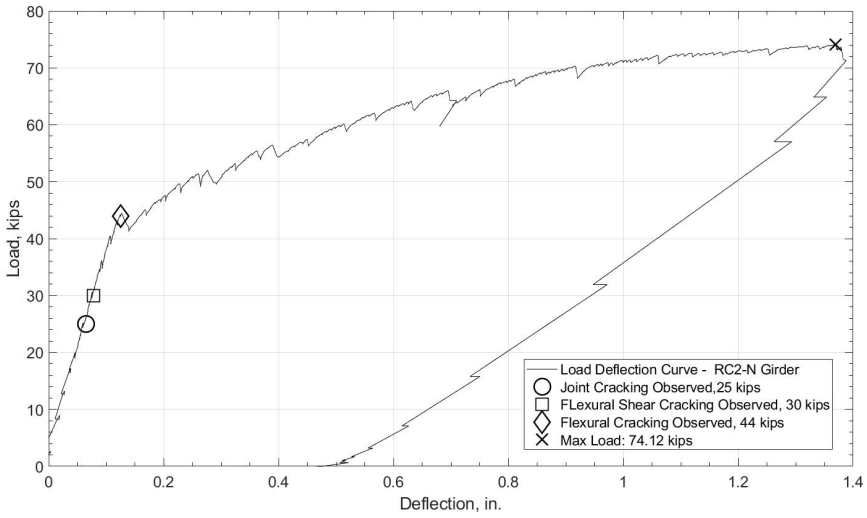

Figure 256. Load-deflection curve for the RC3-N girder

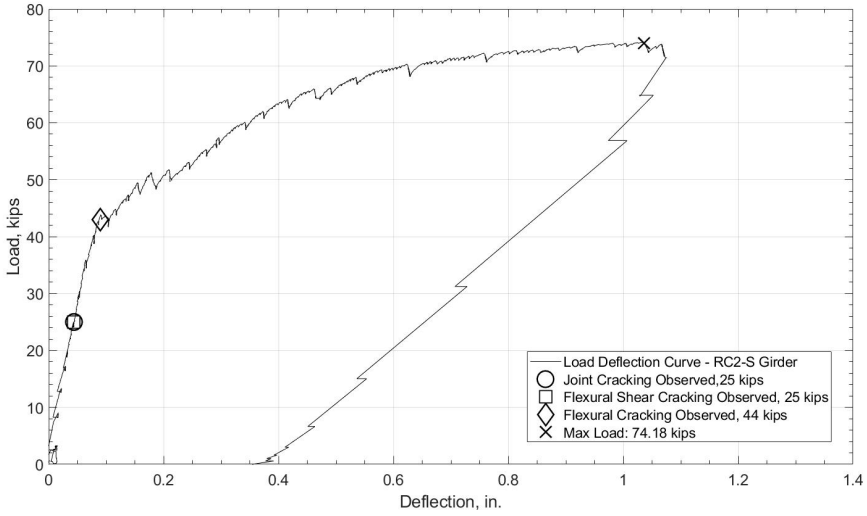

Figure 257. Load-deflection curve for the RC3-S girder

Figure 258 shows the load-joint separation curve between the RC3-N girder's concrete deck and the UHPC joint. This figure only represents LVDT4 on the west face of the deck. LVDT9 did not give accurate data for this test, and measurements from this sensor were excluded. The LVDTs on the joint interface were located 2 in. below the top of the deck. The deck joint had minor separation until reaching the 60 kip load mark. This load-joint separation curve shows the opposite of what was expected. As the girder cracked in flexure, the reduction of girder stiffness appeared to have no effect on the rate of the joint separation. The joint began to separate more significantly after the 60

kip mark because the girder began to have more downward curvature, creating a hinge at the weak point, being the joint interface. Figure 259 shows the load-joint separation curve between the RC3-S girder's concrete deck and the UHPC joint. This figure only represents LVDT11 on the west face of the deck. The NC3-N and NC3-S curves closely match one another in behavior except the NC3-S separation curve shows less separation occurring.

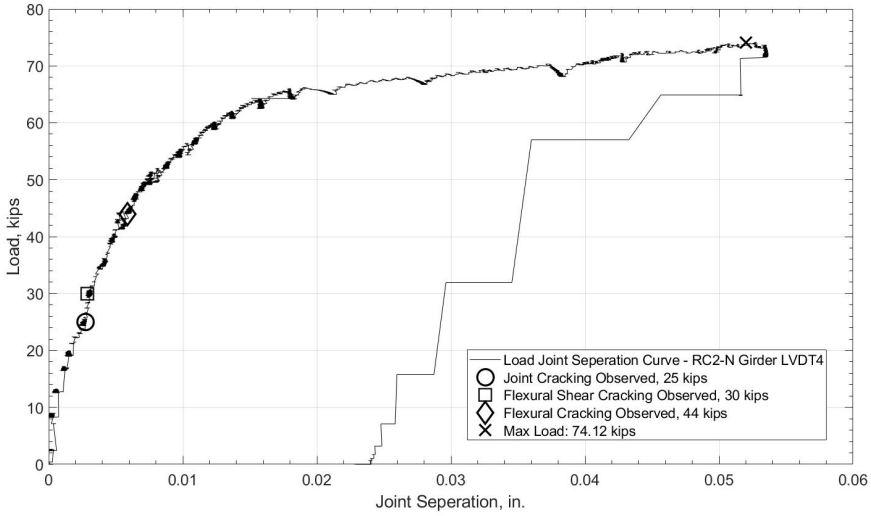

Figure 258. Load-joint separation curve at the RC3-N girder deck to UHPC joint interface west face

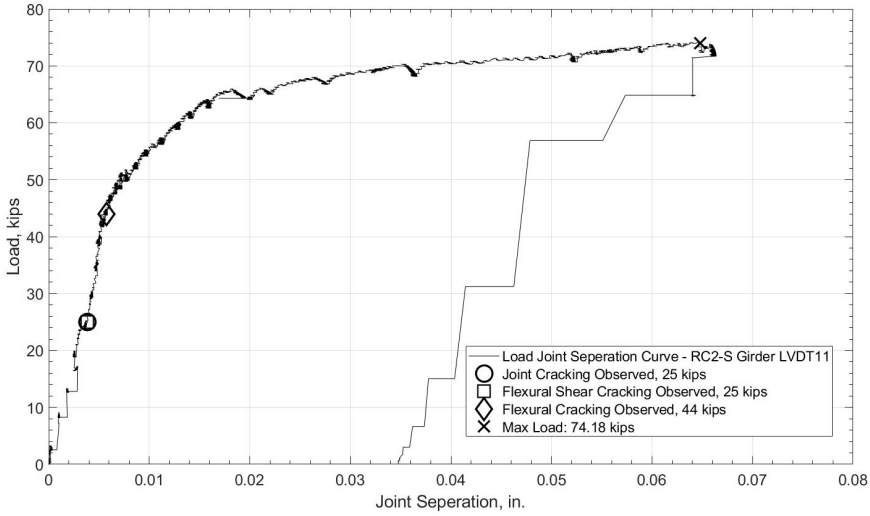

Figure 259. Load-joint separation curve at the RC3-S girder deck to UHPC joint interface west face.

6.3.4 Strain in the Joint Reinforcement

Strain gauges were placed on two of the reinforcing bars resisting negative moment within the UHPC joint. The loads applied on the north and south girders were averaged together to get an average load to plot with the strain gauge data. This was done to reduce the amount of load vs. strain graphs, but was still considered reasonable as the north and south load data tracked closely to one another. Figure 260 shows the load-strain curve for the NC1 specimen. This curve shows the strain increasing in the joint as load was applied. This is to be expected, as the girders begin to deflect in downward curvature as more load is applied, which puts the continuity joint in an upward curvature causing a tension stress at the top of the joint, and in return causing strain in the rebar as load increases. Initial cracking observed on the joint did not appear to have any effect on the load-strain curve. Figure 261 shows the load strain curve for the NC2 specimen. This curve is very similar to the NC1 load strain curve, and observed initial joint cracking did not appear to have any effect on the strain in the rebar. Figure 262 shows the load-strain curve for the NC3 specimen. This curve shows similar behavior to the NC1 and NC2 load-strain curves, and initial joint cracking observed on the continuity joint had no apparent effect on the strain in the steel. On all three NC joints the strain did not reach a value of 0.002 strain, which means the rebar in the joint did not yield (assuming Grade 60 steel) and combined with no crushing of the concrete indicates that the joint did not fail. Overall, the strain measurements only give a small detail of what the actual strain would be across the joint, as the strain can vary location to location depending on the cracking in the continuity joint.

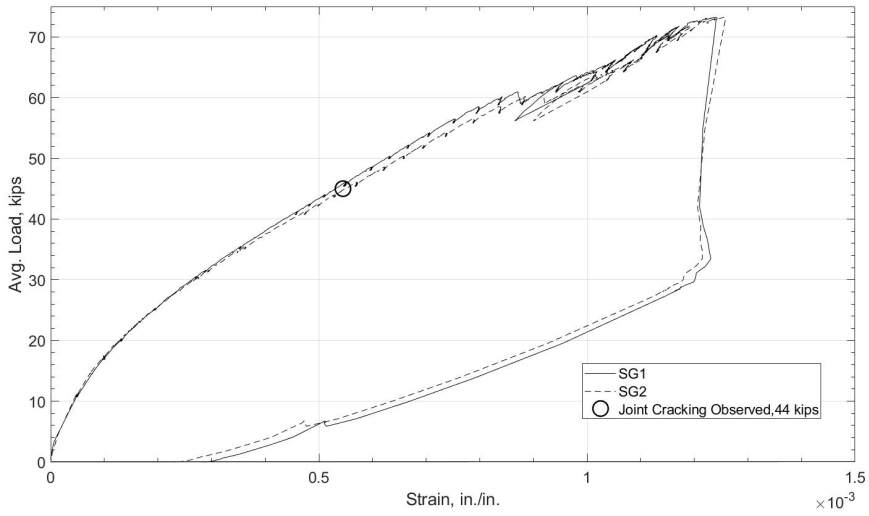

Figure 260. Load-strain curve for the NC1 joint

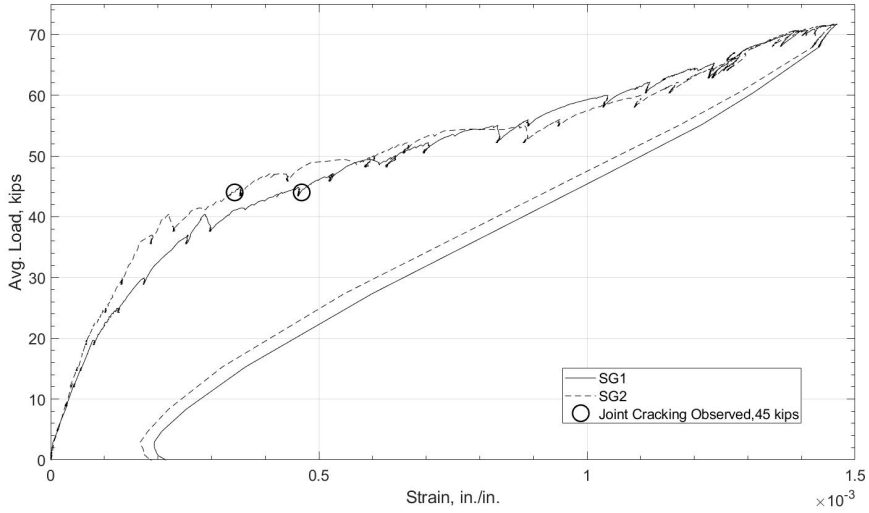

Figure 261. Load-strain curve for the NC2 joint

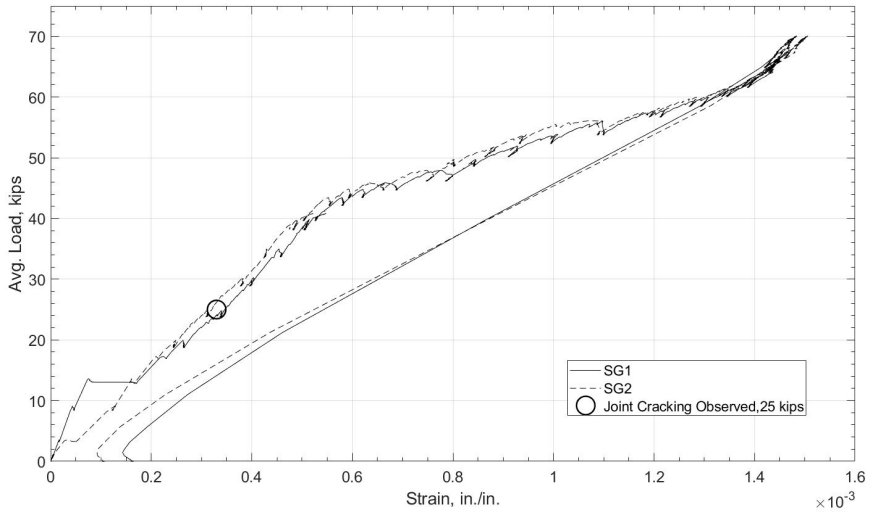

Figure 262. Load-strain curve for the NC3 joint

The load-strain curves for the RC specimens were plotted like the NC load strain curves. The RC joints also tracked similarly the NC joints, as the load increased the strain increased in the joint, which is to be expected. Figure 263 shows the load-strain curve for the RC1 specimen. Initial observed joint cracking did not appear to have any effect on the increase in strain during loading, and both strain gauges tracked together. Figure 264 shows the load-strain curve for the RC2 specimen. Like the RC1 specimen, initial joint cracking did not appear to influence the load strain curve. The strain gauges did not track with one another, as SG1 did not plateau like SG2 had done. Figure 265 shows the load-strain curve for the RC3 specimen. Initial joint cracking had no apparent effects on the strain, as for the RC1 and RC2 load-strain curves. Overall, the RC load-strain curves had similar trends to the NC curves, however, the RC joints had higher strain in the rebar. The max strain in all but one strain gauge read higher than 0.002, meaning the rebar had yielded at the location of the strain gauges. This could be a result of the fact that the RC joints encase the girders' end region, creating a stiffer joint compared to the NC joints, allowing the girders to take on more load before complete failure. This would allow the RC joints to get closer to complete failure resulting in increased strain relative to the NC joints.

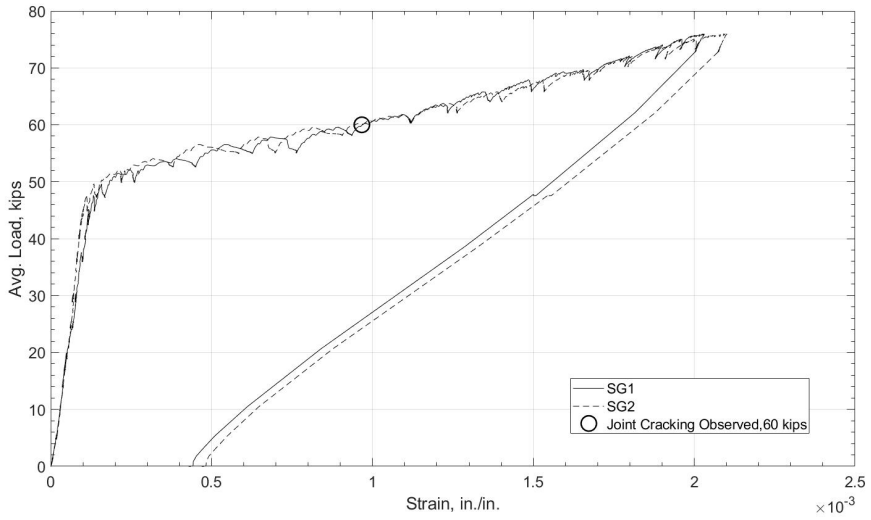

Figure 263. Load-strain curve for the RC1 joint

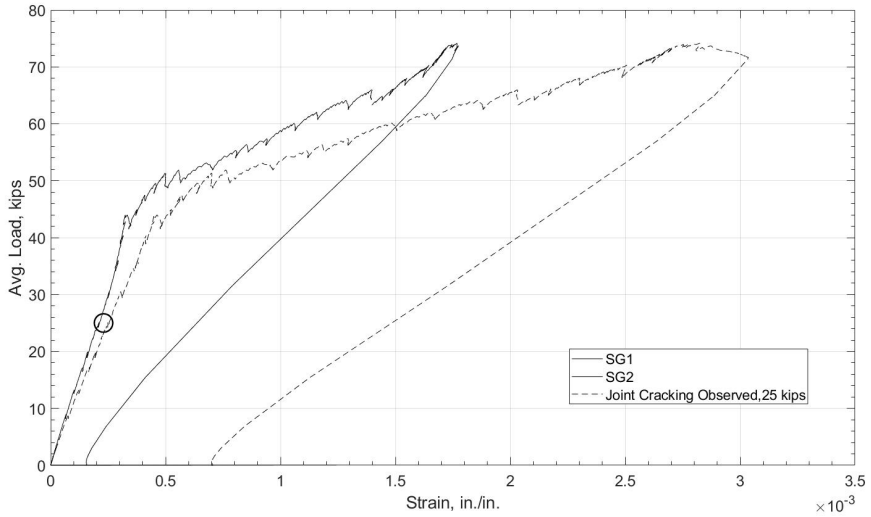

Figure 264. Load-strain curve for the RC2 joint

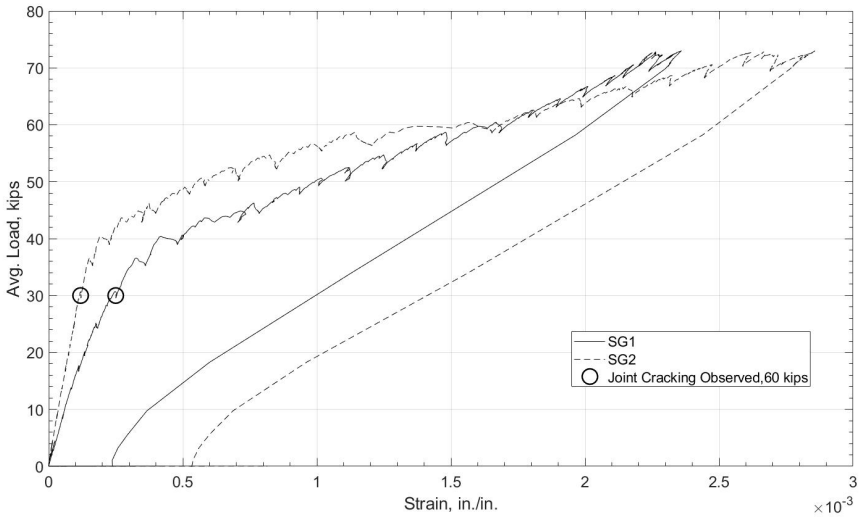

Figure 265. Load-strain curve for the RC3 joint

6.3.5 Summary of Results

There was not a large variation of the maximum loads between the NC specimens or between the RC specimens. However, the RC specimens had higher maximum loads than the NC specimens. The maximum deflections under the load points showed a consistent trend for the most part between specimens, but not necessarily similar magnitudes between the north and south girders. The deflection behavior was very similar for the RC specimens relative to variations and similarities between specimens. Larger maximum deflections under the load point were measured for the NC specimens compared to the RC specimens. The maximum joint separation was not consistent for the NC specimens or for the RC specimens. Both NC and RC specimens had similar maximum joint separation values overall. There was not a large variation between the two strain gauges in each NC specimen, and the maximum values were very similar when comparing the specimens. This was not the case for the RC specimens, as the strains for one gauge were higher compared to the other for all specimens. The RC specimens exhibited higher maximum strains than the NC specimens in general.

Presented in Table 44 and Table 45 is a summary of the maximum values for the load applied to each girder, deflection at mid-span for each girder, joint separation at

each joint interface, and the strain from the rebar in the joint for the NC and RC specimens.

Table 44. Maximum values obtained from testing NC specimens

Property	NC1-N	NC1-S	NC2-N	NC2-S	NC3-N	NC3-S	Average
Max Load (kips)	72.5	73.8	71.5	72	69.8	70.2	71.6
Max deflection (in.)	1.90	2.88	2.00	1.64	2.04	0.91	1.90
Max Joint Separation (in.)	0.17	0.098	0.096	-	0.012	0.086	0.092
Max strain-SG1	0.00124	0.00124	0.00147	0.00147	0.00148	0.00148	0.00140
Max strain-SG2	0.00125	0.00125	0.00146	0.00146	0.00151	0.00151	0.00141

Table 45. Maximum values obtained from testing RC specimens

Property	RC1-N	RC1-S	RC2-N	RC2-S	RC3-N	RC3-S	Average
Max Load (kips)	76.0	75.9	74.1	74.2	76.1	73.3	74.9
Max deflection (in.)	1.58	1.26	1.37	1.07	1.40	1.40	1.35
Max Joint Separation (in.)	0.077	-	0.053	0.066	0.08	0.061	0.067
Max strain-SG1	0.00203	0.00203	0.00177	0.00177	0.00236	0.00236	.00210
Max strain-SG2	0.00210	0.00210	0.00282	0.00282	0.00286	0.00286	.00260

Presented in Table 46 and Table 47 are summaries of initial cracking loads for each type of cracking observed in each region of the specimens. These include flexural and flexure-shear cracks under the load points, flexural cracks near the joint interface, and flexural cracks in the joint.

Table 46. Initial cracking for each region of the NC specimens

Cracking Type	NC1-N	NC1-S	NC2-N	NC2-S	NC3-N	NC3-S
Flexural Crack Under Load Point (kips)	43	45	40	45	41	46
Flexural Crack Near Joint Interface (kips)	43	35	-	-	25	19.5
Flexure-shear Crack Near Joint Interface (kips)	45	43	47	45	41	35
Flexural Crack in Joint (kips)	44	44	45	45	25	25

Table 47. Initial cracking for each region of the RC specimens.

Cracking Type	RC1-N	RC1-S	RC2-N	RC2-S	RC3-N	RC3-S
Flexural Crack Under Load Point (kips)	45	47	44	44	45	46
Flexural Crack Near Joint Interface (kips)	20	20	25	19.5	17	30
Flexure-shear Crack Near Joint Interface (kips)	25	30	30	25	20	30
Flexural Crack in Joint (kips)	60	60	25	25	30	30

6.3.6 Moment Capacity Comparison

The structural analysis program RISA was used to make a model of the NC and RC joint specimens to calculate the moment from the maximum experimental load applied to each individual girder per specimen during testing. This maximum moment from each girder in a specimen was then compared to the nominal moment capacity of an individual prestressed girder with the concrete deck included in the strain compatibility method for prestressed girders. The comparison shows an increase in moment capacity with the spans being continuous in both joint types. Presented in Table 48 and Table 49 are the maximum moment capacity for each girder in a specimen from testing for both joint types, the nominal moment capacity for an individual girder, and the percentage increase for the overall moment capacity.

Table 48. Comparison of maximum experimental moment to the nominal moment of a single span girder for NC specimens.

Result Type	NC1-N	NC1-S	NC2-N	NC2-S	NC3-N	NC3-S
Max Experimental Load w/ Continuity Joint (kips)	72.5	73.8	71.5	72	69.8	70.2
RISA Max Moment from Max. Experimental load w/ Continuity Joint (kip-ft)	211.9	215.6	208.9	210.4	204	205.1
M_n single span girder, (kip-ft)	145.7	145.7	145.7	145.7	145.7	145.7
Moment percentage increase w/Continuity Joint	31.2	32.4	30.3	30.8	28.6	29.0

Table 49. Comparison of maximum experimental moment to the nominal moment of a single span girder for RC specimens.

Result Type	RC1-N	RC1-S	RC2-N	RC2-S	RC3-N	RC3-S
Max Experimental Load w/ Continuity Joint (kips)	76	75.9	74.1	74.2	76.1	73.3
RISA Max Moment from Max. Experimental load w/ Continuity Joint (kip-ft)	217.2	216.9	211.8	212	217.5	209.6
M_n single span girder (kip-ft)	145.7	145.7	145.7	145.7	145.7	145.7
Moment percentage increase w/Continuity Joint	32.9	32.8	31.2	31.3	33.0	30.5

Another comparison was done by finding an applied load on both girders in the continuous span model in RISA for both joint types that would result in the nominal moment capacity for an individual girder for both girders in the continuous span. The applied loads that were applied to the model to obtain a moment equal to the nominal moment capacity were 49.8 kips for the NC joint, and 51 kips for the RC joint. Figure 266 and Figure 267 show the results of the RISA model for both joint types with the applied loads. The point loads were then applied to a simply supported girder in RISA to come up with the maximum moment for that case. The maximum moment for the applied load of 49.8 kips from the NC joint was 224.1 kip-ft, and the maximum moment for the applied load of 51 kips from the RC joint was 229.5 kip-ft. These two values far exceed the nominal moment capacity of a single girder, which means if the continuous span was designed with the intent to increase the overall capacity of the bridge and continuity of the joint is lost, the capacity would be significantly reduced, at which point failure could occur.

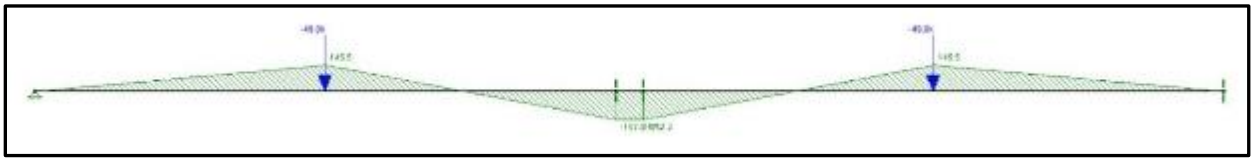

Figure 266. RISA model showing the applied loads to the NC joint configuration to determine the nominal moment capacity of a single span prestressed girder

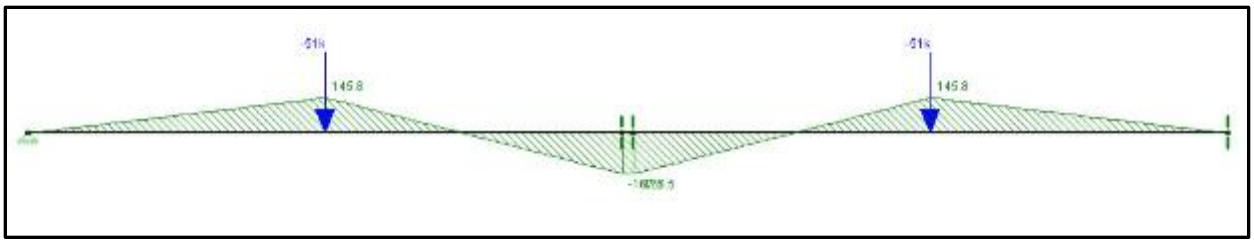

Figure 267. RISA model showing the applied loads to the RC joint configuration to determine the nominal moment capacity of a single span prestressed girder

The configuration of the positive moment test conducted on the NC3 and RC3 specimens was put into a RISA model to calculate the maximum moment from the two point loads applied during the test. The moment calculated from the NC3 specimen test was 67.5 kip-ft. This moment was 2.1 kip-ft from the calculated joint cracking moment of 69.6 kip-ft. As this was within 3% of the cracking moment, the moment capacity for the negative moment test was very comparable to NC1 and NC2 specimens that did not have a positive moment test conducted. The moment calculated from the RC3 specimen was 37.8 kip-ft. Although the moment at cracking was only slightly above half of the calculated joint cracking moment value, the RC3 specimen still performed similarly to the RC1 and RC2 specimens. Figure 268 and Figure 269 show the RISA model with the max load applied in the positive moment tests.

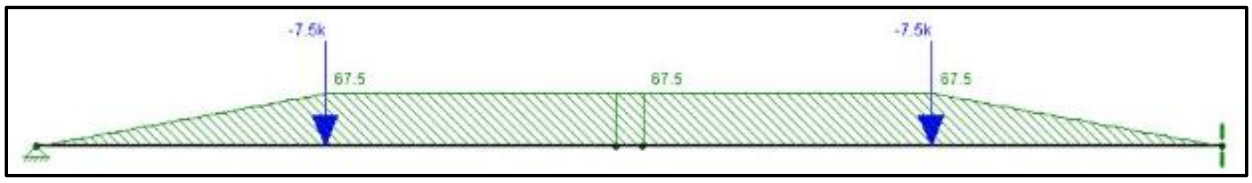

Figure 268. RISA model showing the applied loads to the NC continuity joint configuration from the positive moment test

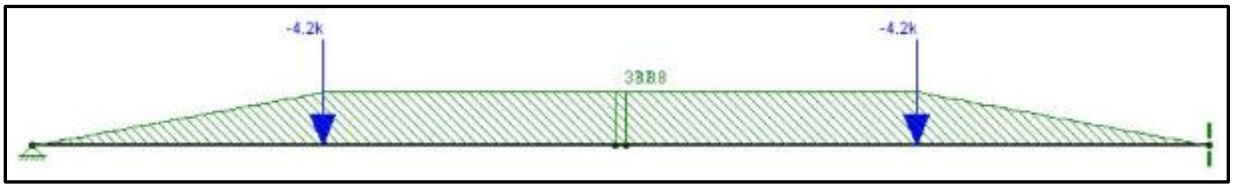

Figure 269. RISA model showing the applied loads to the RC joint configuration from the positive moment test.

7.0 UHPC Durability

7.1 Overview

This section outlines the testing procedure and results of the chloride ion penetration testing, freeze-thaw cycling, and scaling resistance testing of the ODOT Class AA, Ductal®, and J3 concrete mixes tested in this study. Average compressive strengths of the materials used in the following tests are included in Table 50.

Table 50. Summary of concrete compressive strengths

Concrete Type	Average Compressive Strength (psi)
ODOT AA for Small-scale Corrosion Specimens	5620
Other ODOT AA	6560
J3	18560
Ductal®	23850

7.2 Chloride Ion Penetration

7.2.1 Introduction

Rapid Chloride Ion Permeability (RCIP) testing was conducted using ASTM C1202-17 standards. RCIP testing provides a comparative understanding of permeability across different concrete types. However, it should be stated that there is a common misconception that RCIP is a direct test of permeability, which it is not. RCIP testing measures the bulk flow of chloride ions through a specimen, not a specific type of ion movement/how the ions flow through the specimen, meaning it is only appropriate for comparing the overall permeability of different concrete mixes to one another.

7.2.2 Procedure

For this testing, at least three specimens were tested for each mix design at both 28 and 90 days of age. All specimens were moist cured using wet burlap and plastic until the specimens were ready to be demolded, at which point they were put into a lime water bath until one day before testing. All specimens were cut from the top and bottom of two 4 in. x 8 in. (100 mm x 200 mm) cylinders into 2 in. thick slices, so a total of 12 cylinders were cast, 4 for each mix. Slices were cut using a water-cooled diamond saw blade and slice surfaces were ground flat where needed. Testing was accomplished by passing a 60 V potential difference across each slice and measuring the amount of

electrical current that passes through the specimen in a 6-hour period. During testing one side of each specimen was immersed in a 3% NaCl solution, with the other side being immersed in a 0.3 N NaOH solution. Both the 3% by mass NaCl solution and the 0.3 N NaOH solution were made using deionized water and laboratory grade dry 32 reagents. Ultimately this meant using 12 grams of NaOH per 1000 mL of water and 31 grams of NaCl per 1000 mL of water. Testing conditions were achieved using a RCIP testing machine by Germann Instruments and a computer software program called PROOVE'it. At any point during testing, if any of the specimens or their solutions exceeded a temperature of 90°F, that test was ended immediately, with its time of termination noted and a rating of high chloride ion penetrability given. This was done to protect the testing cell and to prevent evaporation of the testing liquids.

One day before testing, specimens were placed in a vacuum desiccator with a pump system capable of maintaining vacuum pressure of less than 50-mm Hg. The vacuum pump was run on the dry specimens for 3 hours before pumping deionized water in and running the vacuum desiccators for another hour with the specimens completely submerged. After this, the pump was turned off and left sealed for 18 hours, at which time testing could begin. The pump system used is shown in Figure 270.

Figure 270. Vacuum desiccator (left) and pump (right) used for RCIP specimen preparation

There is some debate on the viability of this testing procedure, due to the fact that the high voltage applied leads to high temperatures, which in turn increase the total

charge passed through the specimens. Additionally, when measuring the total charge passed the test actually measures all of the ions passing through the specimen, not just the chloride ions. However, since UHPC should be incredibly impermeable, over-estimation is not a large concern, so this testing set-up was determined to be adequate for the purpose of comparative UHPC testing.

It should be note that for the first round of chloride ion testing specimens were cast as they would be in the field. This meant the inclusion of the 0.5 in. steel fibers that give Ductal® and J3 their exceptional tensile strength. Due to this inclusion, however, passageways were opened up in both J3 and Ductal® that disrupted the accuracy of the chloride ion testing. To get an accurate reading of the permeability of the UHPC mixtures, two new cylinders were cast for both J3 and Ductal® without fibers so that new specimens could be made in the same manner as the original specimens, with an additional slice cut out of the center of each cylinder to make a total of three specimens for testing. Only the results from the second round of testing are presented in Section 7.2.4.

7.2.3 Testing

The test set-up used throughout testing is shown in Figure 271.

Figure 271. Typical RCIP testing showing test cells (left) and PROOVE'it apparatus (right)

7.2.4 Results

The average coulombs passed for each set of specimens and the corresponding permeability class for 28-day and 56-day testing are presented in Table 51, with the rating system for chloride permeability presented as in Table 52. Note that a concrete mix with a lower chloride permeability class is considered more resistant to chloride attack, and therefore more favorable, than one with a high chloride permeability class.

Table 51. RCIP testing results at 28 days

Result	AA	J3	Ductal®
Average Coulombs Passed at 28 Days	2465	251	61
Chloride Permeability Class at 28 Days	Moderate	Very Low	Negligible
Average Coulombs Passed at 56 Days	1832	63	28
Chloride Permeability Class at 56 Days	Low	Negligible	Negligible

Table 52. Chloride permeability classifications using RCIP test

Chloride Permeability Class	Charge (Coulomb)
High	>4000
Moderate	2000-4000
Low	1000-2000
Very Low	100-1000
Negligible	<100

Ultimately, all results found for chloride ion testing were as expected. The ODOT AA had high average permeability, but not any more than what is normal and acceptable for a standard concrete mix. Both J3 and Ductal® had quite low average permeability, a result that is also in line with what one would expect based on past studies into UHPC and given the nature of UHPC's dense particle matrix, which works by having very little open space (air pockets) for water or ions to flow through.

7.3 Freeze-Thaw

7.3.1 Introduction

Freeze-thaw testing was conducted to test the durability resistance of each mix when exposed to harsh winter conditions.

7.3.2 Procedure

Freeze-thaw testing was done in accordance with ASTM C666-15 Procedure A (freezing and thawing in water). A total of ten specimens were tested, three for each of J3, Ductal®, and ODOT AA, and one control ODOT AA specimen connected to a temperature probe to monitor the temperature change inside the machine. All freeze-thaw specimens were 4 in. x 4 in. x 15 in. prisms. ASTM C666-15 Procedure A was chosen for freeze-thaw testing because it simulates a more aggressive environment and is easily achievable by the equipment available at the University of Oklahoma Fears Laboratory.

For this procedure, specimens were moist cured for 14 days prior to testing, first using wet burlap, followed by soaking in a lime water bath as soon as the specimens could be demolded, before finally being placed in a freezing-and-thawing apparatus for testing. During cycling, all specimens were surrounded by a layer of water 1/8 in. thick. This was achieved by wrapping each specimen with two coated wires, each 1/8 in. thick, which were also used to help lift the specimens out of their encasements when they needed to be examined. A total of 350 cycles were performed for each specimen, with each cycle taking roughly 4 hours. This number of cycles was chosen because although only 300 cycles are required by the ASTM procedure, it was shown by Chumping (2015) that a significant change in data can occur around 300 cycles for this testing approach, so while unlikely, data was collected past 300 cycles to ensure no drastic changes occurred that meant the specimens needed to be studied for an extended period of time past the required 300 cycles.

Each cycle consisted of two parts, which lowered the temperature from 40 to 0°F and then raised the temperature back from 0 to 40°F, respectively. Freeze-thaw cycling was started from the thaw temperature (40°F), and anytime freeze-thaw cycling needed

to be paused, all specimens were kept in a frozen state. Note that at any point in the cycling, if a specimen was found to have reached the freeze-thaw failure criteria, i.e. relative dynamic modulus (RDM) of less than 60%, the specimen would have been removed from testing and a dummy specimen would have replaced it within the testing apparatus for consistency. At intervals not exceeding 36 cycles, specimens were thoroughly thawed and placed in a lime water bath for 24 hours to prevent moisture loss and prepare the specimens for testing. Soaking for at least 24 hours was essential for all of the specimens to be of the same moisture level whenever they were tested.

Only RDM values of each specimen were taken throughout testing. These values were calculated by measuring the fundamental longitudinal (flexural) frequency and dividing it by the original fundamental longitudinal (flexural) frequency for each specimen. This results in RDM in the form of a percentage, where 100% is the starting point of the internal structure of the specimen, and deterioration results in ever decreasing values. These frequencies were measured with a frequency meter called an Emodumeter, which works by creating a mechanical impact with a small metal ball on one side of a specimen and measuring how long it takes for the impact to be felt by an accelerometer located on the other end of the specimen. This type of measurement is effective because it indicates the internal structure of the specimen (i.e., if a large amount of microcracks are present, it will take longer for the impact to be felt). The decision to only measure RDM was made because while RDM can be unreliable (due to ambient air curing methods resulting in high levels of un-hydrated cement in UHPC), mass loss and length change can be even more unpredictable, changing dramatically with any moisture level change. Figure 272 shows a specimen being tested in the Emodumeter while Figure 273 and 274 show a typical transverse frequency initial measurement and resulting final output, respectively.

Figure 272. Freeze-thaw specimen arranged for dynamic modulus testing

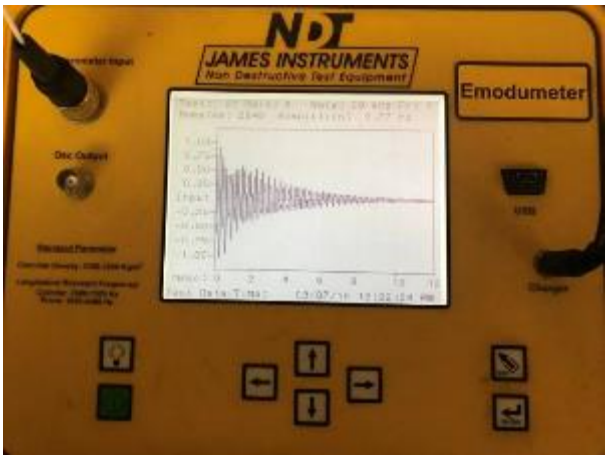

Figure 273. Typical Emodumeter transverse frequency measurement

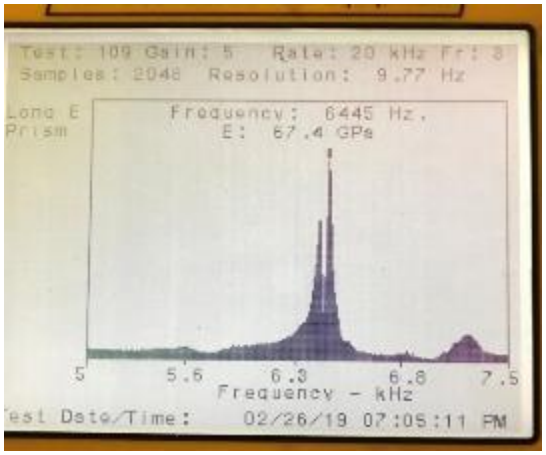

Figure 274. Typical Emodumeter transverse frequency output

Following the guidelines in ASTM C666-15 and ASTM C215-14, the Emodumeter data collection device was set to collect 2048 points per test with a sampling rate of 20 kHz. Additionally, all specimens were tested three times during each round of testing, and their frequencies averaged together. All data points more than 10% apart from the average were rejected and recollected.

After each round of testing the freezing-and-thawing apparatus was rinsed out and all containers were refilled with fresh water. Specimens were then put back into the freezing-and-thawing apparatus in a new location, so that each specimen experienced the conditions of all parts of the apparatus and no one specimen was continuously subjected to harsher conditions than another.

7.3.3 Testing

The freeze-thaw specimens prior to testing are shown in Figure 275 and Figure 276. All specimens had limited surface deterioration at this point in testing, and their starting frequencies were recorded to be used as the original value for finding each specimen’s RDM values throughout testing.

Figure 275. Freeze-thaw specimens in the testing chamber - Cycle 0

Figure 276. Condition of all freeze-thaw specimens - Cycle 0

As evident in Figure 277, after 350 cycles significant deterioration of the ODOT AA specimens could be seen, including chipping of edges and wearing away of the surface to the point of coarse aggregation showing through. Figure 278 and Figure 279 show that the Ductal® and J3 specimens exhibited significantly less deterioration, with only small holes forming along their surfaces for the majority. The exception being a singular large hole that formed between cycle 285 and cycle 315 in specimen D1 (as seen in Figure 280) which triggered a spike in RDM for the specimen due to water now being able to penetrate farther into the specimen and hydrate more of the unhydrated cementitious materials within the specimen.

Figure 277. Deteriorated state of a class AA freeze-thaw specimen - Cycle 350

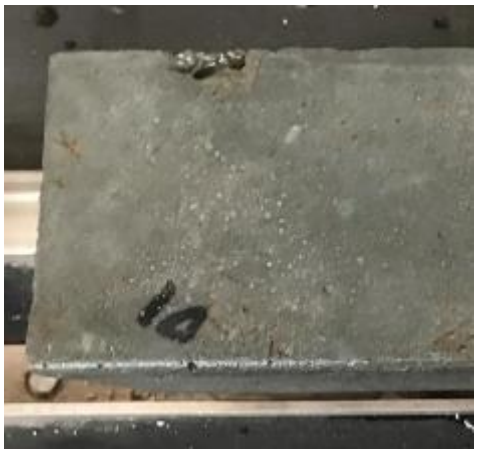

Figure 278. Deteriorated state of a Ductal® freeze-thaw specimen - Cycle 350

Figure 279. Deteriorated state of a J3 freeze-thaw specimen - Cycle 350

Figure 280. Hole formed on the side of Ductal® freeze-thaw specimen - Cycle 315

However, though the Ductal® specimens only experienced a minimum amount of surface spalling, each of the three Ductal® specimens did experience a significant amount of surface corrosion of the steel reinforcing fibers on all four sides of each specimen, as shown in Figure 281. At the conclusion of testing, all three J3 specimens had also begun to show this kind of surface corrosion of fibers, but to a lesser extent. This is significant because very similar corrosion patterns were seen by Ductal® and J3 in scaling testing, as discussed in Section 7.4, and could be indicative of J3 having better fiber suspension during concrete setting. It should be noted, however, that surface corrosion of fibers is expected for UHPC structures in highly abrasive environments like those simulated by freeze-thaw cycling and scaling resistance testing, and is not expected to affect the overall strength or durability of the UHPC. This is unlike the corrosion of internal reinforcing bars, which is extremely detrimental to the strength and durability of the structure.

Figure 281. Surface corrosion of Ductal® freeze-thaw specimen - Cycle 350

7.3.4 Summary of Results

The average RDM values for the different concrete mixtures at 350 cycles are presented in Table 53. From these values it can be seen that a small amount of internal deterioration occurred to the ODOT AA specimens, indicated by a small decrease in RDM, to a final average value of 99%. It should be noted that this value is well above the failure criteria of 60%. Both of the UHPC mixtures, on the other hand, show a slight increase in RDM. This seemingly strange phenomenon is explained by the presence of unhydrated cementitious particles in the specimens prior to testing becoming more and

more saturated as testing progressed due to more and more surface openings occurring in the specimens that water could then penetrate. This is consistent with the results and explanation given by both the Graybeal (2007) and Ahlborn (2011) studies discussed in Section 2.8, which also showed significant average RDM increases for ambient air cured UHPC specimens, with final average RDM values of 110% and 102% respectively.

Table 53. Freeze-thaw testing average RDM at 350 Cycles (%)

AA	J3	Ductal®
99.1	103.1	102.5

However, as was noted by Graybeal (2007), these large RDM values do not guarantee that the internal structures of the UHPC specimens are responding well. In fact, large RDM values only mean that particle saturation is occurring, which at an excessively high rate could actually be a sign of a weak internal structure that allows for the easy passage of water. This leaves assessment of the external structure as the only other means of measuring the response of these mixtures to freeze-thaw cycling. As visible in Figure 277, the AA specimens began to experience noticeable deterioration towards the end of testing. This included significant pocketing of the specimen surfaces and even some large aggregate beginning to show through. None of the specimens for either UHPC mixture exhibited this level of deterioration, with only light pocketing and surface corrosion of steel reinforcing fibers occurring. This low level of deterioration was expected for UHPC under freeze-thaw conditions. In conjunction with the reasonable RDM values obtained and discussed previously, these results are indicate that both J3 and Ductal® would perform well under similar conditions in the field.

7.4 Scaling Resistance

7.4.1 Introduction

Scaling resistance testing was conducted to test the permeability of each mix when experiencing harsh winter conditions with the addition of deicing chemicals.

7.4.2 Procedure

Scaling resistance was tested in accordance to ASTM C672 using two specimens for each of the UHPC mix designs, J3 and Ductal®, and two for the conventional ODOT Class AA concrete mix, for a total of 6 specimens. All scaling specimens were 9 in. x 15 in. x 2 in. Scaling resistance testing was done after 28 days of curing: 14 days of moist curing, done in the same fashion as that of the freeze-thaw specimens, and 14 days of ambient air curing, in accordance with ASTM 672. This testing was conducted by first covering each specimen with a ¼ in. layer of a calcium chloride and water solution containing 4 g of calcium chloride to each 100 mL of solution. Each specimen had a 1 in. x 1 in. foam boarder epoxied around the outside edge to act as a container for the testing solution, as shown in Figure 282.

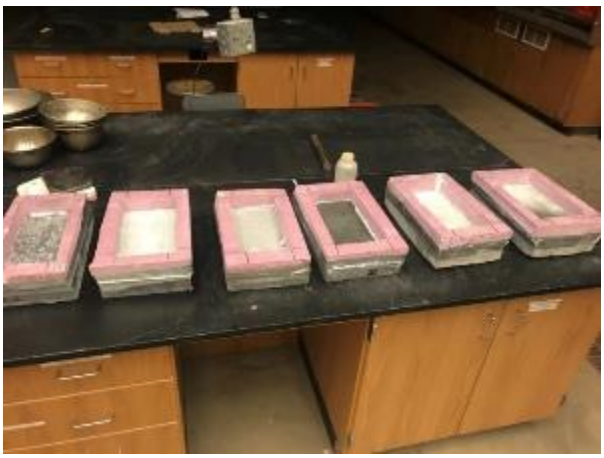

Figure 282. Condition of scaling specimens - Cycle 0

Each specimen was subjected to 50 freeze-thaw cycles, where one cycle involved going from 0° F for 16-18 hours to 40° F for 6-8 hours in an environmental chamber. One cycle was completed daily, with water added when necessary to maintain proper depth of solution. The surface of each specimen was properly flushed at the end of every fifth cycle. If tests needed to be paused for any reason, specimens were kept frozen. At 25 cycles and at the end of testing, all specimens were visually examined using the surface condition rating system in ASTM 672, detailed in Table 54. Note that the as-cast bottom horizontal surface for each specimen was used as the testing surface for scaling due to its consistent finish. This choice was also key for this study in

particular because in practice the top surfaces of Ductal® specimens are always ground to remove any large air pockets.

Table 54. Scaling surface condition rating system in accordance with ASTM C672

Rating	Condition
0	No scaling
1	Very slight scaling (3 mm [1⁄8 in.] depth, max, no coarse aggregate visible)
2	Slight to moderate scaling
3	Moderate scaling (some coarse aggregate visible)
4	Moderate to severe scaling
5	Severe scaling (coarse aggregate visible over entire surface)

7.4.3 Testing

After 7 cycles, slight pockets could be observed on the surface of both of the ODOT AA specimens; though none of the J3 or Ductal® specimens showed any signs of visible deterioration at this stage of testing. At 25 cycles, both ODOT AA specimens had significant pocketing, as shown in Figure 283, almost to the point of exposing coarse aggregate in select places, with a majority of the surface area showing signs of dusting. Also, at this point during testing, one of the Ductal® specimens (D1), shown in Figure 284, began to show significant visual signs of corrosion of the steel fibers along its exposed surface, with slight dusting and pocketing visible. Little to no dusting or pocketing, as well as limited surface corrosion, was observed on the other Ductal® specimen or either of the J3 specimens.

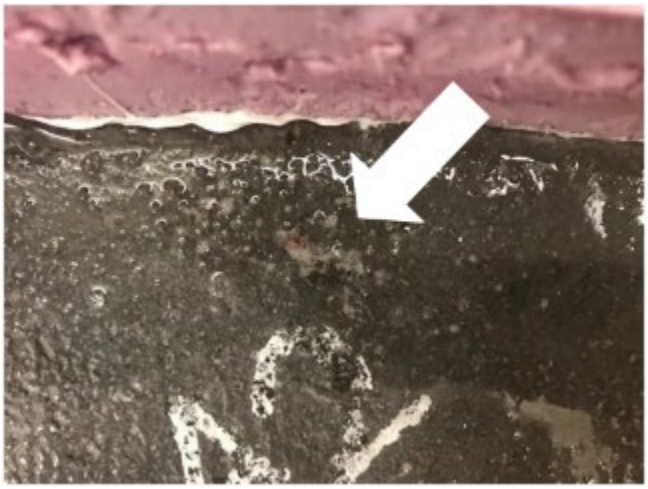

Figure 283. Visual pocketing on AA specimen - 25 cycles

Figure 284. Visual corrosion of steel fibers on Ductal® specimen - 25 cycles

At 50 cycles, the specimens were in the states shown in Figure 285. Since 25 cycles, the pocketing of both of the ODOT AA specimens had increased a considerable amount, and pocketing had begun to occur on specimen D1, as shown in Figure 286 and Figure 287, respectively. Dusting of the entire surface was also noted for each of these three specimens during this period of cycling, with the other Ductal® specimen, D2, experiencing dusting of almost its entire surface as well. No substantial dusting or pitting occurred on either of the J3 specimens, with the final state being almost completely unchanged, as shown in Figure 286.

Figure 285. Visual examination of scaling specimens at 50 Days for ODOT AA (left), Ductal® (middle), and J3 (right)

Figure 286. Progression of visual pocketing on AA specimen - 50 cycles

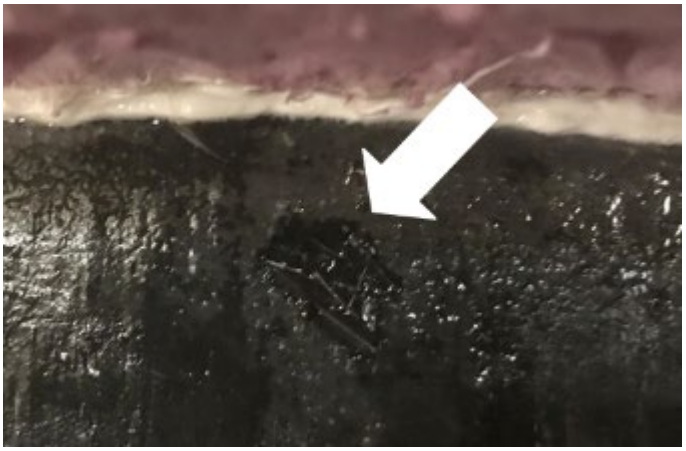

Figure 287. Visual pocketing on Ductal® specimen - 50 cycles

7.4.4 Summary of Results

Visual ratings were given to each specimen at 25 and 50 cycles based on the states of the specimen surfaces and are presented in Table 55.

Table 55. Average scaling visual rating results

Specimen	25 Cycles	50 Cycles
AA1	1.00	1.50
AA2	1.50	2.00
Average AA	1.25	1.75
J1	0.00	0.00
J2	0.00	0.00
Average J3	0.00	0.00
D1	0.75	1.50
D2	0.25	1.00
Average Ductal®	0.50	1.25

These ratings show that both ODOT AA specimens performed as expected, with significant deterioration occurring due to a large amount of both dusting and pocketing of the surface. Both J3 specimens performed very well, with no substantial dusting or scaling occurring at any point during testing. The two Ductal® specimens performed exhibited different performance, with one showing similar levels of deterioration as the ODOT AA specimens, while the other specimen experienced a large amount of dusting but significantly less pocketing. Despite the large difference in deterioration levels, however, these responses still combined to give Ductal® a higher average final rating than expected.

7.5 Joint Corrosion Testing

7.5.1 Overview

This section outlines the testing procedure and results of both small- and large-scale corrosion testing of the ODOT Class AA, Ductal®, J3, and Phoscrete concrete mixes.

To obtain the most accurate understanding of the effects of a UHPC repair joint on reinforcing steel with previous corrosion, the ideal situation would be to test slabs that have been in active use. Therefore, the University of Oklahoma research team worked in conjunction with ODOT to identify and procure slab sections with existing corrosion that had been previously removed from service. These specimens were then retrofitted with a joint made of one of the four test mixes (ODOT Class AA, Ductal®, J3, and Phoscrete) and subsequently corroded in an accelerated test setup to produce insight on the comparative corrosion protection capabilities of each mix through visual examination. This was what was referred to as “large-scale” corrosion testing. In addition, “small-scale” corrosion testing was performed to specifically measure the macrocell outputs, or “Halo Effect”, of each of the four mixes when used as a repair material.

It is important to note here the two distinct types of reinforcing steel corrosion that could occur as a result of this corrosion testing: pitting and surficial (Jones, 1996). Pitting corrosion occurs when corrosion becomes concentrated, burrowing itself into the steel, and shows visually as dark spots of corrosion intermittently placed across the

reinforcing steel's surface. Surficial corrosion, on the other hand, occurs as a light in color, uniform coating of corrosion across the surface of the steel reinforcing. This kind of surface corrosion is much more likely to stick to the concrete surrounding it because it is in direct and constant contact with the concrete. Neither type of corrosion is necessarily more severe than the other, both being quite harmful for the steel reinforcing; however, the "Halo Effect" is typically evident in a concrete repair by the presence of surficial corrosion of the reinforcing steel in the substrate (original) concrete and not of the reinforcing steel within the repair material. However, this is not always the case, and this kind of corrosion is often much harder to identify, since most of the surface corrosion is pulled away when the concrete is removed for visual examination. Therefore, care was taken to identify all levels and kinds of corrosion (as applicable and feasible), since any indication of corrosion could be sign of the "Halo Effect" at work.

7.5.2 Small-Scale Corrosion Testing

7.5.2.1 Introduction

Specific testing for the Halo Effect was accomplished on small scale composite specimens using an ODOT Class AA base concrete in conjunction with a Ductal®, J3, ODOT AA, or Phoscrete "repair". This testing focused on macrocell corrosion, because that is the type of corrosion that is indicative of the "Halo Effect" (i.e., corrosion only due to the contact of the two different materials). Microcell corrosion, despite being known to be the main contributor to corrosion of steel reinforcing, can be assumed to occur throughout all reinforcing, regardless the type of concrete, or whether that concrete is old or new. Therefore, microcell corrosion would not provide any information on the interaction of old concrete and repair material and was not measured in this testing.

The composite specimens used for the small-scale corrosion testing were 24 in. x 12 in. x 3 in., with each specimen consisting of half base concrete and half repair material. The base concrete halves included the addition of NaCl at dosage rates of 0, 4, and 8% by weight of cement, to represent base concrete with differing levels of previous chloride ion penetration. This method of having NaCl directly in the base concrete is more effective and direct than the ponding method employed by other studies for macrocell corrosion testing. This meant a total of 12 specimens were cast,

three for each repair mix and three for the normal 0% NaCl ODOT class AA mix, which acted as a control. Each set of halves were cast one at a time (base concrete followed by repair material), cured for 28 days, and contained three No. 3 bars with electrical wiring soldered to each end, ultimately extending out of the top of the two different concrete halves. After the second 28 day curing time, each bar had its two halves electrically coupled via a 100 ohm resister to allow the measurement of the voltage drop across each bar over time, similar to the set-up of the Hansson (2006) study discussed in Section 2.9. Specimens were cured using a standard 7 days of wet curing and 21 days of air curing for both sets of curing times.

Although the base concrete already contained varying levels of NaCl, specimens were also placed in a 5% NaCl solution, with the water level 0.5 in. below the top of the specimens, to prevent any damage to the electrical wiring coming out of the specimens. This was done to allow for easier passage of ions through the different concrete halves while also accelerating the corrosion within the specimens. The small-scale corrosion molds and testing set-up are shown in Figure 288 and Figure 289, respectively.

Figure 288. Small-scale corrosion specimen molds

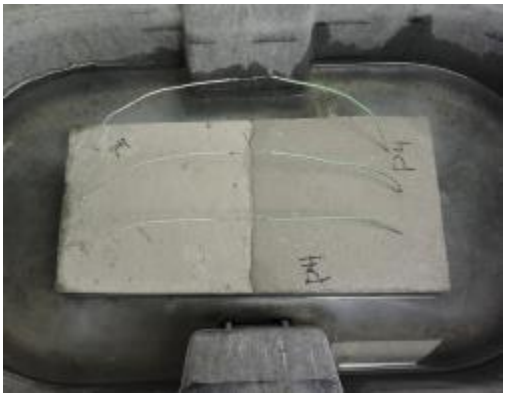

Figure 289. Typical small-scale corrosion testing specimen in the chloride solution

Though not a direct measurement of overall corrosion, the specific effect of different repair materials on the corrosion of steel rebar in base concrete are comparable to one another by comparing their macrocell currents. Macrocell current corrosion testing was done for a total of 10 weeks, after which the steel rebar was exposed in the 4% and 8% NaCl specimens for visual examination. The 0% specimens were left in their testing chambers and allowed to continue to corrode for an extended period of time. Using the visual examinations and the macrocell measurements it was possible to determine if the repair materials were likely to accelerate the corrosion process more or less than a typical bridge joint repair

7.5.2.2 Testing

After a week of testing, the Ductal® small-scale corrosion specimen containing 0% NaCl, D0, began to show signs of corrosion at the joint, unlike any of the other 11 specimens, as shown in Figure 290. By week two, all of the Ductal® specimens began to show signs of corrosion. The second and third specimens, however, showed signs of corrosion not through the obvious patching seen on D0, but through corrosion spotting, as shown in Figure 291. None of the other small-scale specimens exhibited signs of surface corrosion directly at the joint between the two materials, only experiencing light coloration around their edges where they were in contact with the 5% NaCl solution.

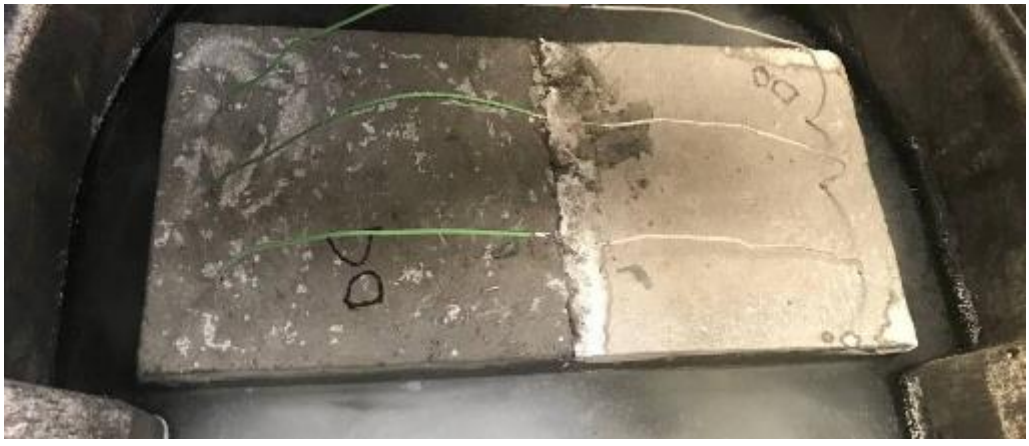

Figure 290. Initial joint corrosion in Ductal® small-scale corrosion testing specimen D0 - patching

Figure 291. Initial joint corrosion in Ductal® small-scale corrosion testing specimen - corrosion spotting

No measurable macrocell currents formed across any of the reinforcing bars in any of the specimens during the duration of this testing. This was due to insufficient amounts of corrosion across the reinforcing bars to induce a current that could travel across the two types of concrete that made up each specimen, despite the high levels of NaCl present in most specimens. This was a good sign for all of the concrete mixtures, since the presence of a measurable macrocell current would have indicated significant corrosion forming across the steel reinforcing on both sides of the bars.

Though no macrocell current values can be reported, the joints of the 4% and 8% NaCl specimens were chipped away to give some comparison of corrosion response of the four different repair materials, as discussed in the rest of this section and shown in Figures 292 – 295. Additionally, a photograph of the type of steel rebar put into these specimens before testing is presented as Figure 296 so that the difference between the typical amount and type of corrosion present on a piece of steel rebar before and after testing can be made clear. This difference is made most clear by the darker color and distinct starting location of the active corrosion (after testing). It is assumed in this testing that all previous surface corrosion was purely superficial and would have come off completely during either casting or chipping, and all actual surficial or pitting corrosion due to testing conditions would have occurred with or without the initial presence of this light surface corrosion.

As illustrated in Figure 293 and Figure 294, the excavation of the Ductal® and J3 specimens with 4% and 8% NaCl in the base concrete revealed minor pitting corrosion on a majority of their reinforcing bars, all congregated at the joint, with some traces of this pitting also forming on the base concrete side. Similarly, but to a higher degree, excavation of the ODOT AA specimens (Figure 292) revealed significant pitting corrosion on all of its reinforcing bars, starting exactly along the line of the joint and moving along the original ODOT AA (base) concrete side, almost to the point of complete coverage. This kind of corrosion happening only in the base material is exactly what could be expected of these specimens from the “Halo Effect” given the time period of testing.

Excavation of the Phoscrete specimens revealed significant amounts of pitting corrosion along the repair material side, with the 8% NaCl specimen also exhibiting a visible layer of surficial corrosion completely covering the reinforcing steel along the base concrete side.

Figure 292. Corrosion state of rebar reinforcing at joint of ODOT Class AA small-scale corrosion specimens with 4% NaCl (left) and 8% NaCl (right)

Figure 293. Corrosion state of rebar reinforcing at joint of J3 small-scale corrosion specimens with 4% NaCl (left) and 8% NaCl (right)

Figure 294. Corrosion state of rebar reinforcing at joint of Ductal® small-scale corrosion specimens with 4% NaCl (left) and 8% NaCl (right)

Figure 295. Corrosion state of rebar reinforcing at joint of Phoscrete small-scale corrosion specimens with 4% NaCl (left) and 8% NaCl (right)

Figure 296. Steel rebar before testing - typical

7.5.2.3 Results

Ultimately, conclusions about the “Halo Effect” taken from the small-scale corrosion testing can only be made through visual examination, and therefore the adequacy of each of the concrete types can only be evaluated on a relative basis with each other. Both the J3 and Ductal® UHPC materials produced similar results, both out-performing the standard ODOT AA mixture that would be used in a simple bridge deck repair. While there were no voltages, and therefore no macrocell currents, formed across any of the reinforcing bars at the conclusion of this initial testing, there were small amounts of voltages measured between adjacent bars within each of the small-scale corrosion specimens. These are not the readings that would indicate a macrocell forming due to the Halo Effect happening across the two different repair materials, but these readings do show a macrocell forming from just having bars adjacent to each other in each of these specimens.

7.5.3 Large-Scale Corrosion Testing

7.5.3.1 Procedure

The retrofitting process for the large-scale joint specimens included cutting the ODOT bridge slabs to an appropriate size (18 in. wide x 60 in. deep x 9 in. thick), chipping away 4 in. of the damaged concrete from the 18 in. width to expose the steel rebar, and casting a 5 in. x 60 in. x 9 in. repair replacement joint, producing a minimum 1 in. cover to the rebar exposed from the chipping process. The exposed No. 5 rebar layer revealed in each slab was connected together using a No. 5 longitudinal bar tied to the far ends of the exposed rebar sections. The longitudinal bar was placed on the topmost layer of reinforcing when laid down flat, putting it closest to what ultimately

became the finished surface, to allow for the needed wires to extend out of the top of the specimens. These electrical wires were soldered onto both ends of each connective longitudinal bar to allow for the DC power supplies to be connected after curing of the specimens. The slabs before and after chipping are shown in Figure 297 and Figure 298, with Figure 299 showing the final rebar construction.

Figure 297. Large-scale corrosion joint specimens before chipping

Figure 298. Large-scale corrosion joint specimens after chipping

Figure 299. Large-scale corrosion joint specimen with longitudinal connection bar in place

One joint specimen was cast for all four of the concrete mixes in this testing: ODOT AA, Ductal®, J3, and Phoscrete. After the joints were cast they were moist cured for 7 days and air cured for another 21 days. The added longitudinal bars were then connected to a DC power supply capable of supplying up to 3 A of current and the specimens were submerged in a 5% NaCl solution to accelerate the reinforcing bar corrosion using electrochemical methods similar to Wang et al. (2014, 2017) and Abosrra et al. (2011). This was accomplished using large wooden containers lined with plastic with a 5% NaCl solution at a level 2 in. below the top of the specimens to prevent any damage to the electrical wiring extending out of the specimens, like the setup of the small-scale corrosion specimens. All the wooden containers were given foam “feet” so that when the specimens were placed inside, they were elevated off the ground 1 in., allowing the testing solution to penetrate the bottom of the specimens.

From there, a proven corrosion testing set-up called the “electrochemical method” was utilized. The electrochemical method works by creating a complete circuit that runs through steel reinforcing (or similar conductive metals), which causes the steel reinforcing to release electrons, in turn oxidizing the steel reinforcing and corroding it. For this testing the required complete circuit was achieved by using a stainless steel rod sitting in the NaCl solution as a cathode (as shown in Figure 300) and the longitudinal steel reinforcing bar in the repair material side of each specimen as the anode. From there, each specimen was connected using electrical wiring so that a 0.2 A current could flow continuously from the positive terminal of the power supply to the steel reinforcing, through the concrete and surrounding NaCl solution to steel rod, and ultimately back to the negative side of the power supply. This test setup is shown in Figure 301.

Figure 300. Stainless steel rod and electrical wiring for large-scale corrosion testing

Figure 301. Large-scale corrosion testing setup showing power supplies (left) and all specimens in place (right)

After one week of supplying a current of 0.2 A through each specimen, the slabs were partially chipped back, starting from the side farthest from the input of the current, so that the first layer of vertical reinforcing could be visibly inspected for corrosion. From there, the slabs were chipped along each reinforcing bar layer by layer until a sufficient amount of corrosion could be observed. Once sufficient corrosion was achieved, chipping was done at the joint interface of each specimen along the same reinforcing bars as those chipped away previously. This was done to confirm if any corrosion had occurred between the base concrete and the repair material, and if so, which side(s) the corrosion occurred on. Once corrosion at the joint was confirmed, roughly ten weeks into the accelerated corrosion process, a final round of chipping was done along the joint, as close to the inflow of current as possible. This was done to observe the highest level of potential corrosion occurring within each specimen. Timing, location, and

progression of corrosion were all closely documented for each of the slabs and are detailed in Section 7.5.3.2.

7.5.3.2 Testing and Results

During the first week of testing, the water pools of each specimen began to fill with a coating of corrosion that had already begun to leech off, except for Phoscrete, which secreted a white film of unknow composition. This film is visible in Figure 302. After a week, the white film was covered with a corrosion film like the rest of the large-scale corrosion specimens. After two weeks of testing, the corrosion that was now in the water of all four specimens became sufficient to be present in all of the testing water, but mostly occupied the bottom of the testing containers. This level of corrosion was maintained through to the end of testing and is shown in Figure 303.

Figure 302. White film in water of Phoscrete large-scale corrosion specimen

Figure 303. Corrosion in water of typical large-scale corrosion specimens

During the first week of testing, a corrosion spot along the joint of the Ductal® specimen began to form. By week two, this corrosion spot was in the state shown in Figure 304. This could have been due to several reasons relating to a poor joint-face connection between the Ductal® and the old conventional concrete it was cast onto, but could also have been due to the Halo Effect occurring rapidly along this joint. The justification for not assuming a simple poor joint-face connection being that previous testing showed that Ductal® possesses exceptional bond strength to substrate (base) concrete, and therefore a poor bond was unlikely in this scenario.

From week three up until testing was concluded after 10 weeks, the surface corrosion along the Ductal® joint progressed at a steady rate, as shown in Figure 305. None of the other specimens showed any significant signs of surface corrosion during testing, except along the anticipated reinforcing bar paths.

Figure 304. Joint corrosion in Ductal® large-scale corrosion testing specimen during week 2 of testing (Ductal® on left side of image)

Figure 305. Joint corrosion in Ductal® large-scale corrosion specimen during week 5 of testing

Though none of the other specimens experienced joint corrosion, a strange interaction did begin to occur at the joint of the Phoscrete specimen starting roughly 45 days (week 7) after corrosion testing began. A thick, dark green liquid began to appear around the joint, similar to what leaked out and caused the white film in the surrounding solution in the first week of testing. The makeup and reasoning for this liquid forming are unknown, and no information on this phenomenon was found in the literature. However, it is hypothesized that something in the chemical make-up of Phoscrete (which contains magnesium, aluminum, phosphate, and multiple other chemicals to try to help prevent corrosion and freeze-thaw damage) reacted with the NaCl in the surrounding solution, and at this point in the testing the solution had made its way far enough into the joint to begin to interact and produce the green substance shown in Figure 306.

Figure 306. Green liquid in joint of Phoscrete large-scale corrosion specimen during week 7 of testing

Roughly 8 weeks into testing, the Ductal® specimen also began to produce a small amount of green liquid from its joint, however this liquid was much lighter in color than that seen on the Phoscrete specimen and was accompanied by streams of white liquid that seemed to trail down the joint, as seen in Figure 307. It is hypothesized that this liquid was also a by-product of a chemical reaction occurring between the NaCl solution and the Ductal® mix. The final states of these two unexpected chemical reactions happening at the surface of the Phoscrete and Ductal® specimens are shown in Figure 308 and Figure 309, respectively.

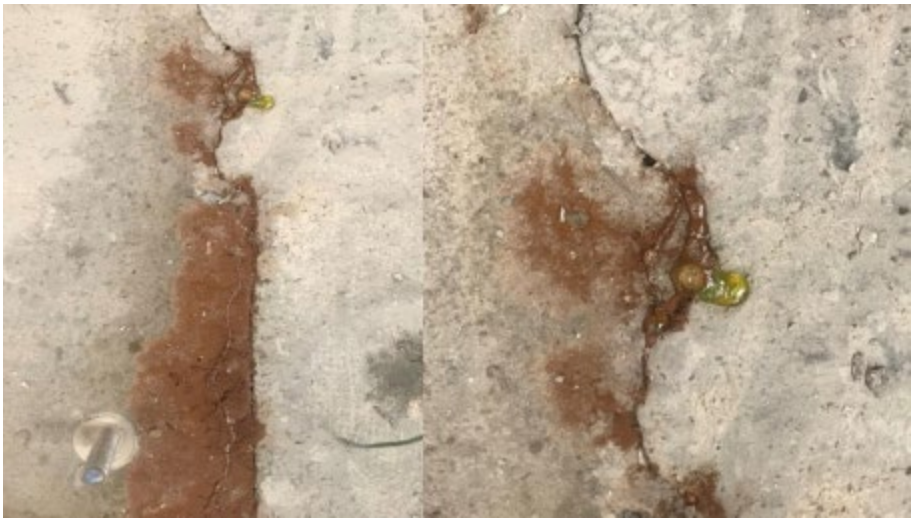

Figure 307. Green liquid in joint of Ductal® large-scale corrosion specimen during week 8 of testing

Figure 308. Green liquid in joint of Phoscrete large-scale corrosion specimen during week 10 of testing

Figure 309. Green liquid in joint of Ductal® large-scale corrosion specimen during week 10 of testing

After only a week of testing, the first sign of rebar corrosion was also visible. As shown in Figure 310, a thick black liquid began to be produced out of the exposed ends of each specimen. Though no more than a few inches of liquid was ever formed on any one bar, and the amount of each rebar end that was completely corroded off due to the formation of this liquid was never significantly high, only reaching a max of 0.75 in., this level of corrosion could still be cause for concern in the field. This is because the chemistry of steel rebar reacts with NaCl and other corrosive solutions found in the field

to produce a volume of reaction products 5 to 10 times that of the original material. This becomes a problem in the field because if internal reinforcing were to experience the kind of corrosion seen on the exposed rebar ends, it could generate large expansive forces that can crack and spall the concrete surrounding the reinforcing steel. The observed level of corrosion of the rebar ends was expected for this testing set-up. By the end of testing, the corrosion of the exposed rebar ends had reached the extent shown in Figure 311.

Figure 310. Visible confirmation of reinforcing bar corrosion during week 1

Figure 311. Typical level of reinforcing bar corrosion at the conclusion of testing - week 10

Figure 312 can be used as a guide to show the order in which sections of each specimen were chipped away to expose the reinforcing bars. Figures 313 – 316 provide updates of the specimens over the 10 week testing period, while Figures 317 – 320

show each layer of reinforcing steel immediately after chipping. The last section of steel reinforcing that was excavated and examined, after being completely removed from the testing setup, chipped, and allowed to sit out in open air for 24 hours, is also presented as Figure 321.This is significant because with no forced current or surrounding NaCl solution, all reactions of this exposed reinforcing steel came only as a result from what had already occurred within the specimens, and all pitting corrosion that revealed itself was previously present in the steel reinforcing.

Figure 312. Chipping sequence of large-scale corrosion specimens

Figure 313. Week 1 update for large-scale corrosion specimens using (a) ODOT AA, (b) J3, (c) Ductal®, and (d) Phoscrete

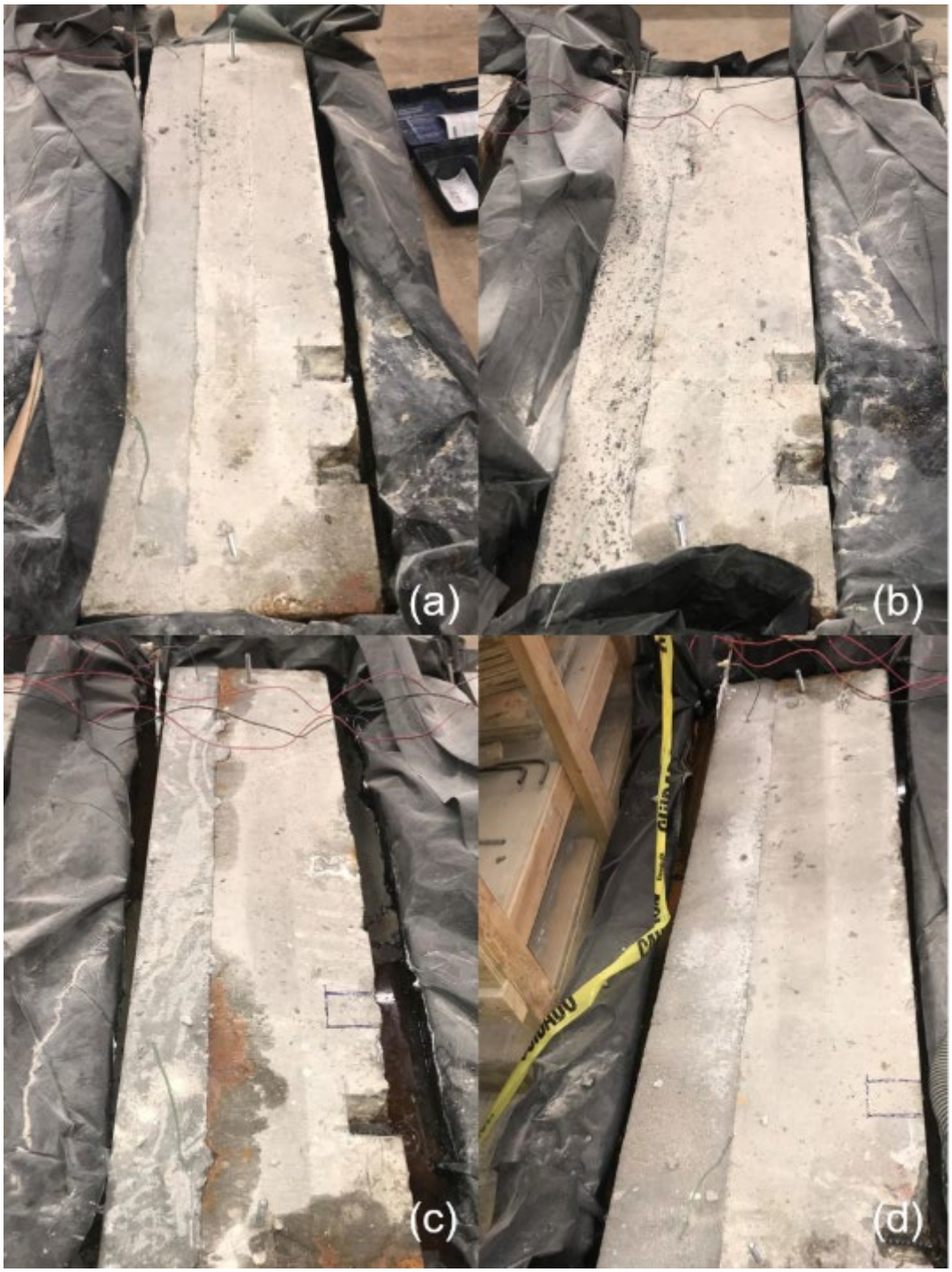

Figure 314. Week 3 update for large-scale corrosion specimens using (a) ODOT AA, (b) J3 (c) Ductal®, and (d) Phoscrete

Figure 315. Week 6 update for large-scale corrosion specimens using (a) ODOT AA, (b) J3, (c) Ductal®,and (d) Phoscrete

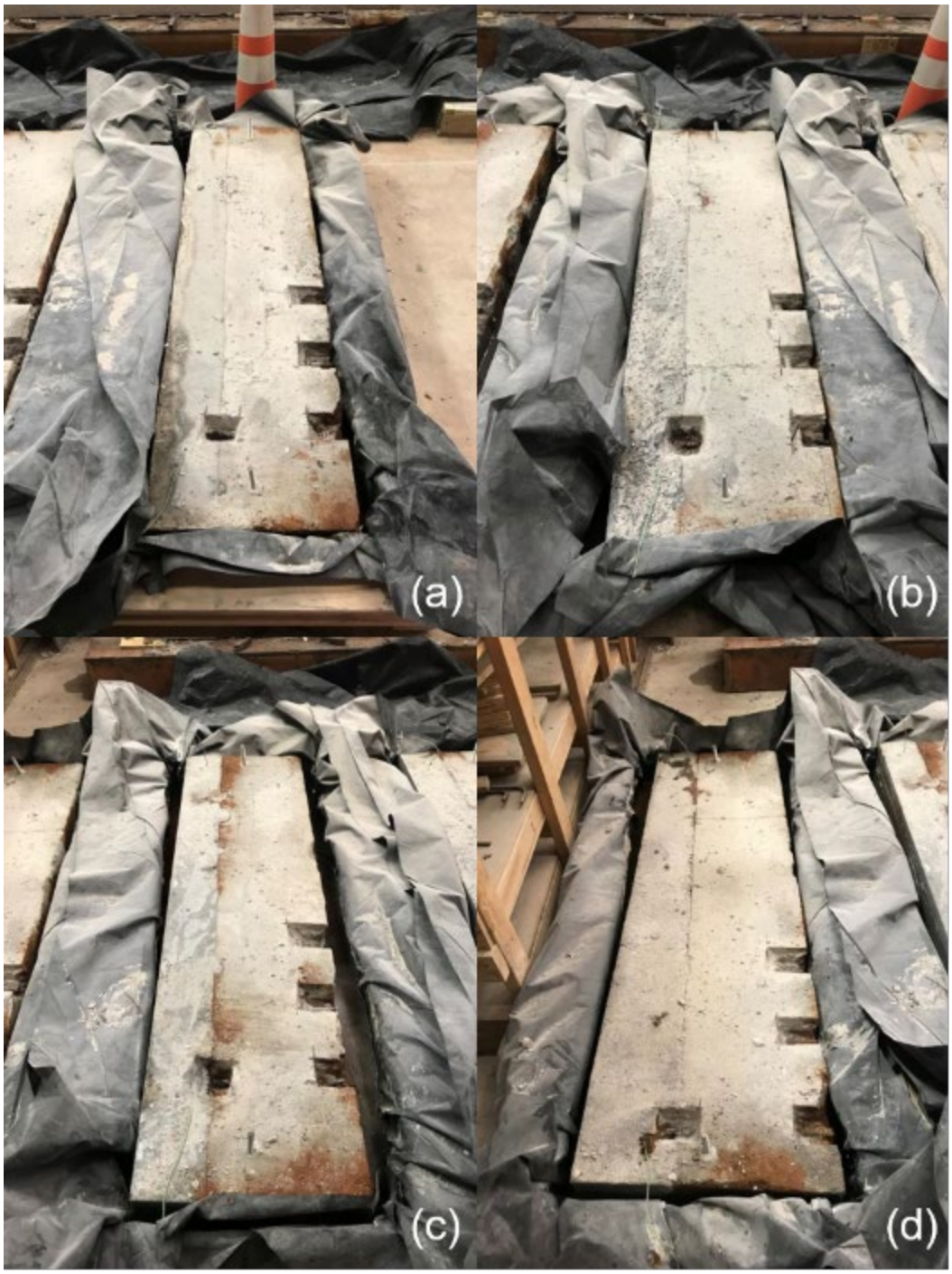

Figure 316. Week 10 update for large-scale corrosion specimens using (a) ODOT AA, (b) J3, (c) Ductal®, and (d) Phoscrete

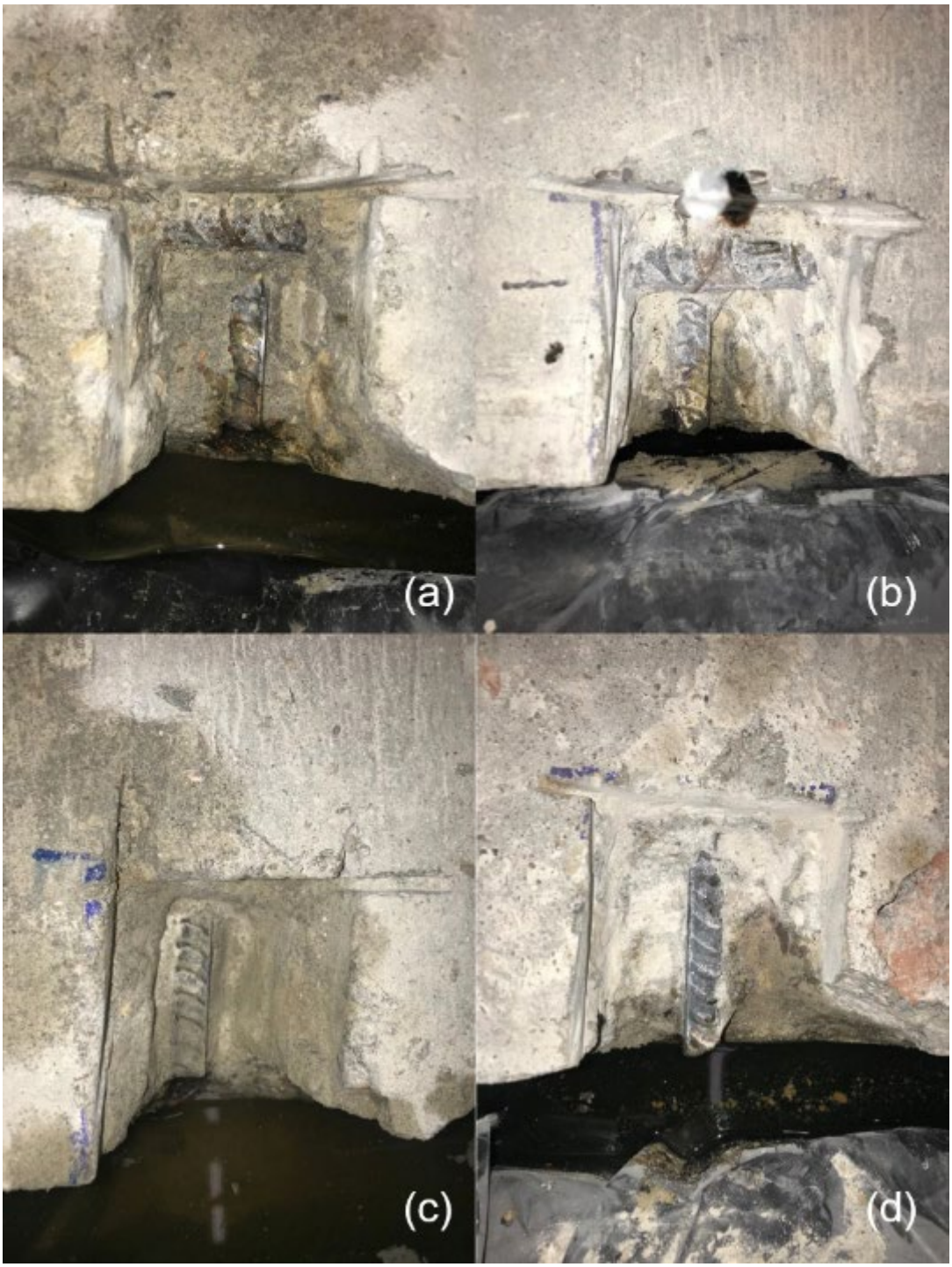

Figure 317. First rebar excavation for large-scale corrosion specimens using (a) ODOT AA, (b) J3, (c) Ductal®, and (d) Phoscrete

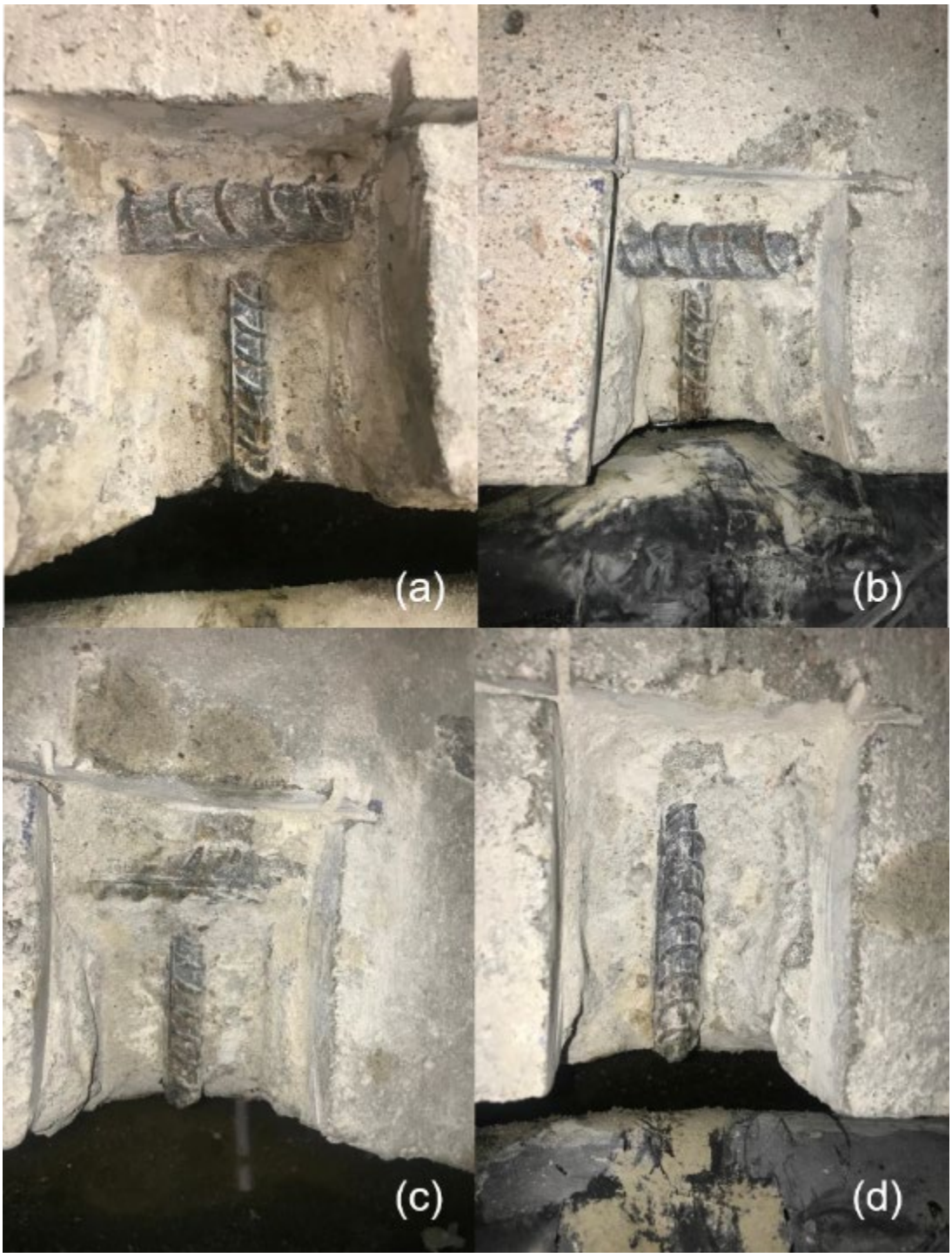

Figure 318. Second rebar excavation for large-scale corrosion specimens using (a) ODOT AA, (b) J3, (c) Ductal®, and (d) Phoscrete

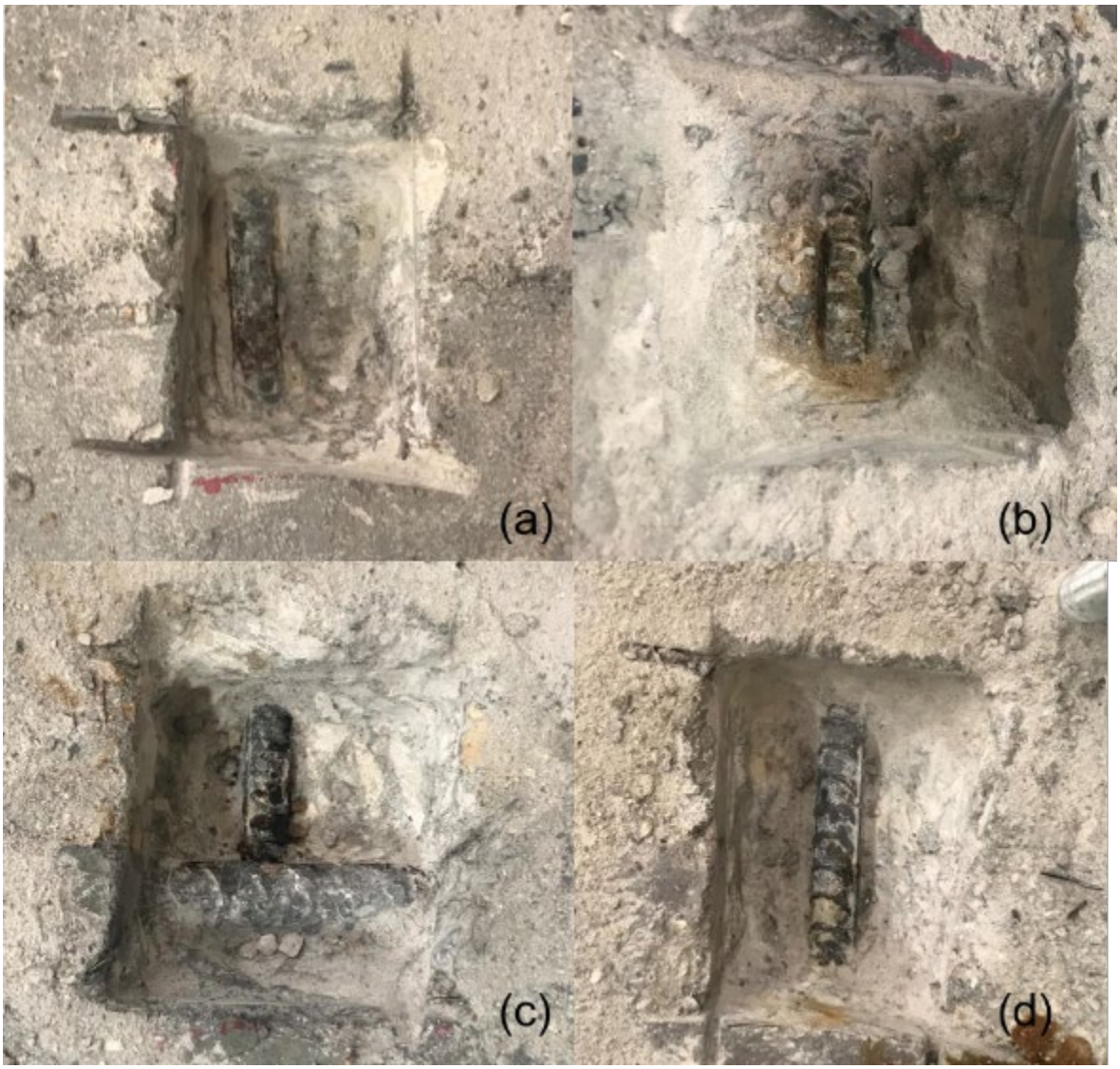

Figure 319. Fourth rebar excavation for large-scale corrosion specimens using (a) ODOT AA, (b) J3, (c) Ductal®, and (d) Phoscrete

Figure 320. Fifth rebar excavation for large-scale corrosion specimens using (a) ODOT AA, (b) J3, (c) Ductal®, and (d) Phoscrete

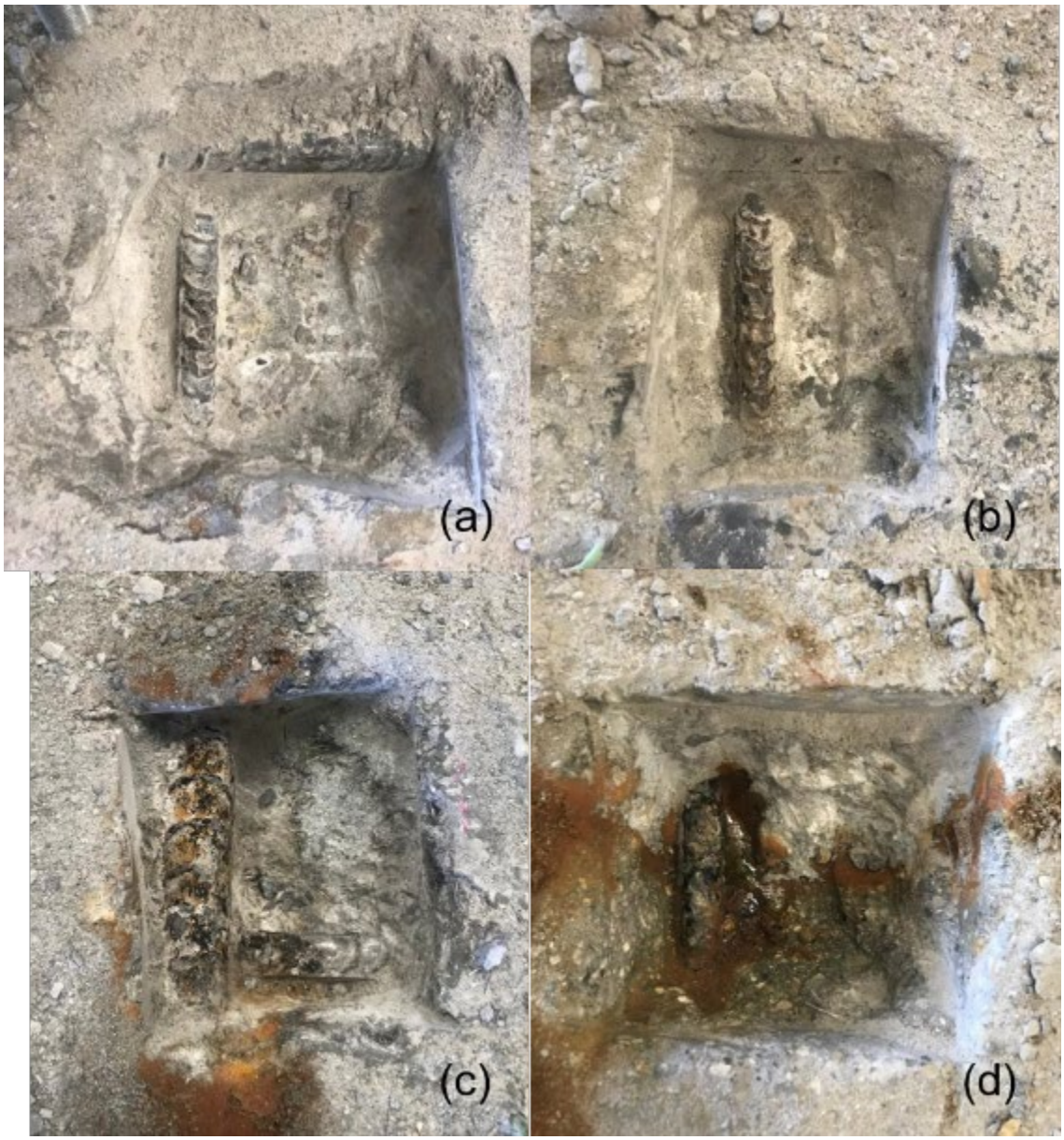

Figure 321. Fifth rebar excavation for large-scale corrosion specimens using (a) ODOT AA, (b) J3, (c) Ductal®, and (d) Phoscrete after 24 hours

The excavation of the reinforcing steel located in the large-scale corrosion specimens for visual examination can be broken up into two parts: excavation of rebar ends (numbers one through three) and excavation of rebar along the joint (numbers four and five). Excavation 1 occurred after 11 days of testing and revealed slight corrosion on the reinforcing steel near the exposed end of the ODOT AA and J3 specimens (up to 0.5 in. maximum), with no corrosion visible on the reinforcing steel of the Ductal® or Phoscrete specimens. Excavation 2 occurred after 25 days of testing and revealed

slightly more reinforcing steel corrosion than was previously seen on the ODOT AA, J3, and Phoscrete specimens, with significantly more corrosion now visible on the steel reinforcing of the Ductal® specimen (up to 1.5 in.). Though no photographs were taken of excavation 3, which occurred after 40 days of testing, similar results as those seen in excavation 2 were observed, with at least 1 in. of corrosion visible on the reinforcing steel of all four specimens. This amount of corrosion was sufficient to indicate that reactions could be occurring along the joint of each specimen. For that reason, excavation 4 was done along the same reinforcing bar revealed during excavation one, only now at the joint of each specimen, after 52 days of testing. This excavation revealed roughly 0.5 in. of surficial corrosion on the ODOT AA specimen, starting at the joint and moving into the repair material side, trace amounts of pitting corrosion around the joint of the J3 and Phoscrete specimens, and heavy amounts of pitting corrosion and staining occurring at the joint of the Ductal® specimen.

Excavation 5 was done after 70 days of testing on the closest layer of rebar to the inflow of current, again along the joint of each specimen to directly monitor the “Halo Effect” occurring in these specimens. This location did overlap the area in which the various liquids were coming out of the joints of the Ductal® and Phoscrete specimens with the intention of identifyiung the effect of these liquids on the reinforcing steel.

Ultimately, there was a surprisingly small amount of corrosion revealed on the ODOT AA specimen, likely because its pH was closest to that of the old concrete, so it did not have as strong of a reaction as the other repair materials did to this type of large-scale testing. The two UHPC repair materials did not hold up quite as well, with J3 showing minor surficial corrosion along the joint and Ductal® showing pitting and surficial corrosion starting at the joint and on both of the visible pieces of reinforcing steel on the base concrete side. Figure 322 provides evidence for the varying levels of complete surface corrosion by presenting pieces of the concrete that were chipped away during excavation 5 that pulled away surficial corrosion, i.e., Figure 322(a) shows a piece of base concrete with minor surficial corrosion on the side that made up the joint of the J3 specimen, while Figure 322(b) shows multiple pieces of base concrete that were covered with heavy surficial corrosion on multiple sides, all from the Ductal® specimen.

Within 60 seconds of revealing the reinforcing of the Phoscrete specimen, a puddle of the green liquid that had been present on the surface of the specimen since week 7 began to leak from the joint, until it reached the point shown in Figure 320(d) and seemed to steady out. After 24 hours however, the liquid had spread and corroded to the point shown in Figure 321(d). Slight pitting corrosion was also immediately visible along the reinforcing steel at the joint of the Phoscrete specimen, which was only exacerbated by the presence of the liquid leaking through. This observation proved that the green liquid seen on the surface of the Phoscrete specimen had to have been coming through the joint to the surface, and was something made and stored within the concrete, since the specimen was taken completely out of the testing set-up and exposed to air for the 24 hour waiting period, so it could not just be the surrounding NaCl solution leaking through.

Figure 322(c) shows pieces of the base concrete that was chipped away during excavation five of the Phoscrete specimen and not only shows the presence of surficial corrosion along the joint of the Phoscrete specimen (like that shown in Figure 322(a) and Figure 322(b) for J3 and Ductal®, respectively) but also the presence of the kind of staining caused by the green liquid that has leaked through the joint, indicating that the liquid was present even before excavation.

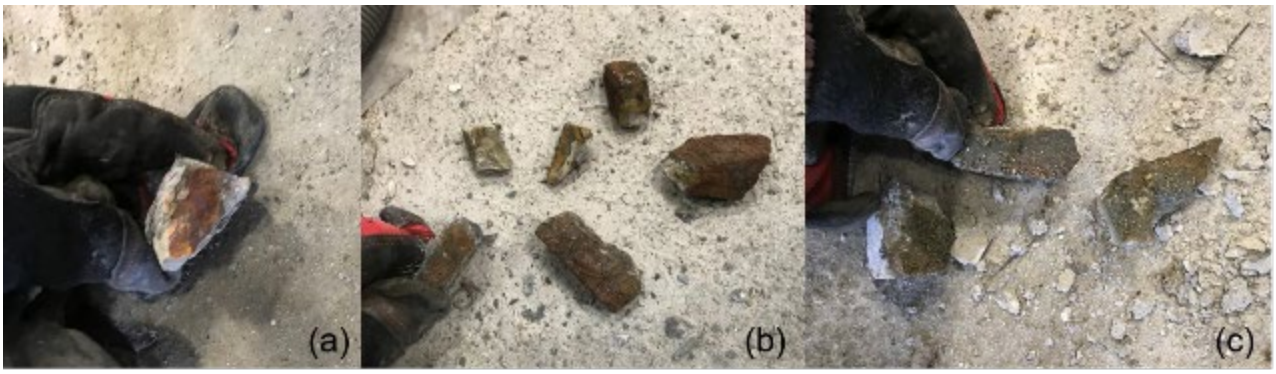

Figure 322. Evidence of surficial corrosion on large-scale corrosion specimens using (a) J3, (b) Ductal®, and (c) Phoscrete

In addition to the visual examination data, measurements of the change in voltage measured by each of the power supplies throughout the study were taken and are presented in Figure 323. In other words, the amount of voltage required to supply each specimen with the 0.2 A of current used throughout testing was recorded on

various dates during testing for comparison. This data is important because a larger voltage represents more energy being needed by the power supply to get the 0.2 A of current all the way through the specimen and back to the power supply. This in turn shows the resistance of the specimen to the flow of corrosion-inducing cycles, like the electrochemical (forced current) method used in this testing, with the specimen with the highest voltage readings being the most resistant. Based on these readings J3 showed to be the overall most resistant, with Phoscrete being the overall least resistant. These findings are very much in line with the visual examinations of both the small- and large-scale specimens.

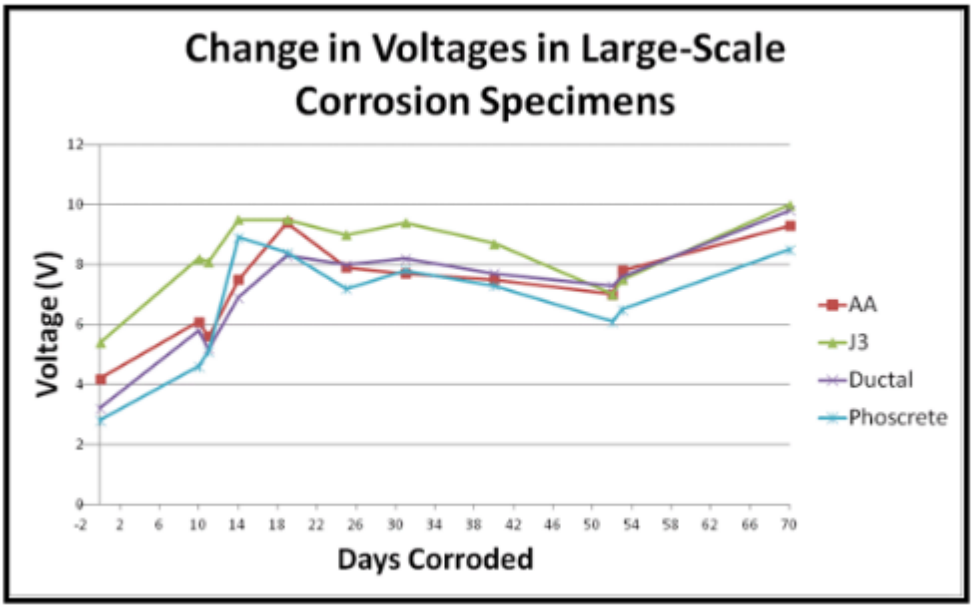

Figure 323. Change in voltage over time for all large-scale corrosion specimens

Based on the observed results additional testing is advised to assess Phoscrete's durability and corrosion properties to fully understand its behavior in the field. The final state of the south side of the large-scale Phoscrete corrosion specimen, the side that experienced the secretion of the unknown green liquid, is shown in Figure 324, which reveals the entire end to be a dark green color.

Figure 324. Final state of Phoscrete large-scale corrosion specimen after week 10

Cores were taken from the large-scale corrosion specimens to evaluate bond between the repair material and substrate. Split cylinder tests were performed to evaluate the relative level of bond at the substrate/repair material interface. The results of the split cylinder testing from cores taken through the repair material/substrate joint indicated bond strengths of 294 psi, 469 psi, and 597 psi for the Class AA, J3, and Ductal® repair materials, respectively. These results indicate excellent bond of the two UHPC mixes and that any corrosion at the joint between the repair materials and the substrate was not the result of water infiltration due to substandard bond. Photographs of the J3 and Ductal® split cylinder specimens are shown in Figure 325.

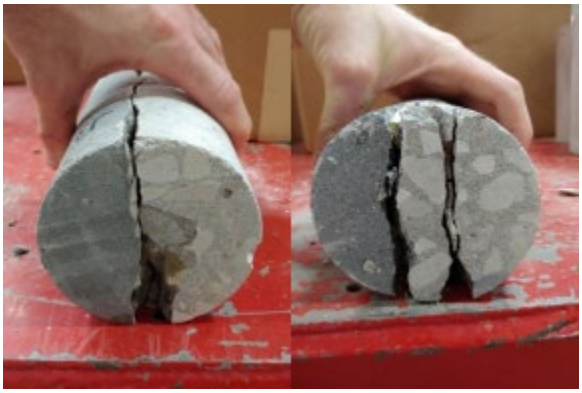

Figure 325. J3 (left) and Ductal® (right) split cylinder test specimens

Similar to the small-scale corrosion testing, visual examination is the primary tool available for analyzing the final results of this large-scale corrosion testing. However, based on all of the results, the large-scale joint corrosion testing revealed J3 to have the highest corrosion resistance followed by the Class AA, Ductal®, and Phoscrete materials.

8.0 Demonstration Joints

8.1 Overview of Joint Replacement

Originally it was planned to identify two damaged bridge expansion joints selected for removal and replacement through collaboration with ODOT, potentially as part of other bridge joint monitoring projects underway across the state. The joints were to be replaced using UHPC in the areas immediately adjacent to the joint (headers). The first bridge was to use the Lafarge product Ductal® and the second bridge was to use the J3 mix design developed as part of this project. Due to logistical difficulties the final replacement included a partial replacement of the areas immediately adjacent to a portion of one of the expansion joints on the SH-3E bridge over the N. Canadian River in Pottawatomie Co. (NBI No. 19276) and two demonstration joints cast at Fears Lab, one using Ductal® and one using the non-proprietary J3 mix.

The SH-3E bridge over the N. Canadian River in Pottawatomie Co. (NBI No. 19276), part of ODOT Division 3, was identified as a good candidate for demonstration of UHPC (an FHWA Every Day Counts Technology at the time) in Oklahoma as it had substantial deterioration around the expansion joints. The bridge was repaired specifically as a demonstration for UHPC, even though the replacement was not part of the ODOT 8 Year Construction Work Plan, using funding from the ODOT sponsored research project and the Division 3 maintenance crew. A portion of a single expansion joint was removed and replaced by Division 3 personnel using Ductal® for the joint headers. Photographs of the candidate bridge and joint are shown in Figure 326. The OU research team met with Mr. Walt Peters, Division 3 engineers, and a representative from FHWA on January 25, 2017 at the Division 3 office in Ada. Methods of joint replacement, general joint issues in Oklahoma, and the bridge to be repaired were

discussed and a plan was formulated at the meeting for retrofit of the bridge in conjunction with Division 3.

Figure 326. SH-3 bridge over N. Canadian River (left) and expansion joint to be replaced (right)

The plan consisted of replacing the joint over the west pier utilizing the unusually wide shoulders on the two-lane bridge to replace the joint in sections with limited disruption of traffic. The OU research team would provide support to the Division 3 crew related to mixing, placing, curing, and testing the UHPC. Approximately 1 ft of concrete was to be removed from either side of the existing joint depending on the condition of the concrete and as much of the reinforcement will be left in place as possible. The top of the joint was to be formed over to finish the joint ¼ in. higher than the surrounding concrete to allow for grinding and a chimney was to be used for placement to ensure positive flow of the UHPC. A vent hole was to be included on the opposite end of the joint. Heat curing would be applied using materials and recommendations to be provided by the OU research team until the compressive strength as determined by cylinder breaks reached 14,000 psi. When the appropriate compressive strength had been achieved, the joint would be ground smooth with the bridge deck, the expansion joint fill material would be placed, and the replaced section would be reopened to traffic. Manhattan Road & Bridge agreed to provide assistance in grinding the planned joint. Vibrating wire strain gauges with internal thermistors would be installed before concrete placement by the OU research team to monitor the joint performance and collect a

temperature history to relate to compressive strength. Data loggers would be placed on the parapet wall to ensure the equipment would be protected. Lafarge was contracted for rental of their mixers appropriate for this project, providing the required quantity of materials, and providing on-site support.

A site visit was made to the candidate bridge in May 2017 to identify potential sensor locations, pathways for sensor cables, and locations for the data acquisition equipment. A location on the parapet wall near the joint to be replaced was selected as a possible location for the data acquisition box and measurements were made across the shoulder to determine required cable lengths. Corrosion damage was visible at most piers in the end diaphragms, underside of the slab, beam ends, or pier caps, providing an indication of the need for joint replacement. Deterioration near the candidate joint is visible in the picture of the underside of the deck overhang shown in Figure 327.

Figure 327. Underside of the SH-3 bridge over N. Canadian River at the candidate joint showing concrete deterioration

A preconstruction meeting was held with Division 3 in Ada on September 8, 2017. At this meeting, modifications to the proposed joint details, methods to be used for construction, traffic control, and logistics of construction were discussed. An additional visit was made to the bridge with Division 3 personnel to discuss constructability issues. It was decided that a partial depth replacement will be sufficient near the expansion joint which would aid in constructability and reduce the time required to form the joint. The final joint detail used for construction is shown in Figure 328.

Concerns with differential shrinkage would be addressed by ensuring properly roughened and dampened surfaces of the existing concrete and exposing the top rebar mat. The deterioration shown in Figure 327 would not be disturbed as part of the proposed half depth patch and additional repairs would be necessary to repair that area. This additional repair was considered outside the scope of the UHPC implementation.

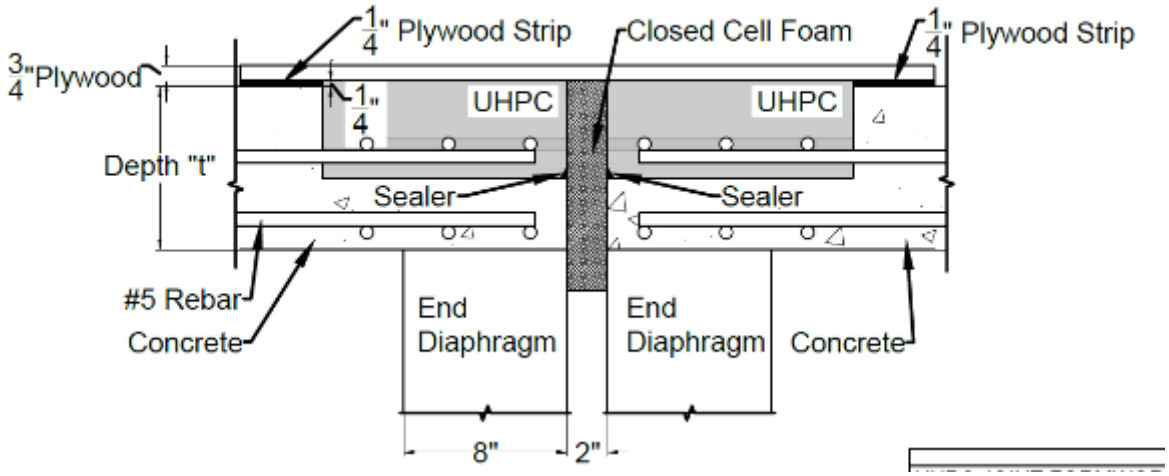

Figure 328. Details of the UHPC expansion joint headers including formwork

8.2 Procedures Developed for Joint Replacement

8.2.1 Overview

Methods of mixing, placement, curing, and strength testing were investigated along with specifications from other states in order to prepare for joint placement with limited data from the current, ongoing project. Results of this investigation were used to develop the following guidelines for joint replacement. Responsibilities for each aspect of the joint replacement are summarized in Table 56 and other procedures are included in the following sections. Some modifications were made to the timeline for grinding and reopening to traffic since the UHPC did not gain strength as quickly as expected. These changes are noted where applicable.

8.2.2 Safety

- All individuals involved in mixing shall wear eye protection, earplugs, dust mask or respirator, and latex or nitrile gloves.

- Gloves are recommended for all personnel.
- Care should be taken with regards to steel fibers by all personnel.

Table 56. Responsibilities for SH-3E bridge joint replacement

Item	Responsible Party	Timeframe
Traffic Control	ODOT Division 3	Before commencement of the project and throughout the duration
Transport of Mixers to the site	ODOT Division 3	Before commencement of the project
Transport of Generator to the site	OU	Before commencement of the project
Wiring Mixers to Generator	OU	Before first joint pour
Joint Demolition	ODOT Division 3	Each of three 15-16 ft sections beginning from the south side section will be removed immediately before joint forming and placement
Surface preparation 1 (roughening)	ODOT Division 3	After joint demolition
Joint Forming	ODOT Division 3	Immediately after joint demolition
Sensor Placement	OU	Concurrent with joint forming and before top is placed on the formwork
Transport of UHPC materials to the site	OU	Day of each section pour
Surface preparation 2 (prewetting)	ODOT Division 3	Immediately before placing formwork top and UHPC
UHPC Mixing	OU	After formwork completed, concurrent with joint placement
UHPC Placement	OU/ODOT Division 3	Concurrent with UHPC mixing
Quality Control (fresh)	Lafarge/OU	Concurrent with UHPC mixing and placement
Heat Curing	OU	After UHPC placement
Temperature Monitoring	OU	After UHPC placement
Quality Control (hardened)	OU	12 hours after UHPC placement, 24 hours, 28 days
Formwork Removal	ODOT	After UHPC reaches required strength
Grinding of Joint	ODOT/Manhattan	After formwork removal
Placement of Expansion Joint Material	ODOT/SSI	After grinding
Shifting Traffic for Subsequent Section	ODOT	After expansion joint material placement

8.2.3 Preparation

- Remove concrete from the old joint using saw and/or jackhammer with care taken to limit damage to the reinforcing steel.

- Roughen exposed surface by removal with jackhammer, intentional use of jackhammer, or by sandblasting.
- Leave rebar in place per the joint detail.
- Construct watertight formwork to the dimensions specified per the joint detail with the top of the formwork ¼ in. above the specified final elevation.
- Place new rebar as specified by the joint detail.
- Wet exposed concrete surfaces prior to casting the joint but do not leave water standing on the surface (i.e. saturated surface dry).
- Form over the top of the formwork to improve the surface and to retain moisture. Alternatively, prepare top formwork to be put in place as UHPC is placed into open joint.
- Cut a fill hole and construct a funnel-like structure at one end of the joint segment and cut a vent hole at the opposite end. Note that the fill hole used was not placed at the highest elevation but should be if used in the future.

8.2.4 Mixing Procedure

- Each batch was approximately 5 ft^3 and 3-4 batches were required per section.
- Weigh all materials and add ½ of the HRWR to mixing water.
- Mix premix dry for 2 minutes for Ductal®, should be modified to 10 minutes for J3.
- Add water (with ½ HRWR) slowly over the course of 2 minutes.
- Continue mixing for one minute.
- Add the remaining HRWR over the course of 1 minute.
- Mix will turn from powder to paste to flowable material (time for this varies but can potentially take up to 30 minutes).
- Once mix turns to flowable material, add steel fibers over the course of 2 minutes.
- Mix for an additional 1 minute after fibers are dispersed.
- Average total mixing time is approximately 20 minutes.
- Discharge an amount sufficient for temperature and flow measurements.
- Add additional HRWR if flow is insufficient.
- Retest temperature and flow if adjustments were made.

- Clean the mixer and simultaneously begin mixing in second mixer (cleaning between mixes may be forgone depending on the number required).
- Note that during the replacement only one mixer was used and it was not cleaned between mixes.

8.2.5 Quality Control

- Take flow and temperature measurements at completion of mixing, including measurement of ambient temperature.
- Test flow using the methods of ASTM C1437.
- Cast at least 18, 3 in. x 6 in. cylinders from a representative batch for each joint segment.
- At a minimum test a set of 3 cylinders at end of heat curing, 24 hours after casting, 3 days after casting, and 28 days after casting. Hold at least 3 additional cylinders in reserve in case additional tests are required. Note that cylinders were tested at 4 days instead of 3 days due to the strength gain of the material.
- Conduct all compression tests using the methods of ASTM C39 with the loading rate increased to 150 psi/s. All cylinders were tested at Fears Structural Engineering Laboratory by the OU research team.

8.2.6 Reporting

- For each batch record and compile the following in a report for each segment:
    - Batch time
    - Testing time
    - Ambient temperature
    - Mix temperature
    - Static flow
    - Dynamic Flow, (note that this was not done as it is no longer required for UHPC according to ASTM C1856)
    - Premix lot
    - Location of placement
    - Notes on weather conditions, deviation from these instructions, and any other issues encountered

8.2.7 Placement

- Transport material from the mixer to joint using buckets or wheelbarrows.
- Pour material into funnel end and allow to flow across the joint segment. Alternatively, fill the joint formwork directly and place top of formwork in place while moving up the cross-slope of the bridge.
- Always pour UHPC into already placed material.
- Fill until material comes out vent hole and comes to equilibrium with fill hole at the high point of the bridge deck cross-slope.
- Leave under head for curing if possible.

8.2.8 Curing

- Cover with plastic as soon as possible.
- Place heat lamps spaced evenly over joint with heat lamp approximately 18 in. above finished surface. Alternatively, use heating mats or an enclosure with forced air heaters to achieve required temperatures.
- Alternatively, do not utilize heat curing, but allow to cure for 72 hours or until desired compressive strength is reached. Joint can be covered with a steel plate to allow reopening to traffic while curing.
- Begin curing.
- Continue heat curing for 12 hours, or as determined by the engineer for the given application.
- Remove heat lamps.

8.2.9 Final Elevation

- The top of the UHPC joint will have air pockets which should be removed by grinding.
- Final elevation shall be met by grinding the UHPC surface to the level specified on the joint detail.

8.3 SH-3E Joint Replacement

The majority of the work on the joint replacement for the SH-3E bridge over the N. Canadian River in Pottawatomie Co. (NBI No. 19276), part of ODOT Division 3, was

completed in December 2017. The original plan for the joint replacement was to replace the joint in three sections with each section completed over the course of two days. For example, the first section would be removed on December 11 and the first UHPC placed on December 12, the second section removed and UHPC placed on December 13 and 14, and the final section on December 18 and 19 leaving a Friday and weekend to correct for any problems. Each section would be heat cured after casting for the 12-hour duration identified during laboratory testing, a set of cylinders would be tested, and the joint re-opened to traffic immediately after the required strength of 14,000 psi was confirmed. The width of the bridge is such that this replacement schedule would always allow for maintenance of two lanes of traffic. The scope of the replacement was adjusted after the first casting day due to slow strength gain of the material in the cold weather.

All required UHPC materials were transported to the ODOT Tecumseh maintenance yard by the OU research team on December 7 and the generator required for powering the concrete mixers was delivered to the Tecumseh yard by the OU research team on December 8. Two high shear mixers rented from Lafarge were transported from Lafarge to the Tecumseh maintenance yard on December 4 and were transported to the bridge site by the OU research team on December 11, the day before the first scheduled pour. The generator was also transported to the bridge site on December 11 and the generator was wired to the mixers by an electrician hired by the OU research team. Figure 329 shows the mixers in place at the bridge site and wired to the generator. Traffic control was put in place by the ODOT Division 3 maintenance crew on December 11 and the first joint section (approximately 12 ft measured perpendicular to the roadway) was removed by the ODOT Division 3 maintenance crew on December 11. Concrete was removed to approximately 2 in. below the top rebar mat, for a total depth of approximately 6 in. which varied due to the roughness of the remaining concrete. Approximately 12 in. of concrete was removed on either side of the joint in the direction parallel to the roadway. The joint detail used for replacement approximately followed what is shown in Figure 328. During concrete removal the remains of an older steel finger expansion joint were discovered, and the crew did their best to work around this material. A decision was made to encapsulate the remainder of

the older joint. Existing rebar was kept in place and cleaned by sand blasting and a single No. 5 rebar (not epoxy coated) was placed parallel to the joint on each side. The concrete surface was roughened during removal and was sand blasted clean. Figure 330 shows the joint after concrete removal and other preparations, except for placement of the top form. All exposed concrete surfaces were wetted to a damp, surface dry condition immediately before the top form was placed.

Figure 329. High shear mixers used for mixing UHPC

Figure 330. Joint after removal of existing concrete and before placement of the top form

Two 6 in. Geokon vibrating wire strain gauges were placed in the joint header on the west side, one with its axis oriented perpendicular to the roadway (parallel to the joint) and one oriented parallel to the roadway (perpendicular to the joint). The gauge perpendicular to the roadway was located 83 in. from the face of the parapet and 4 in.

from the face of the joint. The gauge parallel to the roadway was located 88 in. from the face of the parapet and 7 in. from the joint face. The gauges are shown in Figure 331. Both gauges were connected to a Geokon datalogger placed in a steel box attached to the back side of the bridge parapet.

Figure 331. Strain gages within the joint header

Formwork for the joint opening consisted of sheets of Styrofoam stacked to create the proper opening width. Strips of ¼ in. plywood were attached to the bridge deck on either side of the joint and a top form consisting of sheets of ¾ in. plywood placed on top of the ¼ in. plywood sheets was attached to the concrete deck using screw anchors. The formwork was intended to create a concrete surface ¼ in. above the existing bridge deck to allow for grinding of the top surface to final grade. The top form had two holes cut on either side of the joint, one approximately 2/3 of the pour length from the parapet intended to be the fill hole and one at the parapet acting as a vent hole.

Raw materials were separated into the amount required for separate 5 ft^3 batches and staged on a flatbed trailer backed up to the concrete mixers. The Lafarge representative on site directed the mixing operations with the OU research team responsible for mixing and placement. The mixing procedure used was very similar to that used in the laboratory and consisted of mixing all dry ingredients for approximately 7 minutes followed by adding the required water and chemical admixtures slowly. Steel fibers were added after approximately 20 minutes of mixing. The UHPC was discharged

after approximately 35 minutes of mixing and the next batch was started immediately. The UHPC was transported from the mixers to the joint using four wheeled plastic carts and placed into a funnel in the fill hole using shovels. The east joint header was filled approximately 2/3 full with the first batch, the west side header was filled with the second batch to ensure equal pressure on both sides of the joint formwork, and the third batch was used to top off both sides. The material was allowed to flow from the fill hole to the vent hole and the joint was considered full when material was observed coming out of the vent hole. The Lafarge representative adjusted the water content of the mixture due to the cold weather conditions (30° to 40° F ambient temperature), adding slightly less water than the standard proportion.

The joint, with the top form still in place, was covered with insulating blankets and the heat lamps were put in place at 3:30 pm, approximately 2.5 hours after completion of the pour. The Geokon datalogger did not function properly due to a bad set of batteries, so manual measurements of the vibrating wire strain gages and associated temperatures were taken for the first 10.5 hours after the start of heat curing. The datalogger batteries were replaced and the gages were hooked to this apparatus at 2:00 am on December 13. Throughout heat curing, the internal concrete temperature slowly increased, but the same temperatures measured in the lab were never observed. Measured temperatures were consistently higher than the ambient temperature, which reached freezing during the night. The heat lamps were turned off at 6:00 am and cylinders were taken back to Fears Structural Engineering Lab for testing. Cylinders were tested at an age of approximately 20 hours including 15 hours of heat curing. Compressive strength test results are presented in Table 57.

Table 57. UHPC compressive strength for SH-3E joint

Age (days)	Compressive Strength (psi)
0.83 (20 hr)*	3580
3*	11,110
4	13,280
7*	15,600
14	20,900
28	22,430

Note: *indicates only two cylinders were tested

The compressive strength measured at 20 hours was well below the targeted value of 14,000 psi obtained in the laboratory. Based on the low early age compressive strength, concerns about the time required to achieve strength necessary to reopen the roadway to service, and concerns about potential differences between the material tested in the lab and that in the field, the Division 3 Engineer made the decision to halt the joint replacement after the first section. Traffic control was kept in place to protect the UHPC joint for 3 days at which time the compressive strength was in excess of 11,000 psi. However, the location of the joint on the shoulder of the roadway limits the amount of loading it would receive. The low ambient temperatures at the time of casting were primarily to blame for the poor strength gain. Careful attention should be paid to temperature on casting days and preparation of the constituent material to ensure a proper starting temperature for the UHPC.

The UHPC used for the joint was cast ¼ in. above the intended finished grade to allow for grinding of the portion containing a high concentration of air bubbles that tends to collect at the top of the material. Manhattan Road & Bridge agreed to provide grinding services in conjunction with another project in the area. Grinding was conducted on December 20, 2017 by a subcontractor to Manhattan, with two representatives of Manhattan present at the time of grinding. The UHPC had a compressive strength of approximately 15,500 psi at the time of grinding, and the machinery operator indicated no problems grinding the material. Photos before and after grinding are shown in Figure 332. The difference in elevation between the two bridge sections did create a problem in grinding the UHPC on both sides of the joint to the same elevation. A decision was made by the research team and ODOT maintenance engineers to match the grade of the higher section to avoid any damage to the bridge deck. The dimensions of the grinding equipment also did not allow for grinding immediately adjacent to the parapet. The difference in ground surfaces can be seen in Figure 332 and the entire section after grinding is shown in Figure 333.

Figure 332. UHPC joint before (left) and after (right) grinding

Figure 333. Entire joint after grinding

A representative of SSI Highway Products and the Division 3 bridge maintenance crew installed the joint sealant material in the replaced portion of the joint on the SH-3E bridge on March 30, 2018. Figure 334 shows placement of the sealant material after each header had been coated with epoxy. Figure 335 shows the end of a section of sealant where a bead of epoxy was applied to connect the next section. Since the original joint was wider than the planned 2 in. opening, the new joint headers were formed to produce an opening with a step down from a 2 in. width to a 3 in. width approximately 2 in. from the top of the joint. This prevented the joint material from being installed with the appropriate recess from the top of the joint. It was determined that this should not be a major issue since most of the replacement is on the shoulder area of the bridge but was noted for future installations. The completed joint fill material is shown in Figure 336.

Figure 334. Installation of joint sealant material by SSI Highway Products personnel

Figure 335. End of joint sealant prepared for splicing

Figure 336. UHPC joint headers on SH-3E bridge immediately after joint sealant was placed

Detailed photographs were taken of the joint immediately after formwork removal and grinding to provide a baseline for a visual assessment of joint performance. Visits were made to the SH-3E bridge periodically until December 2020 to take photos of the joint and monitor progress of any cracks. No cracking was observed between the UHPC header and the pre-existing bridge deck. Minor cracking transverse to the joint headers was observed in one of the first visits to the joint spaced along the length of the joint at 6 in. to 12 in. The crack widths were very small, but crack width was not measured and they did not widen over time. These hairline cracks are identified by black arrows in Figure 337. Some surface rusting of the steel fibers was also observed and is shown in Figure 338. Any exposed fibers broke away from the matrix, but no deterioration of the UHPC material around these locations was observed. Figure 339 shows photos of the joint over time. It is apparent from these photos that other than being covered with grit and gravel the joint is in very similar condition to when it was placed after 3 years of exposure. No new cracks or additional deterioration were observed over time.

Figure 337. UHPC joint headers on SH-3E bridge before joint sealant was placed and showing hairline cracks

Figure 338. UHPC joint headers on SH-3E bridge before joint sealant was placed and showing surface rusting of the exposed steel fibers

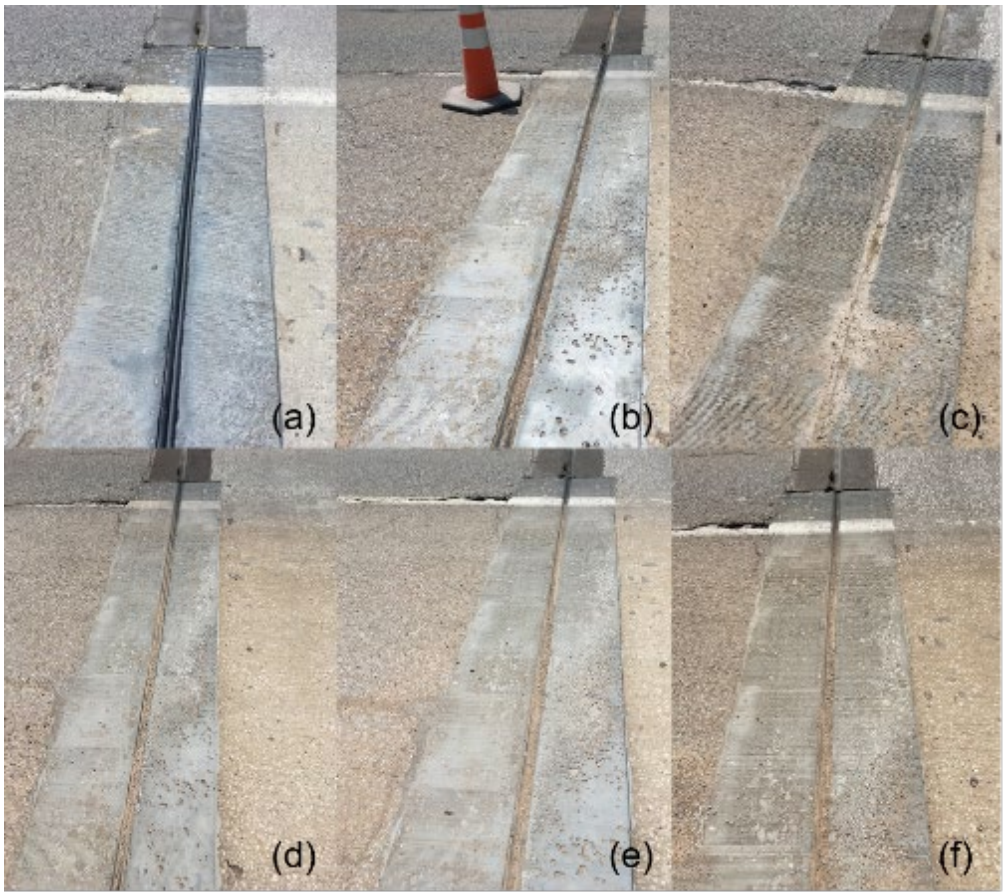

Figure 339. Photos of the UHPC joint on the SH-3E bridge over the North Canadian River (a) immediately after joint seal placement, on March 29, 2018 3 months after casting, (b) 7 months after casting, (c) 14 months after casting, (d) 21 months after casting, (e) 29 months after casting, and (f) 33 months after casting

8.4 Laboratory Demonstration Joints

Two small joint specimens were cast at Fears Lab in conjunction with training provided as part of this project in June 2018. One joint was cast with the Lafarge product Ductal® and one was cast with the J3 UHPC mixture developed by the OU research team. These joints were constructed using details based on those from the SH-3E bridge, but with the slabs placed on the ground. Each slab measured 2 ft wide by 8 ft long and was 8 in. thick. A 12 in. wide, half-depth section was formed into the slab during casting and reinforcing bars were left exposed to simulate removal of the concrete in the immediate vicinity of an expansion joint during retrofit, as shown in Figure 340. The Ductal® joint was cast ¼ in. high, but the J3 joint was cast flush with the top of the slab as air pockets were not observed near the top of cores taken from the slab joints tested and described in Section 5.4.2, making a sacrificial top surface unnecessary. The UHPC was placed into the forms directly (Figure 341) and then covered with plywood with weights placed on the plywood to seal the top. Each of the two UHPC materials had adequate workability to fill the forms under its own weight; however, the J3 mixture exhibited better flowability. All procedures developed from previous testing were implemented successfully. The slabs were cast inside Fears Lab but were moved outside and were monitored visually over time. The finished slab sections after formwork removal, but before placement outside are shown in Figure 342. Figures 343 and 344 shows the demonstration joints over time. No separation between the joint and base concrete nor any significant deterioration was observed.

Figure 340. Demonstration joint specimens before UHPC placement

Figure 341. Placement of the J3 UHPC into the demonstration joint specimen

Figure 342. Completed (a) Ductal® and (b) J3 expansion joint specimens

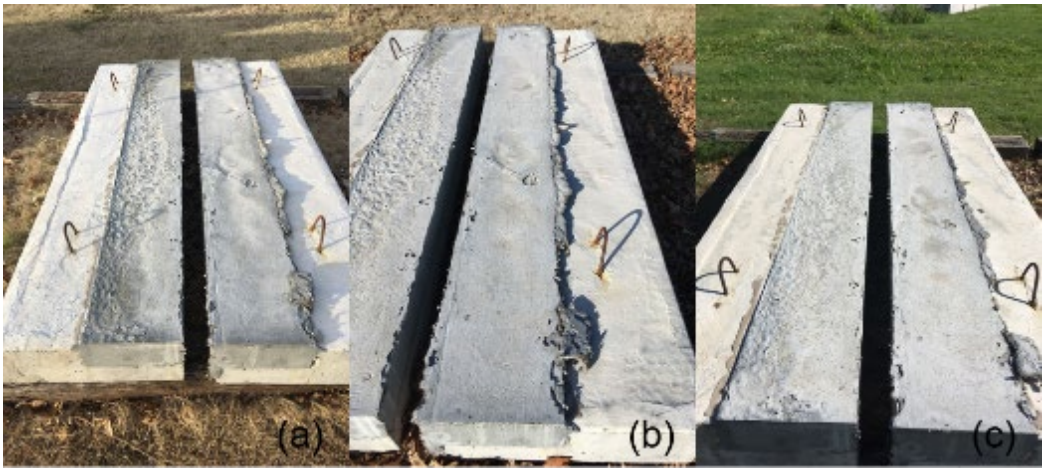

Figure 343. Ductal® demonstration joint (a) 8 months (b) 18 months, and (c) 23 months after casting

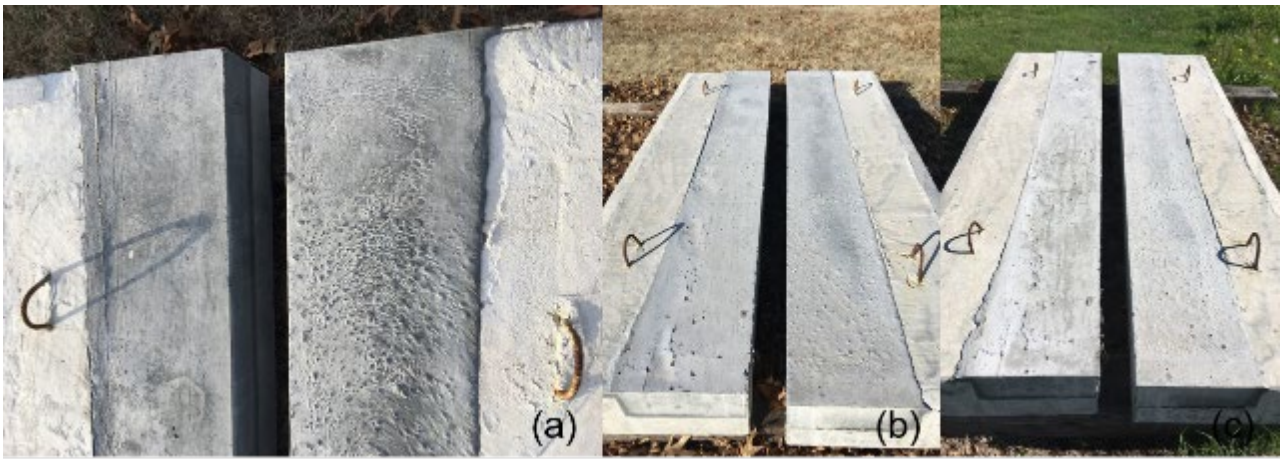

Figure 344. J3 demonstration joint (a) 8 months (b) 18 months, and (c) 23 months after casting

9.0 Cost Analysis

Data were collected on the costs of constituent materials used during development of the non-proprietary UHPC mix and during procurement of the materials for the demonstration joints. The steel fibers have proven to be by far the most expensive component of the non-proprietary mix designs. A comparison of the costs for the three non-proprietary mix designs examined in detail using the original Flex-Ten® stainless steel fibers tested and the Dramix® fibers used for Ductal® is shown in Table 58. This table provides values based on direct calculations using mean values for the costs of the mixture constituents. These estimates are not exact values as the level of precision in the table may imply but provide a value in the range of expected cost for cubic yard of material. Additional data have been collected on costs of non-proprietary UHPC mix designs developed by other researchers, both regionally and across the U.S. Results indicate comparative costs to those developed for the J3 mix.

Table 58. Cost estimates for non-proprietary mix designs

Material	Cost ($/lb)	J3 Flex-Ten®	J8 Flex-Ten®	J13 Flex-Ten®	J3 Dramix®	J8 Dramix®	J13 Dramix®
Type III Cement	$0.11	$0.00	$0.00	$21.25	$0.00	$0.00	$21.25
Silica Fume	$0.35	$68.81	$68.81	$68.81	$68.81	$68.81	$68.81
VCAS	$0.62	$0.00	$184.19	$0.00	$0.00	$184.19	$0.00
Fly Ash	$0.01	$0.00	$4.13	$0.00	$0.00	$4.13	$0.00
GGBFS	$0.02	$11.80	$0.00	$15.73	$11.80	$0.00	$15.73
Type I Cement	$0.06	$67.48	$67.48	$44.99	$67.48	$67.48	$44.99
Masonry Sand	$0.01	$26.05	$26.05	$26.05	$26.05	$26.05	$26.05
Steel Fibers	$1.00 for Flex Ten® $2.00 for Dramix	$255.20	$255.20	$255.20	$510.40	$510.40	$510.40
HRWR	$0.50	$14.75	$14.75	$14.75	$14.75	$14.75	$14.75
Total Cost/yd^3	--	$444	$621	$447	$699	$876	$702

10.0 Summary and Conclusions

10.1 Summary

The project described in this report examined multiple aspects of UHPC for use for bridge element connections and overall bridge repair. Mixing and placement methods were examined and recommendations were made for use of UHPC in Oklahoma. A UHPC mix design (J3) made with material constituents available in the state of Oklahoma and with potential for use in multiple bridge applications was developed by examining previous research, particle packing, and supplementary cementitious reactivity. This mix design was then extensively tested alongside a common proprietary mix design to examine behavior relative to material properties, bond to existing concrete and reinforcing steel, use as a connection material between slab sections, and for durability. Both materials exhibited satisfactory performance for the applications considered and the J3 material performed comparably to the proprietary UHPC material.

Connections of precast bridge girders for live load continuity using a proprietary UHPC material and intended for both new construction and existing bridge retrofit were examined. Structural testing showed that the continuity connections effectively increased the capacity of the girder system and have the potential to improve the performance of this type of construction.

A single implementation of UHPC was conducted in the form of replacement of an existing expansion joint on a bridge in Oklahoma. Proprietary UHPC was used for this construction, and while some difficulties were encountered during placement, the completed joint was a success. The joint was monitored for almost 3 years after construction and it was shown to exhibit excellent performance over time. Two demonstration joints similar to the one repaired in the field were also cast at Fears Laboratory on the OU campus. These joint specimens were cast using both the proprietary UHPC and J3 mixture developed as part of this project. These demonstration joints were monitored for more than two years and exhibited excellent performance.

10.2 Conclusions

10.2.1 Material Evaluation

- The proprietary UHPC material Ductal® was used throughout this project and exhibited satisfactory properties for use in bridge connection and repair applications. In most cases it exhibited better performance than the other materials tested.
- A non-proprietary UHPC class mix design, termed J3, was developed as part of this project. During material evaluation and testing it exhibited satisfactory properties for use in bridge applications. In the case of some durability tests and in terms of air bubbles at the surface of completed material, it exhibited better performance than the other materials tested.

10.2.2 Mixing and Placement

- All high shear mortar mixers examined in this research were able to adequately mix the UHPC materials tested.

- Recommendations were provided for mixing and placing both proprietary and non-proprietary UHPC.
- Heat curing can speed up the strength gain of both UHPC materials tested, but is difficult to successfully utilize in the field.

10.2.3 Bond Testing

- Failure of concrete bond specimens using proprietary UHPC typically occurred in the base concrete indicating excellent performance.
- The J3 material typically exhibited lower bond strength than the proprietary UHPC material but could achieve similar concrete to concrete bond with proper surface preparation. Sufficient workability is also required to achieve high bond strengths between UHPC and conventional concrete.
- In general, either an exposed aggregate surface or a sandblasted surface prepared with a pressure washer produced the best concrete bond results.
- The J3 non-proprietary UHPC material exhibited a lower bond strength than the proprietary UHPC material tested for both the pullout and beam splice testing. However, when normalized for compressive strength, the bond strength of the two materials was similar.
- Bond and slab joint testing indicated that the recommendations from previous research for development length of reinforcement in UHPC are adequate for the J3 mix design.

10.2.4 Slab Joint Testing

- All of the slab joint specimens had an ultimate capacity that exceeded the capacity calculated for a monolithic conventional concrete slab.
- Both the proprietary and non-proprietary slab joints had similar ultimate capacity.
- The half depth slabs had a lower cracking load than the full-depth slabs in general, but both sets of slab joints had similar ultimate capacity.
- All slab specimens exhibited separation at the joint between the conventional concrete and the UHPC joint during testing. This was more evident for the half-depth slab joints, which also exhibited less cracking in the conventional concrete than the full-depth joints.

- The failure modes of all slab joints indicated yielding of the reinforcing bars and no evidence of bar pullout was observed.
- Flexural stiffness of both the full-depth and half-depth slab joints steadily decreased over time when subjected to a cyclic fatigue load.
- The full-depth slab joints subjected to a cyclic load both failed due to reinforcing bar fatigue with no evidence of pullout from the UHPC joint.

10.2.5 Continuity Joint Testing

- The increase of flexural capacity within the girders resulting from the new construction (NC) and retrofit construction (RC) connections shows that precast prestressed girders made continuous for live load using a UHPC connection is a structurally superior system for total load capacity compared to two simple spans for the configuration tested.
- The RC connections had a smaller joint distance between each girder, with the addition of 6 in. of the girders being embedded in UHPC. This detail provided an increased stiffness at the joint compared to the NC continuity joint allowing for an increased girder capacity, less girder deflection, and an increase in reinforcing bar strain at the joint.
- The loads resulting in the girders' initial flexural cracking under the load point were all within a 7-kip range which leads to a good probability of when flexural cracking should occur when the configuration tested is loaded regardless of the joint detailing.
- Failure of the system was pushed out of the joint and into the girder for both NC and RC connections as shown by the lack of cracking occurring within the UHPC continuity joint.
- The RC joint configuration appears to have potential for strengthening existing bridges, if the girders can withstand the additional stresses applied from making them continuous for live load. In addition, the time dependent effects would be non-existent for these bridges and would decrease the amount of stress applied to the joint and girders.

- UHPC is potentially better than conventional concrete for continuity connections since it allows for smaller connections with less congested reinforcement due to shortened required splice lengths. This was demonstrated in the RC connection with the reinforcement yielding at ultimate capacity, and by the NC connection reaching 70 percent of the yielding strain.
- Time dependent effects could still cause cracking for a system with UHPC joints, but cracking would more likely occur along the joint interface, or in the girder as demonstrated in the positive moment testing.

10.2.6 UHPC Durability

- The J3 UHPC material exhibited similar performance to the proprietary material Ductal® in all durability testing and even surpassed Ductal® in some aspects of corrosion resistance.
- Results indicated that ODOT Class AA concrete is sufficient for use in the field in moderate-corrosive environments, and causes very little corrosion in steel reinforcing due to the Halo Effect during repairs.
- J3 exhibited durability performance sufficient for use in projects where UHPC's additional durability is desirable, such as highly corrosive environments or area's prone to freezing and thawing.
- Phoscrete exhibited some negative results relative to corrosion resistance during the lab tests that were not consistent with previous research or field implementation done as part of another project. These results may be a product of the test method and suggest further testing is needed.

10.2.7 Demonstration Joint Performance

- Several important lessons were learned during placement of the SH-3E demonstration joint that were applied in recommendations for future use of UHPC.
- The SH-3E demonstration joint and the demonstration joints cast at Fears Lab exhibited excellent performance over time.

10.3 Recommendations for Future Research

- Additional research is needed on use of the developed J3 UHPC in other applications such as link slabs.
- While the detail used for continuity connections in this research performed well, other potentially better methods for attaching rebar shear studs into the girder ends should be investigated for the retrofit connections.
- More research is need on requirements for shear reinforcement at the girder ends connecting into continuity joints for new construction joints to withstand the redistribution of stresses caused by the joint compared to a simply supported beam.
- Methods for increasing shear capacity of preexisting girder ends that were not intended for continuity connections should be investigated further.
- The effects of time dependent deformation induced forces acting on the joint when prestressed girders are connected shortly after prestress release should be investigated further.
- Results of UHPC continuity joint testing should be compared to tests of similar specimens cast using normal concrete in place of UHPC for the joints.
- Additional test methods for corrosion resistance of UHPC and Phoscrete should be considered along with longer term tests that do not require electrical methods.

References

2009 Standard Specifications Book, Construction Engineering Standards, Specifications, Materials and Testing, http://www.okladot.state.ok.us/c_manuals/specbook/oe_ss_2009.pdf, Oklahoma Department of Transportation, 2009.

Aaleti, S., Honarvar, E., Sritharan, S., Rouse, M. and Wipf, T. (2014) “Structural Characterization of UHPC Waffle Bridge Deck and Connections,” IHRB Project TR-614, Iowa Highway Research Board, Ames, IA.

AASHTO T 277e86 (1990) “Rapid Determination of the Chloride Permeability of Concrete,” American Association of States Highway and Transportation Officials, Standard Specifications - Part II Tests, Washington, D. C.

AASHTO (2017) AASHTO LRFD Bridge Design Specifications 8th Edition, Washington, D.C.

Abosrra, L., Ashour, A. F., and Youseffi, M. (2011) “Corrosion of steel reinforcement in concrete of different compressive strengths,” *Construction and Building Materials*, 25(10): 3915-3925.

ACI Committee 546. (2006) “Guide for the selection of materials for the repair of concrete.” ACI 546.3R-06, American Concrete Institute Farmington Hills, MI.

ACI Committee 408 (2003) “Bond and Development of Straight Reinforcing Bars in Tension (408R-03),” *Technical Documents*, American Concrete Institute, Farmington Hills, MI.

ACI Committee 562 (2013). “Code Requirements for Evaluation, Repair, and Rehabilitation of Concrete Buildings.” ACI 562M-13, American Concrete Institute Farmington Hills, MI.

ACI Committee 318 (2014). “Building Code Requirements for Structural Concrete and Commentary.” ACI 318-14, American Concrete Institute Farmington Hills, MI.

Ahlborn, T M., Harris, D. K., Mission, D. L. and Peuse, E. J. (2011) “Characterization of Strength and Durability of Ultra-High- Performance Concrete under Variable Curing,” *Transportation Research Record*, 2251(1): 68-75.

Anon [Internet], (2016, August) “North American Ductal® Bridge Projects.” www.ductal-lafarge.com

ASTM Standard C39. (2017). “Standard Test Method for Compressive Strength of Cylindrical Concrete Specimens,” ASTM International, West Conshohocken, PA.

ASTM Standard C78. (2016). “Standard Test Method For Flexural Strength of Concrete (Using Simple Beam with Third-Point Loading),” ASTM International, West Conshohocken, PA.

ASTM Standard C109 (2016) “Standard Test Method for Compressive Strength of Hydraulic Cement Mortars (Using 2-in. or [50 mm] Cube Specimens,” ASTM International, West Conshohocken, PA.

ASTM Standard C143. (2015). “Standard Test Method For Slump of Hydraulic-Cement Concrete,” ASTM International, West Conshohocken, PA.

ASTM Standard C231. (2017). “Standard Test Method for Air Content of Freshly Mixed Concrete by the Pressure Method,” ASTM International, West Conshohocken, PA.

ASTM Standard C496. (2017). “Standard Test Method For Splitting Tensile Strength of Cylindrical Concrete Specimens,” ASTM International, West Conshohocken, PA.

ASTM Standard C672. (2012). “Scaling Resistance of Concrete Surfaces Exposed to Dicing Chemicals,” ASTM International, West Conshohocken, PA.

ASTM Standard C882 (2013) “Standard Test Method for Bond Strength of Epoxy-Resin Systems Used with Concrete by Slant Shear,” ASTM International, West Conshohocken, PA.

ASTM Standard C1064. (2017) “Standard Test Method for Temperature of Freshly Mixed Hydraulic-Cement Concrete,” ASTM International, West Conshohocken, PA.

ASTM Standard C1202 (2017) “Standard Test Method for Electrical Indication of Concrete’s Ability to Resist Chloride Ion Penetration,” ASTM International, West Conshohocken, PA.

ASTM Standard C1437 (2015) “Standard Test Method for Flow of Hydraulic Cement Mortar,” ASTM International, West Conshohocken, PA.

ASTM Standard C1583 (2013) ”Standard Test Method for Tensile Strength of Concrete Surfaces and the Bond Strength or Tensile Strength of Concrete Repair and Overlay Materials by Direct Tension (Pull-Off Method),” ASTM International, West Conshohocken, PA.

ASTM Standard C1856 (2017) “Standard Practice for Fabricating and Testing Specimens of Ultra-High Performance Concrete,” ASTM International, West Conshohocken, PA.

ASTM Standard E965. (2015). “Standard Test Method For Measuring Pavement Macrotexture Depth Using a Volumetric Technique,” ASTM International, West Conshohocken, PA.

Berry, M., Snidarich, R., and Wood, C. (2017) “Development of Non-Proprietary Ultra-High Performance Concrete”, FHWA/MT-17-010/8237-001, Montana DOT, Helena, MT.

Bierwagen, D. et al., “Ultra-High Performance Concrete Waffle Slab Bridge Deck for Wapello County, Iowa,” HPC Bridge Views, Issue No. 65, January/February 2011. Available at http://www.hpcbridgeviews.org [Cited November 28, 2017].

Bornstedt, G. “Connecting Precast Concrete Bridge Deck Panels with Ultra High Performance Concrete (UHPC),” Western Bridge Engineer’s Seminar, Phoenix, AZ, September 25–28, 2011. Abstract only.

British Standard. (1999). “Products and systems for the protection and repair of concrete structures. Test methods. Determination of slant shear strength.” BS EN 12615:1999, British Standards Institution, 12.

Carbonell Munoz, M. A., Harris, D. K., Ahlborn, T. M., and Froster, D. C., “Bond Performance between Ultrahigh-Performance Concrete and Normal-Strength Concrete,” *ASCE Journal of Materials in Civil Engineering*, Vol. 26, No.8, Aug 2014.

Casey, C. (2019) “Ultra-High Performance Concrete for Connections of Precast, Prestressed Girders Made Continuous for Live Load,” M.S. Thesis, The University of Oklahoma, Norman, OK.

Chea, K. S. V. (2020) “Comparative study of proprietary and non-proprietary ultra-high performance concrete as partial-depth joint replacement,” M.S. Thesis, The University of Oklahoma, Norman, OK.

Chunping, G. U., Wei, S., Liping, G. U. O., and Quannan, W. (2016 “Effect of Curing Conditions on the Durability of Ultra-High Performance Concrete under Flexural Load,” *Journal of Wuhan University of Technology*, April 2016, 278-285, DOI 10.1007/s11595-016-1365-0

Climaco, J. C. T. S., and Regan, P. E. (2001). "Evaluation of bond strength between old and new concrete in structural repairs." Magazine of Concrete Research, 53(6), pp. 377-390.

Connecticut Department of Transportation (2016) “Repair of Steel Beam/Girder Ends with Ultra High-Strength Concrete – Phase II,” SPR 2295, Newington, CT.

Coleman, R. (2018) “Comparative Study of Surface Preparation and Bond Angle Combinations for Bridge Repair Using Ultra-High Performance Concrete Alternative,” M.S. Thesis, The University of Oklahoma, Norman, OK.

Denarie, E., and Bruhwiler, E., “Structural Rehabilitations with Ultra-High Performance Fibre Reinforced Concretes (UHPFRC),” *Restoration of Buildings and Monuments*, Vol. 12, No. 5/6, 2006, pp. 453-468

Diab, A. M., Eldin, M. R. T., and Elmoaty, (2016) A. E. M. A., “Slant Shear Bond Strength Between Self Compacting Concrete and Old Concrete,” *Construction and Building Materials* 130, pp.73-82.

Eamon, C., Chehab, A., & Parra-Montesinos, G. (2016). Field Tests of Two Prestressed-Concrete Girder Bridges for Live-Load Distribution and Moment Continuity. *Journal of Bridge Engineering, 21*(5).

El-Tawil, S., Alkaysi, M., Naaman, A. E., Hansen, W., and Liu, Z. (2016) “Development, Characterization and Applications of a Non Proprietary Ultra High Performance Concrete for Highway Bridges, RC-1637, Michigan Department of Transportation, Lansing, MI.

El-Tawil, S., Tai, Y.S., Meng, B., Hansen, W., and Liu, Z. (2018) “Commercial Production of Non-Proprietary Ultra-High Performance Concrete, RC-1670, Michigan Department of Transportation, Lansing, MI.

El-Tawil, S., Tai, Yuh-Shiou, and Belcher II, J. A. (2018) “Field Application of Nonproprietary Ultra-High-Performance Concrete, *Concrete International*, January 2018.

Floyd, R.W., and Volz, J. S., (2016) “ODOT Research Project Proposal: Evaluation of Ultra-High Performance Concrete for Use in Bridge Connections and Repair,” The Board of Regents of the University of Oklahoma.

Freyermuth, C. L. (1969) “Design of Continuous Highway Bridges with Precast, Prestressed Concrete Girders,” *PCI Journal*, 14(2): 14-39.

Funderburg, C. (2018) “Evaluation of Surface Preparation and Bond Angle Combinations for Joint Replacement using Ultra-High Performance Concrete,” M.S. Thesis, The University of Oklahoma, Norman, OK.

Funk, J. E. and Dinger, D. R. (1994) “Predictive Process Control of Crowded Particulate Suspensions,” Applied to Ceramic Manufacturing.

Graybeal, B. (2006) *Material Property Characterization of Ultra-High Performance Concrete*, FHWA-HRT-06-103, Federal Highway Administration, McLean, VA.

Graybeal, B. and Tanesi, J. (2007) “Durability of Ultra-High Performance Concrete., ” *Journal of Materials in Civil Engineering*, 19(10): 7 pp. https://doi.org/10.1061/(ASCE)0899-1561(2007)19:10(848)

Graybeal, B.A. (2009). *Structural Behavior of a 2nd Generation UHPC Pi-Girder*, FHWA-HRT-09-069, Federal Highway Administration, Department of Transportation, McLean, VA.

Graybeal, B.A. (2009). *Structural Behavior of a* Prototype UHPC Pi-Girder, FHWA-HRT-09-068, Federal Highway Administration, Department of Transportation, McLean, VA.

Graybeal, B.A. (2010). “Field-Cast UHPC Connections for Modular Bridge Deck Elements,” FHWA-HRT-11-022, Federal Highway Administration, Department of Transportation, McLean, VA.

Graybeal, B. (2010) “Behavior of Field-Cast Ultra-High Performance Concrete Bridge Deck Connections Under Cyclic and Static Structural Loading,” FHWA-HRT-11-023, Federal Highway Administration, McLean, VA.

Graybeal, B., (2011) “Tech Note | Ultra-High Performance Concrete,” FHWA-HRT-11-038, Federal Highway Administration, McLean, VA.

Graybeal, B. (2013) “Development of Non-Proprietary Ultra-High Performance Concrete for Use in the Highway Bridge Sector”, FHWA-HRT-13-100, Federal Highway Administration, McLean, VA.

Graybeal, B., (2014) “Design and Construction of Field-Cast UHPC Connections,” FHWA-HRT-14-084, Federal Highway Administration, McLean, VA.

Graybeal, B.A. (2014). Splice Length of Prestressing Strand in Field-Cast Ultra-High Performance *Concrete Connections*, FHWA-HRT-14-041, Federal Highway Administration, Department of Transportation, McLean, VA.

Graybeal, B. (2016) “Bond of Field-Cast Grouts to Precast Concrete Elements.” FHWA-HRT-16-081, Federal Highway Administration, McLean, VA.

Graybeal, B. and Tanesi, J. (2007) “Durability of Ultra-High Performance

Concrete.” *Journal of Materials in Civil Engineering*.

Graybeal, B.A. & Maya, L. (2017). “Experimental study of strand splice connections in UHPC for continuous precast prestressed concrete bridges.” Engineering Structures, 133, 81-90. doi:10.1016/j.engstruct.2016.12.018.

Habel, K., Denarie, E., and Bruhwiler, E., (2004) “Structural response of composite ‘UHPFRC-concrete’ members under bending,” Proceedings of the International Symposium on Ultra High Performance Concrete, Kassel, Germany.

Hansson, C.M., Poursaee, A., and Laurent, A. (2006) “Macrocell and Microcell Corrosion of Steel in Ordinary Portland Cement and High Performance Concretes.” *Cement and Concrete Research*, 36(11): 2098-2102.

Ibrahim, A., El-Chabib, H., and Eisa, A. (2013) “Ultrastrength Flowable Concrete Made with High Volumes of Supplementary Cementitious Materials, *Journal of Materials in Civil Engineering*, 25(12): 1830-1839.

Jones, D. A. (1966) *Principles and Prevention of Corrosion*. Prentice-Hall.

Keierleber, B. et al., (2010) “FHWA, Iowa Optimize Pi Girder,” ASPIRE, pp. 24–26. http://www.aspirebridge.org.

Khayat, K.H. and Valipour, M. (2018). “Design and Performance of Cost-Effective Ultra High Performance Concrete for Bridge Deck Overlays.” CMR 18-006, Missouri Department of Transportation, Jefferson City, MO.

Kim, H., Koh, T., Pyo, S. (2016) “Enhancing Flowability and Sustainability of Ultra-High Performance Concrete Incorporating High Replacement Levels of Industrial Slags,” *Construction and Building Materials*, 123: 153-160.

Landers, J. (2015) “Accelerating Innovation,” *Civil Engineering*, 85(9): 58-65.

Li, W., Huang, Z., Zu, T., Shi, C., Duan, W. H., and Shah, S. P. (2016) “Influence of Nanolimestone on the Hydration, Mechanical Strength, and Autogenous Shrinkage of Ultrahigh-Performance Concrete,” *ASCE Journal of Materials in Civil Engineering*, 28(1): 04015068.

Looney, T., McDaniel, A., Volz, J., and Floyd, R. (2019) “Development and Characterization of Ultra-High Performance Concrete with Slag Cement for Use as Bridge Joint Material”, *British Journal of Civil and Architecture Engineering*, 1(2): 1-14.

Maya, L., & Graybeal, B. (2017) “Experimental study of strand splice connections in UHPC for continuous precast prestressed concrete bridges.” *Engineering Structures*, 133: 81-90. doi:10.1016/j.engstruct.2016.12.018.

McDaniel, A. (2017) “Development Of Non-Proprietary Ultra-High-Performance Concrete Mix Design”, M.S. Thesis, University of Oklahoma, Norman, OK.

Miller, R., United States. Federal Highway Administration, & National Cooperative Highway Research Program. (2004). *Connection of simple-span precast concrete girders for continuity* (Report (National Cooperative Highway Research Program); 519). Washington, D.C.: Transportation Research Board.

Mobasher, B., Arora, A., Aguayo, M., Kianmofrad, F., Yao, Y., and Neithalath, N. (2019) “Developing Ultra-High-Performance Concrete Mix Designs for Arizona Bridge Element Connections, FHWA-AZ-19-745, Arizona Department of Transportation, Phoenix, AZ.

Momayez, A., Ehsani, M. R., Ramezanianpour, A. A., and Rajaie, H., (2005) “Comparison of Methods for Evaluating Bond Strength Between Concrete Substrate and Repair Materials”, *Cement and Concrete Research*, Vol. 35, No. 4, pp. 748-757.

Moore, B., (2012) “Little Cedar Creek Bridge—Big Innovation,” ASPIRE, p. 27. Available at http://www.aspirebridge.org.

Munoz, M.A.C., Harris, D.K., Ahlborn, T.M., Froster, D.C. (2014). “Bond Performance Between Ultrahigh-Performance Concrete and Normal-Strength Concrete.” ASCE 04014031, *J. Mater. Civ. Engin.*, 26(8):1-8.

Murray, C. D. (2017) “Understanding Ultimate Shear Behavior of Prestressed Concrete Girder Bridges as a System Through Experimental Testing and Analytical Methods, Ph.D. Dissertation, The University of Oklahoma, Norman, OK.

Oesterle, R., Glikin, J. D., & Larson, S. C. (1989). Design of precast, prestressed bridge girders made continuous / R.G. Oesterle, J.D. Glikin, and S.C. Larson. (Report (National Cooperative Highway Research Program); 322). Washington, D.C.: Transportation Research Board, National Research Council.

Oklahoma Department of Transportation, (2009) “ODOT Standard Specifications,” Transportation Commission, pp. 551.

Ozyildirim, H.C. and Volgyi, J.F.J., (2008) “Virginia’s Developments in the Use of Concrete in Bridges,” ASPIRE, pp. 50–52. http://www.aspirebridge.org.

Park, H. (2003). Model-Based Optimization of Ultra-High Performance Concrete Highway Bridge Girders, 139, Massachusetts Institute of Technology, Cambridge, MA.

Phares, B. (2014) “Laboratory and Field Evaluation of an Alternative UHPC Mix and an Associated UHPC Bridge,” Project in Progress, Iowa Department of Transportation, Ames, IA.

Ramirez, J.A. and Russell, B.W. (2008). *Splice Length for Strand/Reinforcement in High-Strength Concrete*, NCHRP Project 12-60 Report, Transportation Research Board, Washington, D.C.

RILEM (1994) “RC5: Bond Test for Reinforcing Steel. 1. Pullout test,” *RILEM Technical Recommendations for the Testing and Use of Construction Materials, 7-II-128*, E&FN Spon, London, U.K.

Royce, M.C., (2011) “Concrete Bridges in New York State,” ASPIRE, pp. 46–48. http://www.aspirebridge.org.

Russel, H. G., Graybeal, B. (2013) “Ultra-High Performance Concrete: A State-of-the-Art Report for the Bridge Community,” FHWA-HRT-13-060, Federal Highway Administration, McLean, VA. June 2013, 176 pp.

Saadeghvaziri, M., Spillers, W., and Yin, L. (2004) “Improvement of Continuity Connection over Fixed Piers,” FHWA-NJ-2004-017, Federal Highway Administration, Department of Transportation, Newark, NJ.

Sarkar, J., (2010) “Characterization of the Bond Strength between Ultra High Performance Concrete Bridge Deck Overlays and Concrete Substrates,” Michigan Technological University.

Sbia, L. A., Peyvandi, A., Lu, J., Abideen, S., Weerasiti, R. R., Balanchandra, A. M. and Soroushian, P. (2016) “Production Methods for Reliable Construction of Ultra-high-performance Concrete (UHPC) Structures,” *Materials and Structures*, 50(1): 1-19.

Shafei, B., Phares, B., and Shi, W. (2020). “Beam End Repair for Prestressed Concrete Beams,” IHRB Project TR-715, Iowa Department of Transportation, Ames, IA.

Shutt, C.A., (2009) “UHPC Joint Provides New Solutions,” ASPIRE, pp. 28–30. http://www.aspirebridge.org.

Tackett, A., Floyd, R., Ruiz, E., and Hale, W. (2009) “Effect of Mixer Type on the Performance of Ultra-High Performance Concrete”. Proceedings of the 11th Annual International fib Symposium, London, United Kingdom, June 22-24, 2009.

Tayeh, B. A., Abu Bakar, B. H., Mehat Johari, M. A., and Voo, Y. L., (2013) "Evaluation of bond strength between normal concrete substrate and ultra-high performance fiber concrete as a repair material," Procedia Engineering 54 pp. 554-563.

Toulemonde, F. and Resplendino, J. (2011) *Designing and Building with UHPFRC*, Wiley.

Wang, L., Yi, J., Zhang, J., Jiang, Y., Zhang, X. (2017) “Effect of corrosion-induced crack on the bond between strand and concrete,” *Construction and Building Materials*, 153: 598-606.

Wibowo, H. and Sritharan, S. (2018). “Use of Ultra-High-Performance Concrete for Bridge Deck Overlays.” IHRB Project TR-683, Ames, IA.

Wille, K. (2013) *Development of Non-Proprietary Ultra-High Performance Concrete for Use in the Highway Bridge Sector*, Report No. PB2013-110587, NTIS, Springfield, VA.

Wille, K., Naaman, A., and Parra-Montesinos, G. (2011) “Ultra-High Performance Concrete with Compressive Strength Exceeding 150 MPa (22 ksi): A Simpler Way,” *ACI Materials Journal*, 108(1): 46-54.

Wille, K., Naaman, A. E., El-Tawil, S., and Parra-Montesinos, G. (2012) “Ultra-High Performance Concrete and Fiber Reinforced Concrete: Achieving Strength and Ductility Without Heat Curing, *Materials and Structures*, 45: 309-324.

Williams, E. M., Graham, S. S., Reed, P. A., and Rushing, T. S. (2009) *Laboratory Characterization of Cor-Tuf Concrete With and Without Steel Fibers*, ERDC/GSL TR-09-22, U.S. Army Engineer Research and Development Center, Vicksburg, MS.

Ye, Y., Hu, S., Daio, B., Yang, S., and Liu, Z. (2012) “Mechanical Behavior of Ultra-High Performance Concrete Reinforced with Hybrid Different Shapes of Steel Fiber,” CICTP (ASCE) 2012, pp. 3017-3028.

Yuan, J., and Graybeal, B. (2014). Bond Behavior of Reinforcing Steel in Ultra-High Performance Concrete, FHWA-HRT-14-090, Federal Highway Administration, Department of Transportation, McLean, VA.

Zmetra, K.M. (2015). “Repair of Corrosion Damaged Steel Bridge Girder Ends by Encasement in Ultra-High Strength Concrete.” PhD Dissertation, University of Connecticut, Hartford, CT.